

UC San Diego

UC San Diego Electronic Theses and Dissertations

Title

Structure and mechanical behavior of bird beaks

Permalink

<https://escholarship.org/uc/item/7064f0k0>

Author

Seki, Yasuaki

Publication Date

2009

Peer reviewed|Thesis/dissertation

UNIVERSITY OF CALIFORNIA, SAN DIEGO

STRUCTURE AND MECHANICAL BEHAVIOR OF BIRD BEAKS

A dissertation submitted in partial satisfaction of the
requirements for the degree
Doctor of Philosophy

in

Materials Science and Engineering

by

Yasuaki Seki

Committee in charge:

Professor Marc A Meyers, Chair
Professor David J. Benson
Professor Falko Kuester
Professor Vlado A. Lubarda
Professor Joanna McKittrick

2009

Copyright
Yasuaki Seki, 2009
All rights reserved.

The dissertation of Yasuaki Seki is approved, and
it is acceptable in quality and form for publication
on microfilm and electronically:

Chair

University of California, San Diego

2009

DEDICATION

Dedicated to My Parents.

TABLE OF CONTENTS

Signature Page	iii
Dedication	iv
Table of Contents	v
List of Figures	ix
List of Tables	xix
Acknowledgements	xx
Vita and Publications	xxii
Abstract	xxiii
Chapter 1 Introduction	1
Chapter 2 Background	7
2.1 Biological Materials	7
2.1.1 Structure and Mechanical Properties	7
2.2 Biomimetic Aspects	11
2.3 Keratins	16
2.3.1 Keratinization	16
2.3.2 Classification	17
2.3.3 Mechanical Properties of Keratins	20
2.3.4 Mammalian Keratins	23
2.3.4.1 Skin	24
2.3.4.2 Hoof	27
2.3.4.3 Horns	33
2.3.5 Reptilian Keratins	37
2.3.5.1 Chameleon	37
2.3.6 Avian Keratins	41
2.3.6.1 Feather	41
2.3.6.2 Claws	45
2.3.6.3 Rhamphotheca	46
2.4 Cellular Solids	48

2.4.1	Structure of Foams	48
2.4.2	Mechanical Properties of Foams	53
2.4.3	Gibson and Ashby Constitutive Equations	54
2.4.4	Cancellous Bone	57
2.4.5	Beak Skull	61
2.5	Sandwich Structures	63
2.5.1	Synergism of Sandwich Structure	64
2.5.2	Force-Displacement Model of Sandwich Structure	66
Chapter 3 Experimental Techniques		70
3.1	Hardness Testing	70
3.1.1	Microindentation	70
3.1.2	Nanoindentation	72
3.2	Tensile Testing	73
3.2.1	Beak Keratin	73
3.2.2	Trabecula	75
3.3	Compression Testing	76
3.3.1	Beak	76
3.3.2	Trabecula	77
3.4	Microscopy for Structural Analyses	78
3.5	Computed Tomography	78
3.6	Transmission Electron Microscopy	79
3.6.1	TEM sample preparation	79
3.6.2	Tomography	80
3.7	Finite Element Method	81
3.7.1	CT Image Based Meshing	81
3.7.2	CAD Based Meshing	82
Chapter 4 Results and Discussion		84
4.1	Structure of Rhamphotheca	84
4.1.1	Scanning Electron Microscopy	86
4.1.2	Composition Analysis on Rhamphotheca	88
4.1.3	Transmission Electron Microscopy	91
4.1.4	TEM Tomography	94
4.2	Structure of Beak Foam	96
4.2.1	Scanning Electron Microscopy	96
4.2.2	Confocal Microscopy	99
4.2.3	Composition of Trabeculae	102

4.3	Mechanical Properties of Rhamphotheca	104
4.3.1	Micro-and Nanoindentation	104
4.3.2	Mechanical Behavior of Beak Keratin under Ambient Conditions	108
4.3.2.1	Tensile Properties	108
4.3.2.2	Fracture Analysis	111
4.3.3	Mechanical Behavior of Beak Keratin at High Humidity	116
4.3.4	Mechanical Role of Melanized Keratin	119
4.3.5	Beak Rhamphotheca	121
4.4	Mechanical Properties of Beak Foam	122
4.4.1	Micro- and Nanoindentation	122
4.4.2	Mechanical Behavior of Foam	124
4.4.3	Fracture Analysis	125
4.4.4	Mechanical Properties of Foam Materials	127
4.4.5	Gibson-Ashby Constitutive Models	133
4.4.6	Beak Foam	136
4.5	Mechanical Functions of Bird Beaks	137
4.5.1	Synergism of Bird Beak	137
4.5.2	Stability Analysis	140
4.5.2.1	Closed-Cell Foam	141
4.5.2.2	Open Cell Foam	149
4.5.3	Optimization Analysis	152
4.5.4	Bird Beak	156
4.5.5	Sandwich Construction of Bird Beak	157
4.6	Computational Modeling	162
4.6.1	Finite Element Analysis	162
4.6.2	Computed Tomography	170
4.6.2.1	Marching Cubes	171
4.6.2.2	Ray Casting Method	176
4.6.3	Finite Element Analysis with Computed Tomography	183
4.6.4	Bending Behavior of Beak	188
Chapter 5 Conclusions		193
5.1	Structure	193
5.2	Mechanical Properties	194
5.3	Sandwich Design	196
5.4	Modeling	196
Chapter 6 Future Work		198

References	199
----------------------	-----

LIST OF FIGURES

Figure 1.1: Schematics of a Toco toucan beak and layers of the beak.	5
Figure 1.2: Schematics of a wreathed hornbill beak and layers of the beak.	6
Figure 2.1: Examples of mineralized biological materials;(a) bone and dentin; (b) nacre (from Gao et al. [60])	9
Figure 2.2: Hierarchical structural organization of bone; cortical and cancellous bone at macrostructure; osteons with Haversian systems at microstructure; lamellae at sub-microstructure; collagen fiber assemblies of collagen fibrils at nanostructure; bone mineral crystals, collagen molecules, and non-collagenous proteins at sub-nanostructure (from Ji and Gao [61]).	10
Figure 2.3: Scanning electron micrographs; (a) nacre (scale bar 0.3 μm); (b) artificial nacre (scale bar 10 μm) (from Deville et al.[100]).	12
Figure 2.4: Force-displacement curves of nacre and artificial nacre tested under three point bending (from Deville et al. [100]).	13
Figure 2.5: Scanning electron micrographs (a) gecko setae (from Rizzo et al. [105]); (b) artificial gecko setae (from Lee et al. [103]).	14
Figure 2.6: (I) Natural and artificial setal array under testing at indicated positions. (II) Shear force-displacement curve;(a) artificial gecko setae;(b) natural setae (from Lee et al. [103]).	15
Figure 2.7: Keratinization process;(a) morphology of cross section of mammalian keratin; (b) flattening process of epidermal cells (from Tomlinson et al. [106]).	16
Figure 2.8: Classification of keratins.	17
Figure 2.9: Structure of α -and β -keratins;(a) α -coiled coil structure;(b) β -sheet (from Alberts et al. [74]).	18
Figure 2.10: (a) One of the pair symmetry related strands of β -sheet that make up the central framework of keratin filament. (b) Model for arrangement of β -sheet proteins of protein molecules in the filament of avian keratin (from Fraser and Parry [25]).	19
Figure 2.11: Material property chart for natural materials, showing Young's modulus vs density (from Wegst and Ashby [108]).	21
Figure 2.12: Material property chart for natural materials, showing strength vs density (from Wegst and Ashby [108]).	22

Figure 2.13: Two phase model of α -keratin. (from Feughleman [115]); (b)Schematic representation of stress-strain curves of wool, filament, and matrix. (from Wartmnn and Zahn [115]).	23
Figure 2.14: Structure of mammalian skin (from Fraser and Macrae [105]).	24
Figure 2.15: Stress-strain curve of elastin (from Fung [66]).	25
Figure 2.16: Comparison of untreated and chloroformmethanol-extracted stratum corneum; (a) delamination energy ;(b) peak stress.(from Wu et al. [124]).	26
Figure 2.17: Schematic of structure of hoof (from [43])	27
Figure 2.18: Diagram of hoof wall tubule composite. ;(A) High-magnification image of transversely sectioned hoof ;(B) Areas with tubules and intermediate filaments (IFs) ;(C) Schematic illustration of cross sections of tubules. ;(D) Three-dimensional reconstructions of tubules showing IF orientations of each cortical lamella (from Kaspi and Gosline [45]).	29
Figure 2.19: Hoof wall intertubular material composite diagram. (A) Cross-section of 10 mm thick hoof wall sample. Blue areas indicate circumferential molecular axial alignment, yellow areas reveal radial orientation. Purple areas in the hoof wall indicate axial alignment out of or perpendicular to the plane of section. ;(B) A three-dimensional representation of the intertubular material extruded from a tracing of Fig.2.18; (C) Three-dimensional models of intertubular material IF organization from each representative region. ; (D) longitudinally sectioned 10 mm thick hoof. Blue areas indicate longitudinal molecular axial alignment, yellow areas reveal radial orientation.(from Kaspi and Gosline [45]).	30
Figure 2.20: Mechanical performance of hoof wall;(a) Initial Young's modulus vs water content (from Kaspi and Gosline [45]);(b) J-integral vs cross head rate (from Kaspi and Gosline [44]).	31
Figure 2.21: Scanning electron microgrphs of fracture surface of hoof. (A)low magnification and (C) High magnification at 1.7×10^{-5} m/s. (B)low magnification and (D) high magnification at 2.5 m/s. Scale bar low magnification 1 mm and high magnification 100 μ m. (from Kaspi and Gosline [45]).	32
Figure 2.22: Tubes of horn (from Ryder [127]).	33
Figure 2.23: Nasal and frontal horns of white rhinoceros in sagittal section. (A) fluorescent light;(B) and (C) horn laminae in white light;(D) CT scan (from Hieronymus et al. [128]).	34

Figure 2.24: (a) Transverse section of rhinoceros horn (from [128]); (b) schematic of structure of white rhinoceros horn (from Hieronymus et al. [127]).	35
Figure 2.25: Stress-strain curve of horn keratin (from Druhala and Feughelman [131]).	36
Figure 2.26: Cross-Section of epidermis of American Chameleon. O: oberhautchen layer, B: beta layer, M: mesos layer, A: alpha layer (from Alexander and Parakkal [133]).	38
Figure 2.27: Cross-section of integument of American chameleon. Co: stratum corneum, G: stratum germinativum, P: xanthophore layer, C: carotenoid containing cell, I: iridophore, M: melanophore layer, L: collagenous basement lamella (from Alexander and Fahrenbach [136]).	39
Figure 2.28: Light micrograph of iridophore crystals (marked I) from American chameleon skin (from Rohrich and Rubin [137]).	40
Figure 2.29: Schematic representation of structure of feather with scanning electron micrographs (from [69]).	42
Figure 2.30: Stress-strain curves in tension of feather rachis at three humidity conditions.(from Taylor et al. [148]).	43
Figure 2.31: Relative Young's modulus vs relative density of feather medulla (Bonser's results [149] with exponential fitting curve x-axis is revised with relative density).	44
Figure 2.32: Breaking stress under tension as a function of fractional distance from feather barb (from Butler and Johnson [150]).	45
Figure 2.33: Stress-strain curves of claw keratin at three different humidity conditions (from Taylor et al. [148]) ;(b) Water content and hardness of ostrich claw keratin (from Bonser [50]).	46
Figure 2.34: Picture of Toucan beak with schematics	47
Figure 2.35: Hardness of melanized and unmelanized bill keratin of European Starling (from Bonser [52]).	48
Figure 2.36: Tri-dimensional structure of foams;(a) aluminium;(b) packing spongy;(c) paper;(d) water bubbles;(e) luffa spongy (from Seki et al.[156]).	49
Figure 2.37: Scanning electron micrographs of natural foams;(a) hawthorn stem;(b) palm petiole (from Gibson et al. [159]).	51
Figure 2.38: Cell structure of cork, showing three different directions (from Siliva et al. [17,160]).	52

Figure 2.39: Typical compressive stress-strain curves of foam;(a) an elastic plastic foam;(b) an elastic brittle foam (from Gibson and Ashby [55]).	53
Figure 2.40: The deformation mechanism foam (a) open cell foam; (b) closed-cell foam. (from Gibson and Ashby [55]).	54
Figure 2.41: Closed cell cubic model;(a) undeformed and;(b) deformed(linear elasticity).	55
Figure 2.42: The formation of plastic hinges in a closed cell foam.	56
Figure 2.43: Vertebra or the femoral head are filled with a spongy structure called trabecular bone. The struts (or trabeculae) have a thickness on the order of a few hundred micrometers (from Fratzl and Weinkamera [70]).	58
Figure 2.44: Material property chart for natural materials (cancellous bone is highlighted in grey), showing Young's modulus vs density (from Wegst and Ashby [108]).	59
Figure 2.45: Material property chart for natural materials (cancellous bone is highlighted in grey), showing strength vs density (from Wegst and Ashby [108]).	60
Figure 2.46: Compressive stress vs. uniaxial compressive strain for three typical specimens of bovine subchondral trabecular bone (from Gibson [18]).	61
Figure 2.47: The cross section of toucan (a) and hornbill foams (b);(I) frontal view;(II) mid view;(III) proximal view.	62
Figure 2.48: Schematic representation of structure of beak foam.	63
Figure 2.49: Sandwich structures;(a) sandwich beam;(b) square column; (c) cylinder column.	64
Figure 2.50: Force-displacement curves of foam, shell, foam + shell, foam filled shell (from Hanssen et al. [57]).	65
Figure 2.51: Deformation pattern of sandwich construction under quasi-static loading; (a) shell thickness 1.95 mm;(b) shell thickness 2.45 mm;(c) shell thickness 1.50 mm. (from Hanssen et al. [57]).	65
Figure 2.52: Terminology applied for axial crushing column (from Hanssen et al. [56]).	67
Figure 2.53: Methodology of design formula for stroke efficiency of foam filled extrusion (from Hanssen et al. [56]).	69
Figure 3.1: Specimen preparation methods;(a) mounted in epoxy;(b) glued on the glass.	71

Figure 3.2: Microindenter (LECO M 400H1).	71
Figure 3.3: Nanoindenter (Hysitron).	72
Figure 3.4: Removal of specimens for tensile test.	73
Figure 3.5: Tensile specimens cut by laser;(a) longitudinal direction;(b) transverse direction.	74
Figure 3.6: Melanized and unmelanized toucan rhamphotheca	75
Figure 3.7: Apparatus of tensile testing of trabecula.	76
Figure 3.8: Specimens for compression test;(a) foam;(b) shell;(c) foam-filled shell.	77
Figure 3.9: Apparatus of compression testing of trabecula.	77
Figure 3.10: Staining process;first row is UA staining; second row is lead staining	80
Figure 3.11: TEM sample holder, rotating from -60° to 60°	81
Figure 3.12: FE beak foam model using CT image based meshing techniques.	82
Figure 3.13: FE beak model, the geometry is imported from CAD (Solid Works).	83
Figure 4.1: Photographs of beaks;(a) Toco toucan;(b) Wreathed hornbill. . .	85
Figure 4.2: Scanning electron micrographs of toucan rhamphotheca; (a) rhamphotheca consisting of multiple layers of keratin scales (side view);(b) overlapped keratin scales (laterally sectioned rhamphotheca) . . .	86
Figure 4.4: Scanning electron micrographs of hornbill rhamphotheca;(a) overlapped keratin scales (laterally sectioned rhamphotheca);(b) ridges (lateral section);(c) casque (lateral section).	87
Figure 4.5: NaCl salts on hornbill rhamphotheca	88
Figure 4.6: Energy disperse X-ray results;(a) toucan rhamphotheca;(b) hornbill rhamphotheca.	89
Figure 4.7: Comparison of scanning electron micrographs and X-ray dot mapping. (a) toucan rhamphotheca;(b) hornbill rhamphotheca.	90
Figure 4.8: Transmission electron micrographs of toucan rhamphotheca;(a) cross section;(b) lateral section (surface).	92
Figure 4.9: Transmission electron micrographs of hornbill rhamphotheca;(a) cross section;(b) lateral section (surface).	93
Figure 4.10: Transmission electron micrographs of toucan rhamphotheca;(a) angle of -60° ;(b) angle of 0° (c) angle of 60°	94
Figure 4.11: (a) Tomogram of toucan beak keratin ;(b) 3D rendering of intermediate filaments of toucan beak keratin.	95
Figure 4.12: Scanning electron micrographs of toucan foam;(a) magnification $\times 80$;(b) magnification $\times 300$	97

Figure 4.13: Scanning electron micrographs of hornbill foam;(a) magnification $\times 28$;(b) magnification $\times 150$	98
Figure 4.14: Mosaic of cross section of toucan lower beak captured by confocal microscopy.	100
Figure 4.15: (a) Confocal image magnification $\times 40$;(b) Confocal image processed with VisIt.	101
Figure 4.16: Energy disperse X-ray results;(a) toucan trabeculae;(b) hornbill trabeculae.	102
Figure 4.17: Amino acid analysis of toucan trabeculae.	103
Figure 4.18: Comparison of micro- and nanohardness of toucan and hornbill trabeculae.	104
Figure 4.19: Force-displacement curve. Nanoindentation load were applied $1000 \mu\text{N}$ on toucan keratin surface.	106
Figure 4.20: Scanning probe micrographs of toucan keratin surface;(a) polished keratin surface;(b) $500 \mu\text{N}$ applied surface;(c) $1000 \mu\text{N}$ applied surface.	107
Figure 4.20: Scanning probe micrographs of toucan keratin surface;(a) polished keratin surface;(b) $500 \mu\text{N}$ applied surface;(c) $1000 \mu\text{N}$ applied surface.	108
Figure 4.21: 14% elongation of a toucan longitudinal specimen.	109
Figure 4.22: Stress-strain curves of beak keratins;(a) toucan beak keratin;(b) hornbill beak keratin.	110
Figure 4.23: Scanning electron micrographs of tensile fracture of toucan keratin, strain rate 5.0×10^{-5} ;(a) magnification X2400;(b) magnification X5000.	112
Figure 4.24: Scanning electron micrographs of tensile fracture of hornbill keratin, strain rate 3.0×10^{-4} ;(a) magnification X300;(b) magnification X2000.	112
Figure 4.25: Scanning electron micrographs of tensile fracture of toucan beak keratin, strain rate 1.5×10^{-3} ;(a) magnification X1500;(b) magnification X6000.	113
Figure 4.26: Scanning electron micrographs of tensile fracture of hornbill beak keratin, strain rate 5×10^{-2} ;(a) magnification X300;(b) magnification X2000.	113
Figure 4.27: UTS and yield vs strain rate plot of longitudinal and transverse directions (toucan beak).	115

Figure 4.28: Histogram of rupture force from 200 SMC simulation of bond breakage at widely separated loading rate (From Evans and Ritchie [193] in Fig 4.).	115
Figure 4.29: Stress-strain curves of keratins at RH 45% and 95%.	117
Figure 4.30: Scanning electron micrographs of fractured toucan ramphotheca;(a) the fractured keratin surface ;(b) cross section of torn keratin. . .	118
Figure 4.31: Comparison of melanized and unmelanized keratins;(a) HV vs ap- plied loads; (b) Stress-strain curves of melanized and unmelanized keratins.	120
Figure 4.32: Comparison of micro and nano hardness of toucan and hornbill trabeculae.	122
Figure 4.33: Force-displacement curve. Nanoindentation load were applied $1000\mu\text{N}$ on toucan trabecula.	124
Figure 4.34: Typical compressive stress-strain curves for beak foam; (a) tou- can; (b) hornbill.	125
Figure 4.35: Fracture morphology of toucan closed-cell foam showing profuse trabecula bending ; (a) overall view ; (b) “green twig” fracture; (c) total fracture of trabecula.	126
Figure 4.36: Fracture morphology of hornbill hornbill closed-cell foam; (a) magnification $\times 32$;(b) magnification $\times 38$	127
Figure 4.37: (a) Typical stress-strain curve of toucan trabecula;(b) Scanning electron micrographs of fractured trabecula with EDX dot map- ping ;(c)Young’s modulus vs calcium.	128
Figure 4.37: (a) Typical stress-strain curve of toucan trabecula;(b) Scanning electron micrographs of fractured trabecula with EDX dot map- ping ;(c)Young’s modulus vs calcium.	129
Figure 4.38: Weibull distribution (strength vs probability).	130
Figure 4.39: Euler curve of trabeculae.	132
Figure 4.40: (a) Comparison data normalized relative strength $\sigma_{pl}^*/\sigma_{ys}$ plotted relative density. Lines represent open cell and closed cell foams;(b) Relative strength vs Relative density for toucan foam.	135
Figure 4.41: Stress-strain curves, shell+foam and foam-filled shell (toucan). .	137
Figure 4.42: Pictures of compressed specimens;(a) toucan beak shell;(b) tou- can foam filled shell.	138
Figure 4.43: Comparison of compressive response of foam-filled shell between experiment and model. The model is indicated by black lines (F_{avg}^{mo} and D_S^{ex}) and experimental results are indicated by black dotted lines (F_{avg}^{ex} and D_S^{ex}).	140

Figure 4.44: Radius to thickness ratio a/t for typical engineering cylindrical structures (from Karam and Gibson [58]).	141
Figure 4.45: (a) Cross section of top and bottom portion of beak;(b) equivalent circular section for stability analysis;(c) equivalent beam subjected to compression and (d) equivalent beam subjected to bending.	142
Figure 4.46: Ratio of buckling load in uniaxial compression between hollow circular shell with and without cellular core, at the same weight ($\rho^*/\rho_s = 0.1$).	147
Figure 4.47: Ratio of:(a) maximum (Brazier) and (b) buckling moments between hollow cylinder shell with and without cellular core, at the same weight ($\rho^*/\rho_s = 0.1$).	148
Figure 4.48: Ratio of (a) buckling load in uniaxial compression and (b)buckling moment and (c) maximum (Brazier) between hollow circular shell with and without cellular core, at the same weight ($\rho^*/\rho_s = 0.1$).	150
Figure 4.48: Ratio of (a) buckling load in uniaxial compression and (b)buckling moment and (c) maximum (Brazier) between hollow circular shell with and without cellular core, at the same weight ($\rho^*/\rho_s = 0.1$).	151
Figure 4.49: Load ratio vs modulus ratio for a range of materials ;(a)uniaxial compression; (b) pure bending (From Dawson and Gibson [59])	155
Figure 4.50: Axial load ratio vs. modulus ratio, $a/t=100$ (adapted from Dawson and Gibson [59]) ,transition from buckling to material failure occurs at much higher normalized axial load for toucan and hornbill beaks than for synthetic sandwich structures.	156
Figure 4.51: Wegst-Ashby plot showing Young's modulus as a function of density. This is simplified diagram of Fig 2.11	157
Figure 4.52: Hierarchical structure of toucan beak; (a) picture of toucan beak, hollow parts are indicated by schematics; (b) surface morphology of beak keratin by SEM;(c) keratin scale structure by TEM, intermediate filaments are indicated by arrows; (d) cross sectional mosaic of lower beak by confocal microscopy; (e) cross section of keratin exterior by SEM ; (f) TEM of cross section of beak keratin, arrows indicate intermediate filaments; (g) scanning electron micrograph of foam structure, the cells are sealed by membranes.	159
Figure 4.53: Structure of hornbill beak with scanning electron micrographs and X-ray dot map; (a) interior foam structure ;(b) structure of keratin scales;(c) structure of casque; (d) structure of ridges with X-Ray dot mappings	160

Figure 4.54: Comparison of Young's modulus between keratin and trabeculae;(a) toucan; (b) hornbill.	161
Figure 4.56: FEM simulation of the beak shell under compression testing;(a) FEM model of shell; (b) onset of folding;(c) buckled shell;(d) completely collapsed shell.	163
Figure 4.56: FEM simulation of the beak shell under compression testing;(a) FEM model of shell; (b) onset of folding;(c) buckled shell;(d) completely collapsed shell.	164
Figure 4.57: FEM simulation of the beak foam under compression testing;(a) undeformed foam;(b) deformed foam.	166
Figure 4.59: Comparison between load vs.displacement curves from FEM calculation and experimental test results for thickness of 0.6 mm;(a) shell compression;(b) foam compression;(c) shell + foam compression (shell thickness: 0.4 mm).	168
Figure 4.59: Comparison between load vs.displacement curves from FEM calculation and experimental test results for thickness of 0.6 mm;(a) shell compression;(b) foam compression;(c) shell + foam compression (shell thickness: 0.4 mm).	169
Figure 4.60: Computed tomography;(a) toucan foam;(b) hornbill foam.	170
Figure 4.61: 16 cases for marching squares (from [180])	171
Figure 4.62: (a)Process of marching cube;(b)15 cases for marching cube (from [180]).	172
Figure 4.63: Algorithm of marching cube method in VTK	173
Figure 4.64: The original image is convert to image that marching squares are applied.	174
Figure 4.65: 3D models generated by marching cube;(a) toucan foam;(b) hornbill foam.	175
Figure 4.66: The ray casting method	176
Figure 4.67: Hornbill beak visualized with maximum intensity value.	177
Figure 4.68: Algorithm of ray casting method in VTK	178
Figure 4.69: 3 dimensional rendering of maxillary and mandibular beaks of toucan generated by ray casting ;(a) entire beak; (b) longitudinal sectioned entire beak.	180
Figure 4.70: 3 dimensional rendering generated by ray casting;(a) toucan foam with two cross sections (front and back side) ;(b) hornbill foam with two cross sections (front and back side).	181

Figure 4.71: 3 dimensional rendering generated by ray casting;(a) an edge of toucan foam captured by 27 μm resolution of $\mu\text{-CT}$. (arrows indicate concave) ;(b) casque region of hornbill captured by 45 μm of $\mu\text{-CT}$	182
Figure 4.72: Comparison of image to the model for finite element analysis;(a) CT image; (b) tri-dimensional models of cortical shell and trabeculae; (c) FE models of cortical shell and trabeculae, finally assembled.	184
Figure 4.73: (a) Deformation of foam in FE calculation;(b) Deformation of foam in experiment; (c) Deformation of hollow foam in experiment.	186
Figure 4.74: (a) Splitting of cortical shell at 0.1 strain;(c) Complete Buckled foam at 0.5 strain.	187
Figure 4.75: Comparison of experiment and finite element analysis in compression.	188
Figure 4.76: Experimental setup;(a) Bending configuration in experiment; (b) bending configuration in finite element model.	189
Figure 4.77: (a)Initial condition;(b)buckling	190
Figure 4.78: Comparison of experimental results and computational results with three different thickness of shell.	191

LIST OF TABLES

Table 2.1: Model parameters	68
Table 4.1: Mean elastic modulus and hardness of beak keratins	105
Table 4.2: Mean elastic modulus and hardness of trabeculae	123
Table 4.3: Model parameters of toucan foam	134
Table 4.4: Model parameters of toucan beak	139
Table 4.5: Material parameters of hornbill and toucan beaks	154
Table 4.6: Experimental and optimum modulus ratio	154
Table 4.7: Summary of Young's modulus of trabeculae and beak keratins . .	161

ACKNOWLEDGEMENTS

This research was inspired by a hunting trip taken by Marc A Meyers forty years ago. Walking through the forest with his father, Marc A Meyers found a toucan skeleton. He lifted the beak and was struck by its light weight and mechanical robustness. Hence, a posthumous acknowledgement is given to H. Meyers.

Matthew S Schneider guided me and Frank Grignon provided valuable help in finite element analysis during the early stage of this research. I greatly acknowledge support from Dr. Bimal Kad for providing the universal testing machine and for generous help in carrying out the mechanical testing in his laboratory. The author thanks to Robert Bailey for the help with tensile testing. A special gratitude goes to Professor Frank Talke and his students Yusuke Matsuda and Yeoung Chin Yoon for allowing and supervising equipment access for the nanoindentation tests. Professor Robert Mattrey and his scientist Jacqueline Corbeil at Moores Cancer Center for Computed Tomography provided valuable help. The author thanks Evelyn York at Scripps Institute (Analytical facility) for assisting with scanning electron microscopy and energy dispersive X-ray analysis. Professor Paul Price and Matthew Williamson at UCSD in Biology department guided us to conduct the structure analysis of beaks. Mason Mackey guided us to conduct transmission electron microscope analysis at National Center for National and Image Research Facility (NCMIR) at UCSD. Special thanks goes to undergraduate students at UCSD, Jai Parekh, Brandy Pearson, Joseph Sorrentino and Thomas Yang, who constructed environmental chamber for humidity testing. The author thanks the beak providers, Jerry Jennings of Emerald Forest Birds Gardens and Micheal Mace of San Diego Wild Animal Park. Sara G. Bodde gave me the valuable information about birds and helped me not only the experiments but also editing texts.

I would like to thank my adviser, Professor Marc A. Meyers for the special opportunity that he has given me to study a Toco toucan beak at UCSD. It is a still vivid memory when I have first received a toucan beak from him with a surprise. His

guidance and encouragement toward the research and mentoring have motivated me during my six years of study at UCSD. I cannot express my gratitude to him with a few words.

I would like to thank my committee members, Professor David J. Benson, Professor Falko Kuester, Professor Vlado A. Lubarda, Professor Joanna McKittrick, for their time and careful consideration of my work.

This research is supported by National Science Foundation, Division of Material Research, Biomaterials program (Grant DMR 0510138)

Chapter 3 and 4 are full reprints of the materials as it appeared in the following journals.

Yasuaki Seki, Matthew S. Schneider, Marc A. Meyers, "Structure and mechanical behavior of a Toco toucan beak ", *Acta Materiala*, 53, 5281-5296,2005.

Yasuaki Seki, Bimal Kad, David J Benson, Marc A. Meyers, "The toucan beak: Structure and mechanical response", *Materials Science and Engineering C* , 26, 1412-1420,2006.

Y.Seki, Sara G. Bodde, Marc A. Meyers, "Toucan and Hornbill Beaks:Comparative Study", *Acta Biomaterialia* submitted 2009.

VITA

- 2002 B. S. in Mechanical Engineering, Kumamoto University, Japan
- 2004 M. S. in Mechanical Engineering, University of California, San Diego
- 2009 Ph. D. in Materials Science and Engineering, University of California, San Diego

PUBLICATIONS

Yasuaki Seki, Matthew S. Schneider, Marc A. Meyers, "Structure and mechanical behavior of a Toco toucan beak ", *Acta Materiala*, 53, 5281-5296,2005.

Yasuaki Seki, Bimal Kad, David J Benson, Marc A. Meyers, "The toucan beak: Structure and mechanical response", *Materials Science and Engineering C* , 26, 1412-1420,2006.

Marc A.Meyers, A.Y. Lin, Y. Seki, P. Chen, S. G. Bodde "Structural biocomposites: An overview", *JOM*, 58, 35-41, 2006.

M.A. Meyers, P.Y. Chen, A.Y.M. Lin, Y. Seki "Biological Materials: Structure and mechanical properties" *Progress in Materials Science*, 53, 1-206, 2008.

P.Y. Chen, A.Y.M. Lin, Y.S. Lin, Y. Seki, A.G. Stokes, M.A. Meyers and J. McKittrick, "Structure, Function and Mechanical Properties of Selected Biological Materials", *Journal of the Mechanical Behavior of Biomedical Materials.*, 1, 208-226, 2008.

P.Y. Chen, A.Y.M. Lin, Y.S. Lin, A.G. Stokes, Y. Seki, S.G. Sara, J. McKittrick and M.A. Meyers, "Structural Biological Materials:Overview of current research", *JOM*, 60, 23-32, 2008.

H.J. Yang, Y. Xu, Y. Seki, V.F. Nesterenko, M.A. Meyers,"Analysis and Characterization by EBSD of Microstructural Evolution in Adiabatic Shear Bands in Fe-Cr-Ni-Alloys. *Journal of Materials Research* accepted 2008.

Y.Seki, Sara G. Bodde, Marc A. Meyers, "Toucan and Hornbill Beaks:Comparative Study", *Acta Biomaterialia* submitted 2009.

R.S. Fecchio, Y.Seki, S.G. Bodde, M.S.Gomes, J.Kolososki,J.L. Rossi, M.A. Gioso, M.A. Meyers, "Mechanical Behavior of Prosthesis in Toucan Beak(Ramphastos toco)", In preparation.

Y. Seki, M. Mackey, M.A. Meyers, "Three dimensional mechanical and structural modeling of Toucan beak", In preparation.

ABSTRACT OF THE DISSERTATION

STRUCTURE AND MECHANICAL BEHAVIOR OF BIRD BEAKS

by

Yasuaki Seki

Doctor of Philosophy in Materials Science and Engineering

University of California San Diego, 2009

Professor Marc A Meyers, Chair

The structure and mechanical behavior of Toco toucan (*Ramphastos toco*) and Wreathed hornbill (*Rhyticeros undulatus*) beaks were examined. The structure of Toco toucan and Wreathed hornbill beak was found to be a sandwich composite with an exterior of keratin and a fibrous bony network of closed cells made of trabeculae. A distinctive feature of the hornbill beak is its casque formed from cornified keratin layers. The casque is believed to have an acoustic function due to the complex internal structure. The toucan and hornbill beaks have a hollow region that extends from proximal to mid-section. The rhamphotheca is comprised of superposed polygonal scales (45 μm diameter and 1 μm thickness) fixed by some organic adhesive. The branched intermediate filaments embedded in keratin matrix were discovered by transmission electron microscopy (TEM). The diameter of intermediate filaments was ~ 10 nm. The orientation of intermediate filaments was examined with TEM tomography and the branched filaments were homogeneously distributed. The closed-cell foam is comprised of the fibrous structure of bony struts with an edge connectivity of three or four and the cells are sealed off by the thin membranes. The volumetric structure of bird beak foam was reproduced by computed tomography for finite element modeling.

The mechanical behavior of bird beaks was evaluated by tensile and compression testing. Micro and nanoindentation hardness measurements were used to corroborate these values. The mechanical response of toucan rhamphotheca exhibits isotropy whereas hornbill rhamphotheca may behave anisotropically in tension. The Young's moduli of toucan and hornbill rhamphotheca were found to be ~ 1.0 GPa. The Young's modulus of rhamphotheca at high humidity condition dropped by a order of magnitude. The rhamphotheca exhibits a strain-rate sensitivity with a transition from slippage of the scales due to release of the organic glue, at a low strain rate, to fracture of the scales at a higher strain rate. The compressive strength of beak foam is dependent on the density. The higher apparent density of hornbill foam provides a four-fold higher strength than toucan foam. The mechanical behavior of beak skulls were modeled by the Gibson-Ashby constitutive equation. The compressive response of the beak revealed that there is a synergistic effect between foam and shell evidenced by the separate response of shell, foam, and foam + shell.

The sandwich design of bird beaks were evaluated by the Karam-Gibson and Dawson-Gibson models. The models proved that the design of bird beaks was optimized for effectively achieving high resistance to buckling when they are subjected to bending rather than uniaxial loads. The synergistic interaction between foam and shell is also successfully confirmed by a finite element analysis (LS-DYNA). The foam stabilizes the deformation and prevents local buckling of the keratin shell by providing an internal support which increases its buckling load under compressive loading. The bending behavior of bird beak in finite element analysis was successfully compared with experimental results. The volumetric structure of bird beak foam was reconstructed in 3D by a visualization technique and this rendering was successfully applied to finite element calculations which predict compressive strength in agreement with experimental results.

Chapter 1

Introduction

The study of biological materials can provide insights into heretofore unexploited mechanisms of designing and toughening synthetic materials [1–4]. Shells have received a great deal of attention over the past years [1, 5–9] and are inspiring new processing methods for materials. The spicule of the sea urchin is another example of a biological material with mechanical properties far surpassing those of synthetic materials [10, 11]. It is composed of concentric layers of amorphous silica, providing a flexure strength four times higher than synthetic silica [12]. In addition, the failure is graceful and not catastrophic. Other examples, silk and spider web are comparable to the strength of steel [13, 14]. A fascinating class of biological materials is sandwich structures consisting of a solid shell and a cellular core. Gibson and coworkers [15–18] include porcupine quills, hedgehog spines, plant stems, cork, and skull in this category; the cellular core increases the resistance of the shell to buckling, leading to a synergism between the two constituents. The bird beak is an excellent example of sandwich construction in nature.

Bird beaks usually fall into two categories: short/thick, and long/thin. The toucan and hornbill are an exception. They have long beaks that are also thick, a necessity for food gathering in tall trees. The large beak of hornbill helps to crush

dangerous prey. This is accomplished by an ingenious solution, enabling a low density and high stiffness: a composite structure consisting of an external solid keratin shell and a cellular core. The toucan (*Ramphastos toco*) beak, comprising one third of the length of the bird and yet only about 1/30~1/40th of its mass, has a low density of $\sim 0.1\text{g/cm}^3$, which allows the toucan to engage in foraging and aggressive social activities such as bill fencing activities. [19]. The hornbill (*Rhyticeros undulatus*) beak, made from one fourth of the total length and 1/30th of total weight, has a density of $\sim 0.3\text{g/cm}^3$.

The structure of toucan and hornbill beaks is shown in Figures 1.1 and 1.2. The epidermis that covers beak bone is called rhamphotheca, composed of a multilayer of β -keratin scales. Dermis, made of collagen and elastin based fibrous protein, is the connective tissue between epidermis and bony foam. The foam is constructed by criss-crossed bony fibers or trabeculae. A distinctive feature of hornbill is its "casque" fused into bony foam and it has an acoustic function [20]. The ridges are another form of keratin plate and located at the proximal end in Fig. 1.2.

A biological composite, keratin, consists of crystalline filament and amorphous matrix. Keratins are classified into α -keratin and β -keratin, depending on the compositions and structure of their filaments [21–25]. α -keratin is typically mammalian whereas β -keratin is found in reptiles and birds. The structural and compositional studies of α -keratin are abundant in literature [26–32]. The molecular structure of β -keratin has been studied in avian integument [24, 33, 34]. A few studies confirmed the structure of bird beak by gel electrophoresis [35–37]. Frenckel [35] revealed that avian beak keratin is very rich in glycine, containing moderate levels of tyrosine and serine. The content of cystine is relatively low [35]. Brush [36] reported that the molecular weight of the toucan beak keratin has a major band at 16,750 g/mol and a minor band of 25,500 g/mol.

The integument provides enough strength for activities such as foraging, locomotion, and flight. Mechanical properties of keratins have been investigated for both

mammalian and avian keratins. In mammalian keratins, hair and human skin is a popular subject for scientists [38–41]. Horn, used for defense from predators and fighting members for territory, has relatively high stiffness among keratinous materials. The Young’s modulus of horn keratin is 6.1 GPa in dry condition [42]. One of the toughest keratins is hoof wall, which is a hierarchically organized biological composite material. The multi-level structure increases the toughness and redirects the direction of crack growth to prevent the failure [43–47]. The study of mechanical properties of avian keratins devoted to feathers and claws [48–51]. There have been few studies on mechanical properties of avian beak keratin [52].

The interior of avian beak is an extension of bird skull. The structure of beak skull is analogous to that of human cancellous bone. The avian bone shows comparable hardness to human bone [53]. A low density foam supports rhamphotheca and bears external cyclic loadings. As examples, the density of toucan beak foam is $\sim 0.05 \text{ g/cm}^3$ and hornbill beak foam is $\sim 0.1 \text{ g/cm}^3$. Woodpecker can peck on trees with their beaks at high accelerations. The skull of woodpeckers is strong enough to drill on wood. Woodpeckers avoid the brain damage not only tolerance of skull due to their small brain size, short duration of impact, and orientation of brain [54].

This study is concerned with both mechanical properties and structure of bird beaks. Tensile and compression tests were used to ascertain the mechanical performance of the outer shell and internal foam core. Additionally, micro- and nanoin-dentation hardness tests were carried out. Scanning electron microscope (SEM) and energy dispersive X-ray (EDX) spectroscopy were used to analyze the structure and mineralization of the beaks. Confocal microscopy is used for structural analysis of beak foam. Transmission electron microscopy was employed to analyze the internal structure of keratin tiles. From the experimental data, we used the Gibson and Ashby [55] constitutive equations to model the mechanical behavior of beak foam. Further, the mechanical response of bird beaks was modeled by comparing the separate response of shell and foam with sandwich structured beaks [56,57]. The

sandwich design of beaks was evaluated by two models; Karam-Gibson and Dawson-Gibson models for stability and optimization [58,59]. The structure of beak foam was analyzed by micro-CT. Further, visualization techniques are used for 3D rendering of the beak after the data acquisition from micro-CT. Finite element calculations for determining synergistic effect, bending behavior of beak, and foam model from micro-CT, are compared with the experimental results.

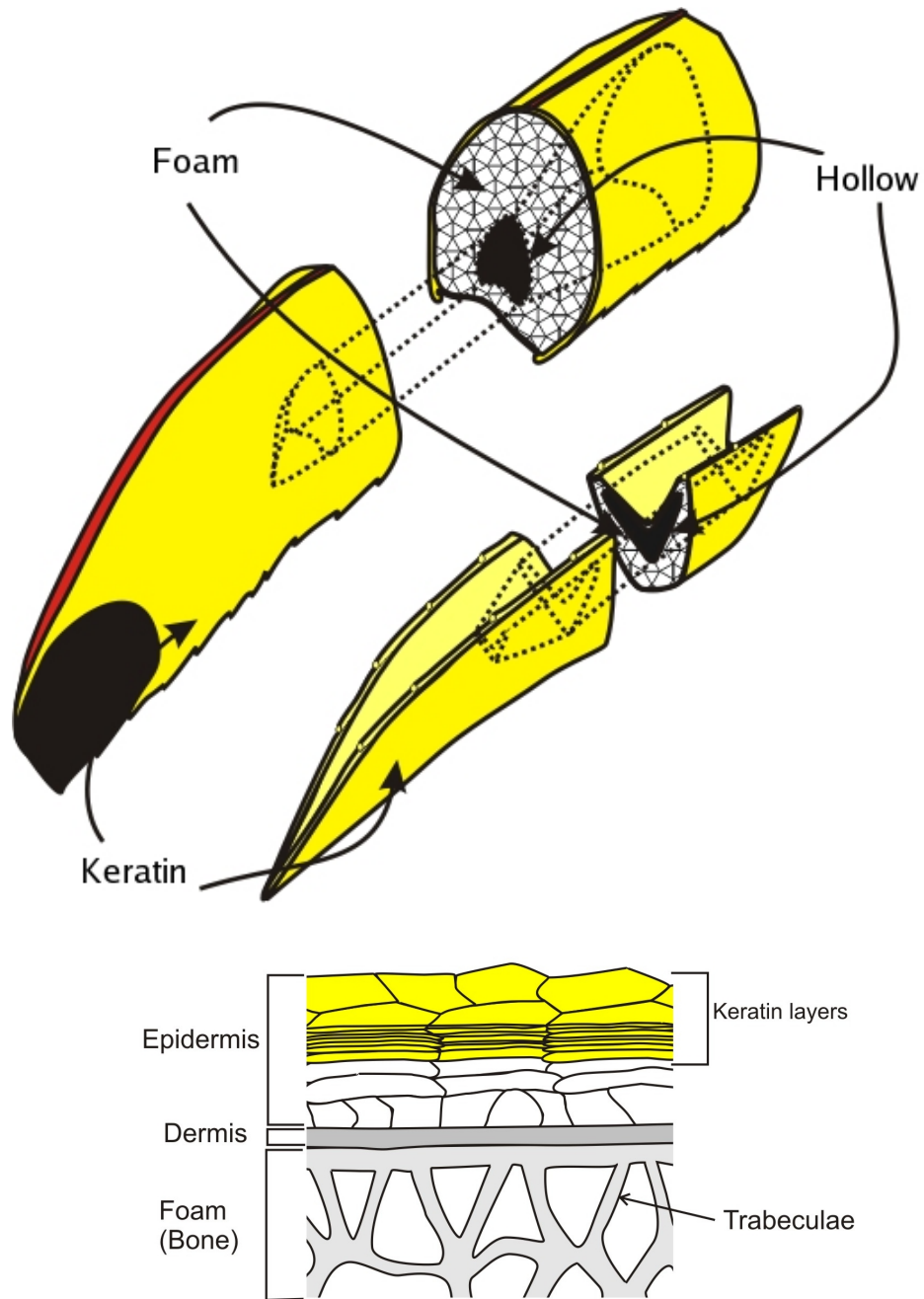


Figure 1.1: Schematics of a Toco toucan beak and layers of the beak.

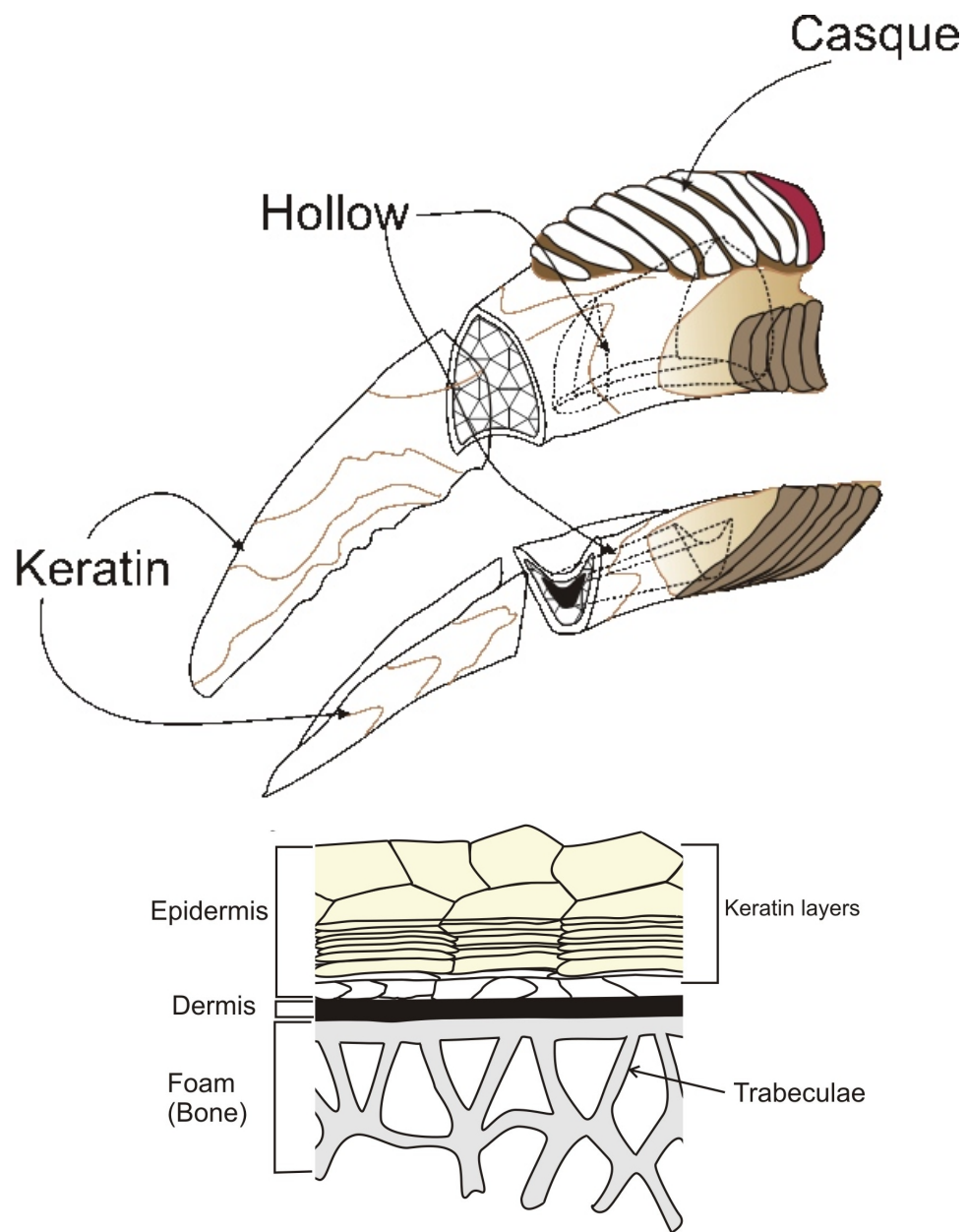


Figure 1.2: Schematics of a wreathed hornbill beak and layers of the beak.

Chapter 2

Background

2.1 Biological Materials

2.1.1 Structure and Mechanical Properties

Biological materials have been extensively studied by biologists in the past and received great attention from materials scientists in recent years [7, 8, 60–64]. Early descriptive work on biological materials is found in Darcy Thompson’s classical book “On Growth and Form” [65]. Vincent [3] illustrated biological materials with biologist’s aspects on structural materials with a description of simple mechanics. Fung [66] introduced biomechanics utilizing a mathematical treatment to describe the complicated biological systems. Currey wrote textbooks that overview the structure and mechanical properties of bone [67, 68]. Meyers et al. [69] reviewed a wide range of biological materials in structure and mechanical properties. There is an excellent review paper by Fratzl [70] in particular on bone and wood. The Meyers group at UCSD extensively studies biological materials in terms of structure and mechanical properties [71–73].

The biological materials basically are made from soft and hard components: pro-

teins and minerals, respectively. The protein molecule is made from amino acid components linked by polypeptide covalent bonding so that protein is known as polypeptide [74]. The basic elements of minerals are Ca, Mg, Si, Fe, Mn and provide biological materials with stiffness. The minerals usually are embedded in the protein matrix and the content of minerals varies in different biological materials. The minerals are produced by biomineralization that converts chemical species into inorganic crystals under biological control. As a result of the cellular activity, the mineral formation and crystal growth occur in organism. Biomineralization offers the organism not only structural support, but also mechanical strength [5, 75, 76]. Figure 2.1 shows the microstructure and degrees of mineralization of dentin, bone, and nacre. Bone and dentin contain approximately 50 % minerals and nacre is 98 % minerals. The degree of mineralization affects the mechanical properties. The Young's moduli of dentin and bone range from 10~20 GPa in literatures [77–83]. In the highly mineralized abalone shell, a self assembly of the aragonite calcium carbonate, is organized as a laminated composite and produces the remarkable mechanical properties. The tensile strength is 150 MPa and Young's modulus is 70 GPa in dry and 60 GPa in hydrated conditions [84]. The abalone shell demonstrates higher compressive strength of 233~540 MPa under quasi-static loading [85].

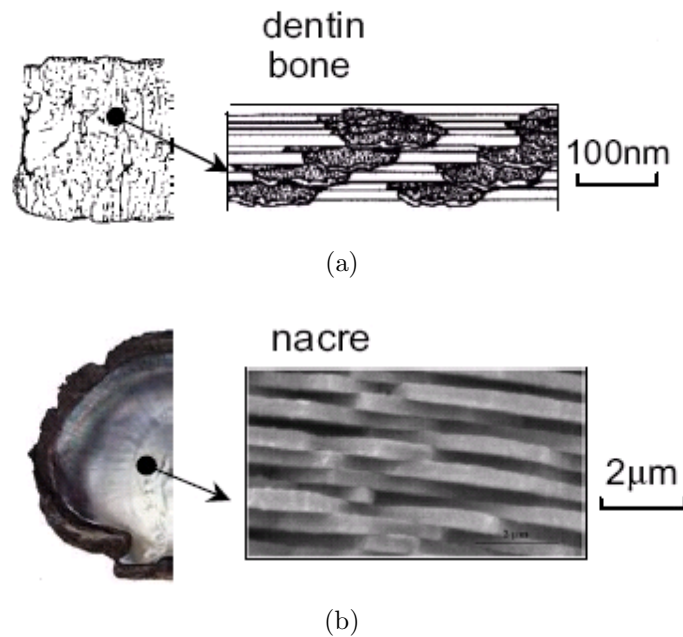


Figure 2.1: Examples of mineralized biological materials;(a) bone and dentin; (b) nacre (from Gao et al. [60])

The another feature of biological materials is the hierarchical structure at different structural levels which help to prevent a catastrophic failure. Figure 2.2 shows the hierarchically organized bone structure. The structure is principally divided into; macrostructure (cancellous and cortical bone); microstructure (osteon and single trabeculae);and nanostructure (collagen fiber). The mechanical properties of bone vary at different structural levels [86]. Tensile strength of the human arm bone is approximately 154 MPa and the Young's modulus is about 20 GPa in hydrated conditions [87] at the macro-structural level. The osteons consist of mineralized collagen fiber and range 200~250 μm in diameter. The mechanical properties of single osteon have been studied by Ascenzi and co-workers [88–93]. The osteon was found to have a Young's modulus of 12 GPa and strength of 120 MPa in tension [88]. Asenzi's group found that osteon is half of Young's modulus in compression and the

compressive strength is almost the same as in tension [89]. The Young's modulus is 2.3 GPa and 398 MPa of strength in bending [91]. The shear moduli of osteons are 23 and 17 GPa in different directions [90]. The strength of osteons is 205 and 170 MPa in torsion [92]. A recent nanoindentation study on osteons by Rho et al. revealed that the Young's modulus and hardness of osteons were 22.4 GPa and 0.617 GPa, respectively [94]. The scaling effect changes the mechanical properties of the hierarchically arranged structure of bone.

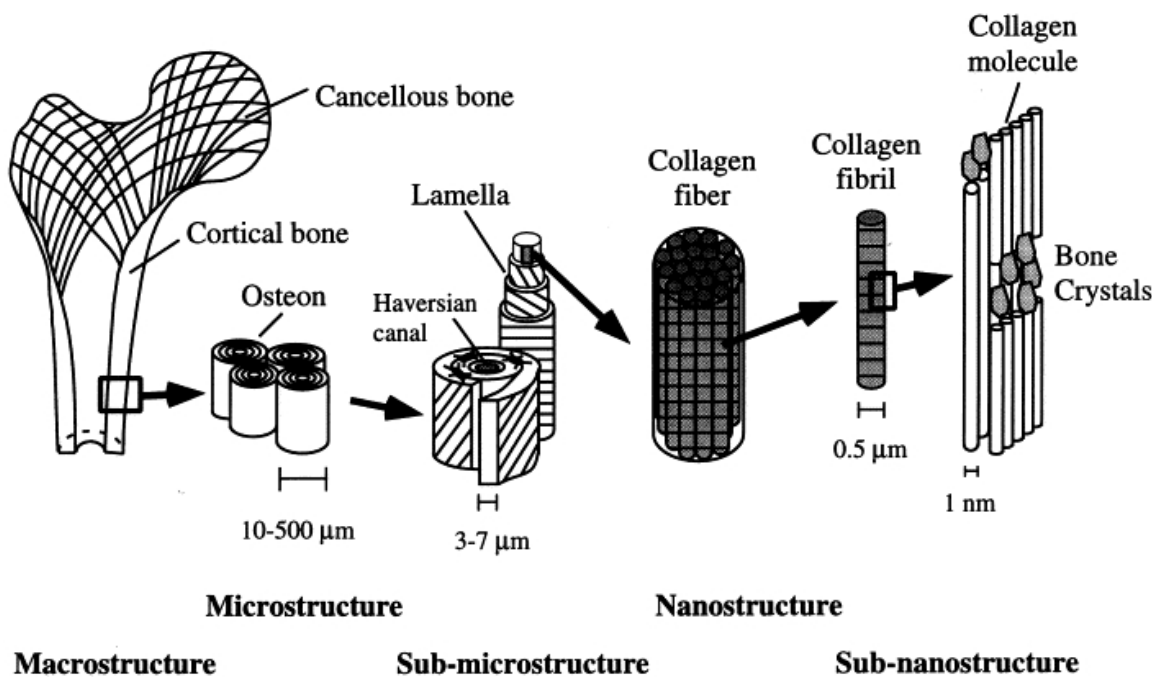


Figure 2.2: Hierarchical structural organization of bone; cortical and cancellous bone at macrostructure; osteons with Haversian systems at microstructure; lamellae at sub-microstructure; collagen fiber assemblies of collagen fibrils at nanostructure; bone mineral crystals, collagen molecules, and non-collagenous proteins at sub-nanostructure (from Ji and Gao [61]).

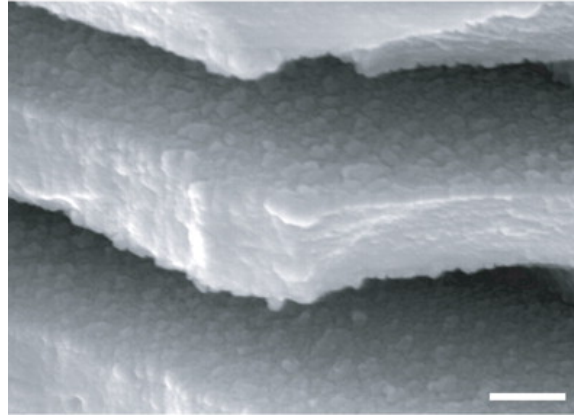
2.2 Biomimetic Aspects

The biological systems have fascinating properties and structure that evolve through 100 million years. The optimized structure, outstanding properties, and functionalities are still far beyond engineered synthetic materials. One can still exploit from the biological systems and apply to engineering materials to develop the properties from the molecular levels and enhance the mechanical properties. Indeed, the field of biomimetic research is growing among materials scientists and engineers [95–99]. I will briefly discuss topics in biomimetic research by using examples of abalone shells and gecko foot.

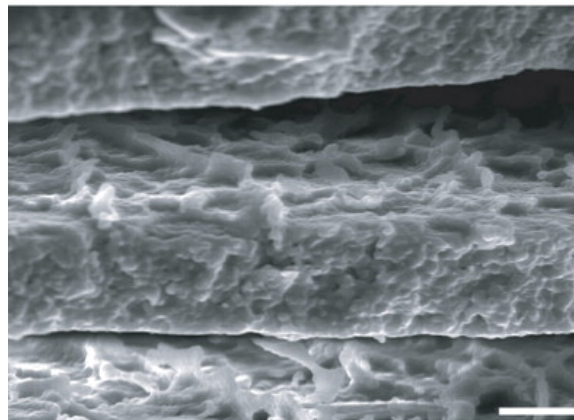
As I shortly described in the previous section. The abalone shell has outstanding mechanical properties even though the main structural component is calcium carbonate, which is the same as chalk. The structure of abalone shell is composed of 8-10 μm diameter hexagonal tiles. There is a difficulty in synthesize a material that have abalone like laminate structure. However, Deville et al. [100] have developed a method to create the composites that possesses nacre shell structure [100, 101]. Figure 2.3 shows the comparison of microstructure between nacre and artificial nacre made of alumina. The force-displacement curve of nacre and artificial nacre shows brittle behavior in Fig. 2.4. The maximum load of synthetic nacre structure is three folds higher than nacre in three point bending.

The adhesive properties of gecko setae stimulate interests among scientists because the adhesive properties are reversible and non-destructive to the contact surface and still produce strong adhesiveness. As served as a topic of biomimetic [62, 102–104], scientists put great efforts to replicate the micro- or nanostructure of gecko setae with polymeric materials to reproduce the adhesive properties. Figure 2.5 shows the comparison of gecko setae and artificial gecko setae. The artificial gecko setae, having sufficient adhesive properties, was reproduced with polymeric materials by Lee et al. [103]. The adhesive properties of gecko setae and artificial gecko setae

are compared by the shearing force between surface and setae in Figure 2.6. In terms of shear force, the artificial gecko setae hold the shear force of 4 N and the shear force of natural gecko setae is 0.24 N. Lee et al. estimated that the shear stress of artificial gecko setae is greater than 9 N/cm^2 , corresponding to approximately 15% of the natural gecko lamella patch [103].



(a)



(b)

Figure 2.3: Scanning electron micrographs; (a) nacre (scale bar $0.3 \mu\text{m}$); (b) artificial nacre (scale bar $10 \mu\text{m}$) (from Deville et al.[100]).

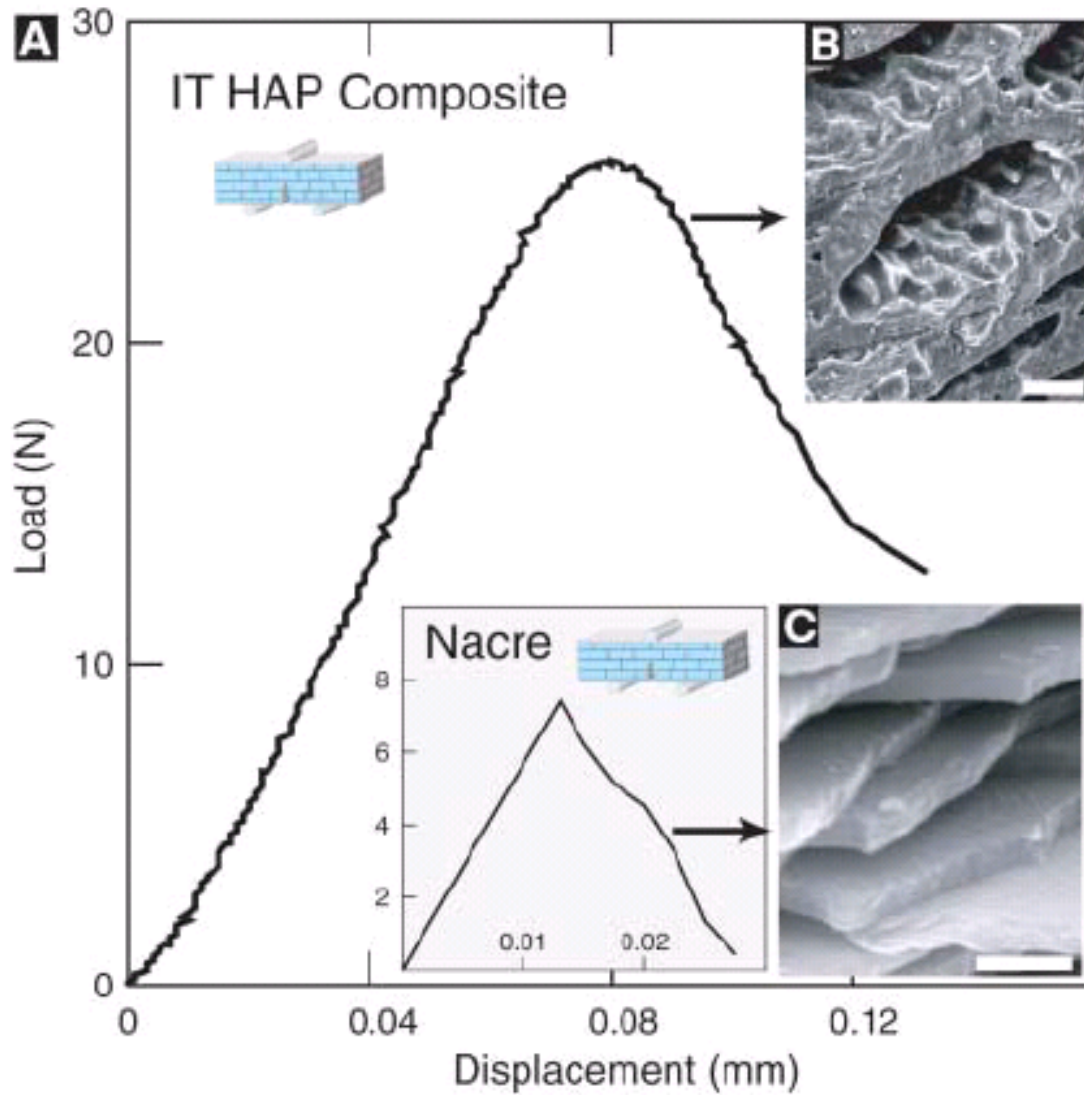
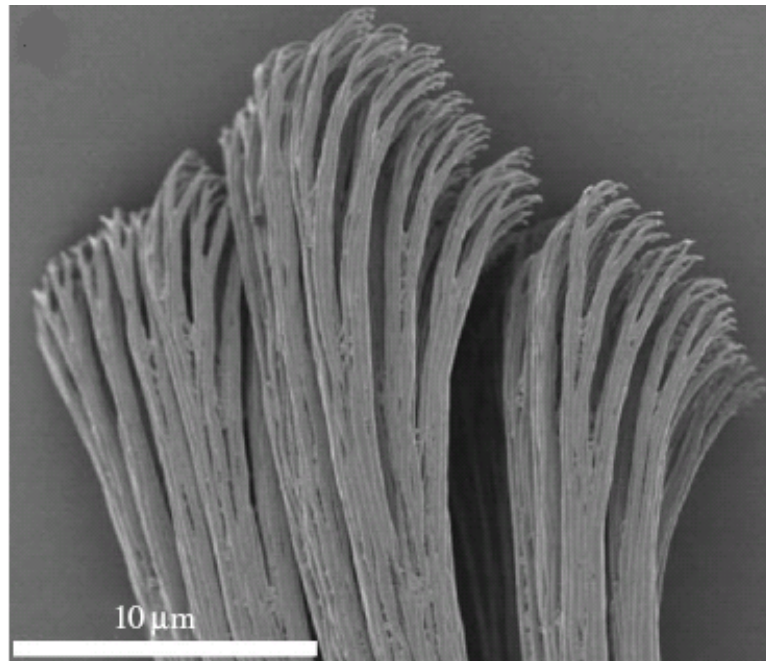
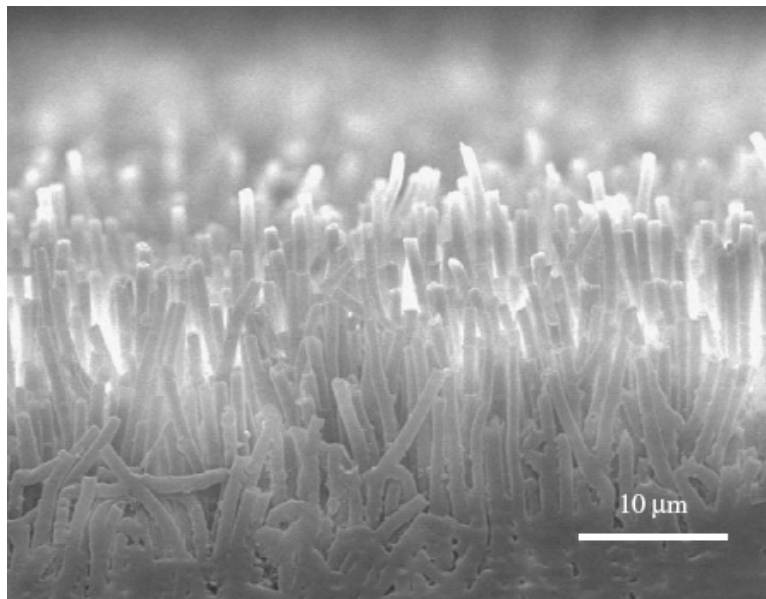


Figure 2.4: Force-displacement curves of nacre and artificial nacre tested under three point bending (from Deville et al. [100]).

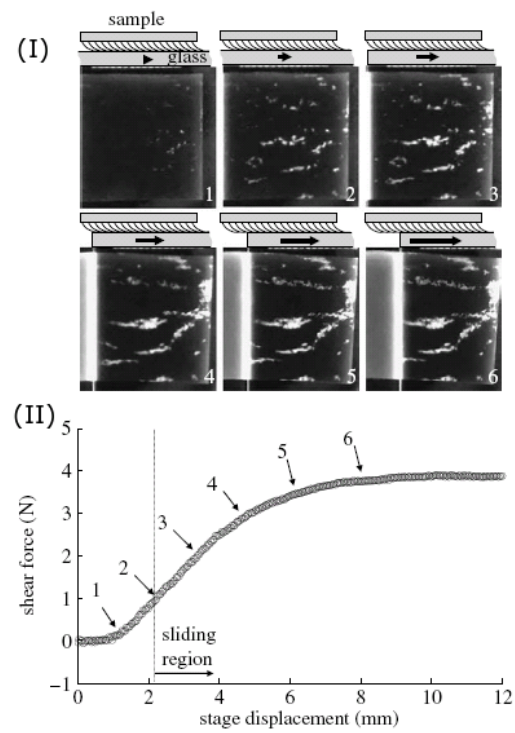


(a)

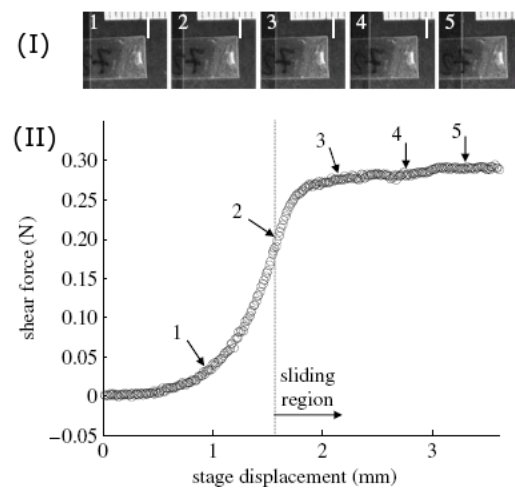


(b)

Figure 2.5: Scanning electron micrographs (a) gecko setae (from Rizzo et al. [105]); (b) artificial gecko setae (from Lee et al. [103]).



(a)



(b)

Figure 2.6: (I) Natural and artificial setal array under testing at indicated positions. (II) Shear force-displacement curve;(a) artificial gecko setae;(b) natural setae (from Lee et al. [103]).

2.3 Keratins

2.3.1 Keratinization

Keratins are produced by complex differentiation process of epidermal cells, called keratinization. The keratinization process is terminated by the death and hardening of epidermal cells, which is called "*cornification*". Figure 2.7(a) shows the cross section of mammalian skin. The connective tissue, dermis, is covered by the dense layers of stratum basal that is responsible for proliferation of epidermal cells. The differentiation process takes place in next thick layer of stratum spinosum, shown in Fig 2.7. Stratum granulosum layer indicates the border between differentiation and cornification processes. The keratinization process is finalized by deposition of stratum corneum layers. Figure 2.7(b) shows the formation of keratin. The nuclei of epidermal cells disappears as the cells are homogeneously strained. The cornification is completed with flattening of epidermal cells.

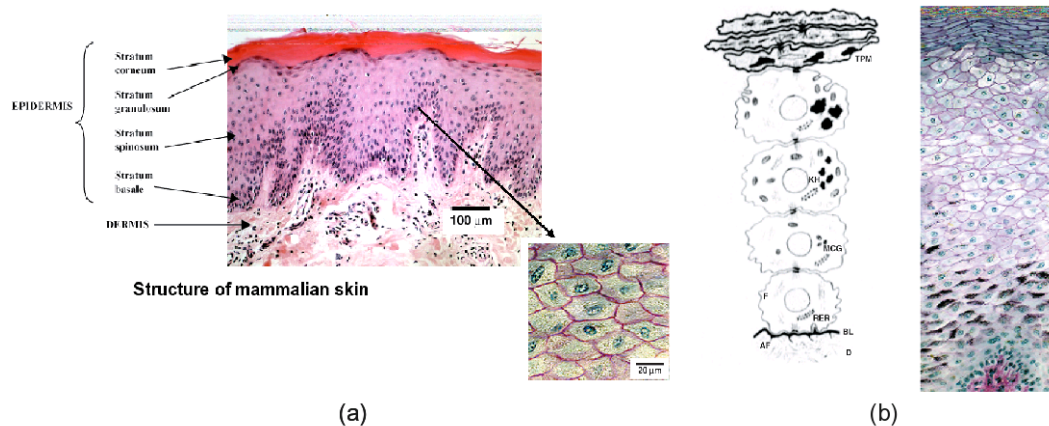


Figure 2.7: Keratinization process;(a) morphology of cross section of mamalian keratin; (b) flattening process of epidermal cells (from Tomlinson et al. [106]).

2.3.2 Classification

Keratin is a special type of structural protein containing sulfur, that distinguishes it from other proteins [105]. Keratin is durable, insoluble, and unreactive to natural environment. Keratin is conventionally classified in terms of two different modes of biosynthesis leading to hard and soft keratins [21]. Soft keratins include stratum corneum, corns, and cellouse. Hard keratins are found in hair, claws, and beaks. Soft keratins are usually weakly consolidated and function as desquamating tissues [106]. It contains 1% sulfur and 4 % lipids. Hard keratin has a more coherent structure and a high amount of sulfur or cysteine produced during keratinization. The presence of lipid is also lower than in soft keratins. Keratin is further classified as α -pattern, β -pattern, feather pattern, amorphous pattern, depending on the secondary protein structure of the X-ray diffraction patterns [22, 23, 26]. α -pattern is found in the mammals, β -pattern is found in birds and reptiles. For simplicity, we consider the feather pattern as β -pattern while there is a difference between other β -keratins and feather keratin in the secondary structure. The amorphous pattern is found in cuticle of animal hair [21] and will be included in α -pattern for simplicity. Figure 2.8 shows the classification of keratins with integuments. Avian integuments including beaks, claws, and feathers, are categorized as β -keratin.

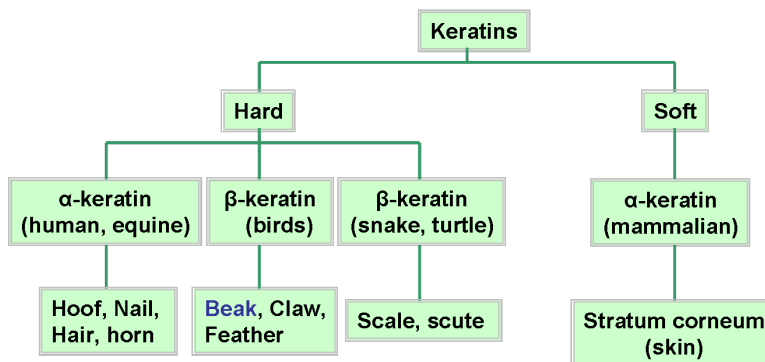


Figure 2.8: Classification of keratins.

The major difference between α -keratin and β -keratin is their filament texture. The filament of the α -keratin structure is based on the α -helix folding pattern, coiled coil structure, shown in Fig 2.9 (a). The folding pattern of β -keratin is the β -sheet [24,25] in Fig 2.9 (b). Fraser and Parry determined the structure of β -filaments by the investigation on reptilian keratin. Figure 2.10 shows the molecular structure of β -sheet conformation. The reptilian and avian β -filaments are considered to have the same structure. There is a difference in diameter of α - and β -filaments. The diameters of the filament of α - and β -keratins are 7 nm and 4 nm, respectively.

Gillespie and Frenkel [107] have measured amino acid composition of mammalian keratins and found a wide variation in the compositions. Avian and reptilian keratins are similar in molecular structure and protein composition and distinguishable from mammalian keratins. X-ray diffraction detects the secondary structure of beak protein: it is similar to the feather pattern [105]. However, the major protein of the beak is different from the feather. The avian beak is more closely related to avian claws in molecular structure and composition [37].

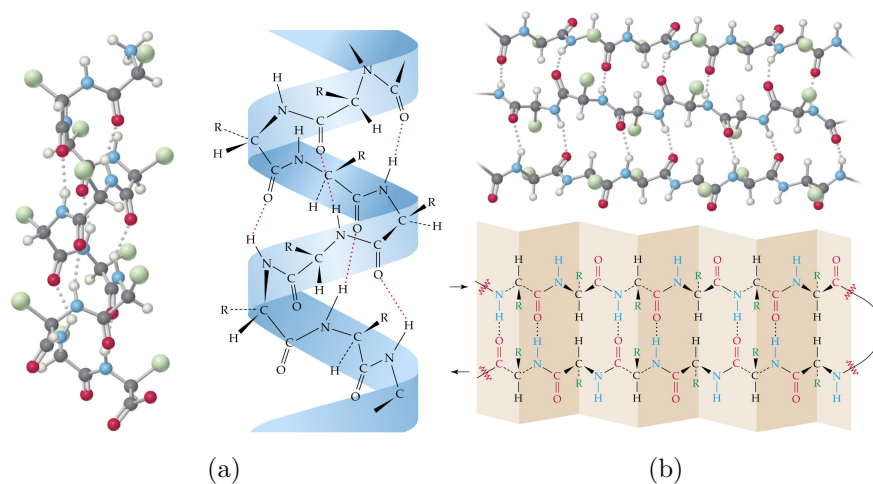


Figure 2.9: Structure of α - and β -keratins; (a) α -coiled coil structure; (b) β -sheet (from Alberts et al. [74]).

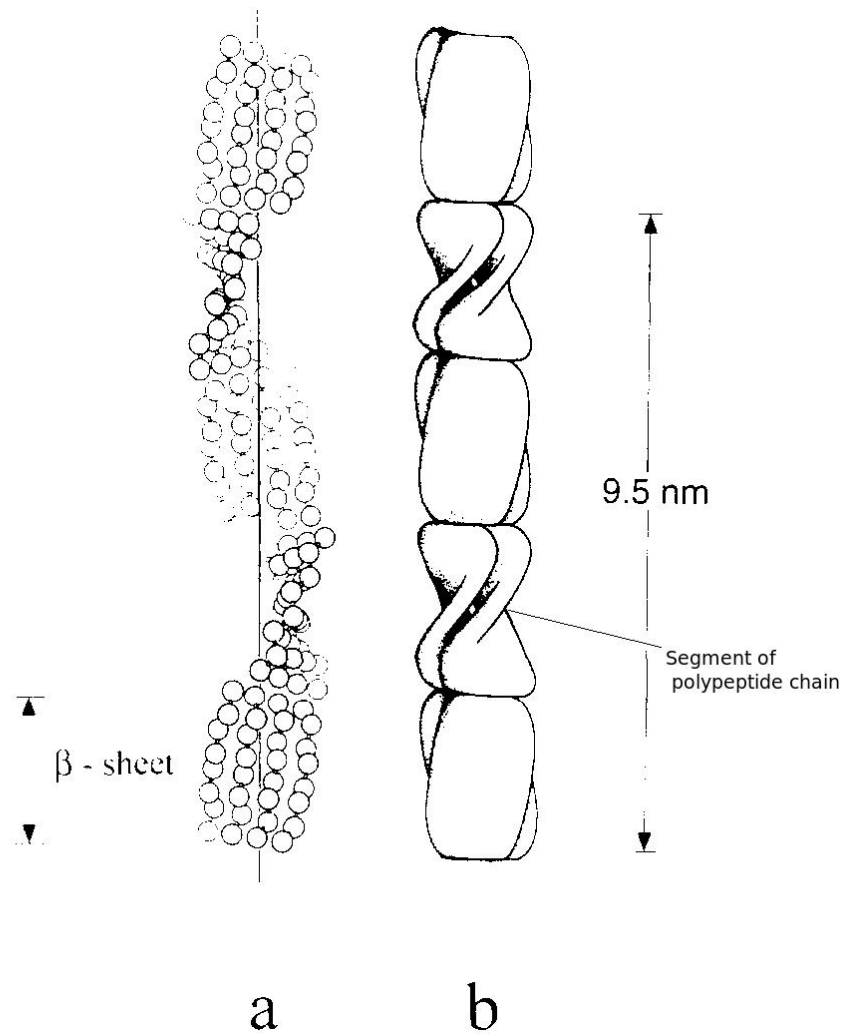


Figure 2.10: (a) One of the pair symmetry related strands of β -sheet that make up the central framework of keratin filament. (b) Model for arrangement of β -sheet proteins of protein molecules in the filament of avian keratin (from Fraser and Parry [25]).

2.3.3 Mechanical Properties of Keratins

The mechanical properties and structure of various keratinous tissues were discussed by Fraser and Macrae [105]. The keratin is a protein-based fiber reinforced composite: a high modulus fiber is embedded in a low modulus viscoelastic matrix. The matrix plays the role of a medium to transfer the applied load to the fiber thus preventing crack propagation from local imperfection or point of rupture [105]. The minerals such as calcium and other salts contribute to the hardness of keratins [76]. Figures 2.11 and 2.12 show material property charts for biological materials [108,109]. The Young's modulus and strength of biological materials are plotted as a function of density. The red colored regions indicate keratinous materials. The skin is categorized as a natural elastomer while other hard keratins fall into natural polymers in the material property chart. The density of keratin, $\sim 1 \text{ g/cm}^3$, is consistent with soft and hard keratins. By contrast, the stiffness and strength of keratins exhibit a wide range, from soft to hard keratins. The Young's modulus of soft keratins ranges from 0.01 to 0.1 GPa and that of hard keratins ranges from 1 to 10 GPa. In terms of strength, the hard keratins range from 10 to 100 MPa whereas soft keratin is within the range of 1 to 10 MPa. There is an order of magnitude difference in Young's modulus and strength between soft and hard keratins.

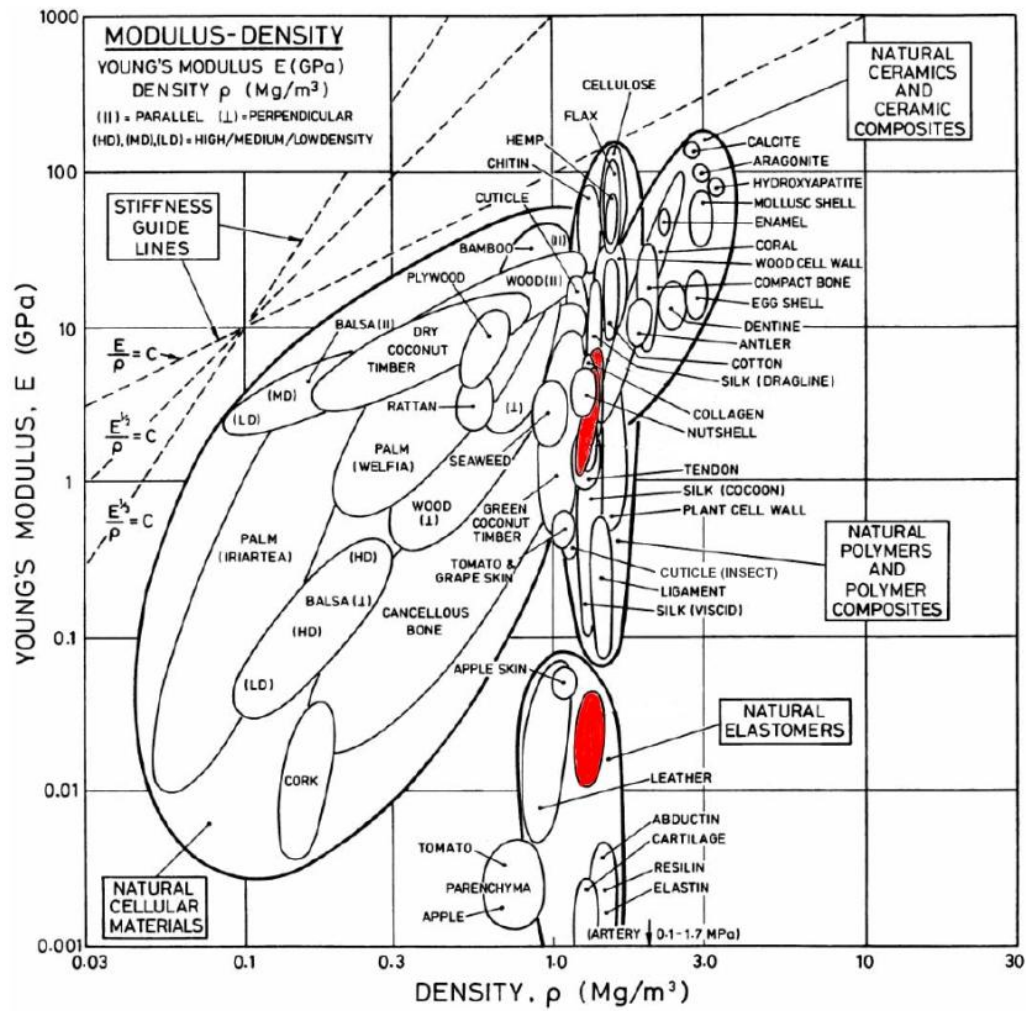


Figure 2.11: Material property chart for natural materials, showing Young's modulus vs density (from Wegst and Ashby [108]).

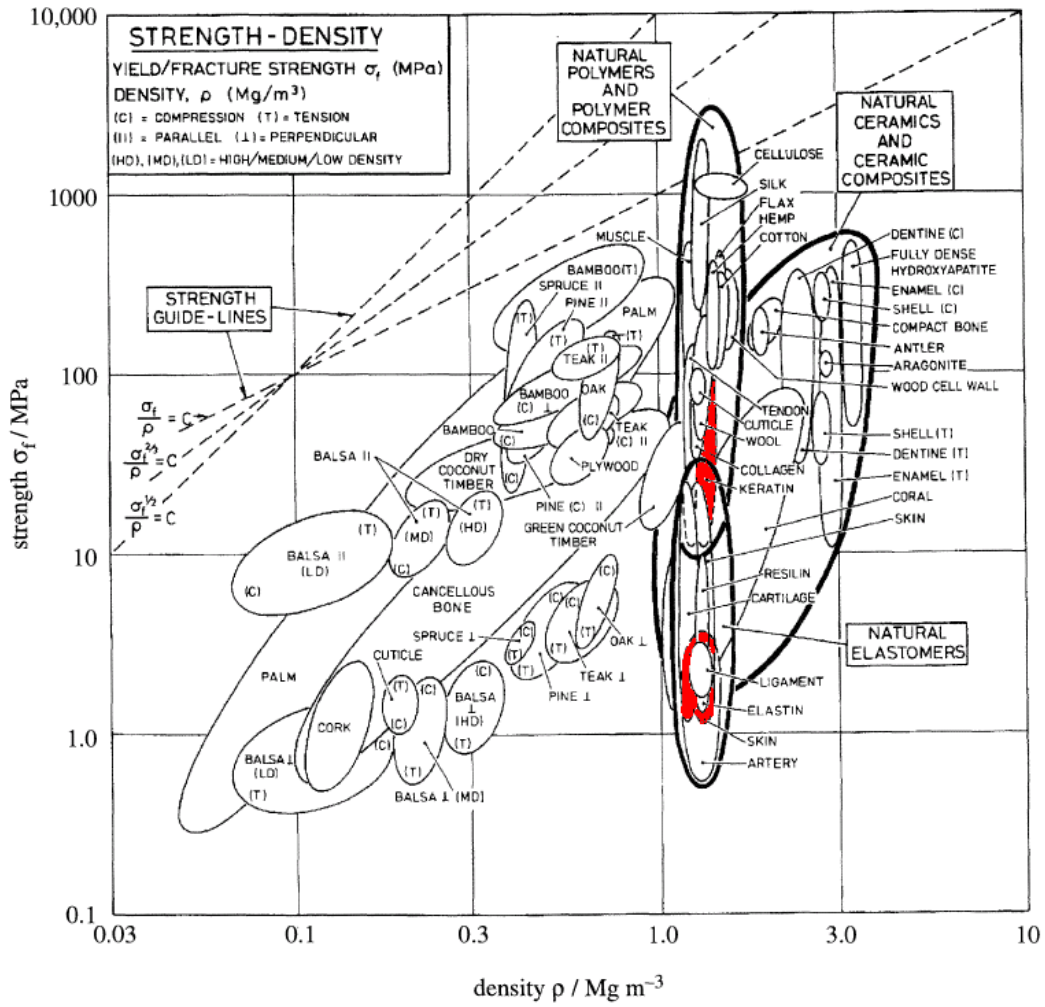


Figure 2.12: Material property chart for natural materials, showing strength vs density (from Wegst and Ashby [108]).

2.3.4 Mammalian Keratins

Wool and hair have the simplest structure among keratins and have been extensively studied in structure and mechanical properties [40,41,110–112]. The structure of hair and wools is described by two phase model proposed by Feughleman [113]. The α -helices are embedded in matrix and are aligned almost parallel to the filament, shown in Fig 2.13(a) [114]. The structure of α -filament is discussed by the number of studies [26–31]. Fig 2.13(b) shows a schematic fashion of typical stress-strain curves of wool fiber, filament, and matrix in water [115]. The crystalline filament is responsible for mechanical properties of wool fiber. There are three distinct regions: Hookean region, yield region, and post-yield region. The Hookean region is a linear elastic portion of α -keratin fibres. The stress of filament and wool fiber does not increase remarkably in yield region where wool fiber and filament go through a first order of phase transition [114]. The unfolding of α -helices occurs and α -helices transform to β -sheet. The α - β transition is not only initiated by mechanical deformation [116,117] but also by an increase of temperature [118]. The stress increases dramatically in post-yield region where further develops unfolding of α -helices, which leads to β -sheet stretching .

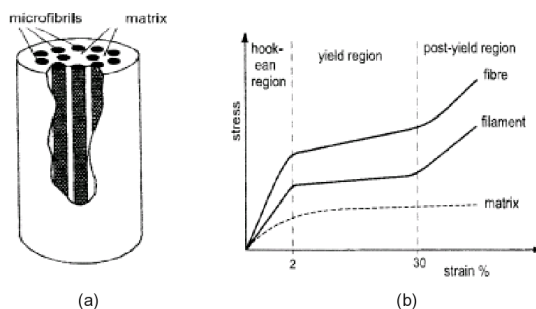


Figure 2.13: Two phase model of α -keratin. (from Feughleman [115]); (b) Schematic representation of stress-strain curves of wool, filament, and matrix. (from Wartmann and Zahn [115]).

2.3.4.1 Skin

Skin is a multifunctional organ that provides temperature regulation, protection from environment, and even camouflage from predators. The layered structure of the skin is composed of the epidermis and dermis layers. The epidermis is a protective layer of the skin and consists of several layers including stratum corneum, stratum granulosum, stratum germinativum, shown in Fig. 2.14 [105]. The outermost layer of the mammalian skin is stratum corneum made from thin soft keratin. Stratum corneum plays a role as a barrier between environment and organism [32,119]. Dermis is a connective tissue between epidermis and organism. Primary proteins of the dermis are elastin and collagen. Elastin has outstanding elastic properties, shown in Fig.2.15. After stretching to 15% of strain, elastin recovers to the original position without inducing plastic strain. While elastin exhibits a remarkable elasticity, collagen is the main source of mechanical response of skins. The contribution of elastin is not significant when skin is subjected to large deformation. Elastin is responsible for the small deformation of the skin and helps it to recover to the original position [120].

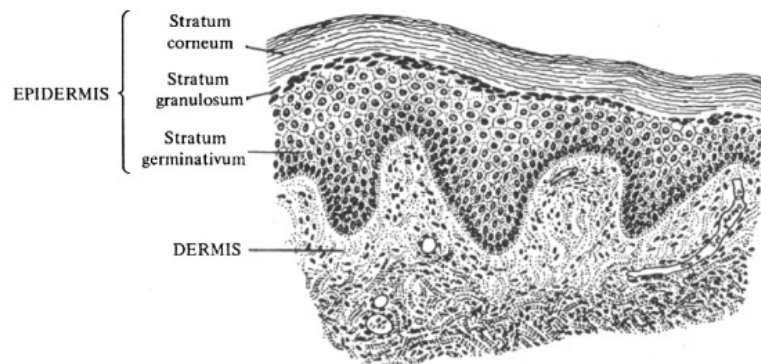


Figure 2.14: Structure of mammalian skin (from Fraser and Macrae [105]).

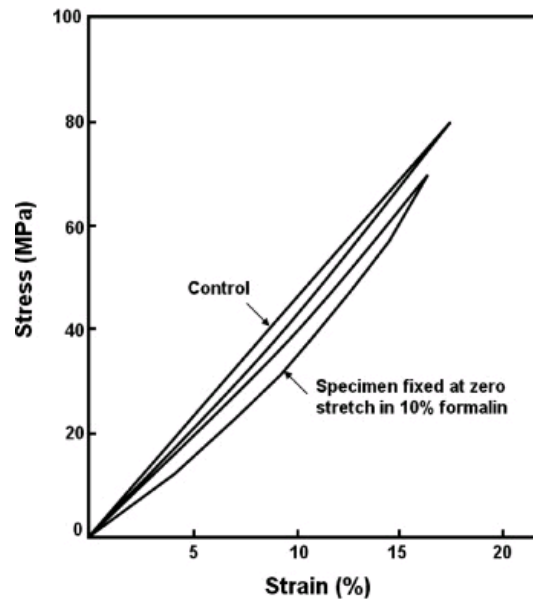
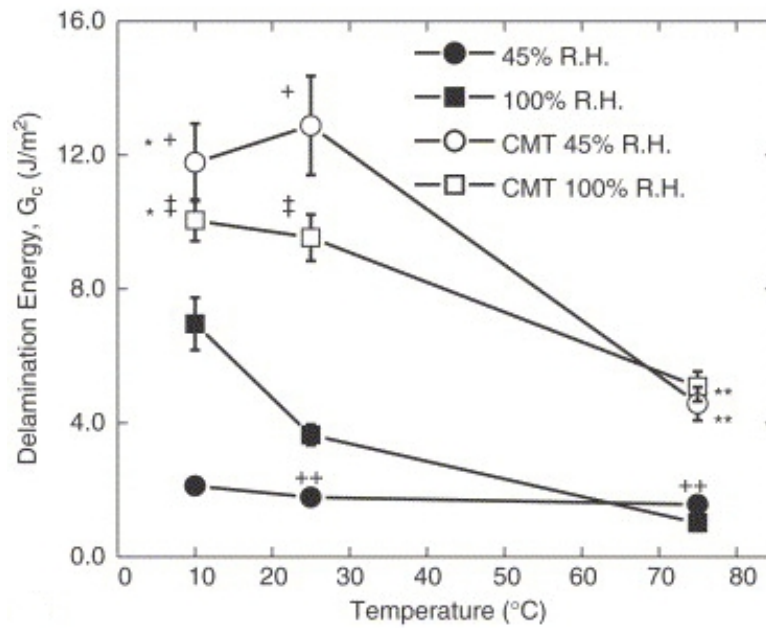
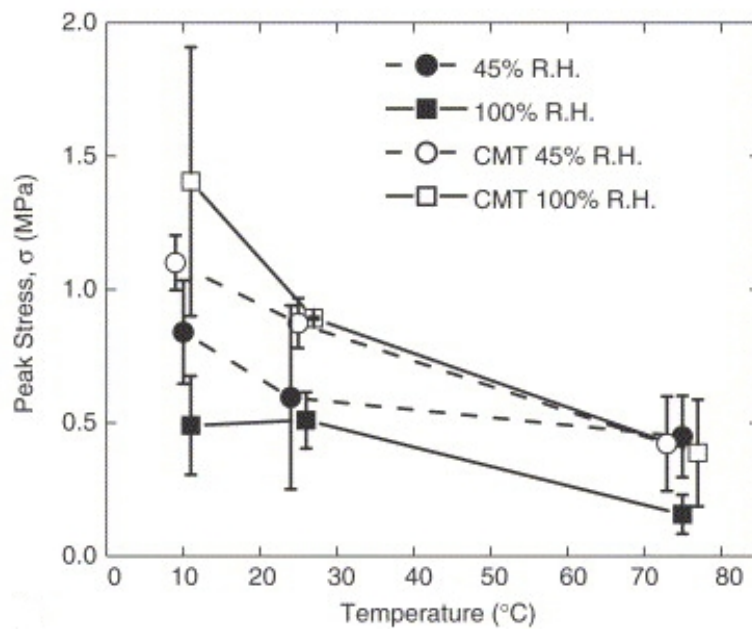


Figure 2.15: Stress-strain curve of elastin (from Fung [66]).

Although there are many studies of stratum corneum [32,38,39,119,121], surprisingly few studies are conducted on mechanical properties of stratum corneum; it is difficult to find a simple stress-strain relation of stratum corneum in tension [122,123]. Recent studies by Wu et al. revealed the delamination properties of stratum corneum. They evaluated the adhesive properties of stratum corneum layers under different environmental conditions [124,125]. Figure 2.16 shows the variation in delamination stress and peak stress with different temperature and hydration levels. The delamination energy and peak stress decreases with an increase of temperature. Chloroformmethanol-extracted stratum corneum, having lower lipid content, shows higher mechanical properties than untreated stratum corneum, which indicates the lipid plays a vital role changing the mechanical responses [124,125]. When the water pools into intercellular substances or lipid layers, the adhesive properties of stratum corneum decrease.



(a)



(b)

Figure 2.16: Comparison of untreated and chloroformmethanol-extracted stratum corneum; (a) delamination energy ;(b) peak stress.(from Wu et al. [124]).

2.3.4.2 Hoof

The equine hoof wall is known as one of the toughest keratins. The hoof wall modulates the irregularity of the ground and transfers weight-bearing between bone and the ground. The studies of equine hoof wall revealed that a complex structure of hoof redirects the crack growth and prevents catastrophic failure [43–47]. The hoof consists of two structural components: tubules and intertubular material. Figure 2.17(a) shows a schematic of the equine hoof wall. Tubules occupy half of the wall and are parallel to the surfaces. The intermediate filament, a fibrous structure of keratin, is embedded in the keratin matrix and is composed of α -helical protein bundles with a diameter of 8 nm.

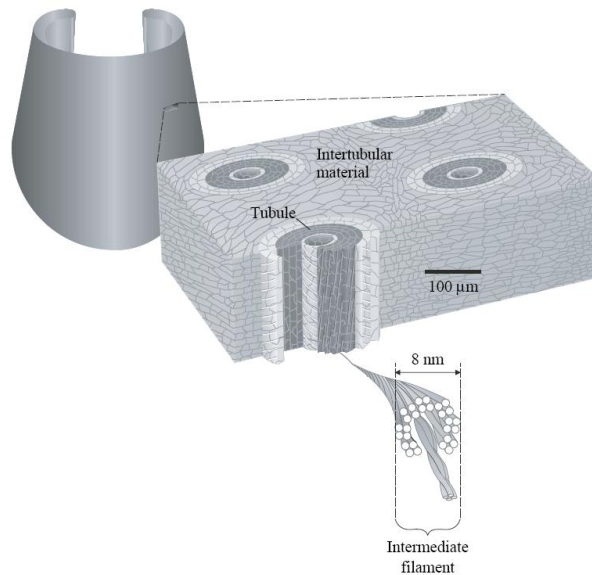


Figure 2.17: Schematic of structure of hoof (from [43])

Kasapi and Gosline studied the entire hoof wall structure and mechanical responsibility of the intermediate filaments [45]. Figure 2.18 shows a hoof wall tubule composite diagram. A micrograph with high magnification of the cross section of hoof wall of tubules is shown in Figure 2.18 A and B. Schematic representation of 2D and 3D structure of tubules is illustrated in Figure 2.18 C and D. The shape of tubules changes from circular to elliptic toward outer wall. The tubules are made from inner, middle, and outer lamellae, which can be seen from IIa region. Outer lamellae is not distinguishable in tubules from regions Ia and Ib. The orientation of intermediate filaments in intertubular material is summarized in Figure 2.19. The top photograph in Fig.2.19 A shows the cross section of hoof wall illuminated with circularly polarized light. Areas with fibers generally aligned radially appear yellow and those running circumferentially are illuminated in blue. Fig.2.19 B and C shows three-dimensional renderings of the intertubular material. The fibers are oriented horizontally at Ia region in contrast to the orientations observed at other regions. The orientation of fibers influences on the mechanical properties of hoof wall, as confirmed by Kasapi and Gosline. [45].

The complex design of the hoof wall provides a wide range of the mechanical properties in 0% to 100% of humidity condition [44, 45]. The hoof normally contains 17-24 % of water [126]. Figure 2.20(a) shows initial Young's modulus is plotted as a function of water content. There are two orders of magnitude difference in Young's modulus between high and low water contents. The mechanical role of the tubules and orientation of the intermediate filaments are to control the crack propagation process and enhance fracture toughness of the wall. Fig.2.20(b) shows that the J-integral of the hoof wall is not very sensitive to the rate of load application. The average J-integral is 12 ± 3 kJ/m² and the variation is due to variable age and unknown condition of hooves; the hoof wall prevents brittle failure in the entire strain rate range investigated: 1.6×10^{-3} equal to 70 s⁻¹. This covers most situations encountered by ungulates.

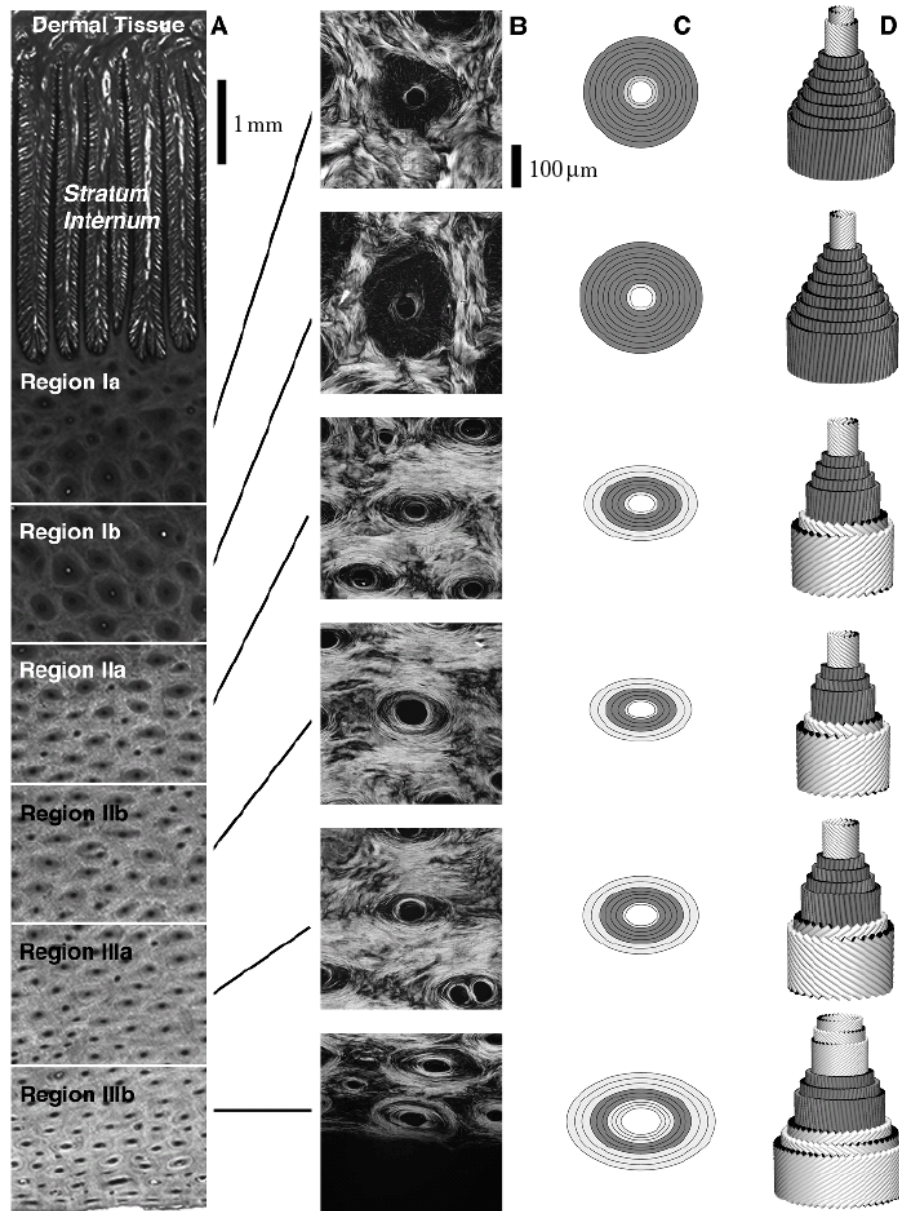


Figure 2.18: Diagram of hoof wall tubule composite. ;(A) High-magnification image of transversely sectioned hoof ;(B) Areas with tubules and intermediate filaments (IFs) ;(C) Schematic illustration of cross sections of tubules. ;(D) Three-dimensional reconstructions of tubules showing IF orientations of each cortical lamella (from Kaspi and Gosline [45]).

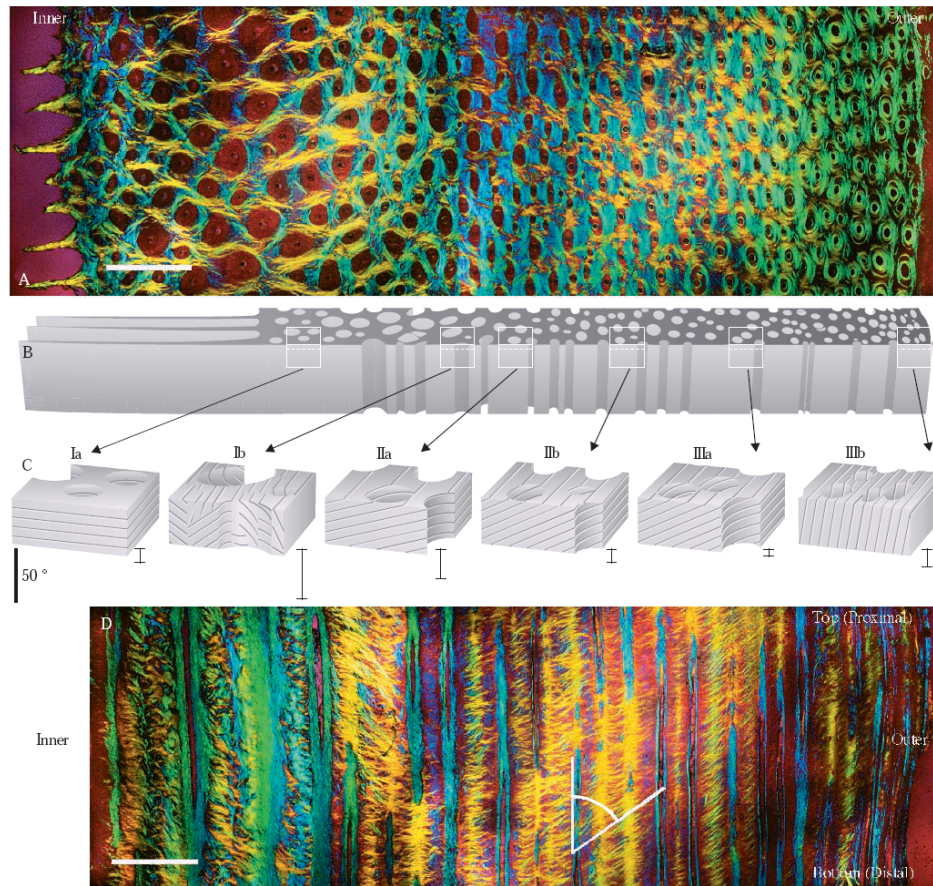
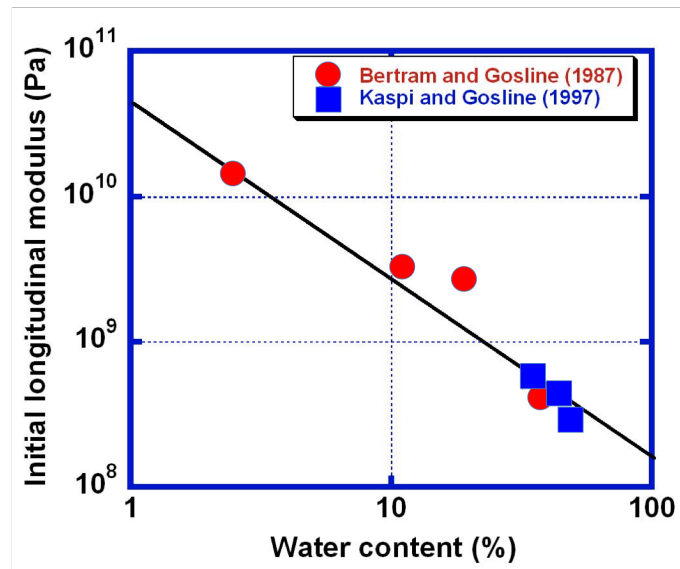
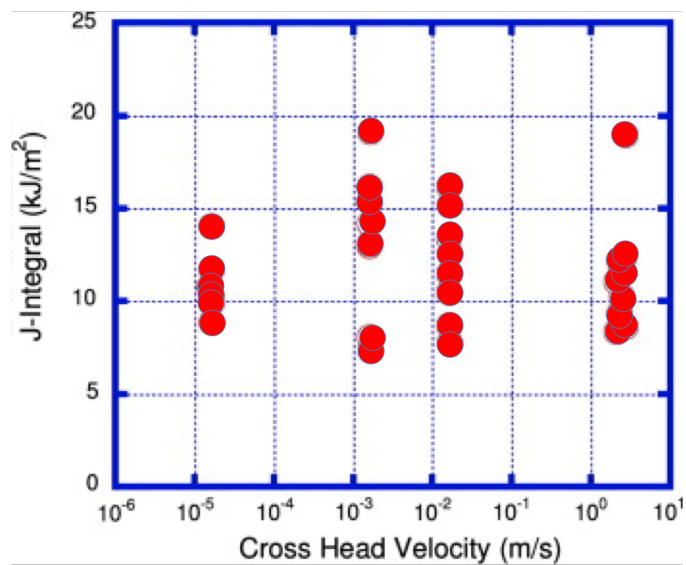


Figure 2.19: Hoof wall intertubular material composite diagram. (A) Cross-section of 10 mm thick hoof wall sample. Blue areas indicate circumferential molecular axial alignment, yellow areas reveal radial orientation. Purple areas in the hoof wall indicate axial alignment out of or perpendicular to the plane of section.;(B) A three-dimensional representation of the intertubular material extruded from a tracing of Fig.2.18; (C) Three-dimensional models of intertubular material IF organization from each representative region.; (D) longitudinally sectioned 10 mm thick hoof. Blue areas indicate longitudinal molecular axial alignment, yellow areas reveal radial orientation.(from Kaspi and Gosline [45]).



(a)



(b)

Figure 2.20: Mechanical performance of hoof wall;(a) Initial Young's modulus vs water content (from Kaspi and Gosline [45]);(b) J-integral vs cross head rate (from Kaspi and Gosline [44]).

Kaspi and Gosline demonstrated that the fracture morphology of hoof wall is strain rate dependant. Scanning electron micrographs of fracture surfaces after tensile testing conducted at low and high strain rates are shown in Fig.2.21. Tubule pull-out was evident at low and high strain rate; however, the degree of pull-out increases with slower tests, compared to fracture surface at high strain rate in Figure 2.21 A and C. The fracture surface at low strain rate is smooth and visible in Figure 2.21 B and D. Cracks travelled across the tubule axis and followed cellular planes of the intertubular material.

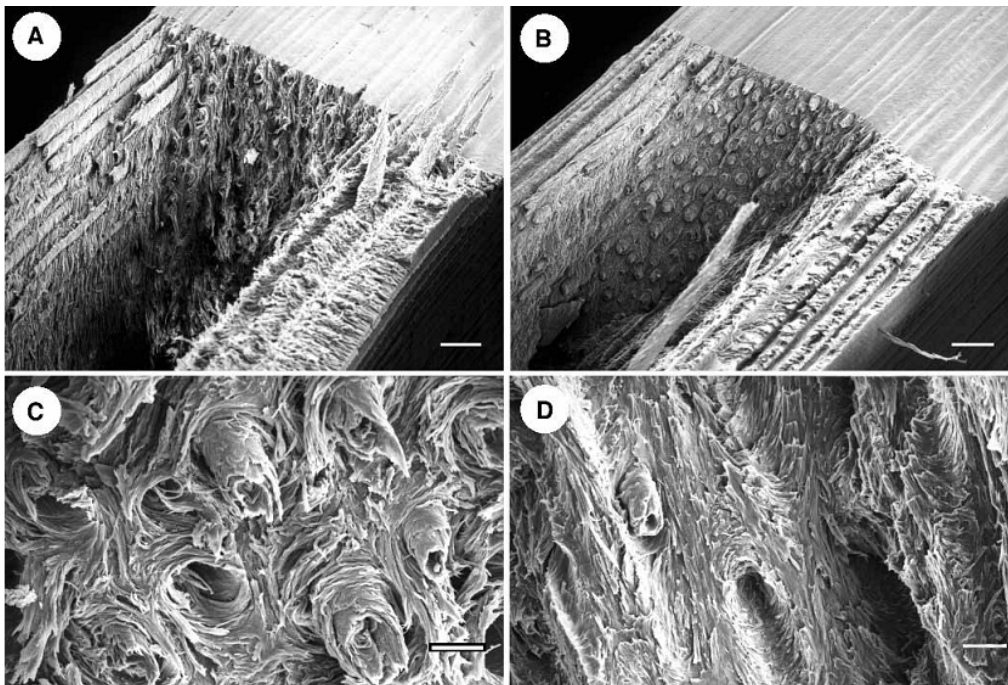


Figure 2.21: Scanning electron micrographs of fracture surface of hoof. (A) low magnification and (C) High magnification at 1.7×10^{-5} m/s. (B) low magnification and (D) high magnification at 2.5 m/s. Scale bar low magnification 1 mm and high magnification $100 \mu\text{m}$. (from Kaspi and Gosline [45]).

2.3.4.3 Horns

Rhinoceros horns consist purely of keratin having a laminated structure of tubules, similar to the structure of hoof. Ryder [127] described the tubules to be composed of horn filaments and range from $300 \sim 500 \mu\text{m}$ in diameter, shown in Figure 2.22. The horn tubules are placed more closely to each other, unlike hoof tubules. Hieronymus et al. [128] analysed rhinoceros horn keratin by light microscope and computed tomography, shown in Fig.2.23. Fig. 2.23 A shows sagittal section of entire rhinoceros horn with fluorescent light and dark patches at center of horn are heavily pigmented keratin. Fig. 2.23 B and C show banded fine horn laminae. Figure 2.23 D shows computed tomography and change in radiodensity of horn. The periodic banding in radiodensity is associated with growth rate of horn [128,129]. The transverse section of horn, consisting of intertubular matrix and tubules, is shown in Figure 2.24. The melanized intertubular matrix is visible in Fig. 2.24 (a). Schematic representation of white rhinoceros horn, showing tubules, cortex, medullary cavity, and intertubular matrix, is given in Fig. 2.24 (b).

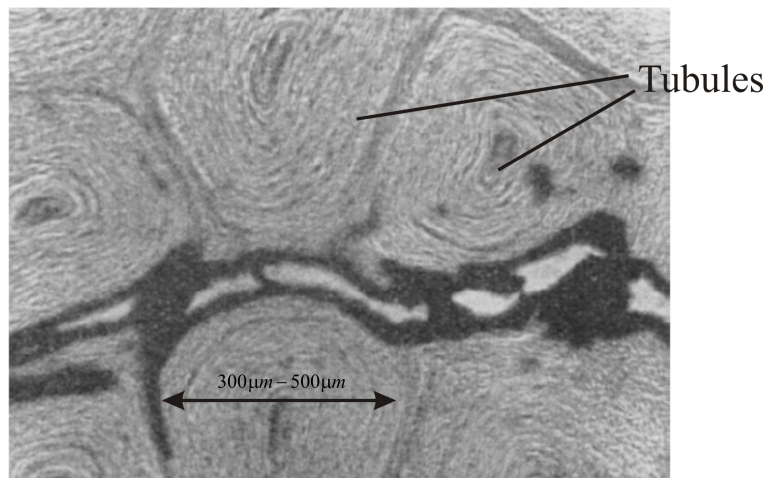


Figure 2.22: Tubules of horn (from Ryder [127]).

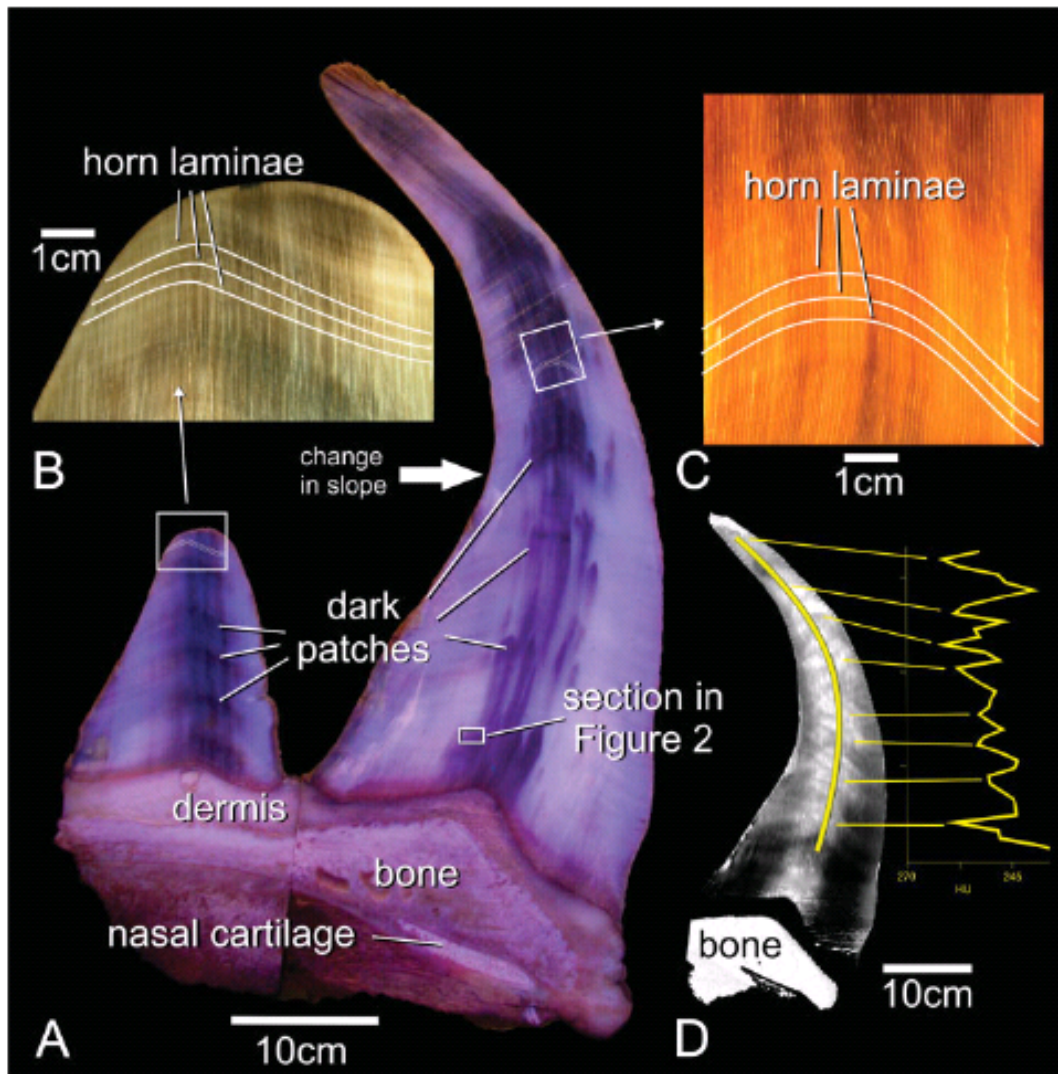
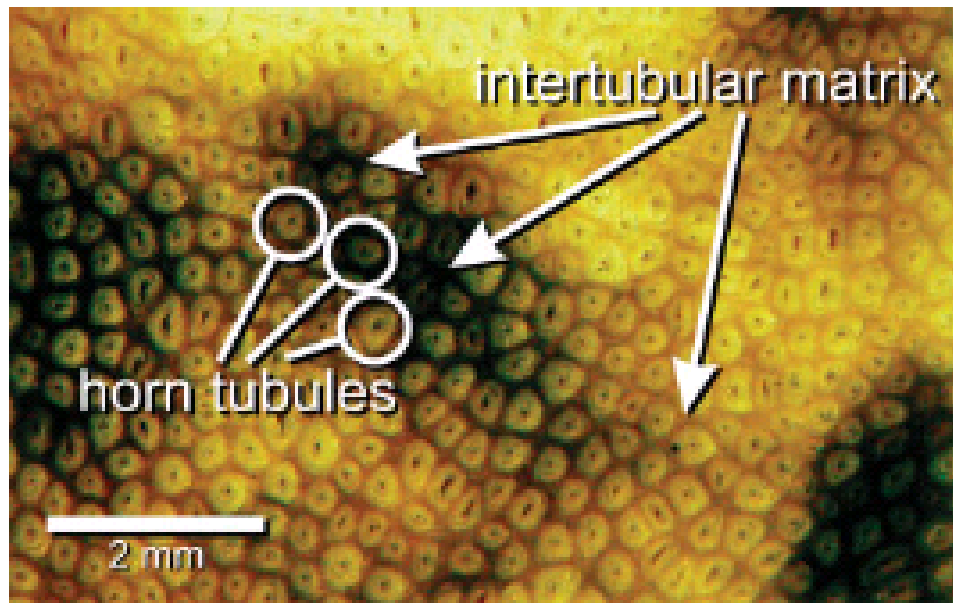
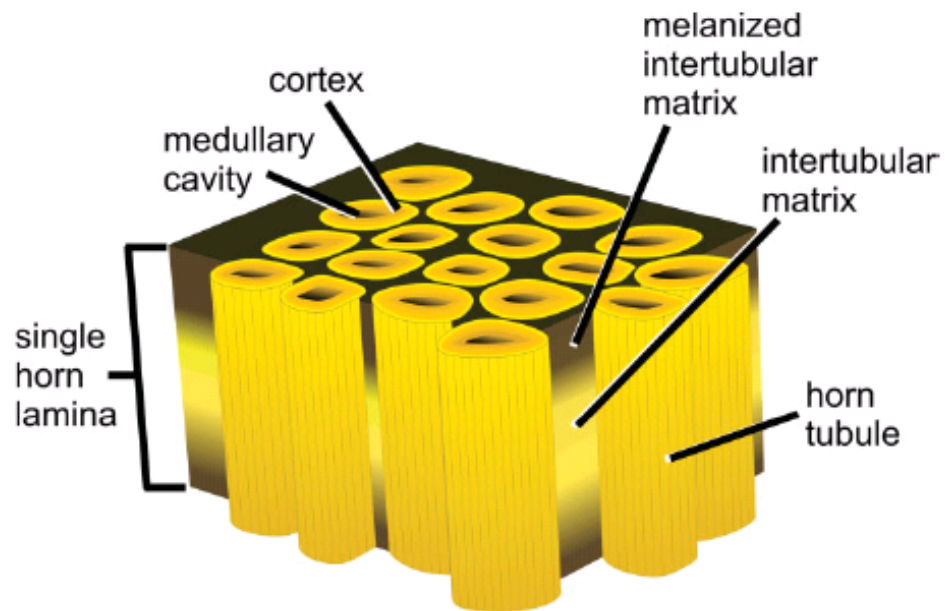


Figure 2.23: Nasal and frontal horns of white rhinoceros in sagittal section. (A) fluorescent light; (B) and (C) horn laminae in white light; (D) CT scan (from Hieronymus et al. [128]).



(a)



(b)

Figure 2.24: (a) Transverse section of rhinoceros horn (from [128]); (b) schematic of structure of white rhinoceros horn (from Hieronymus et al. [127]).

Horns are used for protection from predators and fight against members of own kind for territory. Mechanical properties of horns are great concern and interest in order to prevent breakage from the fight. Kitchener and Vincent [42] have studied oryx horn and applied the composite theory to predict the stiffness [42]. The Young's modulus of oryx horn is 6.1 GPa in dry condition and decreases 2.4 GPa and 1.8 GPa in hydrated conditions of 20% and 40% water, respectively. The mechanical properties of keratin are sensitive to water content. Kitchener observed stress relaxation of gemsbok horn as the content of water increases [130]. The orientation of tubules is responsible for anisotropic behavior of horn. Figure 2.24 shows stress-strain curves of horn in transverse and longitudinal directions [131]. The longitudinal direction shows higher stiffness and elongation because tubules are oriented parallel to loading axis.

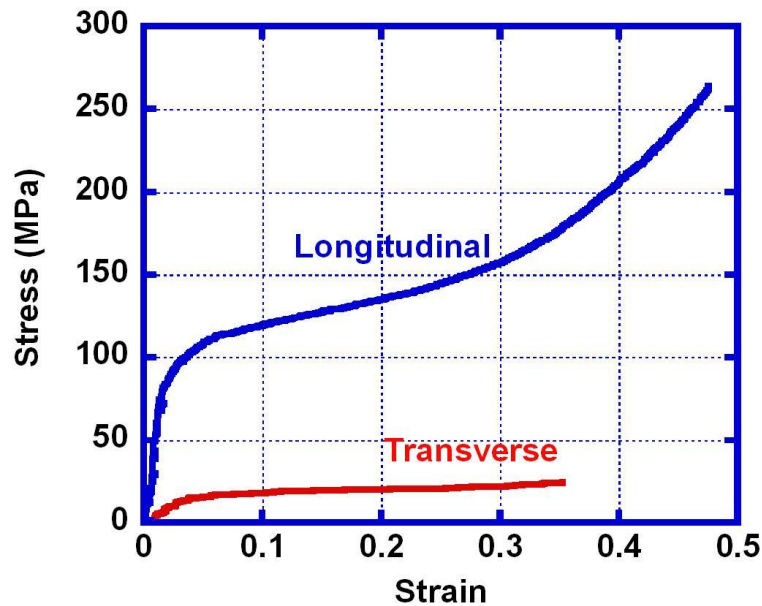


Figure 2.25: Stress-strain curve of horn keratin (from Druhala and Feughelman [131]).

2.3.5 Reptilian Keratins

2.3.5.1 Chameleon

We have seen earlier that α -keratin is mammalian, whereas β -keratin is avian; the epidermis of the reptiles is unique, consisting of both α - and β -keratins. Metachrosis (changing color) in lizard is the most famous and complex feature in the reptile family [132]. The structure of the chameleon skin consists of several layers. The thin outermost layer of oberhautchen consists of cornified cells with spinules throughout its surface. This covers a thicker β layer which decreases in thickness along its hinges [133] and [134]. Fig. 2.26 shows the cross-section of epidermis of the American chameleon (*Anolis carolinensis*) and the meso-layer between the α -layer and β -layer [133]. Below the α -layer, the structure is similar to a mammalian epidermis. The chameleon has pigment-containing cells called chromatophores, embedded in the dermal layers. The chromatophores allow the chameleon to change its skin color. Two or three kinds of pigments have been detected in the body of the American chameleon [135] while the African chameleon has five pigments. Fig. 2.27 shows vertically sectioned back scale of American chameleon [136]. The hexagonal scale of epidermis varies with position from 250 μm to 400 μm . There are two types of chromatophores containing yellow pigment (xanthophore) and red pigments (erythrophore). The xanthophore (cells containing yellow pigment) layer lies under the stratum germinativum layer, providing 10 m of the dermal layer [136]. There is a 10-20 μm in thickness of iridophore layer below the xanthophore layer. This contains inorganic crystalline pellets that reflect blue or white light. Erythrophores (cells containing red pigment) have been found in the basal zone of the iridophore layer of American chameleon [136]. Fig. 2.28 shows iridophore platelets in the iridophore layers. The crystalline structure of iridophore platelets yields blue-green light [137]. The melanophores, which contain melanin, are the largest of the chromatophores. These produce black or brown colors. This layer is followed by the iridophore layer

which reaches the xanthophore layer [136]. The collagenous basement lamella lies at the bottom of dermal layer. The skin color is controlled by the expansion or contraction of the chromatophores producing a variety of colors from the different combination of chromatophores. The light modulation of color is provided by the melanophores. Although the chameleon does not contain any green pigmentation, the yellow pigment and the reflecting blue light at iridophore layer produce the green color of the skin.

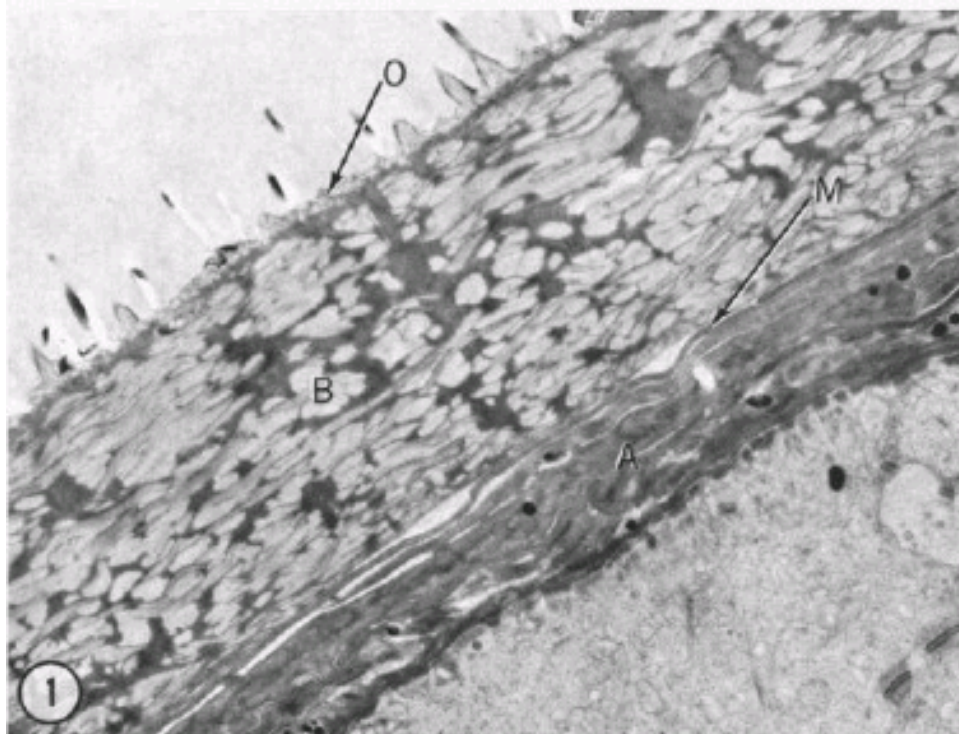


Figure 2.26: Cross-Section of epidermis of American Chameleon. O: oberhautchen layer, B: beta layer, M: mesos layer, A: alpha layer (from Alexander and Parakkal [133]).

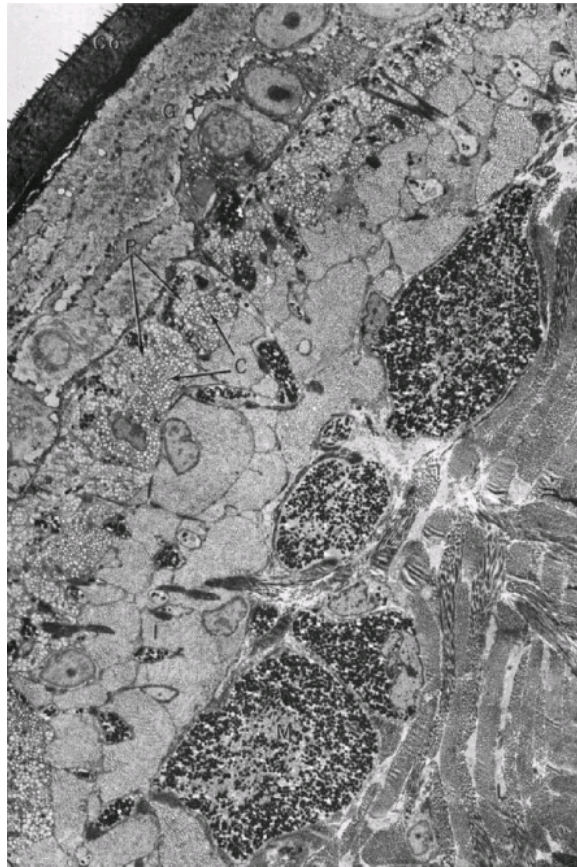


Figure 2.27: Cross-section of integument of American chameleon. Co: stratum corneum, G: stratum germinativum, P: xanthophore layer, C: carotenoid containing cell, I: iridophore, M: melanophore layer, L: collagenous basement lamella (from Alexander and Fahrenbach [136]).

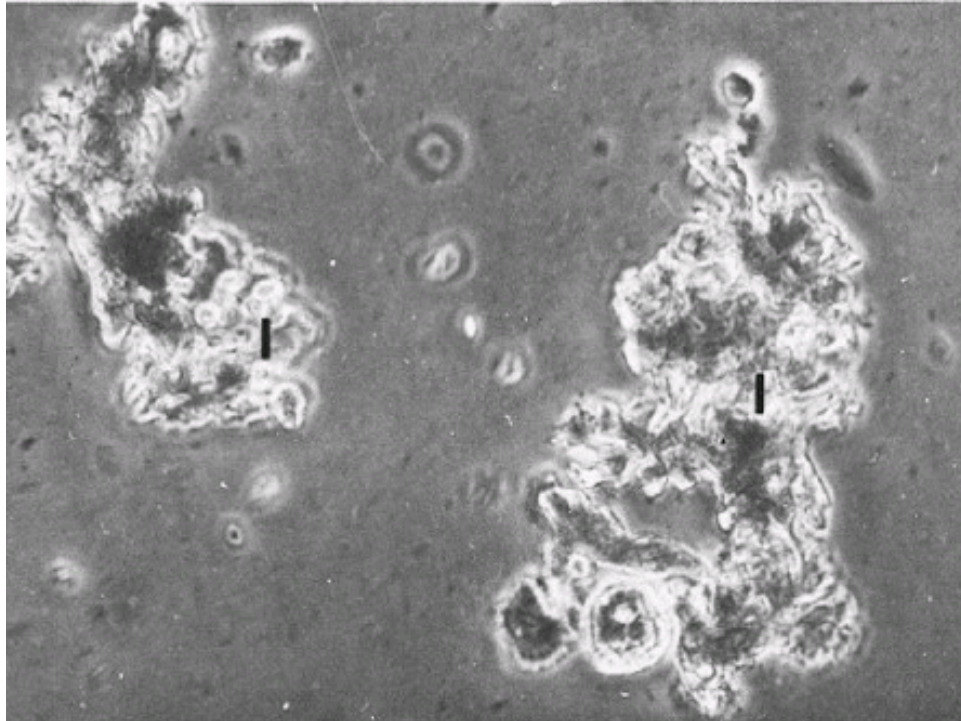


Figure 2.28: Light micrograph of iridophore crystals (marked I) from American chameleon skin (from Rohrlich and Rubin [137]).

2.3.6 Avian Keratins

Avian integuments (beaks, feathers and claws) were developed for different purposes: foraging activity, locomotion, and flight activity. All integuments are made from keratins. Bonser extensively studied mechanical properties of avian integuments including beaks, feathers, and claws [50, 51, 138–141]. Especially, the feathers have been extensively studied on not only mechanical properties but also the photonic properties and colorization [142–145]; bird feathers are also used as ornaments or accessories due to their beautiful colors.

2.3.6.1 Feather

The feathers are very light and stiff and supported by the skin. There are many types of feathers in different species and individual feathers possess a complex structure. The structure of bird feather is composed of a main shaft called "*rachis*" and side branches called "*barb*". Figure 2.29 shows a schematic representation of feather; the microstructure is presented by scanning electron micrographs. The fine branches extending from barb are called "*barbules*" that tie together with hooklets, creating the "*vane*" of feather. The rachis consists of a hollow cylinder called *cortex* and supporting foam core called "*medulla*". The scanning electron micrographs of cross section of feather rachis and barbs shows that both consist of closed-cell foam. X-ray diffraction detects the crystallinity of feather and the pattern is very similar to other avian keratins such as claws, beaks, and scales [105]. However, there are differences in composition between feather and other avian keratins [36, 37]. Brush measured the molecular weight of avian keratins and found 10500 *g/mol* for feather, which is lowest among other avian integuments [37].

The bending behavior of feather is of great importance in the failure of bird feather. The feather must have sufficient stiffness and flexibility in order to withstand some degree of bending caused by flight activity. Purslow and Vincent [146] showed

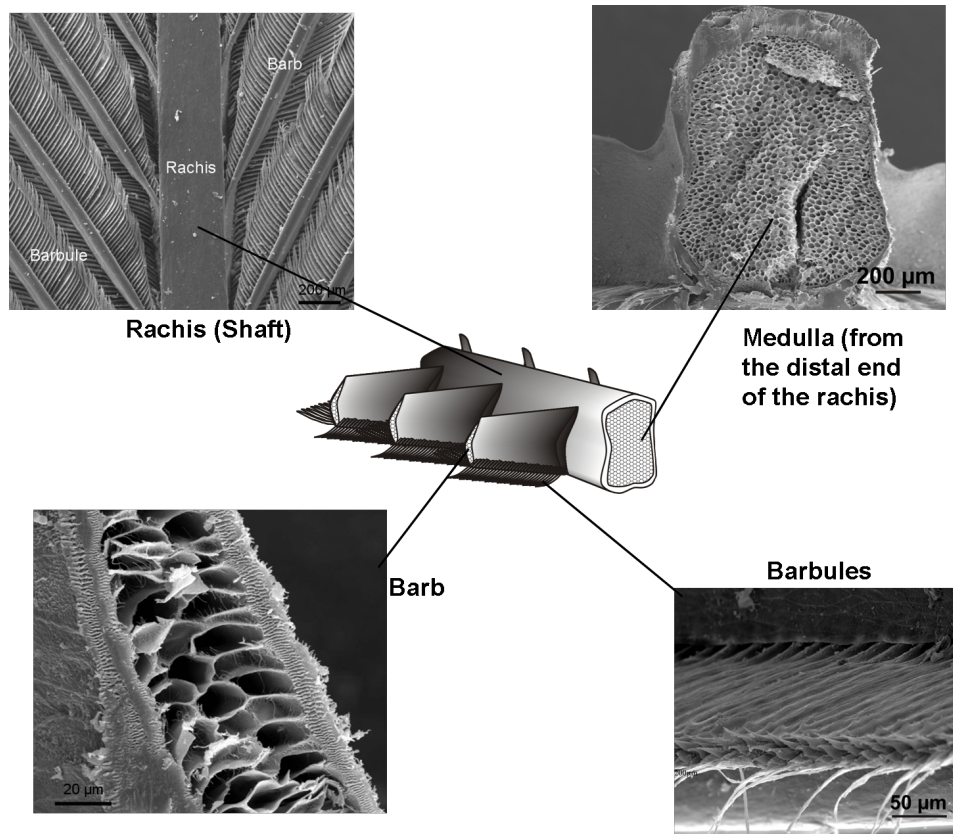


Figure 2.29: Schematic representation of structure of feather with scanning electron micrographs (from [69]).

that the bending behavior of rachis depends on the size and shape of the cortex. The root of feather is circular and the shape becomes elliptic toward the tip. Bonser and Purslow found average Young's modulus from eight birds to be 2.5 GPa in tension [48]. Comparing the feather of volant (flying) and flightless birds, the Young's modulus of volant bird feather varies with the orientation of the rachis and that of flightless bird feather is almost the same at any position of rachis due to the absence of aerodynamics requirement [49]. Volant bird feather experiences frequent changes in strain during the flight. Corning et al. [147] investigated the uniaxial oscillatory strain

pattern of feather during flight and the peak strain under compression was found to be 2.2 times higher than the peak under tensile strain. The feather experiences a maximum compressive strain throughout downstroke stage.

Mechanical properties of feather keratin demonstrate humidity sensitivity. The stiffness of feather rachis decreases with increased moisture content, which is similar to the behavior of other keratinous tissues [148]. Figure 2.30 shows the stress-strain curves of feather rachis at three different humidity levels. The stiffness and strength of feather decreases as the humidity level increases. The decrease of mechanical properties of feather in high humidity condition is associated with water absorption level of keratin matrix.

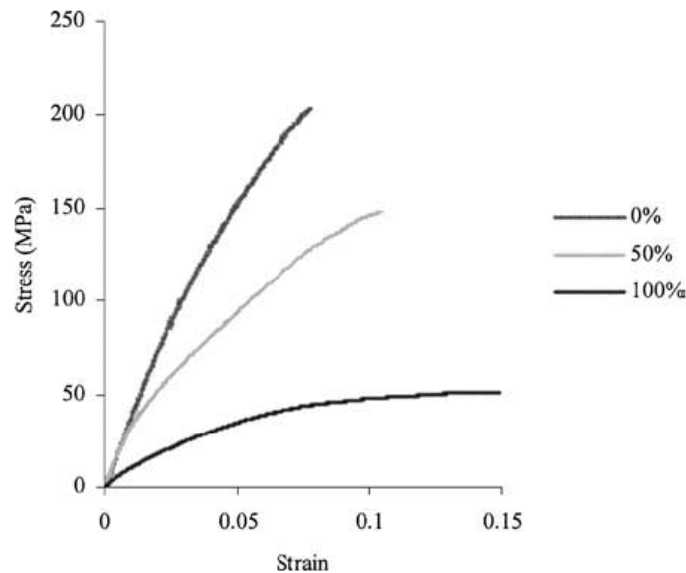


Figure 2.30: Stress-strain curves in tension of feather rachis at three humidity conditions.(from Taylor et al. [148]).

Bonser investigated the compressive response of medullary foam of rachis. He showed that the relative Young's modulus of medulla in compression increases with apparent density [149]. We revised Bonser's results [149] with relative Young's mod-

ulus and relative density. and obtained the same results. The Young's modulus of medulla also increases as the relative density increases, shown in Figure 2.31.

The relationship between the colorization and mechanical properties of avian keratins received great attentions. Most of the studies on this topic are not persuading. However, Cameron et al. [150] studied the effect of location on the melanized and non-melanized barbs of feather with stress-strain relation and locations. They considered not only color but also the locations of the barb along the rachis. Figure 2.32 shows the stress plotted as a function of functional distance along rachis. Black dots represent melanic and white dots are the non-melanic regions. There are no significant differences in color but the breaking stress level decreases from proximal to distal.

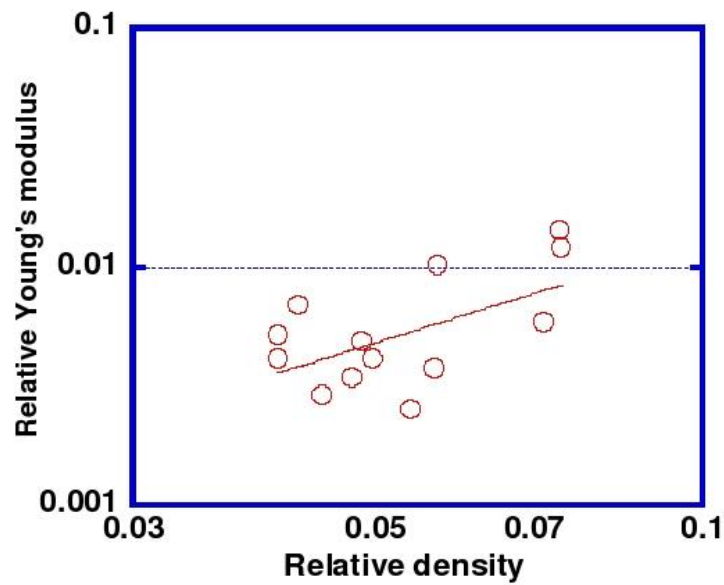


Figure 2.31: Relative Young's modulus vs relative density of feather medulla (Bonser's results [149] with exponential fitting curve x-axis is revised with relative density).

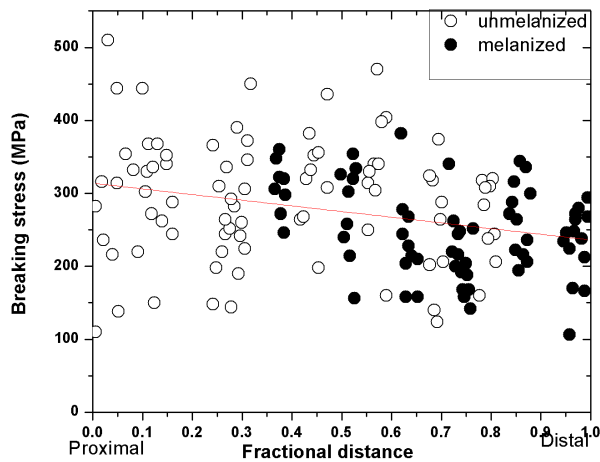


Figure 2.32: Breaking stress under tension as a function of fractional distance from feather barb (from Butler and Johnson [150]).

2.3.6.2 Claws

Avian claws are coverings of heavily cornified integument. All birds have toe claws, composed of dorsal plate and ventral plate. The dorsal plate is harder than the ventral plate. The dorsal plate contains heavy deposits of beta-keratin and calcium salts [151]. Toe claws are used for catching prey, and even as a weapon. Wing claws also are found in most primitive bird form, “*Archaeopteryx*”, which lived in 145 million years ago.

Claws are as stiff as feather and sensitive to water like other keratinous materials. Bonser et al. [139] compared water sensitive of claw keratin in three different RH conditions, shown in Figure 2.33(a). The highest Young’s modulus and tensile strength are 2.7 GPa and 90 MPa at 0 % RH. The Young’s modulus is 2.07 GPa and tensile strength is 68.7 MPa at 50% RH. The decrease is dramatic at 100 % RH. Young’s

modulus and tensile strength dropped to 0.14 GPa and 14 MPa, respectively. This trend is similar to the feather. A decrease in mechanical properties at high humidity conditions is also observed in hardness [50]. Figure 2.33(b) shows the comparison of water content and hardness of ostrich claw keratin. Comparing with low and high water content of claw keratin, the hardness decreases by five folds from low to high water content whereas the influence is not as significant as Young's modulus.

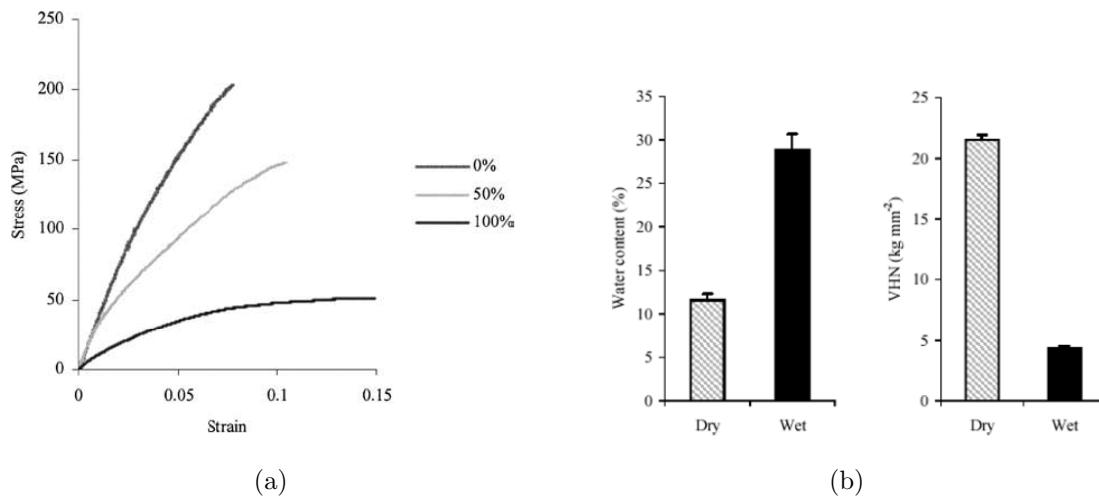


Figure 2.33: Stress-strain curves of claw keratin at three different humidity conditions (from Taylor et al. [148]) ;(b) Water content and hardness of ostrich claw keratin (from Bonser [50]).

2.3.6.3 Rhamphotheca

The avian beak is a continuously growing and dynamic structure composed of bone, vascular layers, keratin, dermis, and a germinative layer. Figure 2.34 depicts a picture of Toco toucan beak with a schematic. The keratinized shell covering bone is called '*rhamphotheca*' and can be divided into the rhinotheca, or maxillary keratin for upper rhamphotheca, and the gnathotheca, or mandibular keratin for lower

rhamphotheca. The median dorsal border of the rhinotheca is called the '*culmen*', and the median ventral border of the gnathotheca is called the '*gonys*'. The edges of the rhamphotheca are called the '*tomia*' [152]. Toucan as for other Toucans as for many other Ramphastids, are serrated or marked with Schaugebiss [153].

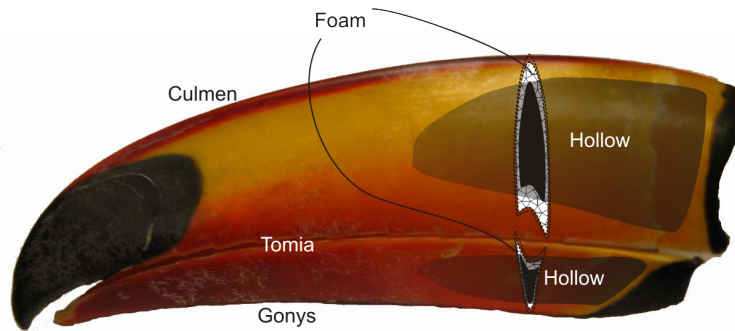


Figure 2.34: Picture of Toucan beak with schematics

The beak is used for foraging, feeding, social interaction, prehension of food or of nesting material, grooming, and locomotion [152, 154]. The rate of keratin replacement is strongly dependent on the use of the beak. Toucans are also known to engage in bill fencing behavior which is speculated to be an assertion of dominance [152]. In large Parrots, the complete rhinotheca is entirely replaced in about six months, while in Toucans, the rhinotheca grows approximately 0.5 cm over a two-year period [154]. Bird bills are mainly adapted for foraging and the stiffness of rhamphotheca is sufficient for this purpose. Bonser and Witter [52] have first measured the hardness of European Starling bill and compared the melanized and unmelanized rhamphotheca. Figure 2.35 shows the hardness of bill keratin. The melanized keratin exhibits $\sim 67\%$ higher hardness. In the case of the Starling, the melanized bill is a seasonal change, so it can be an adaptation to eat food that are harder.

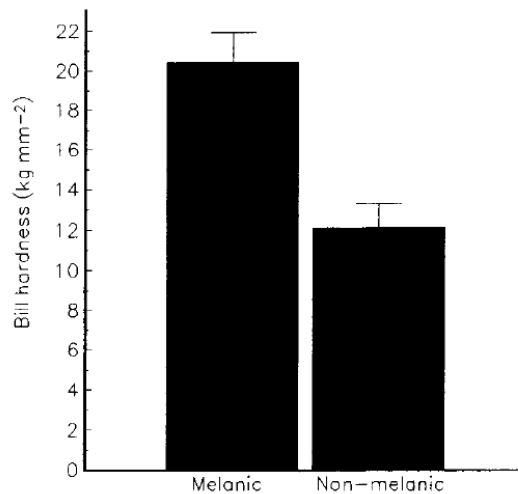


Figure 2.35: Hardness of melanized and unmelanized bill keratin of European Starling (from Bonser [52]).

2.4 Cellular Solids

2.4.1 Structure of Foams

Many researchers are fascinated to study the properties of cellular solids because they often prevail over bulk materials by weight and efficiency. Cellular solids are made from an interconnected network of solid struts which form edges or cell faces. The simplest structure is the two-dimensional cellular network, honeycomb. Commonly, the three-dimensional network structure is referred as foam. Because of its unique structure, foam can even have negative Poisson's ratio [155]. Figure 2.37 shows examples of three-dimensional foam materials, used for different purposes [156]. Aluminium foam, one of the metallic foams, is used for a structural application in Fig 2.37(a). Polyurethane foam, a polymeric foam, is often used as packaging materials in Fig 2.37(b). Fig. 2.37(c) show the fibrous structure of papers. Water bubbles also are considered as a type of foam and have closed-cell structure

in Fig 2.37(d). Fig. 2.37 (e) shows the internal structure of luffa with open cell configuration.

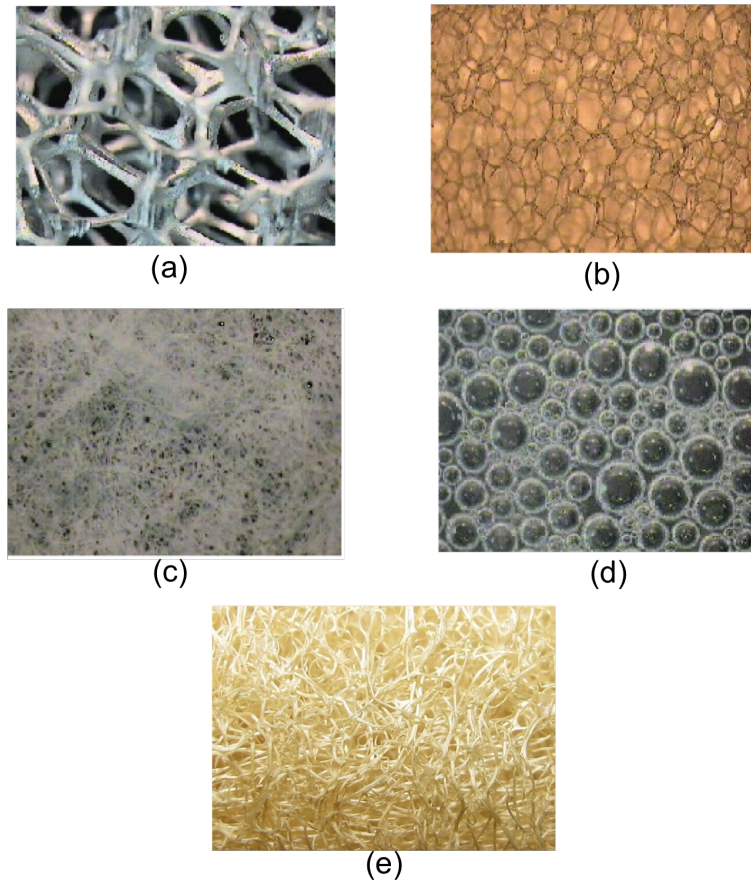
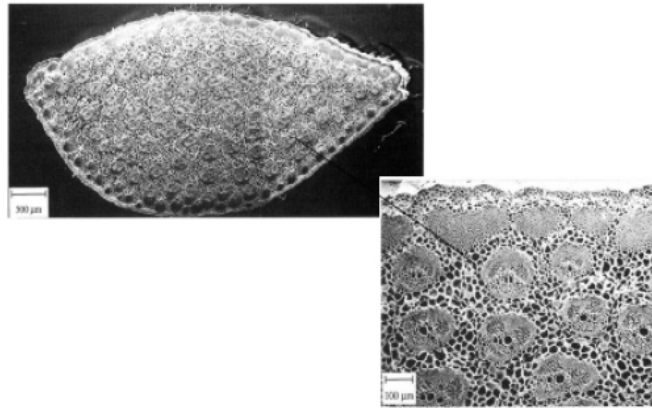


Figure 2.36: Tri-dimensional structure of foams;(a) aluminium;(b) packing spongy;(c) paper;(d) water bubbles;(e) luffa spongy (from Seki et al.[156]).

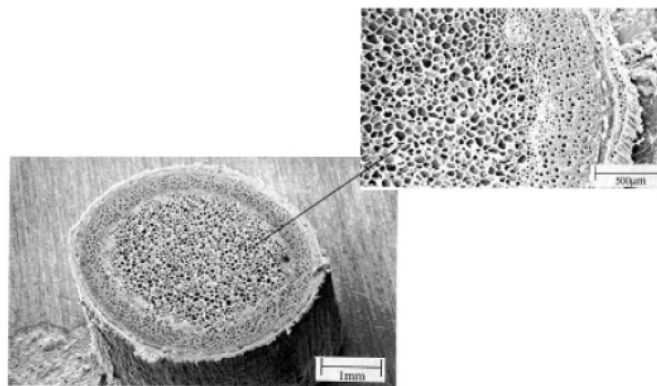
Natural materials that are cellular solids like wood, leaves, and bone abound. The arrangement of cells of cellular solids ranges from nearly perfect order of bee's honeycomb to disorder. The function of cellular solids is to increase the mechanical stability and efficiency of the materials, which can be found in nature and in industrial applications. Wood, a natural foam, is the most common material for beams and

columns. The honeycomb is an efficient structure for bending stiffness. Bamboo, another type of cellular solid, is designed with the significant flexural rigidity [157, 158]. Figure 2.37 shows examples of natural cellular solids [159]. Palm petiole made from dense vascular bundles embedded in porous parenchyma matrix shown in Figure 2.37(a). Most plant stems have cellular structure and Figure 2.37 (b) shows scanning electron micrographs of hawthorn stem. The cylindrical shell is filled with the different porosities of foam.

Cork, widely used for bottle stoppers, has a cellular structure. Individual cells of cork are regularly arranged with thin wall homogeneous tissues and form a closed cell structure with internal gas. Cells consist of hexagonal prisms and Figure 2.38 shows the anisotropy of the structure [17, 160]. The radial direction has hexagonal cells and the face resembles squares in tangential and axial directions. Three edges usually meet at the vertex. The lateral faces of cell are corrugated, which is responsible for a Poisson's ratio of nearly zero.



(a)



(b)

Figure 2.37: Scanning electron micrographs of natural foams;(a) hawthorn stem;(b) palm petiole (from Gibson et al. [159]).

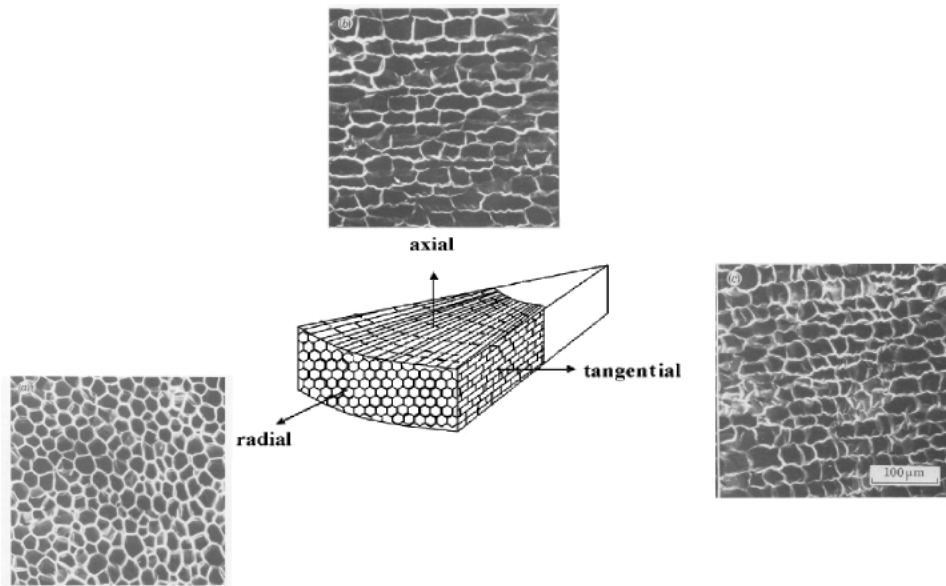


Figure 2.38: Cell structure of cork, showing three different directions (from Siliva et al. [17,160]).

2.4.2 Mechanical Properties of Foams

The deformation of foam is mostly described by compressive stress-strain curves typified in Figure 2.39 [55]. At low strain, stress-strain curve shows linear elasticity followed by long plateau region where cell wall deformation including buckling and yielding occur. Figure 2.39 (a) shows smooth plateau and Figure 2.39 (b) shows a number of spikes due to brittle crushing. After the plateau, the foam starts to densify itself, and the stress rises steeply.

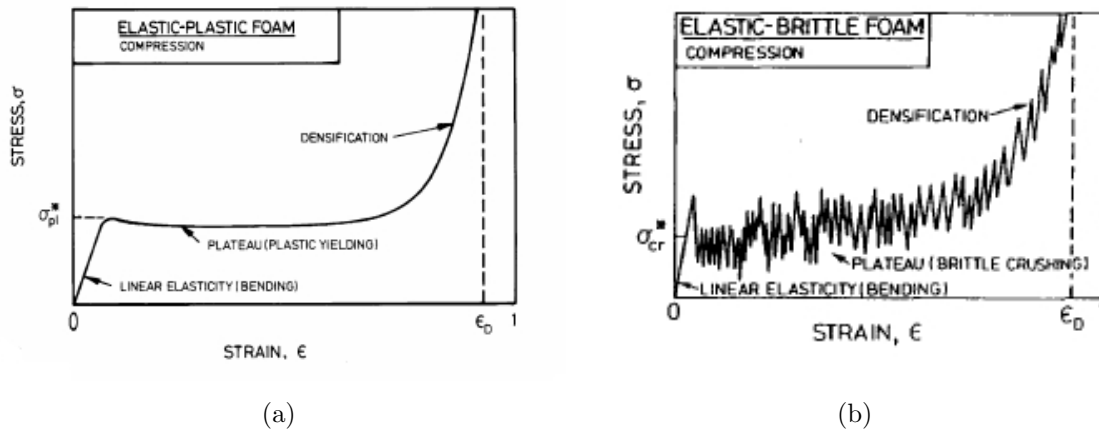


Figure 2.39: Typical compressive stress-strain curves of foam;(a) an elastic plastic foam;(b) an elastic brittle foam (from Gibson and Ashby [55]).

The deformation mechanisms of foam are associated with the cell geometry. The cell wall dimensions (length and thickness) are proportional to the relative density, which is the density of the cellular material divided by the density of the material making cellular solids. Gibson and Ashby describe the mechanical behavior of the foam by using the geometry of the foam associated with the relative density [55]. For low density (<0.1), the relative density of closed-cell foam is given by:

$$\frac{\rho^*}{\rho_s} = C_1 \frac{t}{l} \quad (2.1)$$

where ρ^* is the density of foam, ρ_s is the density of solid, C_1 is a numerical constant, t is uniform thickness, l is the face of side.

The deformation of foam involves in several mechanisms. Figures 2.40 (a) and (b) show the deformation mechanism of open-cell foam and closed-cell foam subjected to uniaxial compressive loading. Open cell foam involves in cell wall rotation, bending and stretching in Fig.2.40 (a). The deformation of the closed-cell is more complicated than the open-cell. When closed-cell foams are deformed, the deformation involves in not only rotation and bending of cell wall, but also stretch of the membranes and gas pressure. Figure 2.40 (b) shows the contribution of cell fluid and membrane stress in cell faces.

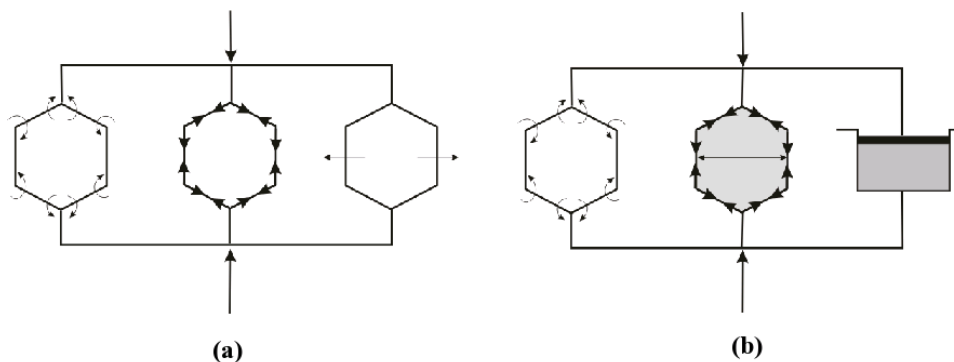


Figure 2.40: The deformation mechanism foam (a) open cell foam; (b) closed-cell foam. (from Gibson and Ashby [55]).

2.4.3 Gibson and Ashby Constitutive Equations

Gibson and Ashby [55] introduced a simple cubic model to describe the deformation of foams. They presented two models: open-cell and closed-cell configurations.

The use of two models depends on the structure of cellular solids. We describe closed-cell model here for our analysis. Figure 2.41 shows the undeformed and deformed closed-cell cubic models. The foams made from materials possessing the plastic yield point are subjected to plastic collapse when loaded beyond the linear elastic regime. The linear elastic region is limited to small strain for this model. When plastic collapse occurs, there is a long horizontal plateau in the stress-strain curve [15].

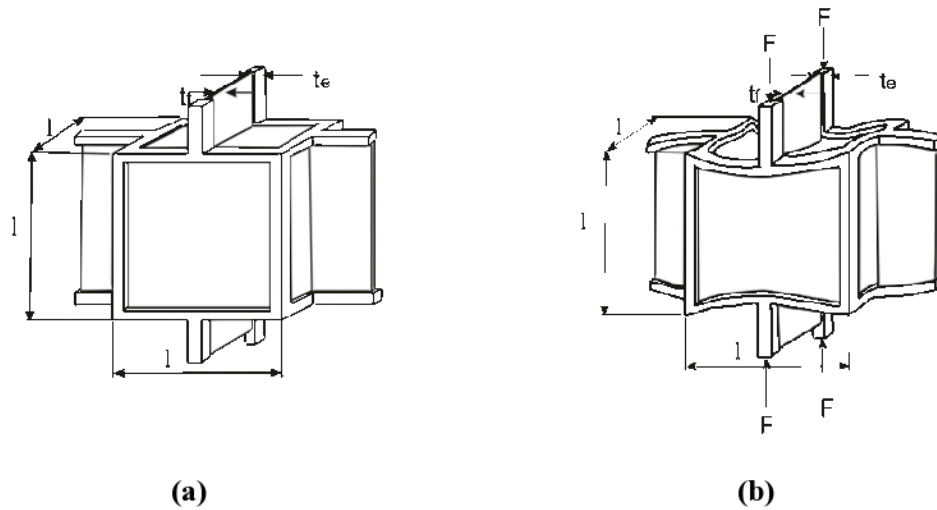


Figure 2.41: Closed cell cubic model;(a) undeformed and;(b) deformed(linear elasticity).

The plastic collapse occurs when the moment applied by the force F exceeds the plastic moment of the cell walls. The bending moment of the beam is given by

$$M_p = \frac{1}{4}\sigma_{ys}t^3 \quad (2.2)$$

where σ_{ys} is the yield strength of the cell wall material, t is the thickness of the cell edge.

In closed cell, the plastic collapse causes the membranes to crumple in compressive direction. However, the membranes are stretched at the horizontal direction.

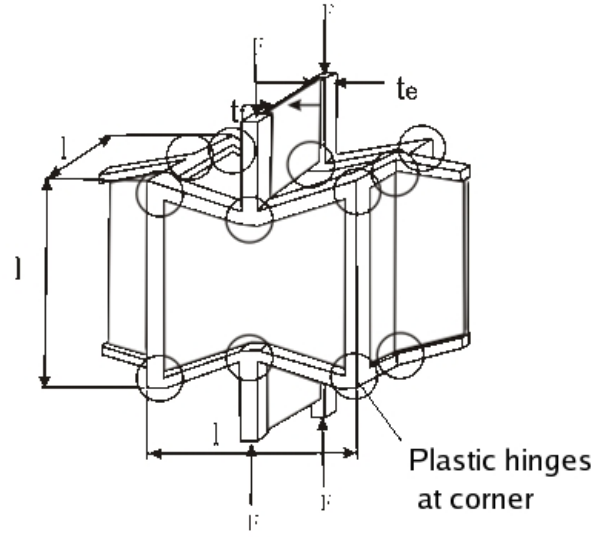


Figure 2.42: The formation of plastic hinges in a closed cell foam.

The displacement Δ and force F perform a work $F\Delta$. The rotation of the edge is proportional to Δ/l and the plastic work is $M_p\Delta/l$. The cell face stretched by a distance that is proportional to Δ , doing work is $\sigma_{ys}\Delta t_f l$,

$$F\Delta = \alpha M_p \frac{\Delta}{l} + \beta \sigma_{ys} \Delta t_f l \quad (2.3)$$

where α and β are constants. Substituting F by σl^2 and equation 2.3 gives.

$$\frac{\sigma_{pl}^*}{\sigma_{ys}} = \frac{\alpha}{4} \left(\frac{t_e}{l} \right)^3 + \beta \left(\frac{t_f}{l} \right) \quad (2.4)$$

Equations for t_f/l , t_e/l are given by

$$\frac{t_f}{l} = 1.4(1 - \phi) \frac{\rho^*}{\rho_s} \quad (2.5)$$

$$\frac{t_e}{l} = 0.93\phi^{1/2} \left(\frac{\rho^*}{\rho_s} \right) \quad (2.6)$$

Finally equating Equations 2.5 and 2.6 give:

$$\frac{\sigma_{pl}^*}{\sigma_{ys}} = C_1 \left(\phi \frac{\rho^*}{\rho_s} \right)^{3/2} + C_2 (1 - \phi) \frac{\rho^*}{\rho_s} \quad (2.7)$$

Experimental data including contribution of gas pressure equation 2.7 lead to: where C_1 and C_2 are constant parameters

$$\frac{\sigma_{pl}^*}{\sigma_{ys}} = 0.3 \left(\phi \frac{\rho^*}{\rho_s} \right)^{3/2} + (1 - \phi) \frac{\rho^*}{\rho_s} + \frac{p_0 - p_{at}}{\sigma_{ys}} \quad (2.8)$$

where p_0 is a pressure inside the cell and p_{at} is atmospheric pressure.

2.4.4 Cancellous Bone

Cancellous, or trabecular bone is a porous bone that often fills in empty space of marrow bone and increases the energy absorption. Figure 2.43 shows the structure of cancellous bone having open-cell structure. The thickness of struts or trabeculae is usually a few hundred micron. There are three types of strut structures; rod like structure, prismatic cell structure, parallel plate structure [55]. The change in structure is associated with the load that cancellous bone bears. The density of cancellous bone also depends on the load that it is experienced [55]. The optimal structure of cancellous bone generation is governed by the load transfer. The structure is maintained and adapted by the internal or external load [161]. The cancellous bone is composed of inorganic calcium compounds such as hydroxyapatite and amorphous calcium phosphate; it provides cancellous bone with the stiffness.

The mechanical properties of cancellous bone have been widely studied [162–165]. Since it is porous, cancellous bone is not as quite strong as compact bone. Figures 2.44 and 2.45 show material property charts for biological materials. The mechanical domain of cancellous bone is colored in grey. The density and mechanical properties shows wide variations. The density ranges from 0.1 to 1 g/cm^3 . The Young's modulus ranges from 0.01 to 10 GPa and strength ranges from 0.8 to 90 MPa.

The compressive response of cancellous bone is a typical behavior of cellular solids, shown in Figure 2.46. Three distinct regions are evident in stress-strain curve of cancellous bone; linear elastic regime, non-linear regime, and densification regime. The strength and stiffness increase with apparent density [166] in Figure 2.46. Each cell deforms by elastic buckling or brittle fracture after linear elastic regime under compression. The Gibson-Ashby constitutive equations apply for modeling mechanical behavior of cancellous bone [18].

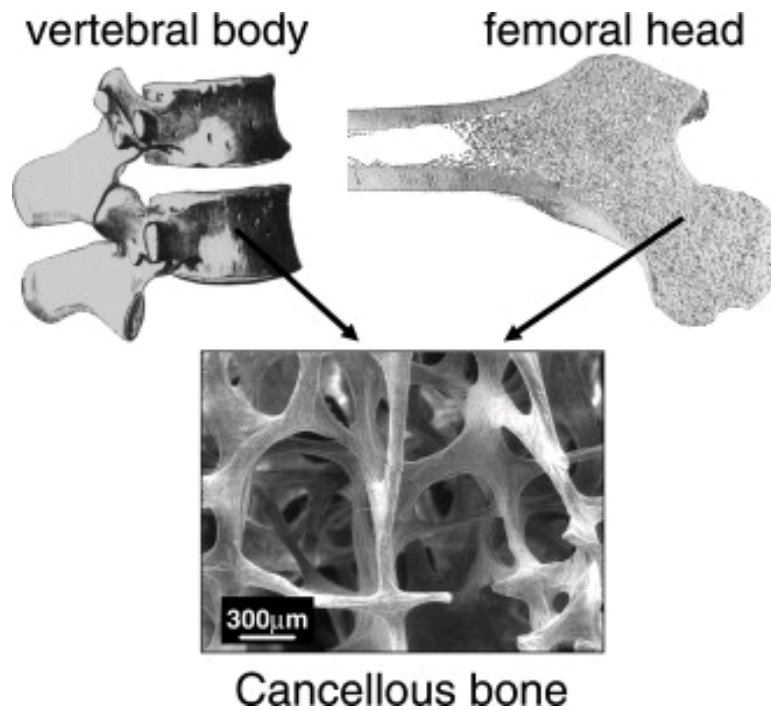


Figure 2.43: Vertebra or the femoral head are filled with a spongy structure called trabecular bone. The struts (or trabeculae) have a thickness on the order of a few hundred micrometers (from Fratzl and Weinkamera [70]).

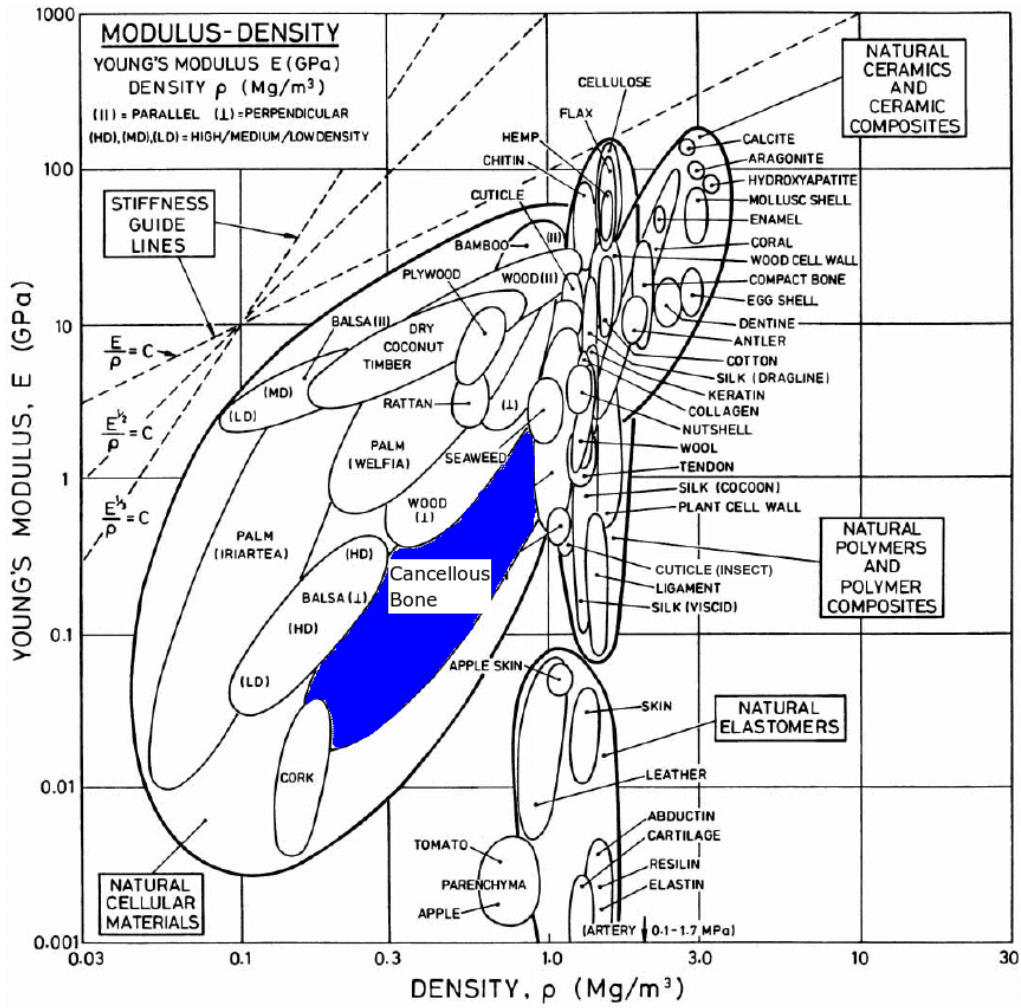


Figure 2.44: Material property chart for natural materials (cancellous bone is highlighted in grey), showing Young's modulus vs density (from Wegst and Ashby [108]).

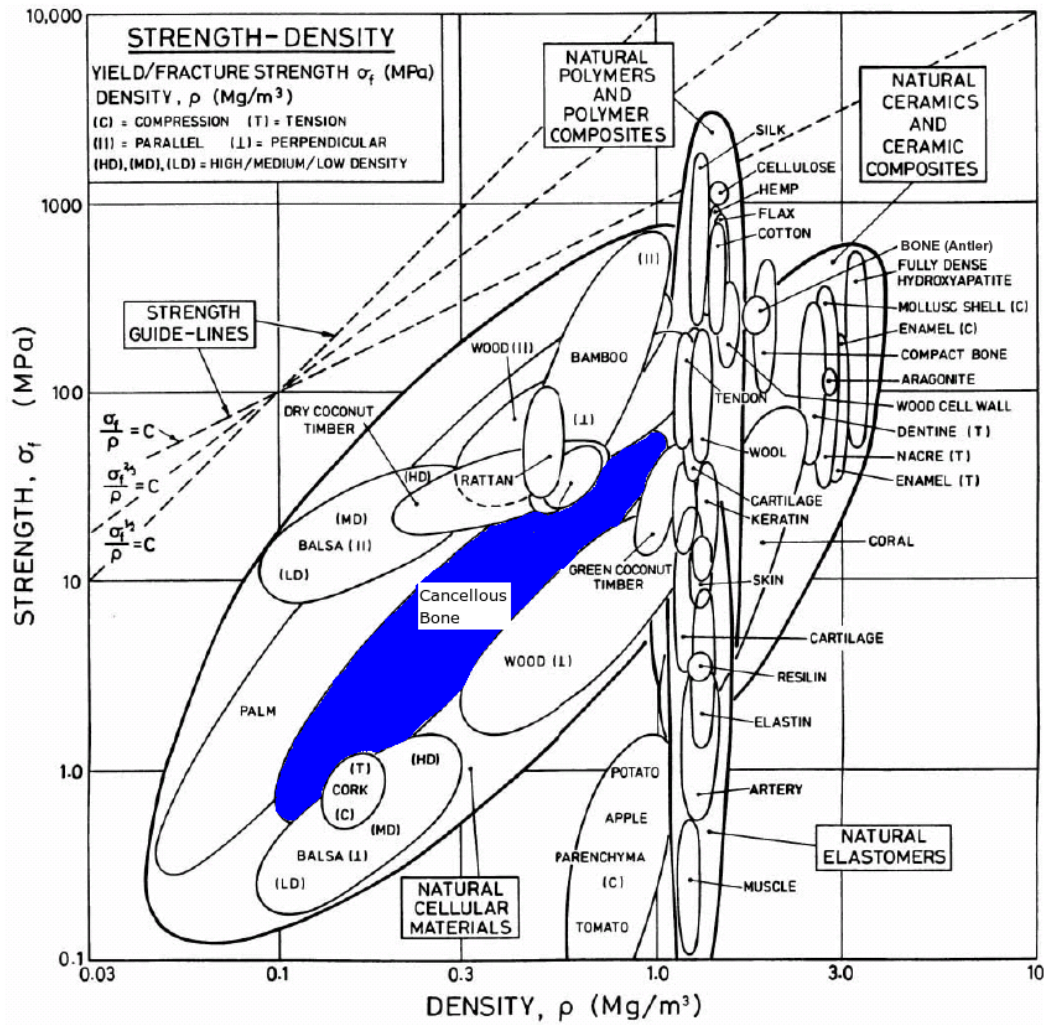


Figure 2.45: Material property chart for natural materials (cancellous bone is highlighted in grey), showing strength vs density (from Wegst and Ashby [108]).

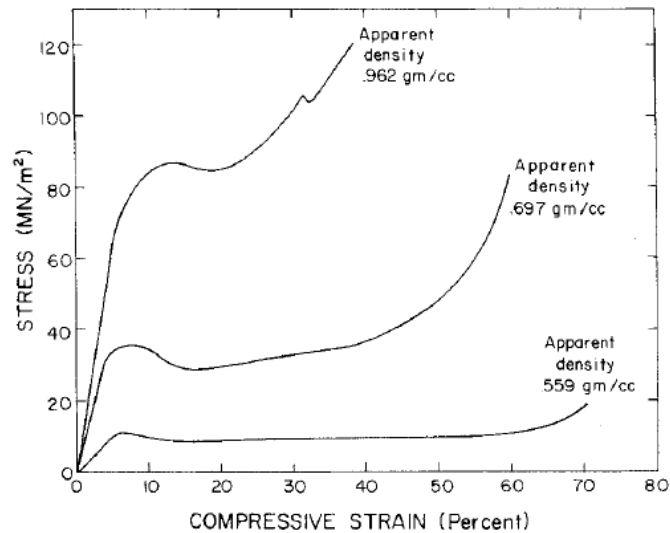


Figure 2.46: Compressive stress vs. uniaxial compressive strain for three typical specimens of bovine subchondral trabecular bone (from Gibson [18]).

2.4.5 Beak Skull

The Toco toucan and wreathed hornbill foams consist of honeycomb-like cellular structure. The structure is similar to the rod like structured cancellous bone. Indeed, the toucan foam has a low density with asymmetrical fine rod-like structure. The hornbill foam has a higher density with thick rod-like structured trabeculae. Unlike the typical human cancellous bone, most of the cells are closed by thin membrane, shown in Fig.2.48. Interestingly, a hollow extends to mid region in both upper and lower beaks, which is one of the reasons for lightness of the beak. Figure 2.47 shows the pictures of the toucan and hornbill foams with three sections, respectively; it is a thin-walled shell structure crisscrossed by many bony struts with membranes along the radial direction. In the hollow region, the bony struts are crisscrossed not only along the radial direction, but also along the longitudinal direction.

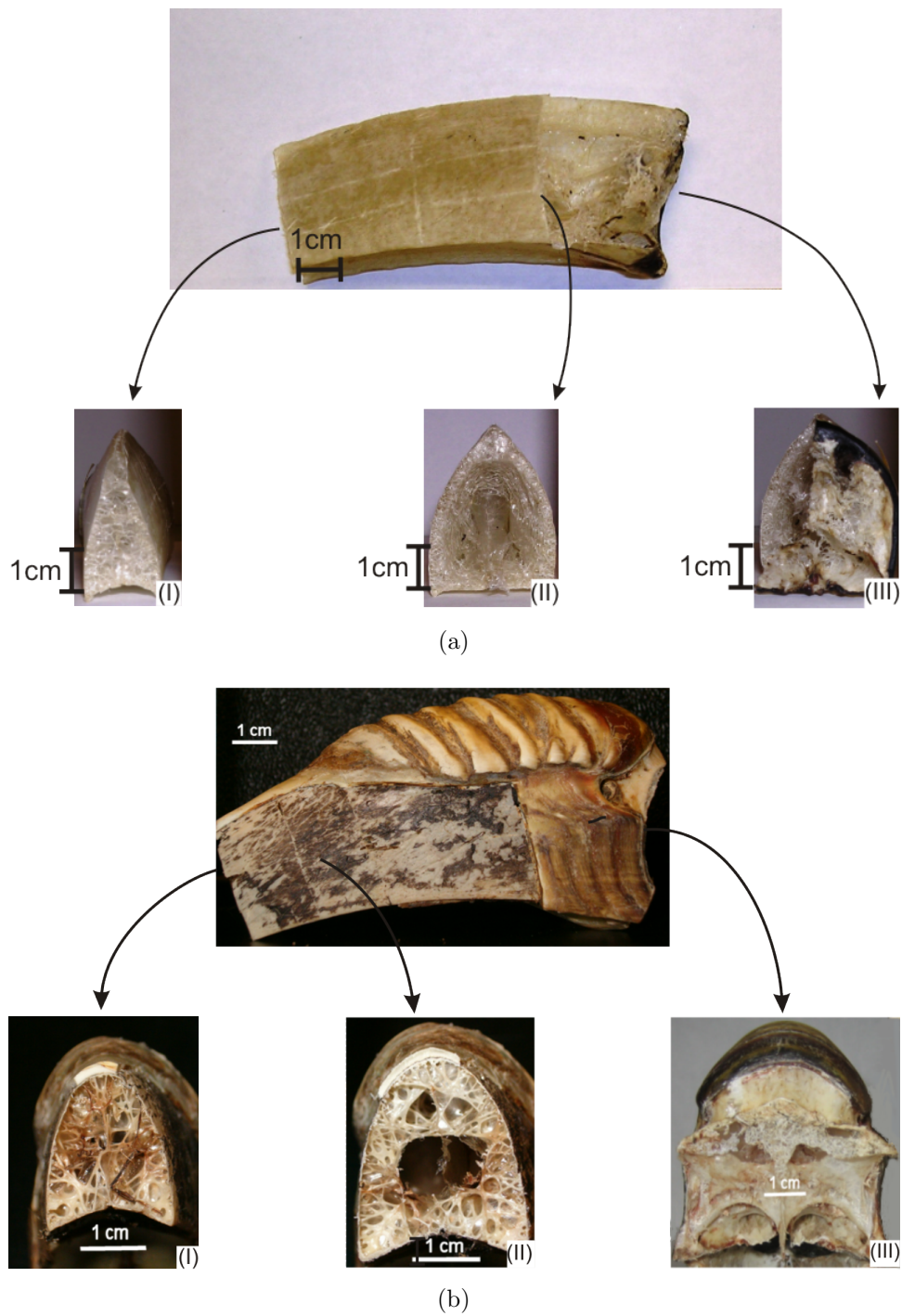


Figure 2.47: The cross section of toucan (a) and hornbill foams (b);(I) frontal view;(II) mid view;(III) proximal view.

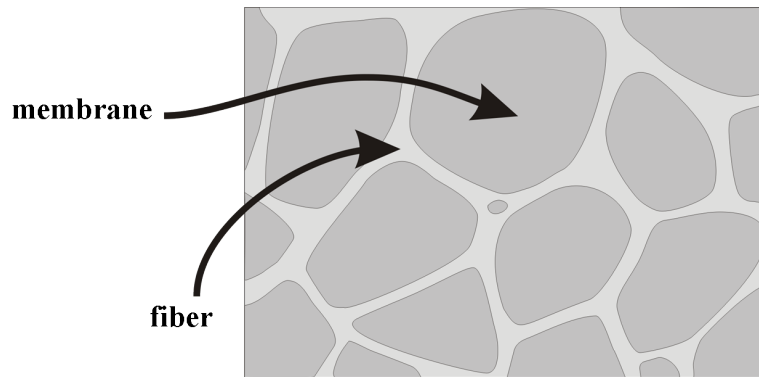


Figure 2.48: Schematic representation of structure of beak foam.

2.5 Sandwich Structures

The sandwich structure is abundant in nature and has been applied to many industrial materials. It consists of a low density of foam core and stiff solid exterior faces, which achieves ultra-light weight, better energy absorption capacity with comparable mechanical strength to bulk materials. There are numerous applications of sandwich structure in aerospace applications and structural materials.

A new class of materials, metallic foams [167–170], has been introduced and applied to make sandwich panels that have superior properties to sandwich panels with polymeric foams [171–174]. Figure 2.49 shows typical sandwich shapes used as structural materials. The properties of sandwich panels are controlled by changing the combination of face and core materials. Most of the sandwich panels are made from high modulus of shell and low modulus of core materials. The recent development of metallic foam allows having the combination of equivalent modulus of shell and core materials that can be used for automobiles and aircrafts. Additional information on mechanics of sandwich structure is found in several books [55, 175–177].

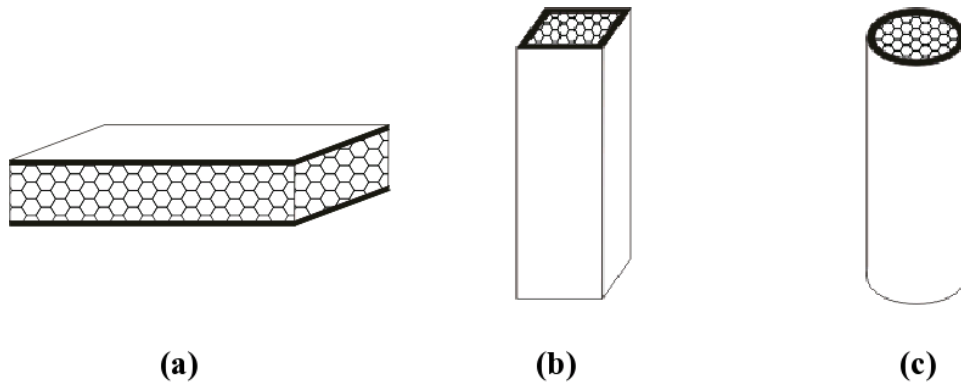


Figure 2.49: Sandwich structures;(a) sandwich beam;(b) square column; (c) cylinder column.

2.5.1 Synergism of Sandwich Structure

Hanssen et al. studied the mechanical response of sandwich square column in uniaxial compressive loading [56, 57, 178, 179]. Figure 2.50 shows typical force-displacement curves of sandwich column. The force-displacement curves of shell, foam, and superposition of foam and shell are also included in Fig.2.50. Because of synergism between shell and foam, the force level of a foam filled-shell is significantly higher than that of superposition of foam and shell. Figure 2.51 shows pictures of compressed sandwich columns with different shell thickness and foam density. The shell without foam creates 5 ~ 6 symmetric lobes. The number of lobes increases with an increase of the density. The deformation of thinner shell walls with lower density is asymmetric, compared to thicker shells.

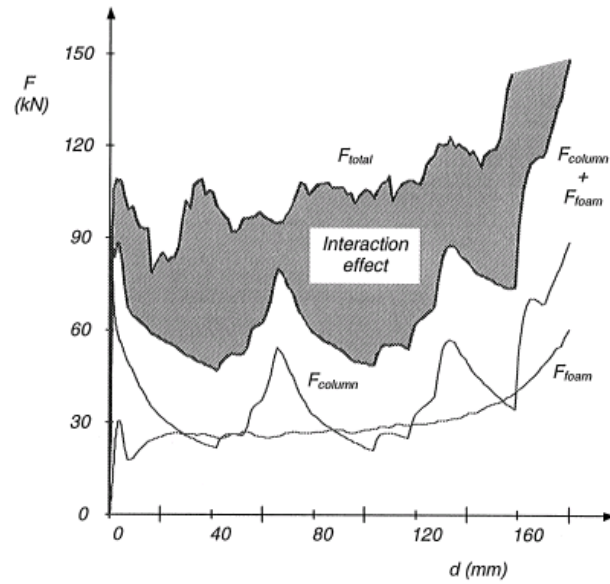


Figure 2.50: Force-displacement curves of foam, shell, foam + shell, foam filled shell (from Hanssen et al. [57]).

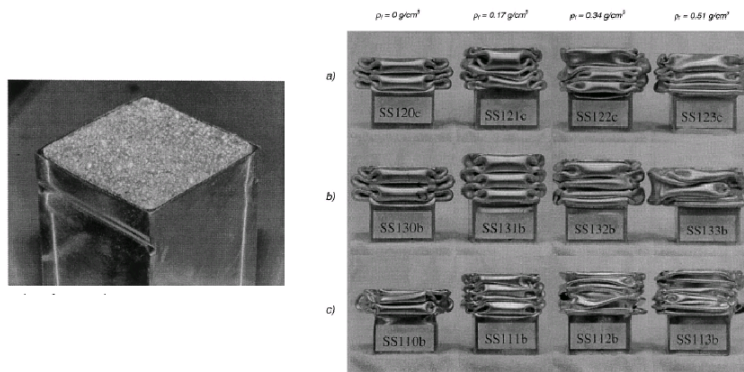


Figure 2.51: Deformation pattern of sandwich construction under quasi-static loading; (a) shell thickness 1.95 mm; (b) shell thickness 2.45 mm; (c) shell thickness 1.50 mm. (from Hanssen et al. [57]).

2.5.2 Force-Displacement Model of Sandwich Structure

Hanssen et al. developed an analytical treatment of sandwich structure made from aluminium exterior and interior [56, 57, 178]. Figure 2.52 illustrates the terminology for crushing behavior of column. The relative deformation, actual deformation d divided by the original length l of crushing component, is termed the deformation capacity D_c or strain. The average force is F_{avg} is given by absorbed energy $E(d)$ divided by actual deformation d . Stroke efficiency S_E or densification strain is that maximum displacement d_{max} divided by the original length l . The crushing efficiency $A(d)$, which never reaches the value 100%, is given by the ratio between the average force F_{avg} and the maximum force F_{max} . Total efficiency of T_E is defined by total energy absorbed E divided by the maximum force F_{max} . The maximum value of the total efficiency T_E occurs at a deformation of d_{max} . The relative deformation at which the maximum value of occurs represents the stroke efficiency S_E .

The presence of the foam changes the energy absorption compared to the non-foam shell. Hanssen et al. [56, 57, 178] introduced average force model described by separate average forces when square foam filled extrusion was crushed statically. The equation for the average force is

$$F_{avg} = F_{avg}^0 + \sigma_f b_i^2 + C_{avg} \sqrt{\sigma_0 \sigma_f} b_m h \quad (2.9)$$

where $F_{avg}^0 = 13.06 \sigma_0 b_m^{1/3} h^{3/5}$ is the average crushing force of non-filled extrusion, $\sigma_f b_i^2$ is the uniaxial resistance of the foam, $C_{avg} \sqrt{\sigma_0 \sigma_f} b_m h$ is the contribution from the synergistic effect between foam and extrusions. C_{avg} is a dimensionless parameter.

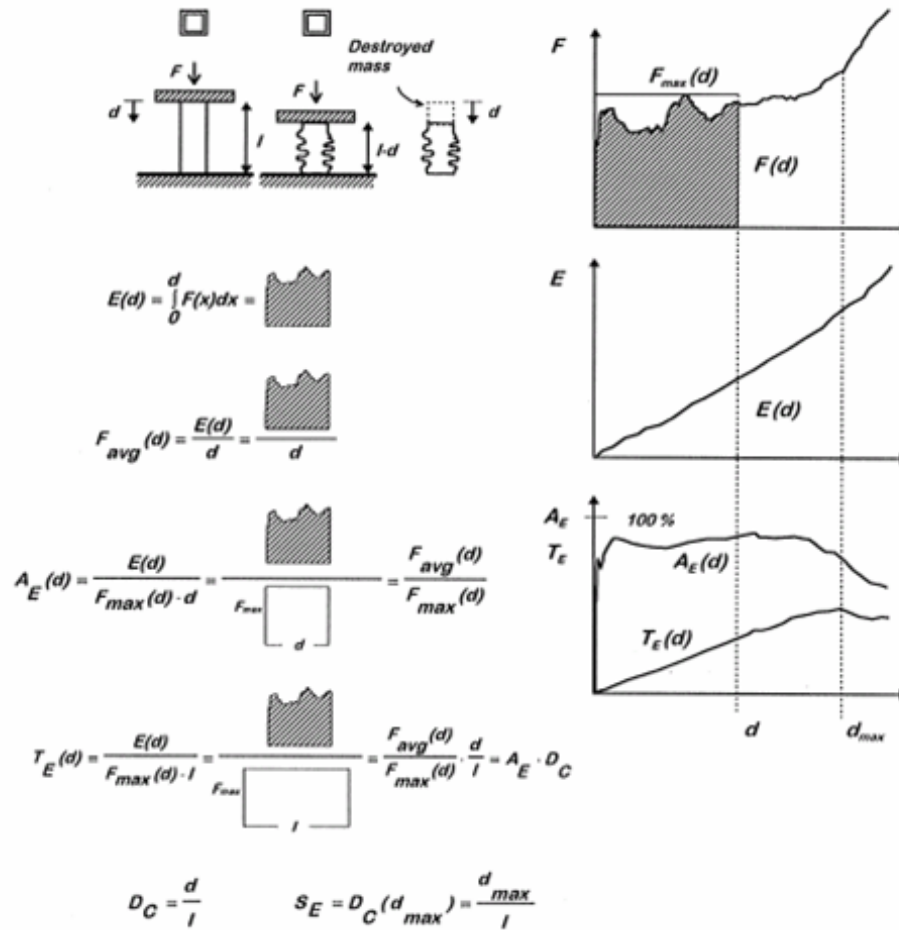


Figure 2.52: Terminology applied for axial crushing column (from Hanssen et al. [56]).

Table 2.1: Model parameters

Model parameters	
σ_0	Extrusion wall characteristic, $0.5(\sigma_{0.2} + \sigma_u)$
$\sigma_{0.2}$	Extrusion wall stress at 0.2% plastic strain
σ_u	Extrusion wall ultimate stress
σ_f	Foam plateau stress
b	Outer component cross section width
h	Component wall thickness
b_m	$b - h$
b_i	$b - 2h$
C_{avg}	Interaction constant of average force

Foam filled extrusion reduces the densification strain of the component compared to non filled extrusion from impact. The densification strain is the same as the effective crushing length S_E . The mechanism responsible for the reduction of S_E , which involves the increased number of contacting lobes from the extrusion and densification strain of the foam. The densification of the foam can be described by [55]:

$$\varepsilon_D = 1 - 1.4 \left(\frac{\rho^*}{\rho_s} \right) \quad (2.10)$$

where ρ^* is density of the foam, and ρ_s is density of solid. Stroke efficiency S_E or densification strain of foam filled extrusion is modeled as a force-weighted average of foam affected by stroke efficiency S_E^F and densification strain of foam.

$$S_E = \frac{(F_{avg}^0 + C_{avg} \sqrt{\sigma_0 \sigma_f} b_m) S_E^F + (\sigma_f b_i^2) \varepsilon_D}{F_{avg}} \quad (2.11)$$

where all parameters are defined in Figure 2.53.

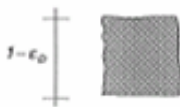
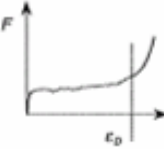

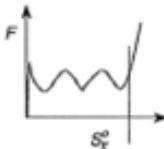

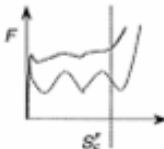

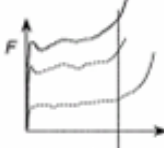
Component type	Average force	Force vs. deformation	Stroke efficiency
<p>Foam alone</p> 	$= \sigma_c b_f^2$		$\epsilon_D = 1 - 1.5 \left[\frac{\rho_f}{\rho_{fo}} \right]$
<p>Extrusion alone</p> 	$F_{avg}^0 = 13.06 \sigma_c b_m^{1/2} h^{3/2}$		$S_c^0 = 0.76$
<p>Non-filled extrusion, but same deformation pattern as foam filled</p> 	<p>Assumption:</p> $= F_{avg}^0 + C_{ext} \sqrt{\sigma_c \sigma_e} b_m h$		$S_c^1 = S_c^0 \left(1 - C_{ext} \left[\frac{\rho_f}{\rho_{fo}} \right] \right)^{1/2}$
<p>Foam filled extrusion</p> 	$F_{avg} = F_{avg}^0 + \sigma_c b_f^2 + C_{ext} \sqrt{\sigma_c \sigma_e} b_m h$		$S_c^2 = \frac{(F_{avg}^0 + C_{ext} \sqrt{\sigma_c \sigma_e} b_m h) S_c^1 + (\sigma_c b_f^2) \epsilon_D}{F_{avg}}$

Figure 2.53: Methodology of design formula for stroke efficiency of foam filled extrusion (from Hanssen et al. [56]).

Chapter 3

Experimental Techniques

The toucan and hornbill beaks were obtained after the natural death of animals and stored in a desiccator at room temperature and 50 % relative humidity. The maxilla (upper beak) and mandible (lower beak) were used for all mechanical tests and structural analyses. Humidity and temperature were measured by a hygrometer to determine the environmental condition.

3.1 Hardness Testing

3.1.1 Microindentation

The beak shell was cut into small pieces by knife and mounted in epoxy. Figure 3.1 shows preparation methods for hardness test. The experimental set up followed the hardness testing of European Startling bill [52]. LECO M-400-H1 hardness testing machine (Figure 3.2) was used. The different loads were applied to all tests. The indenter was applied for 15 sec, and a further 45 sec was allowed to elapse before the diagonals of the indentation were measured. This procedure was adjusted to minimize the effect of the creep. Vickers hardness is calculated according to:

$$HV = \frac{0.00018544P}{d^2}(GPa) \quad (3.1)$$

where P is applied load (N) and d is the mean length of diagonal (mm)

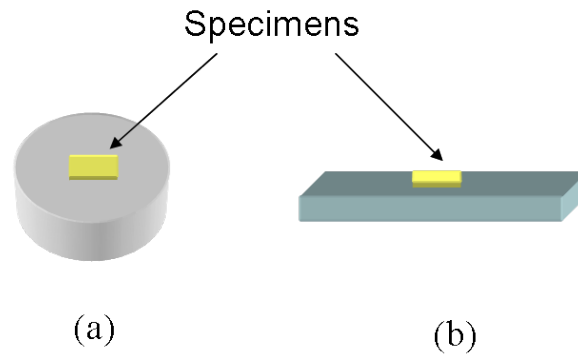


Figure 3.1: Specimen preparation methods;(a) mounted in epoxy;(b) glued on the glass.

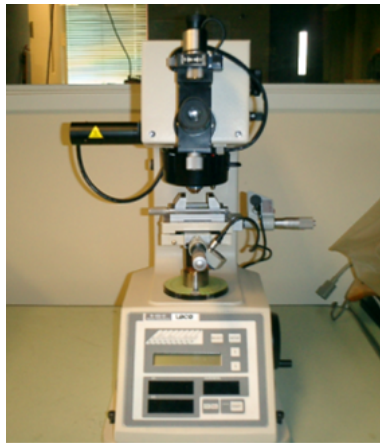


Figure 3.2: Microindenter (LECO M 400H1).

3.1.2 Nanoindentation

Specimen preparation is the same as for microindentation. Since nanoindentation is highly sensitive to the roughness of the samples, specimens were polished down to 0.05 μ alumina power. Both the interior and exterior of beaks were tested. The pictures of the samples before and after the testing were taken by scanning probe microscopy (SPM). A Hysitron Triboindenter, shown in Figure 3.3, was used to determine the reduced Young's modulus and hardness of the samples.

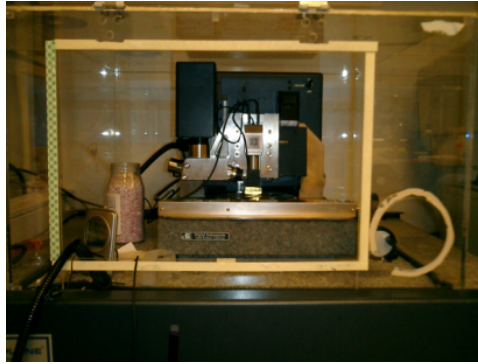


Figure 3.3: Nanoindenter (Hysitron).

Loads of 500 μ N and 1000 μ N were applied to all specimens. Berkovich and cube corner tips were used. Nanoindenter was held for a period of 5 sec after loading to eliminate the creep effect. Hardness is calculated by:

$$H = \frac{P}{24.5h_p^2} (GPa) \quad (3.2)$$

where P is applied load (N), h_p is the depth of the penetration, the face of the indenter is 63.5°.

The reduced Young's modulus is calculated according to:

$$\frac{1}{E_r} = \frac{1 - \mu^2}{E} + \frac{1 - \mu_0^2}{E_0} \quad (3.3)$$

where E_r is reduced Young's modulus, E and μ are Young's modulus and Poisson's ratio of specimen. E and μ are respective parameters of the machine. Since the materials we used were soft, E_r and E are identical.

3.2 Tensile Testing

3.2.1 Beak Keratin

The rhamphotheca or beak shell was cut into rectangular shape with knife and dremel. The specimens were inserted into a laser cutting machine to create dog-bone shape specimens. Figure 3.5 shows a sampling methods from the rhamphotheca.

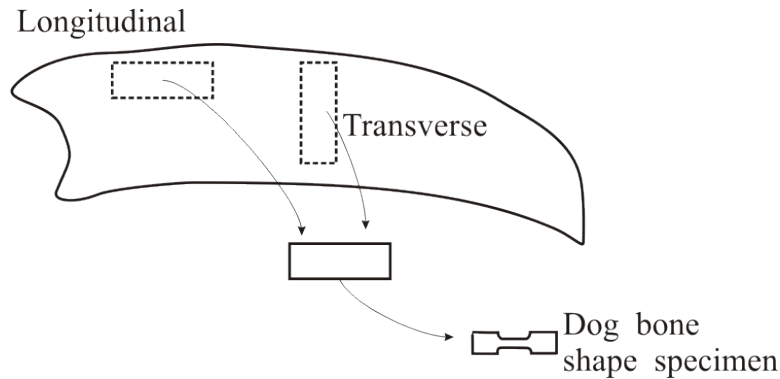


Figure 3.4: Removal of specimens for tensile test.

The dog-bone shape dimensions were: length 25.4mm, width 2.3 mm, and gage length 6.35 mm. The thickness of toucan specimen is approximately 0.5 mm and that of hornbill is 1.5 mm. The beak was cut along longitudinal direction, and along the transverse direction. The longitudinal and transverse directions of the tensile specimens from toucan rhamphotheca is presented in Figures ??(a) and (b) . To avoid the effect of curvature of samples, a preload of 22 N (5lb) was applied. A universal testing machine United, equipped with 0.22 kN (50lb) load cell, was used.

An Instron 2242 equipped with 500 N load cell was also used. The tests were carried out at room temperature and approximately 50 % relative humidity. The cross head speed was 0.5 mm/min (0.03 in/min).

We used environmental chamber to measure the mechanical response of beak keratin in high humidity and temperature condition (RH 97% and 37°C). The cross head speed for this experiment was the same as the experiment at room temperature. The output of the testing machine was transferred to a computer. Time, displacement, load, strain, stress were stored by Lab View and Blue Hill 2. Calculation was done by Microsoft Excel.

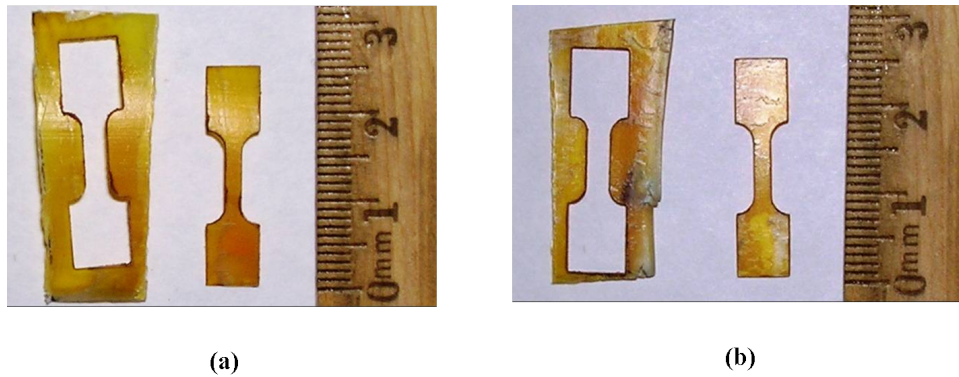


Figure 3.5: Tensile specimens cut by laser;(a) longitudinal direction;(b) transverse direction.

In order to determine the effect of melanin in the beak, we have used the transverse sections of melanized and unmelanized toucan rhamphotheca for comparison. Figure 3.6 shows a picture of melanized and unmelanized toucan rhamphotheca. The tensile testing was conducted under ambient condition.

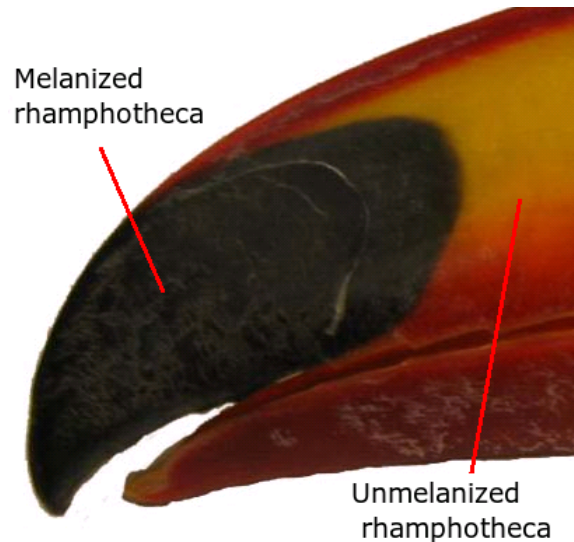


Figure 3.6: Melanized and unmelanized toucan rhamphotheca

3.2.2 Trabecula

The individual trabecula was sectioned from beak foam by razor blade and tested in tension. The cross section of trabecula is elliptical or circular shape. The approximate gauge length of trabeculae is 1.6 mm. The trabeculae were glued in the mold, shown in Fig.3.7. We used Instron model 3342 with 500 N load cell and cross head speed was 0.5 mm/min. After tensile testing, a fractured cross-section area was observed by Zeiss Axio Imager Optical Microscope and the area was measured by using ImageJ. The specimens fractured at edge were eliminated from the analysis to avoid the effect of glue.

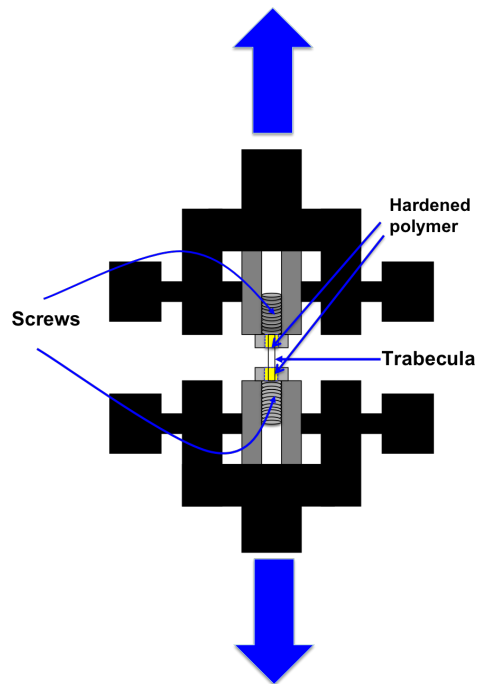


Figure 3.7: Apparatus of tensile testing of trabecula.

3.3 Compression Testing

3.3.1 Beak

The compression specimens were cut by diamond saw and jeweler saw. The compression tests were performed with cross head speed 1.27 mm/min (0.05 in/min). These samples were placed on the universal machine, equipped with 22 kN (5000 lb) load cells. Figure 3.8 shows the toucan foam, shell, and foam-filled shell specimens. The gauge length of samples was 1.5 cm. The output of the machine was transferred to a computer. Time, displacement, load, stress were stored by Lab View. Calculation was done by Microsoft Excel.

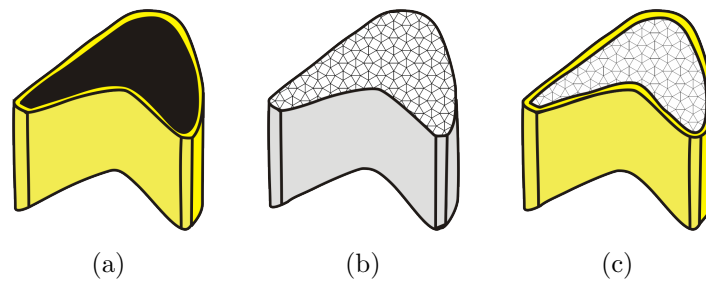


Figure 3.8: Specimens for compression test;(a) foam;(b) shell;(c) foam-filled shell.

3.3.2 Trabecula

The trabeculae were glued onto metal plate and tested under compression in Figure 3.9.

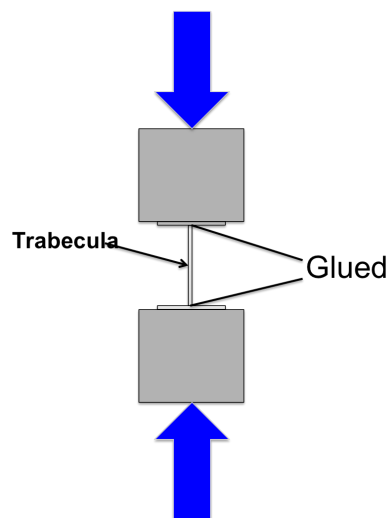


Figure 3.9: Apparatus of compression testing of trabecula.

The dimension of the compression samples vary from 2.5 to 4.5 mm in gauge length; 0.09 to 0.16 mm in thickness; 0.12 to 0.28 in width. We used Instron model 3342 with 500N load cell and cross head speed of 0.05 mm/min. The specimens fractured at edge were removed to eliminate the effect from adhesive. The cross

section of fractured trabeculae was examined by SEM (FEI, Quanta 600) and the dimension of trabeculae is carefully measured by optical microscope (Zeiss Axio Imager).

3.4 Microscopy for Structural Analyses

The exterior of the beak and interior foam were coated with gold-palladium before the analysis. Environmental scanning electron microscopes (SEM) equipped with a energy dispersive X-ray detector (EDX) at Scripps Institute and Nano3 facility at Calit2 at UCSD was used for the observation. After the tensile and compression tests, the fracture of the specimens was analyzed by SEM. Chemical compositions of the exterior and interior of the beak were determined by energy dispersive X-ray (EDX).

The structure of beak foam was analyzed by a confocal microscope (Olympus spinning disk confocal microscope) at the National Center for Microscopy and Imaging Reserch (NCMIR) at UCSD. The cross section of beak foam was obtained by confocal microscopy with commercial mosaic acquisition software. The image series were aquired with depth of 0 to 500 μm by the confocal microscope.

3.5 Computed Tomography

X-ray Computed Tomography was used to study and reproduce, for purpose of stability analysis, the foam structure. We used $\mu\text{-CT}$ (G.E. explore RS rodent CT scanner). The 3D interior foam structure is visualized by the software VTK (Visualization Toolkit) [180,181], and we have implemented a ray casting algorithm for volumetric rendering. The DICOM images, captured by 93, 43, and 27 μm resolution $\mu\text{-CT}$, were converted to TIFF format and rescaled using ImageJ. The dimension of the images for the Toucan maxilla is 121 x 156 pixels with 1168 images

and for the Toucan mandible is 115 x 85 pixels with 991 images. The model was created from the six sets of stitched images for maxillary beak and the five sets of stitched images for mandibular beak. For the rendering of Toucan and Hornbill beak foam segment, 435 images were used for Toucan and 430 images were used for Hornbill. The image size of Toucan is 225 x 255 pixels and that of Hornbill is 252 x 277 pixels. A segment of Toucan beak foam was scanned at a resolution of $27\mu\text{m}$. The image is 330 x 130 pixels with 130 images. The Hornbill casque, was scanned at a resolution of $45\mu\text{m}$, has the size of 312 x 237 pixels with 80 images.

3.6 Transmission Electron Microscopy

3.6.1 TEM sample preparation

We have based on the TEM protocol for the investigation on the study of Peguin beak keratin by Dresp et al. [182, 183]. The beaks were transversely sectioned and soaked in the water for 2 hours. The specimens were fixed in 2.5 % of glutaraldehyde in 0.2 M of Phosphate Buffer Saline (PBS) overnight. After rinsing in 1% of PBS for four times, specimens were postfixed in osmium tetroxide for 5 hours and washed with double distilled water (DDW) three times. Before the dehydration process, specimens were soaked in uranyl acetate overnight. For dehydration, graded 20%, 50%, 70%, and 90% of Ethanol series was used. The samples were dehydrated in each Ethanol solution for 15 min. For the polymerization process, Spur's low viscosity (Ted Pella Spurr low viscosity) was used. The sample were slowly polymerized in the mixture of 100 % ethanol and resin. The ratio of ethanol and resin was 1:2, 1:1, 2:1, respectively. Finally we polymerized with 100% resin. We changed the solution approximately in 2-4 hours. After the polimarization process, the specimens were baked in the oven at 50°C for 48 hrs. The polymerized specimens were sectioned by ultramicrotome (Reichert-Jung UltracutE) at a thickness of 80 nm. We prepared

four boats for uranyl acetate (UA) and five boats for lead and NaCl staining, shown in Fig. 3.10. The sample grids were stained with UA for 20 min and rinsed with DDW, shown in the first row of Fig. 3.10. After the UA treatment, the samples treated with lead for 1 min were also rinsed with NaCl and DDW in the second row of Fig. 3.10. A Joel-1200 (120KV), transmission electron microscope, at the National Center for Microscope and Imaging Research Facility (NCMIR) was used to analyze the beak keratin structure.

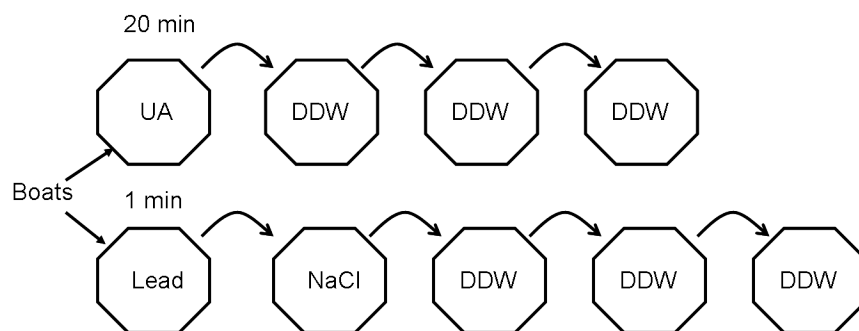


Figure 3.10: Staining process; first row is UA staining; second row is lead staining

3.6.2 Tomography

For TEM tomography, 250 nm thick sections of beak keratin were prepared. The TEM protocol and staining process were the same as that for the 80 nm sections. After the staining, the samples treated with 15 nm of gold particles were dried at the ambient condition; finally, the samples were coated with carbon for 20 sec. A JEM-4000EF IVEM (400 kV) at NCMIR was used for TEM tomography. The sample holder can rotate from -60° to 60° , shown in Fig.3.11. We took images every 2° step in single rotation. The set of images is aligned and assembled by IMOD (software for tomographic reconstruction, developed by Boulder Laboratory for 3-D Electron Microscopy of Cells and the Regents of the University of Colorado).

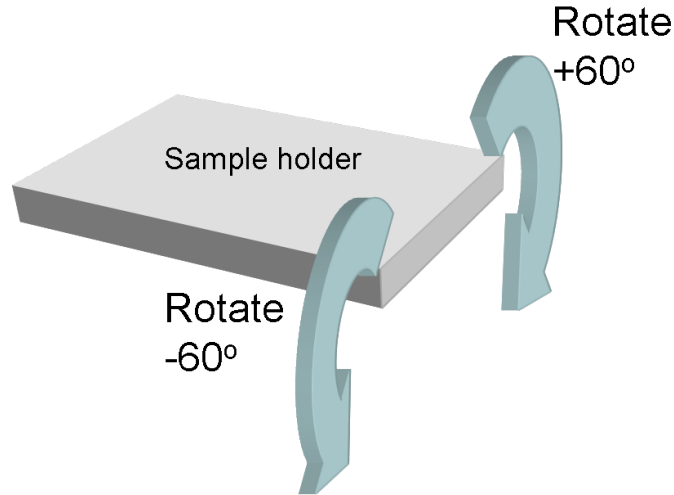


Figure 3.11: TEM sample holder, rotating from -60° to 60° .

3.7 Finite Element Method

3.7.1 CT Image Based Meshing

In this study, 150 images, scanned by 93μ resolution of μ -CT, were used for creating a model. We divided the beak foam into trabeculae and cortical shell for solids elements and shell elements, respectively. We processed the CT images with DDV (Digital Data Viewer) at first in order to create a surface mesh and only the trabeculae components are processed. The rough trabeculae model was cleaned and smoothed with the software (Right Hemisphere 5 Deep Exploration CAD Edition and Rhinoceros). The cortical shell model was created at this stage by Rhinoceros. The trabeculae and cortical shell models were meshed with ANSYS ICEM CFD and LS-PrePost for LS-DYNA. The model consists of approximately 36,500 triangular shell elements and 670,400 of tetrahedron solid elements, shown in Figure 3.12. The height of the model is ~ 13 mm and the foam was completely filled with the trabecular rods. The model was subjected to compressive loading to compare with experimental

results. The material parameters for the modeling were obtained from our mechanical testing results.



Figure 3.12: FE beak foam model using CT image based meshing techniques.

3.7.2 CAD Based Meshing

To model the bending behavior of toucan beak, Solid Works (CAD software) is used for creating FE models. The dimension of mandibular beak was measured including the geometry of keratin shell and foam interior. The tri-dimensional structure of shell exterior and foam interior components are created by Solid Works. The model was meshed with ANSYS ICEM CFD and LS-PrePost. The model consists of $\sim 5,500$ triangular shell elements and $\sim 37,000$ tetrahedron solid elements. The

internal foam core is allowed to be hollow from the proximal end in Figure 3.13. The proximal end was fixed and the load was applied at the distal end to evaluate the bending response of the beak. The computational results were compared with experimental results. The bending experiments of toucan beak were conducted in Brazil by Fecchio.

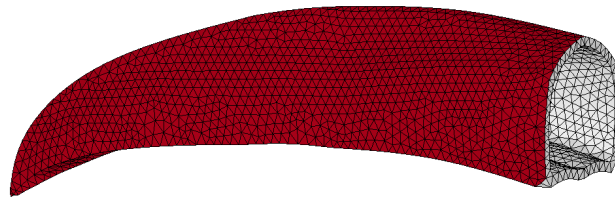


Figure 3.13: FE beak model, the geometry is imported from CAD (Solid Works).

The experimental methods in this chapter are quoted from the materials published in the following journals.

Yasuaki Seki, Matthew S. Schneider, Marc A. Meyers, "Structure and mechanical behavior of a Toco toucan beak ", *Acta Materialia*, 53, 5281-5296,2005.

Yasuaki Seki, Bimal Kad, David J Benson, Marc A. Meyers, "The toucan beak: Structure and mechanical response", *Materials Science and Engineering C* , 26, 1412-1420,2006.

Y.Seki, Sara G. Bodde, Marc A. Meyers, "Toucan and Hornbill Beaks:Comparative Study", *Acta Biomaterialia* submitted 2009.

Chapter 4

Results and Discussion

4.1 Structure of Rhamphotheca

The beak consists of the underlying bone covered by the hard sheath (epidermis) made from β -keratin. Figure 4.1 shows pictures of toucan and hornbill beaks covered by β -keratin layers. This integument covering is called "*rhamphotheca*" and is cornified in most of the avian species [151]. The rhamphotheca is strengthened by deposited calcium salt that adds the hardness to keratinous proteins [52, 76]. The shape of the rhamphotheca is altered by the bone and the thickness is changed with local thickenings. The tip of the beak is modified by the food habits; the toucan beak is serrated for holding fruits. The rhamphotheca exhibits a variety of forms; plates; knobs; ridges. The hornbill beak is differentiated by a thick and heavily cornified helmet like projection on maxilla (upper beak). It is known as a "*casque*" and is fused into bone. The casque of wreathed hornbill and side ridges can be seen from Figure 4.1 (b). The number of ridges and knobs on the casque increases with age. The rhamphotheca contains pigments such as melanin and carotene. Carotene provides beautiful colors such as red and yellow. The melanin is found in the tip of toucan beak, for example. The function of melanin is to thicken and harden the keratin for

abrasion resistance [52].



(a)



(b)

Figure 4.1: Photographs of beaks;(a) Toco toucan;(b) Wreathed hornbill.

4.1.1 Scanning Electron Microscopy

Figure 4.2 shows scanning electron micrographs of transversely and longitudinally sectioned toucan rhamphotheca. The rhamphotheca is composed of polygonal keratin scales that have a thickness of $\sim 1 \mu\text{m}$ and a diameter of $30\sim 60 \mu\text{m}$. The total thickness of the toucan rhamphotheca is approximately 0.5 mm.

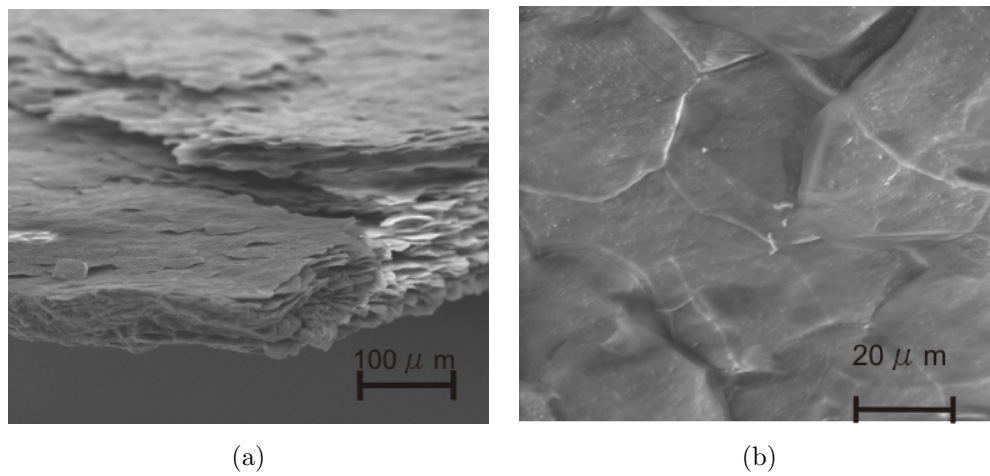


Figure 4.2: Scanning electron micrographs of toucan rhamphotheca; (a) rhamphotheca consisting of multiple layers of keratin scales (side view);(b) overlapped keratin scales (laterally sectioned rhamphotheca)

Figure 4.4 shows scanning electron micrographs of the hornbill rhamphotheca at three different areas; lateral side, casque, ridges. The geometry of the keratin scale of hornbill rhamphotheca is similar to the toucan keratin scale and is slightly elongated, ranging $20\sim 60 \mu$ in diameter, shown in Fig 4.4(a). The total thickness of the hornbill shell varies with location from 1 mm to 2 mm at lateral side. The thickness increases toward distal end of beak. While the lateral section of hornbill rhamphotheca consist of keratin scales identical to toucan rhamphotheca, the microstructure of casque and ridges exhibits a different morphology. The connecting glues are visible along the

keratin scale boundaries at the ridges, shown in Figure 4.4 (b). The keratin scales at ridges are irregular and merge with neighboring scales. The cell boundaries on casque are not as clear as other locations and the scales are more tightly connected as if forming a single cell, Fig.4.4(c).

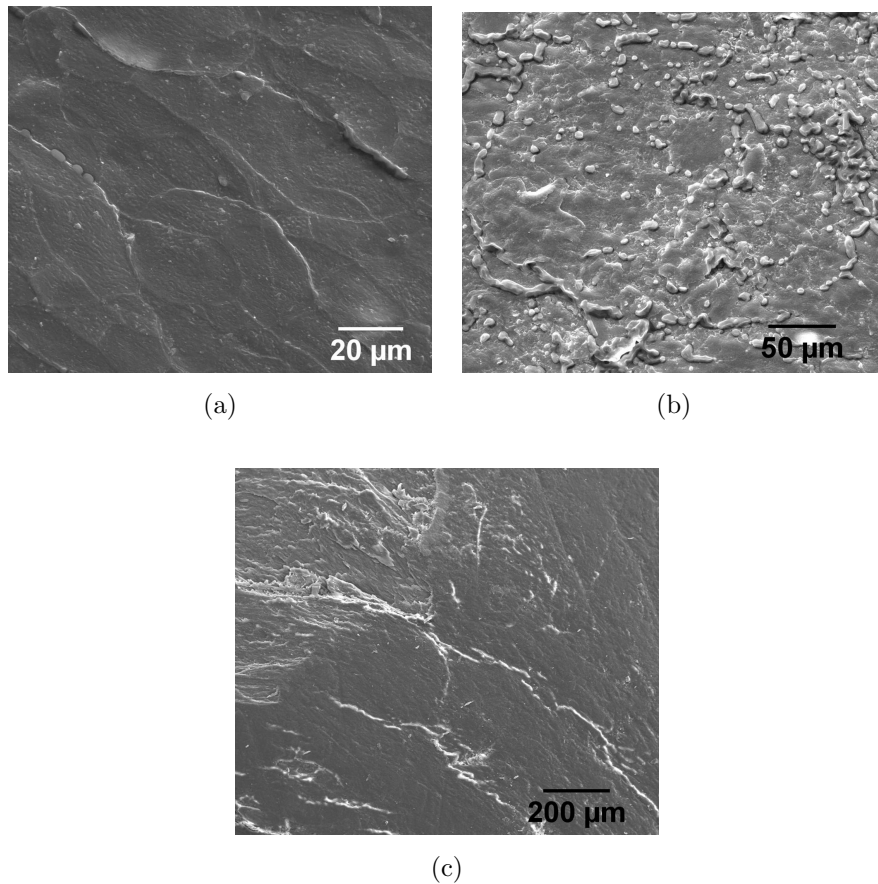


Figure 4.4: Scanning electron micrographs of hornbill rhamphotheca;(a) overlapped keratin scales (laterally sectioned rhamphotheca);(b) ridges (lateral section);(c) casque (lateral section).

4.1.2 Composition Analysis on Rhamphotheca

The presence of minerals, especially calcium, in beak keratin contributes to the hardness whereas the beak keratins contains little amount of minerals. The presence of salts in beak keratin were also detected from microscopy analysis. We observed the local concentration of NaCl by scanning electron micrograph with back scattering mode in Fig.4.5.

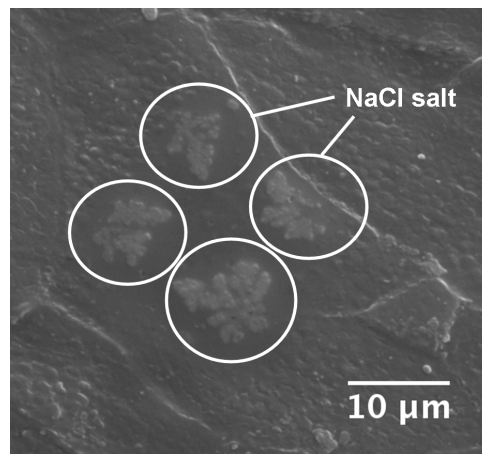
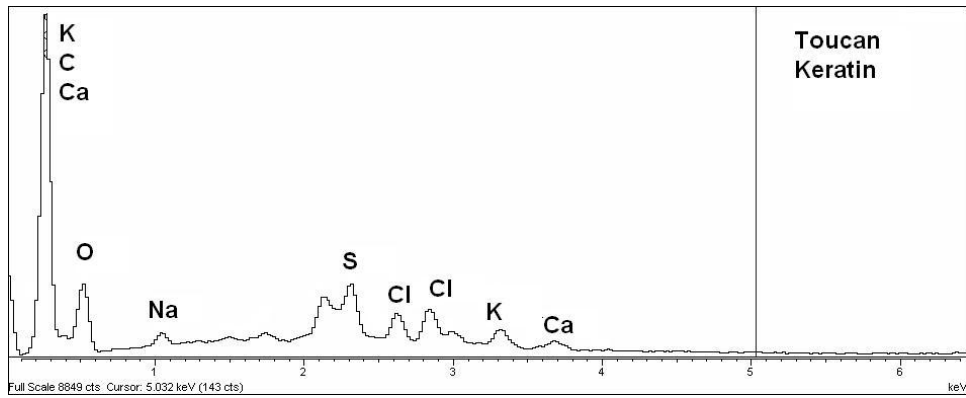


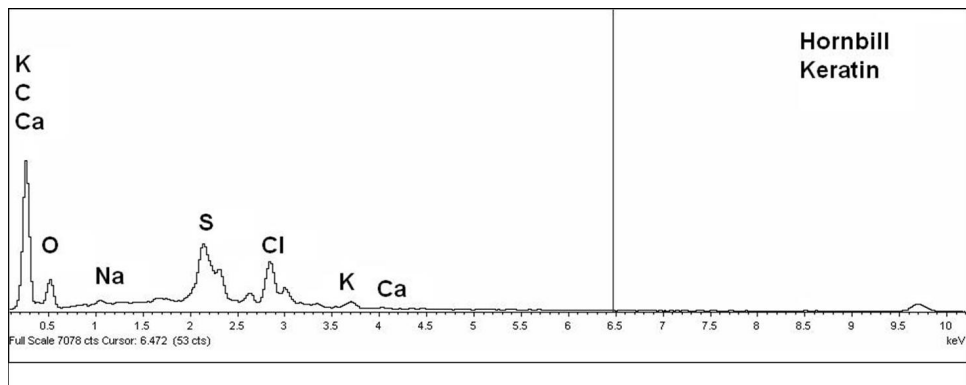
Figure 4.5: NaCl salts on hornbill rhamphotheca

Energy dispersive X-ray results revealed that the keratin contains mainly carbon and oxygen, Fig 4.6. The beak keratin is composed of more than 70 % of protein. We confirmed the presence of sulfur or cystine in beak keratin, approximately 3 % of sulfur in toucan beak keratin and 4 % of sulfur in hornbill beak keratin. We could not observe hydrogen in the beak keratin because during the analysis high voltage of X-ray beam burned the keratin cells and hydrogen disappeared. The other existing elements in beak keratins are calcium, potassium, chlorine, and sodium. The calcium found in toucan beak keratin ranges from 0.2 to 0.7 % and that in hornbill beak keratin is within the range of 0.4 ~ 1.4 %. The content of calcium in hornbill casque and ridges is ~0.5 and ~2%, respectively. The calcium in hornbill ridges and

toucan rhamphotheca exhibits a homogeneous distribution, exhibited by Figure 4.7. The glues on the hornbill ridges that we observed by scanning electron micrographs typified by high content of carbon in Figure 4.7(b).



(a)



(b)

Figure 4.6: Energy disperse X-ray results;(a) toucan rhamphotheca;(b) hornbill rhamphotheca.

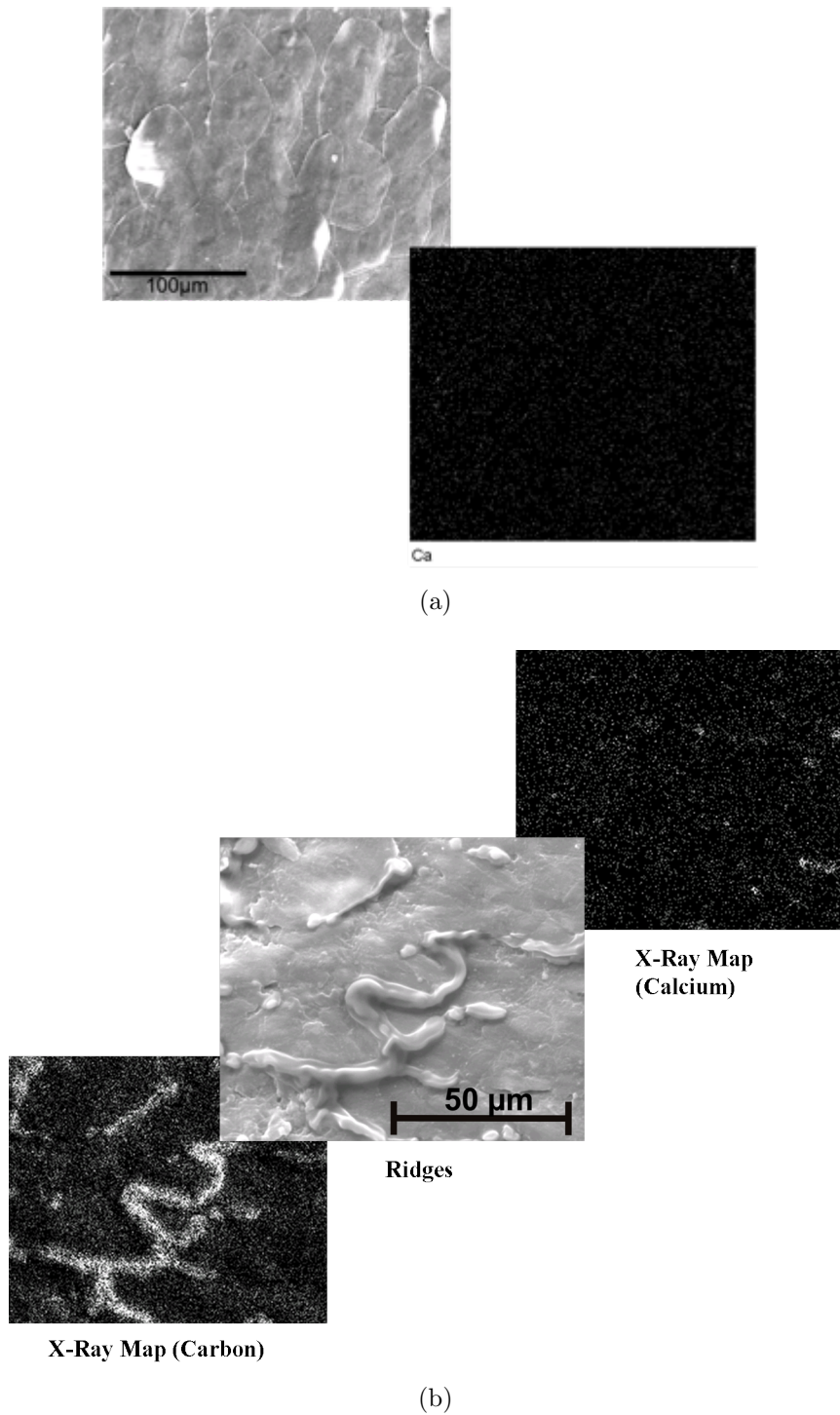
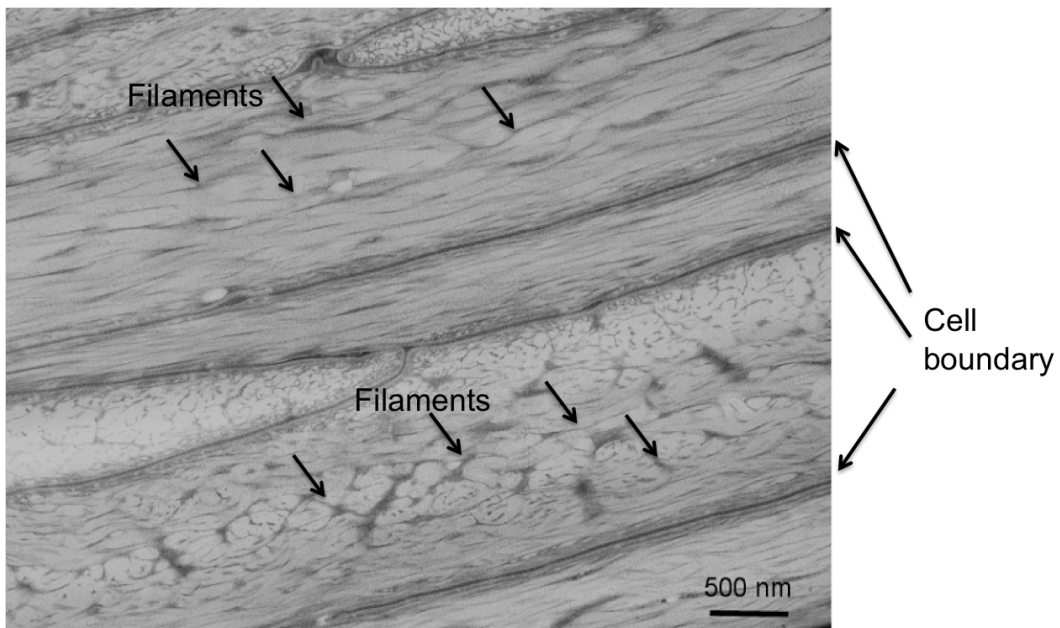


Figure 4.7: Comparison of scanning electron micrographs and X-ray dot mapping.
 (a) toucan rhamphotheca;(b) hornbill rhamphotheca.

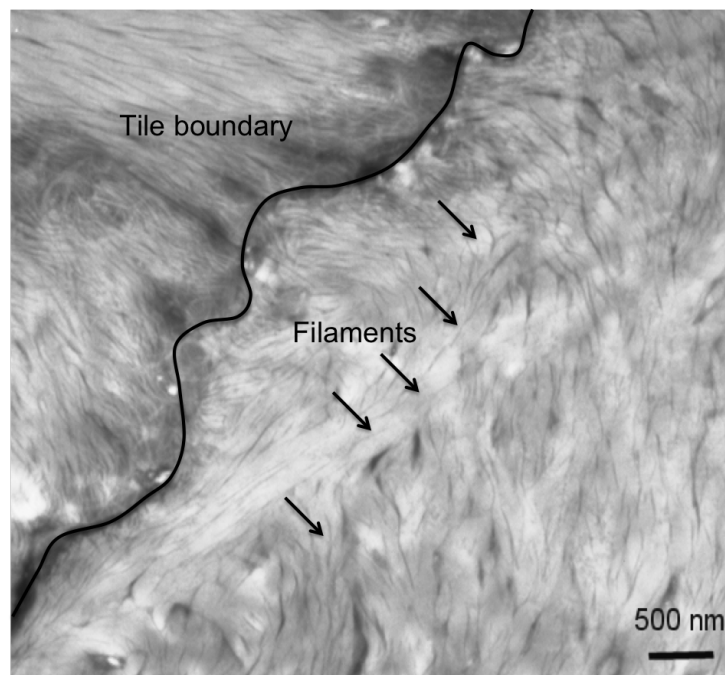
4.1.3 Transmission Electron Microscopy

Figure 4.8 shows transmission electron micrographs of longitudinal and transverse sections of toucan rhamphotheca. The keratin scales are connected by an adhesive substance, Fig 4.8(a). The inter-tile spacing is 18.44 ± 3.6 nm. The intermediate filaments are embedded in keratin matrix and are sometimes branched. The diameter of toucan keratin filament or β -keratin filament is 7.53 ± 2.2 nm. The filaments run parallel in transversely sectioned beak keratin in Figure 4.8(a). Figure 4.8(b) shows the longitudinally sectioned toucan rhamphotheca where the undulating cell boundary is observable as a dark curve on the micrograph. The toucan filaments are oriented in preferentially in each keratin cell and intercrossed at the cell boundaries. The area fraction of intermediate filaments ranges from 10 to 20%.

Figure 4.9 shows TEMs of transverse and longitudinal sections of hornbill rhamphotheca. The filaments are branched and create a foam-like network. The diameter of the hornbill keratin filaments is 10.7 ± 2.5 nm. The spacing between cell boundaries is 17.7 ± 3.5 nm. There are periodic voids along the cell boundaries in Figure 4.9 (a). In the longitudinal section, the hornbill keratin filaments are oriented in certain direction within cells, Figure 4.9(b). Voids are seen at the cell boundaries. Dresp et al. [182, 183] observed the diameter of 3.5 nm of intermediate filament of penguin beak by TEM. Fraser and Parry [25] have reported the diameter of β -keratin filament to be ~ 4 nm. Our results are two to four times higher than reported values [25, 182, 183]. This may be associated with high degree of variability in diameter along the filament length and with tangling of filaments. The tri-dimensional structure of intermediate filaments will be discussed in the next section.

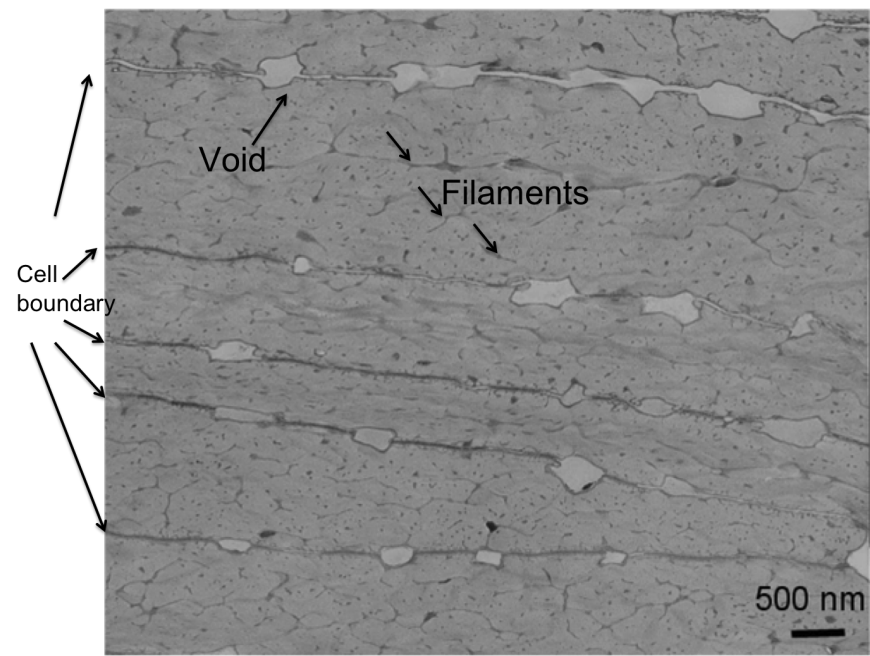


(a)

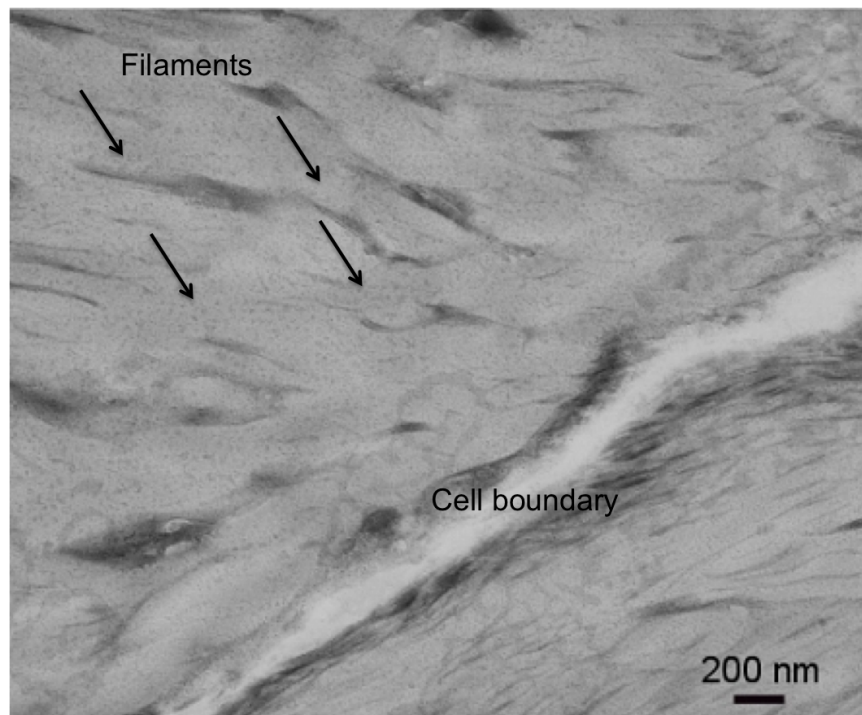


(b)

Figure 4.8: Transmission electron micrographs of toucan rhamphotheca;(a) cross section;(b) lateral section (surface).



(a)



(b)

Figure 4.9: Transmission electron micrographs of hornbill rhamphotheca;(a) cross section;(b) lateral section (surface).

4.1.4 TEM Tomography

Figure 4.10 shows the transmission electron micrographs taken at the angles of -60° , 0° , and 60° with a magnification of 3K. The cell boundaries are drawn by white lines and the black dots in the micrographs represent 15 nm of gold particles, which sometimes agglomerate. The gold particles are used for aligning the images. The tomogram of toucan beak keratin was generated from 250 nm thick section Fig.4.10. The intermediate filaments and boundary of keratin scales are outlined with the volumetric representation in the tomogram. The tomogram consists of 3996 sections of images through z direction.

Figure 4.11(b) shows the structure of intermediate filament with a 40 nm thickness section in 3D. The rendering was produced by Amira (commercial software). The intermediate filament is branched and creates a spongy network. Again the diameter of intermediate filaments are larger than the reported diameter of β -sheet [25, 182, 183].

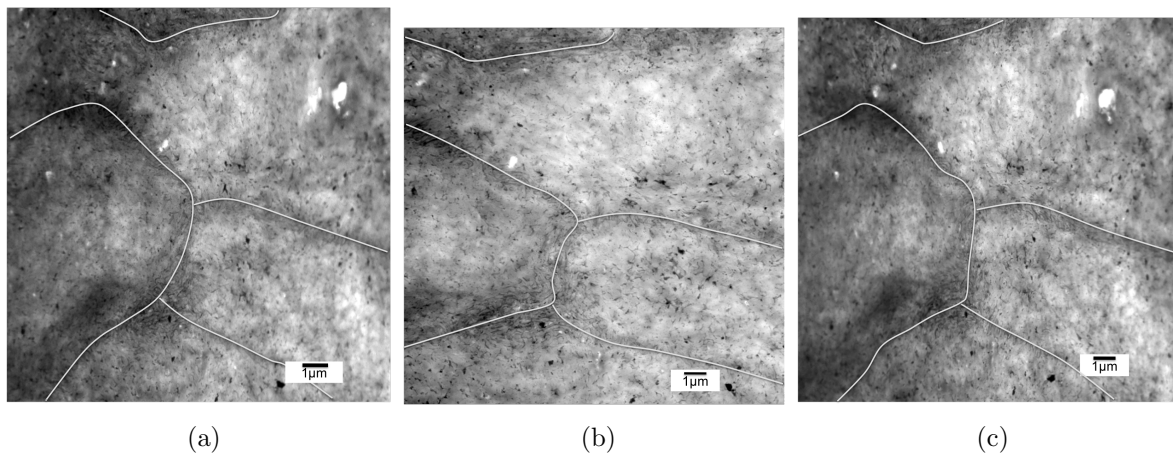
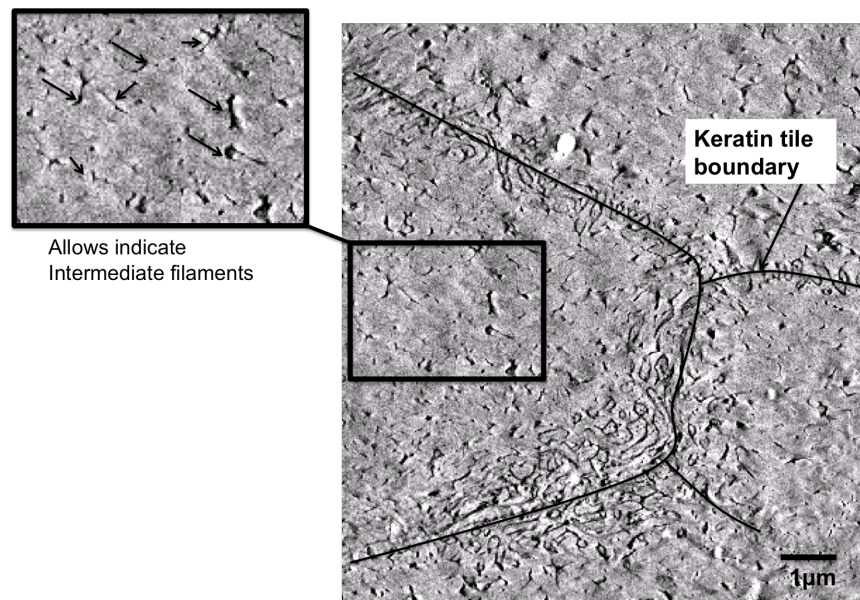
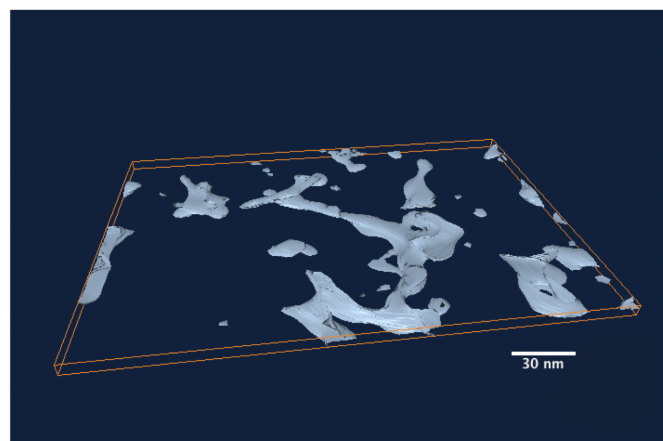


Figure 4.10: Transmission electron micrographs of toucan rhamphotheca;(a) angle of -60° ;(b) angle of 0° (c) angle of 60° .



(a)



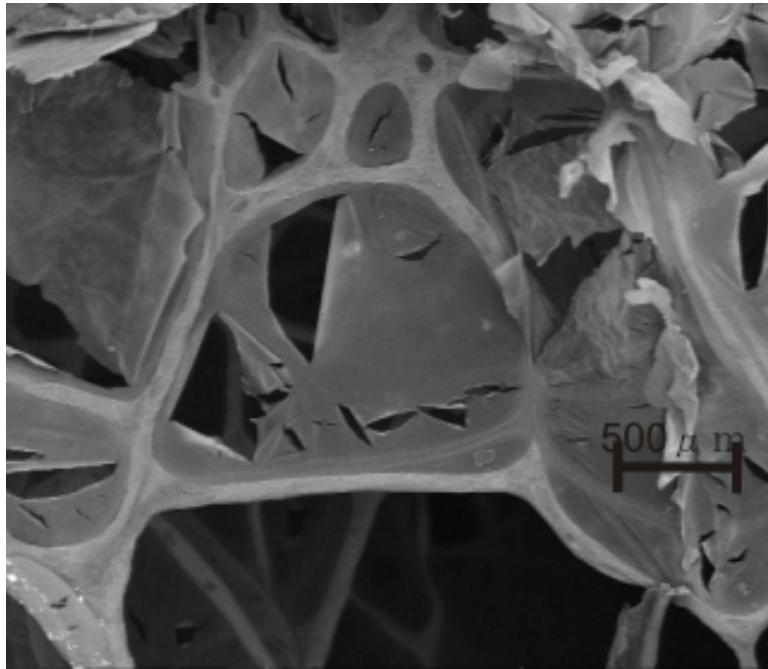
(b)

Figure 4.11: (a) Tomogram of toucan beak keratin ;(b) 3D rendering of intermediate filaments of toucan beak keratin.

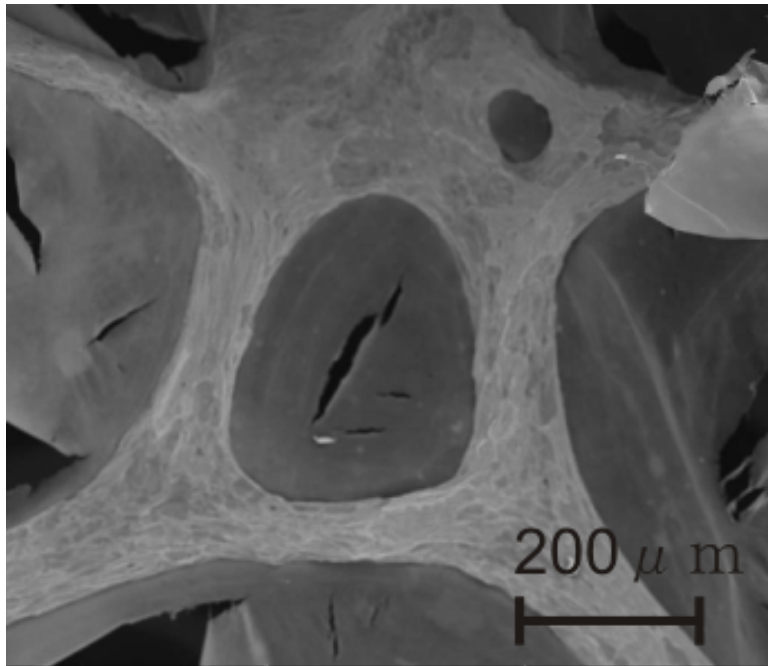
4.2 Structure of Beak Foam

4.2.1 Scanning Electron Microscopy

Scanning electron micrographs show the microstructure of toucan and hornbill beak skulls, Figures 4.12 and 4.13. Most of the cells are closed by thin membranes thus we consider as closed-cell foam. The trabecular bone of toucan and hornbill is composed of rod like structure. The shape of the struts is cylindrical or elliptical. The struts meet at the nodes with an edge connectivity of three or four. The diameter of toucan trabecula is $\sim 100 \mu\text{m}$ and that of hornbill trabecula is $\sim 200 \mu\text{m}$. The cell size is approximately 3 mm for hornbill and 1~2 mm for toucan. The thickness of membranes is less than $1 \mu\text{m}$. The membranes are torn or cracked due to the dessication after the death of the birds. The membranes might also be damaged by the cutting procedure. The structure of beak skull suggests that beaks do not experience high magnitude of external loads. The cancellous bone of toucan and hornbill beaks provides enough support for foraging activity. However, this is not the case for beak skull of woodpeckers, which have to be resist repeated impact.

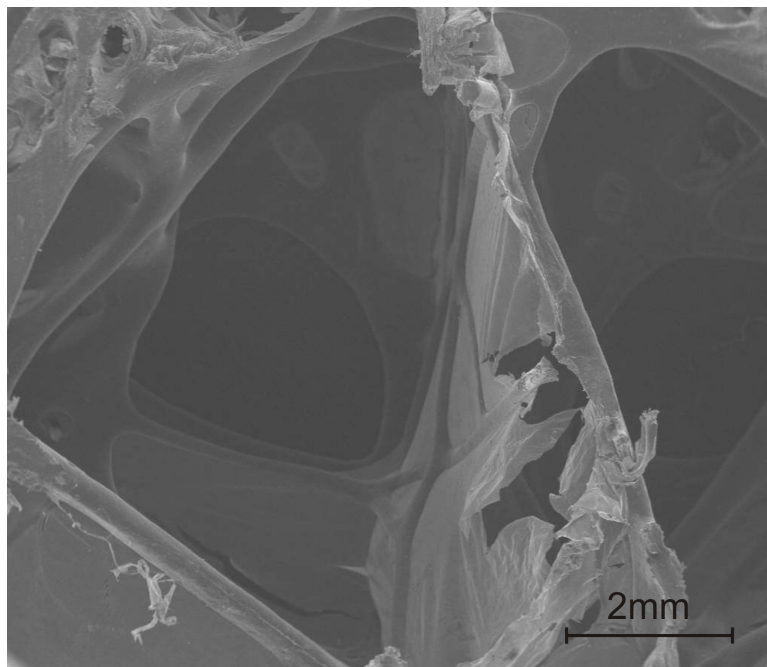


(a)

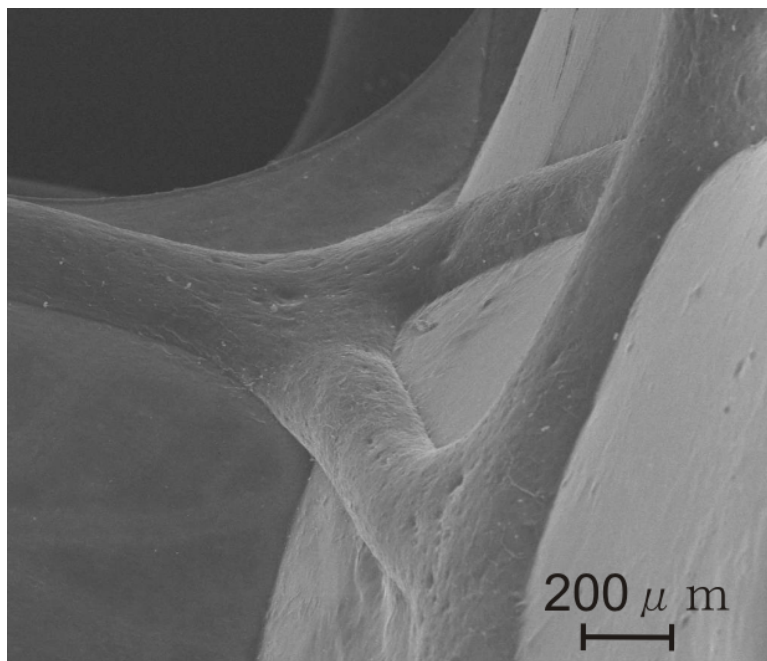


(b)

Figure 4.12: Scanning electron micrographs of toucan foam;(a) magnification $\times 80$;(b) magnification $\times 300$.



(a)



(b)

Figure 4.13: Scanning electron micrographs of hornbill foam;(a) magnification $\times 28$;(b) magnification $\times 150$.

4.2.2 Confocal Microscopy

We used confocal microscopy to investigate the detailed features of trabecular bone of beak. A number of studies have been carried out to investigate fatigue damage induced by accumulation of microcrack damage in the bone by confocal microscope observations [184–187]. The confocal microscopy can be used as a tool to construct 3 dimensional microstructure of bone [188,189]. Smith et al. that reported laser confocal microscopy produces better image quality of pore structure, compared to scanning electron microscopy [190]. Figure 4.14 shows a mosaic of cross sections of lower toucan beak. The confocal microscopy scanned the entire section of beak with a better resolution. We have evaluated a part of scanned image segments with a depth that ranges from 0 to 500 μm . Figure 4.15 (a) shows the original confocal image at a depth of 500 μm . The confocal image shows trabeculae cells are closed by thin membranes. The focus point for this image is a trabecula at the center. The original image was colored according to the volumetric intensity in Figure 4.15 (b). We processed the original confocal image with volumetric rendering in 2D. The scalar value in the pixel ranges from 7 to 255. The minimum value of 7 is color with blue and the maximum value of 255 is colored with red. The image processing techniques for tri-dimensional visualization will be discussed in detail in Section 4.6. The colored image enhances the contours of trabecular bone and membranes, compared to the original confocal image.

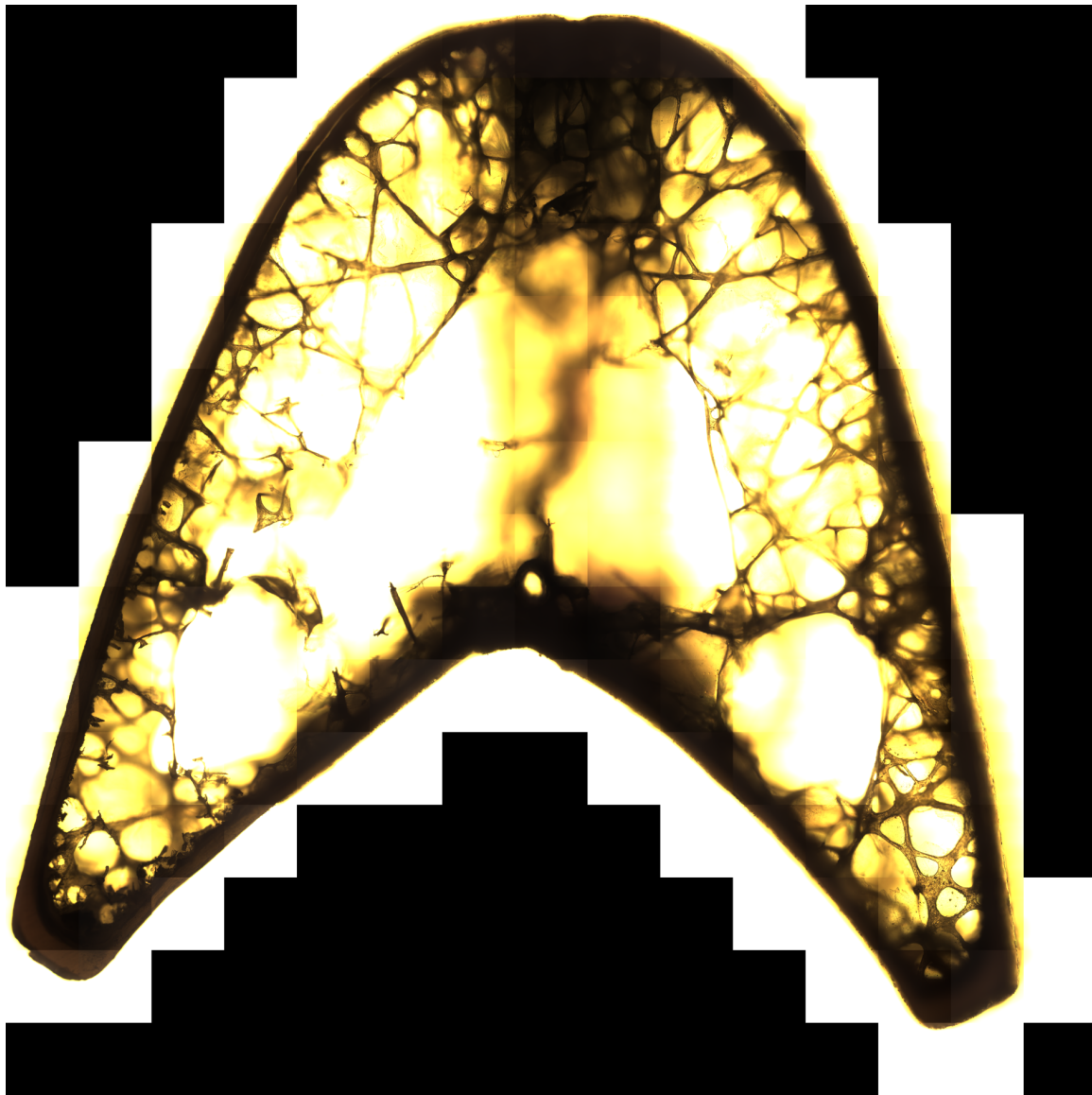
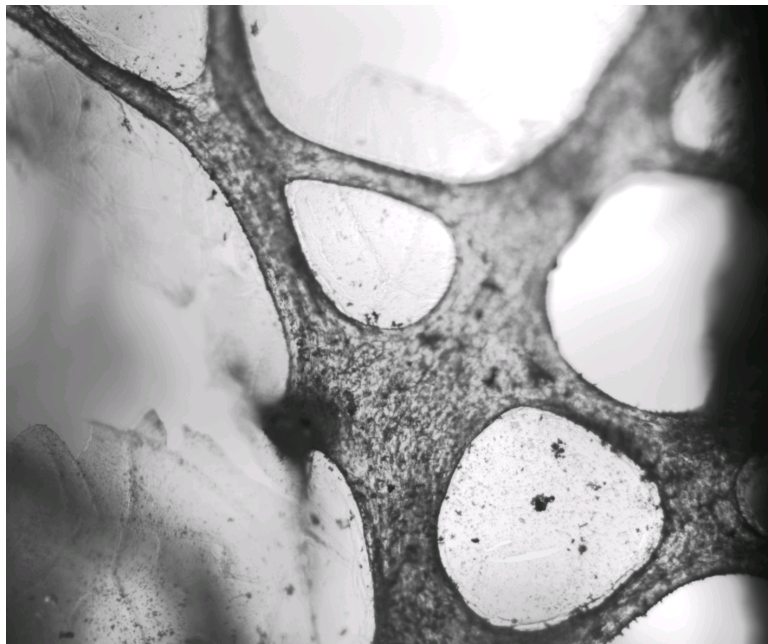
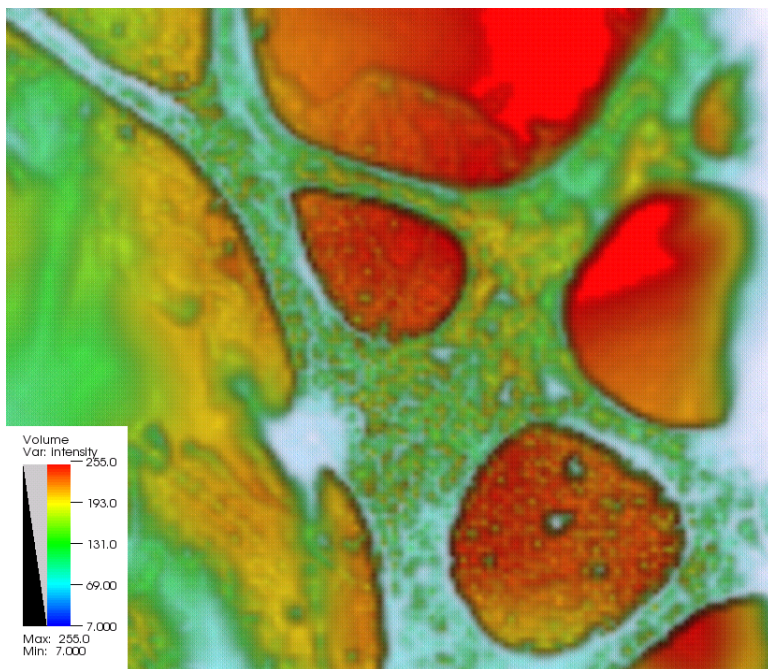


Figure 4.14: Mosaic of cross section of toucan lower beak captured by confocal microscopy.



(a)

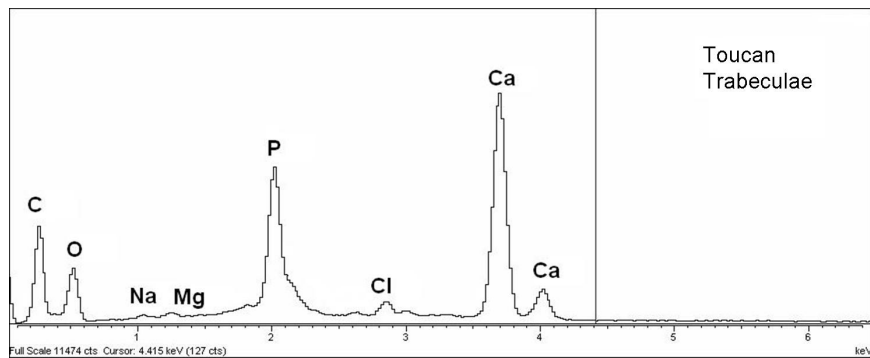


(b)

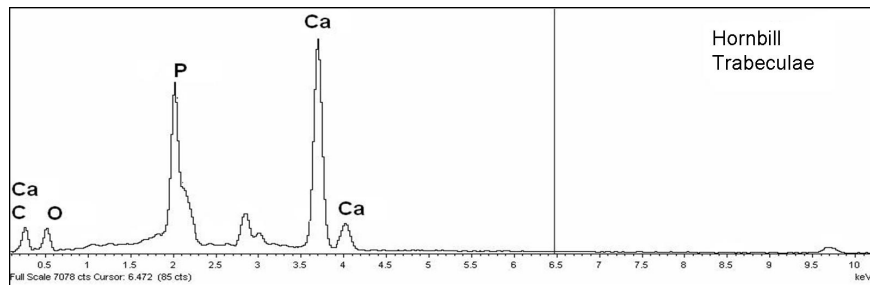
Figure 4.15: (a) Confocal image magnification $\times 40$;(b) Confocal image processed with VisIt.

4.2.3 Composition of Trabeculae

Figure 4.16 shows EDX results for toucan and hornbill trabeculae. The human trabeculae are composed of approximately 25 % of minerals [191]. The dominant mineral is calcium in beak trabeculae. We observed 24.6% of calcium in toucan trabeculae and 29.3 % of calcium in hornbill trabeculae, which is significantly higher than beak keratins. Additionally, we have examined the amino acid sequence of toucan beak skull, shown in Fig.4.17. The molecular fraction of glycine is approximately 33 %. Typically human bone consists of 1/3rd of glycine. In terms of mineral density and amino acid analysis, the beak trabeculae is composed of a similar amount of minerals and glycine of human trabecular bone.



(a)



(b)

Figure 4.16: Energy disperse X-ray results;(a) toucan trabeculae;(b) hornbill trabeculae.

Amino acid	pmole analyzed	mol. %	Residue wt.	wt/wt. %
CYS02 (C)	0	0.00	151.2	0.00
HYP (Z)	1532	9.29	113.12	11.50
ASP (D)	817	4.95	115.09	6.24
THR (T)	349	2.12	101.11	2.34
SER (S)	560	3.39	87.08	3.23
GLU (E)	1282	7.77	129.12	10.99
PRO (P)	2072	12.56	97.12	13.36
GLY (G)	5321	32.26	57.05	20.15
ALA (A)	1892	11.47	71.08	8.92
VAL (V)	294	1.78	99.13	1.93
MET (M)	148	0.90	131.2	1.29
ILE (I)	209	1.27	113.16	1.57
LEU (L)	497	3.01	113.16	3.73
NLE	0	0.00	0.00	0.00
TYR (Y)	59	0.36	163.18	0.63
PHE (F)	204	1.24	147.18	2.00
HIS (H)	59	0.36	137.14	0.54
TRP	0	0.00	186.20	0.00
LYS (K)	460	2.79	128.18	3.91
ARG (R)	741	4.49	156.19	7.68
		100.00	Total ng	
Total pmole analyzed	16,495			

Figure 4.17: Amino acid analysis of toucan trabeculae.

4.3 Mechanical Properties of Rhamphotheca

4.3.1 Micro-and Nanoindentation

The microhardnesses of toucan and hornbill rhamphotheca, shown in Figure 4.18, are comparable. However, there is a distinct difference in nanoindentation hardness. The nanoindentation hardness of hornbill rhamphotheca is twice that of toucan. Table 4.1 shows a summary of indentation results of beak keratins

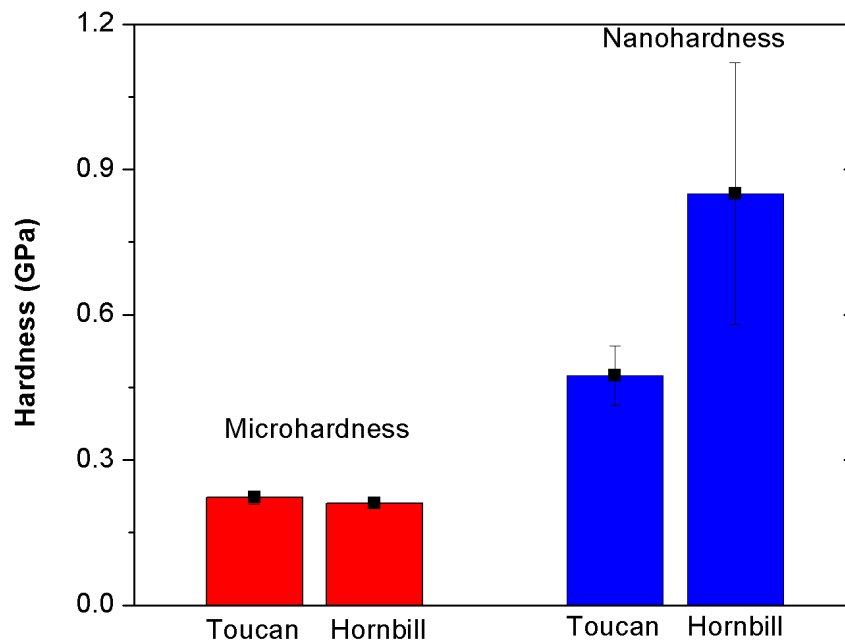


Figure 4.18: Comparison of micro- and nanohardness of toucan and hornbill trabeculae.

The hardness of toucan beak keratin is 0.22 ± 0.01 GPa from microindentation and 0.50 ± 0.06 GPa from nanoindentation. Higher nanohardness is also observed

for hornbill rhamphotheca. The micro and nanohardness of hornbill keratin is 0.21 ± 0.01 GPa and 0.85 ± 0.27 GPa, respectively. The difference between micro- and nanohardness of hornbill keratin is more significant than toucan. The nanoindentation of hornbill keratin is four times higher than its microindentation and it exhibits 70 % higher than nanohardness of toucan.

Table 4.1: Mean elastic modulus and hardness of beak keratins

	Hardness (GPa) Mi- croindentation	Hardness (GPa) Nanoin- dentation	Reduced Young's modu- lus (GPa)
Toucan keratin	0.22 ± 0.01	0.50 ± 0.06	6.5 ± 0.78
Hornbill keratin	0.21 ± 0.01	0.85 ± 0.27	9.3 ± 1.76

Figure 4.19 shows a typical force-depth displacement curve of toucan beak keratin from Berkovich tip. The hornbill beak keratin exhibits the same behavior. The slope of the unloading curve shows the reduced Young's modulus. The viscoelastic and viscoplastic behavior of the toucan beak is presented after a holding period of indenter. While indenter is held constant for 5 s after maximum loading, there is an increase in depth. Creep occurred in all tested keratin samples. When we applied lower load, the load after load held constant slightly dropped due to stress relaxation.

Figure 4.20 shows scanning probe micrographs of toucan beak keratin before indentation and after indentation. Figure 4.20 (a) is the picture of keratin surface after it was polished by $0.05 \mu\text{m}$ compound powder. When the contact involved viscoplastic deformation, the material may either sink in (if material work hardens) or pile up (if material does not work harden) around the indenter. Figures 4.20 (b) and (c) show piling-up after 500 and 1000 μN of loads were applied on the surface. The keratins, a softer material, are more susceptible to viscoplastic deformation as a indenter proceeds so that plastic flow went through easily and piling-up occurred. When a higher indentation load was applied, the height of the piling-up increased on

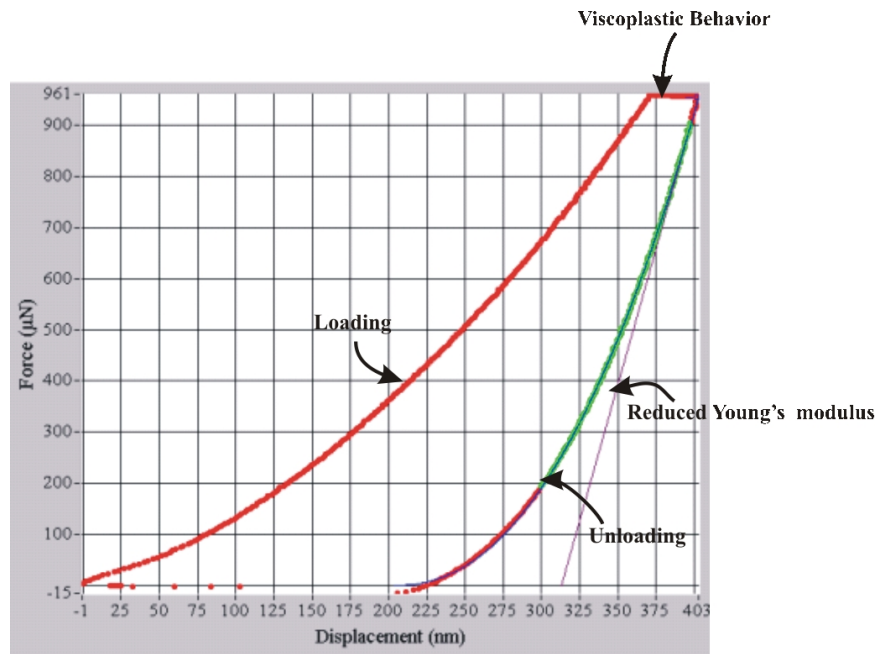
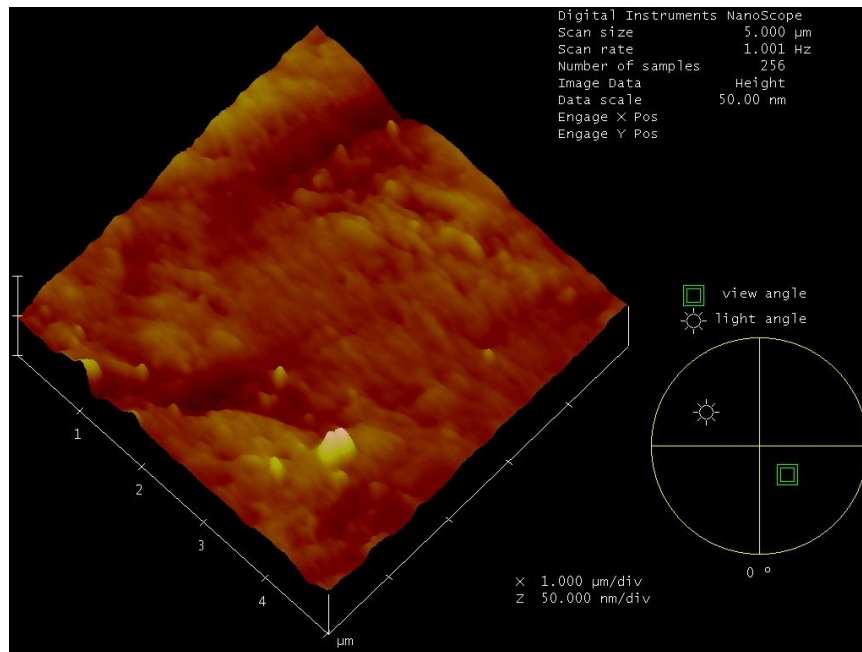
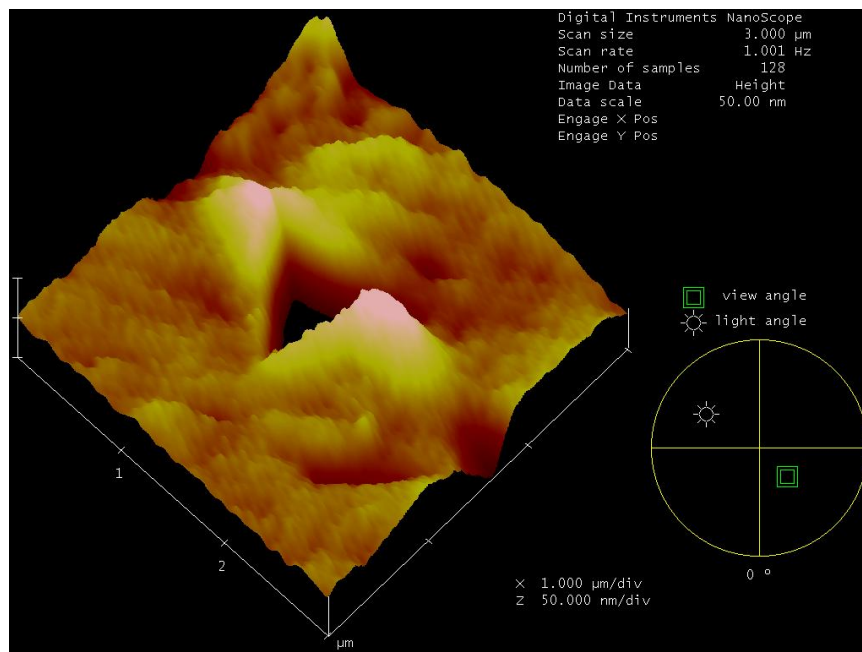


Figure 4.19: Force-displacement curve. Nanoindentation load were applied $1000 \mu\text{N}$ on toucan keratin surface.

the keratin surface, shown in Figure 4.20 (b) and (c). This result indicates that the degree of work hardening is very low and keratin is obviously a non-work hardening natural material.

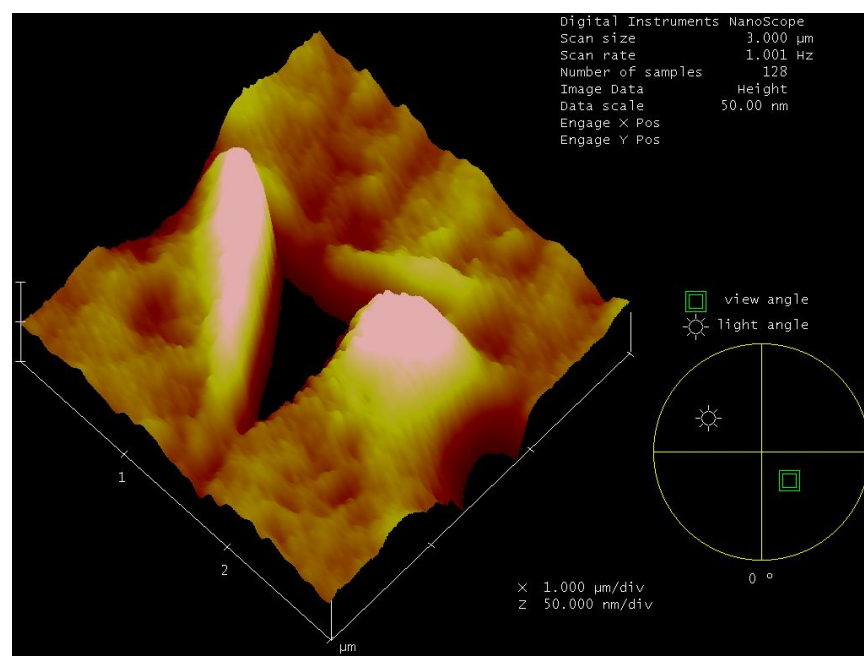


(a)



(b)

Figure 4.20: Scanning probe micrographs of toucan keratin surface;(a) polished keratin surface;(b) $500\mu\text{N}$ applied surface;(c) $1000\mu\text{N}$ applied surface.



(c)

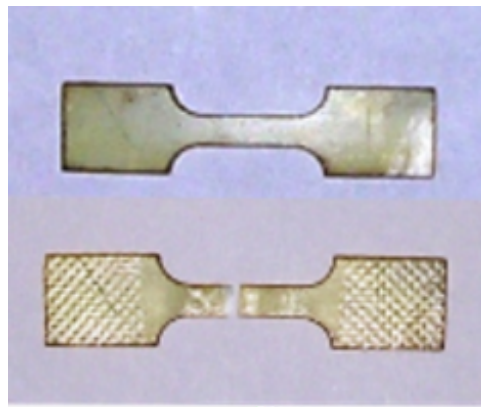
Figure 4.20: Scanning probe micrographs of toucan keratin surface;(a) polished keratin surface;(b) $500\mu\text{N}$ applied surface;(c) $1000\mu\text{N}$ applied surface.

4.3.2 Mechanical Behavior of Beak Keratin under Ambient Conditions

4.3.2.1 Tensile Properties

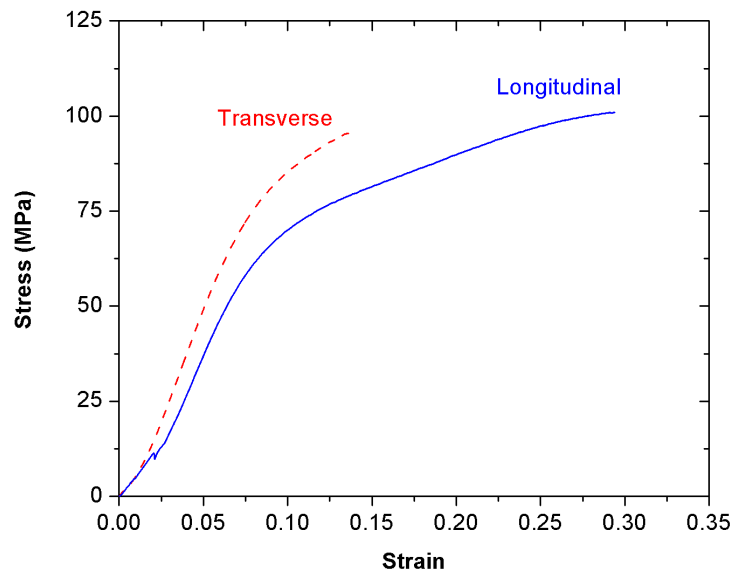
Figure 4.22 shows typical tensile stress-strain curves of toucan and hornbill beak keratins tested under atmospheric condition. Both beak keratins were measured in longitudinal and transverse directions. The bottom plate of hornbill maxillary ramphotheca is also measured in longitudinal direction. The Young's modulus of toucan beak keratin in two directions ranges from 1.04 ± 0.06 GPa (longitudinal) to 1.12 ± 0.13 GPa (transverse). The tensile strength of toucan beak keratin in transverse

direction was higher than in longitudinal direction, 85.7 ± 23.4 MPa in longitudinal direction and 112.9 ± 19.9 MPa in transverse direction; however, the longitudinal direction exhibits more ductility. Figure 4.21 shows 14 % elongation of toucan longitudinal tensile specimen; a part of keratin layers were peeled off at the gauge. The Young's modulus of hornbill keratin is 1.22 ± 0.34 GPa and the tensile strength is 114.9 ± 10.3 MPa in longitudinal direction. The transverse direction has a lower Young's modulus of 0.813 ± 0.06 GPa and tensile strength of 56.33 ± 8.9 MPa. The bottom plate of hornbill keratin in longitudinal direction has the highest Young's modulus of 1.57 ± 0.06 GPa and tensile strength of 180 ± 11.7 MPa. Interestingly, the orientation effect of the hornbill beak keratin is the opposite to that of toucan beak keratin, the lowest strength in transverse direction and highest strength in longitudinal direction. This difference may originate from the arrangement and geometry of keratin scales. The keratin scales of hornbill rhamphotheca was elongated compared to that of toucan, shown in Figs. 4.2 and 4.3. Further investigation of the relationship between mechanical properties and microstructure of rhamphotheca needs to be conducted to verify the difference.

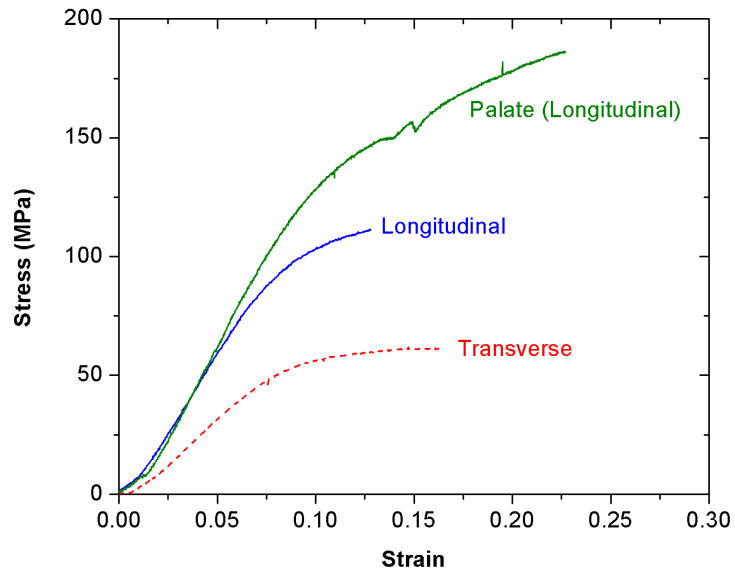


(a)

Figure 4.21: 14% elongation of a toucan longitudinal specimen.



(a)



(b)

Figure 4.22: Stress-strain curves of beak keratins;(a) toucan beak keratin;(b) hornbill beak keratin.

4.3.2.2 Fracture Analysis

It is well known that brittle and ductile fracture of polymers are strain rate dependent. The beak keratin, a biological composite, also shows two different fracture modes. Figures 4.23 and 4.24 show scanning electron micrographs of fracture surfaces from a tensile specimen tested at the low strain rate of 5×10^{-5} /s for toucan and 3×10^{-4} /s for hornbill. The fracture surface is smooth and pull-out is evident from the fracture surface of toucan beak keratin. The toucan beak keratin scales show no breakage and were completely slipped from glued cell-to-cell interface shown in Figure 4.23. In the case of the hornbill beak keratin, the pull-out mode is barely seen from scanning electron micrographs in Figure 4.23. Most of the keratin scales were fractured after the test shown in Figure 4.24.

The pull-out mode tends to occur at low strain rate. At low strain rate, large molecules can move and change their configurations during stretching. The pull-out mode occurred when plastic flow occurred along the keratin scale interfaces, the glued region. The organic macromolecules exhibits a high strain-rate-dependence, that was modeled by Freund [192] and observed by Evans and Ritchie [193, 194].

The fracture surface at low strain rate, that at two order of magnitude higher strain rate was analysed for comparison. Figures 4.25 and 4.26 show scanning electron micrographs of fracture surfaces from tensile specimens deformed at strain rate of 1.5×10^{-3} /s for toucan and 5×10^{-2} /s for hornbill. Both keratin scales were completely torn and experienced severe viscoplastic deformation. The fracture surface of hornbill keratin shows more severe spikes and some areas are charged with electrons. The strain rate was not high enough to confirm the brittle fracture mode of keratin at high strain rate. However, the fracture surface of keratin seems to favor brittle fracture at high strain rate. At high strain rate, viscosity increases and large molecular movement is limited. As a result, the keratin scales fractured when molecules are fully extended and disulfide covalent bonding is broken.

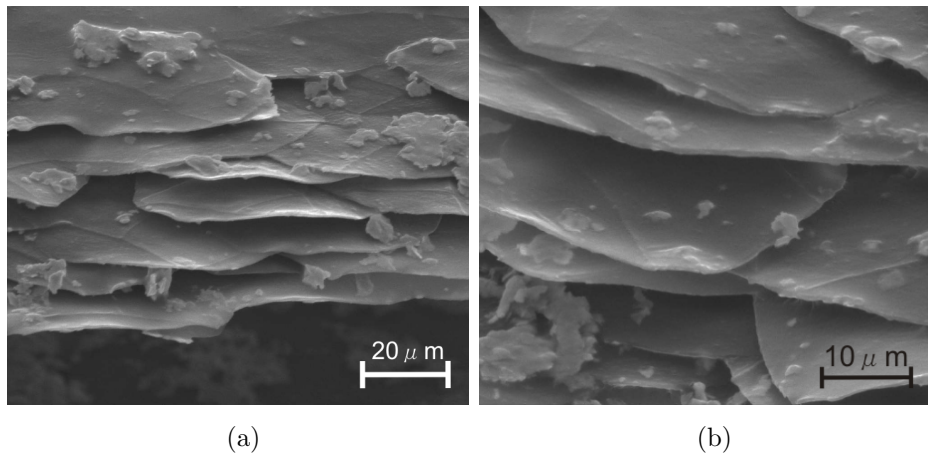


Figure 4.23: Scanning electron micrographs of tensile fracture of toucan keratin, strain rate 5.0×10^{-5} ; (a) magnification X2400; (b) magnification X5000.

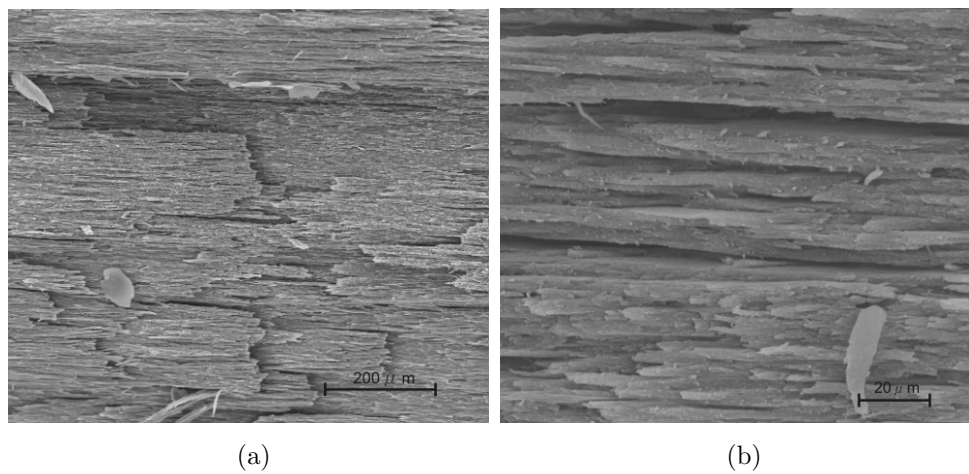


Figure 4.24: Scanning electron micrographs of tensile fracture of hornbill keratin, strain rate 3.0×10^{-4} ; (a) magnification X300; (b) magnification X2000.

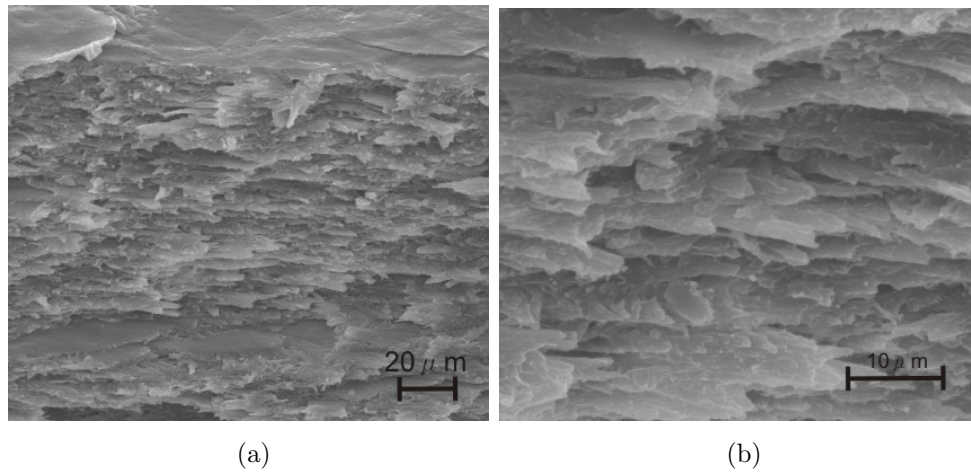


Figure 4.25: Scanning electron micrographs of tensile fracture of toucan beak keratin, strain rate 1.5×10^{-3} ; (a) magnification X1500; (b) magnification X6000.

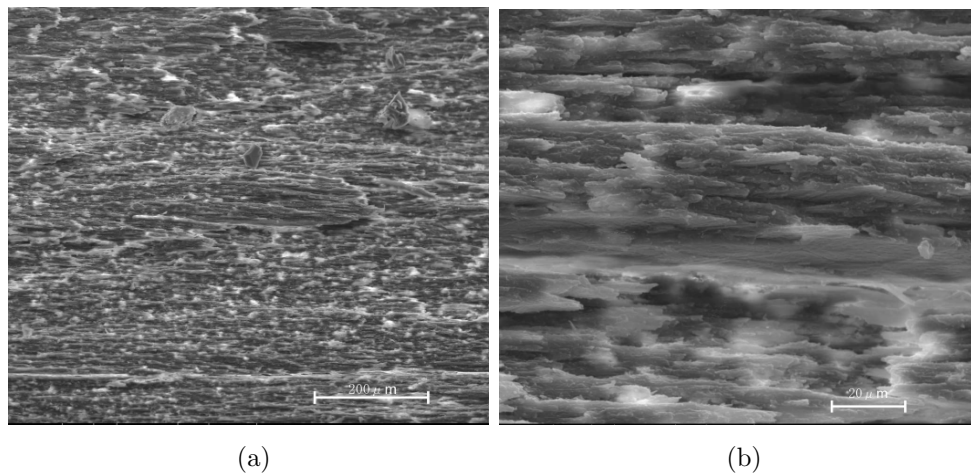


Figure 4.26: Scanning electron micrographs of tensile fracture of hornbill beak keratin, strain rate 5×10^{-2} ; (a) magnification X300; (b) magnification X2000.

One possible explanation for the change in fracture mode is given by Figure 4.27, which shows both the yield stress and UTS as a function of the strain rate from toucan beak keratin. The glued stress is quite sensitive to the strain rate because this is composed of macromolecules whose breaking strength decreases with increasing time. This can be understood by the viscoplastic response of the interscale glue. When the yield stress approaches (or exceeds) the UTS, fracture is preferred over viscoplastic deformation of the glue. The transition from ductile to brittle fracture would, in this case, be governed by whether the yield stress is lower or higher than the fracture is governed by the criterion.

$$\sigma_t \leq \sigma_g \quad (4.1)$$

$$\sigma_g = k\dot{\varepsilon}^m \quad (4.2)$$

where m is the strain rate sensitivity, σ_t is fracture stress, and σ_g is flow stress.

This competition between viscoplastic shear of the interscale glue and tensile fracture of the scales is similar to the response exhibited by the abalone shell in tension. In the case of abalone, the tiles are composed of the biomineral aragonite. We could not obtain sufficient data for modelling fracture behavior of the beak keratins. In spite of this, the exterior of the toucan and hornbill beak seem to be dependant on the strain rate and orientation of the keratin. The UTS increased with strain rate and fracture modes also change from pull-out to brittle fracture mode. The strain rate dependence of macromolecules was observed by Freund [192] and Evan and Ritchie [194]. Figure 4.28 shows the rupture force with different loading rate. As the loading rate increases, the rupture force increases.

The beak keratin becomes stiffer by changing fracture mode in longitudinal direction as strain rate increases. We still need to test the keratins at a wide range of strain rate to verify the strain rate dependency of fracture mode of beak keratin.

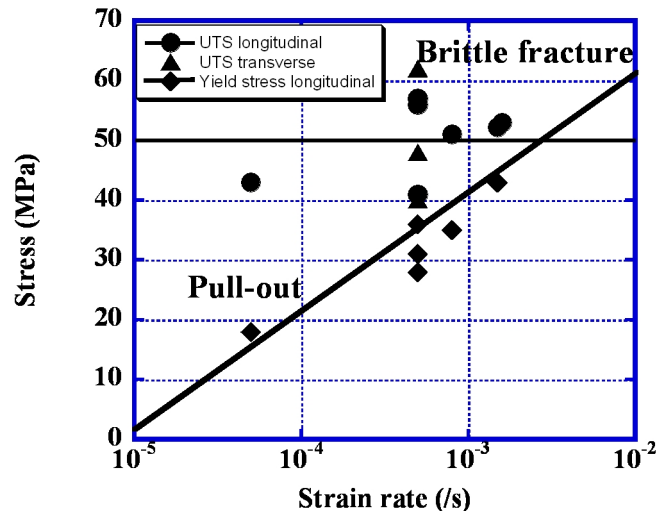


Figure 4.27: UTS and yield vs strain rate plot of longitudinal and transverse directions (toucan beak).

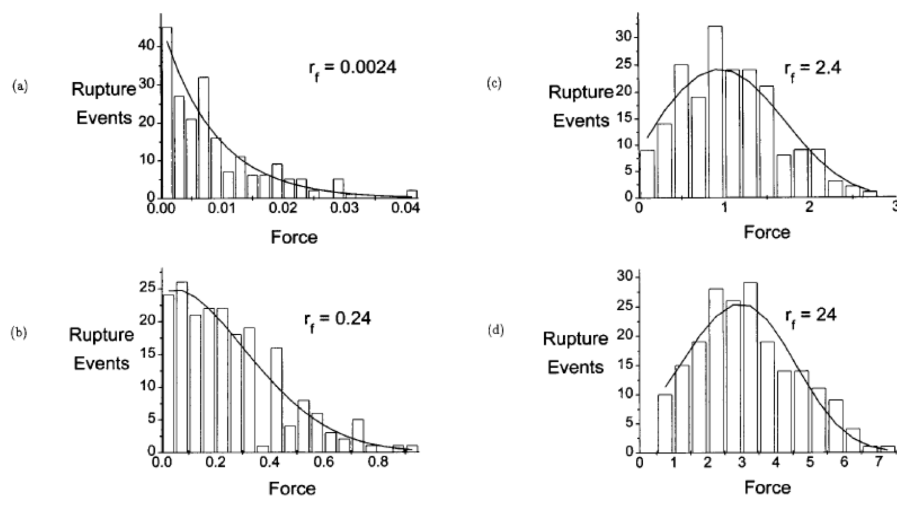


Figure 4.28: Histogram of rupture force from 200 SMC simulation of bond breakage at widely separated loading rate (From Evans and Ritchie [193] in Fig 4.).

4.3.3 Mechanical Behavior of Beak Keratin at High Humidity

The mechanical properties of mammalian keratins are highly influenced by their moisture content [42, 46, 124, 125, 130]. In the case of avian keratins, Taylor et al. reported that the stiffness of feathers and claws at high humidity conditions significantly decreased [148], as discussed in Chapter 2. The representative tensile stress-strain curves of toucan beak keratin under two conditions (23°C and 45 % RH, 38°C and 95% RH) are shown in Fig. 4.29. At low humidity, the Young's modulus of toucan keratin is plane isotropic, ranging from 1.04 ± 0.06 GPa (longitudinal) to 1.12 ± 0.13 GPa (transverse). The tensile strength of toucan beak keratin in the transverse direction was approximately 32% higher than in longitudinal direction, as shown in Fig.4.29. The strength of toucan beak keratin significantly decreases under the high humidity condition as shown in Fig.4.29. The elongation at 95% RH is approximately twice higher than that at 45% RH. The variation in strength in longitudinal and transverse directions is also more distinctive under the high humidity condition. The average strength is 16.7 ± 2.2 MPa in longitudinal direction and 31.0 ± 4.4 MPa in transverse direction. The Young's modulus is 0.093 ± 0.02 GPa (longitudinal) and 0.17 ± 0.003 GPa (transverse). The stiffness in the high humidity condition drops by approximately an order of magnitude. The mass of hydrated keratin increases 10 % for 5 h of exposure in 95% RH condition, which significantly decreases the mechanical properties of toucan beak keratin.

Figure 4.30 shows scanning electron micrographs of hydrated toucan rhamphotheca after fracture. The keratin scales are completely torn whereas scales are slipped from glued keratin scale interface. When keratin is hydrated, the stiffness of keratin decreases as the keratin matrix absorbs the water yet the crystalline filaments is not affected by water. As a result, the keratin scales become soft and behave like elastomer.

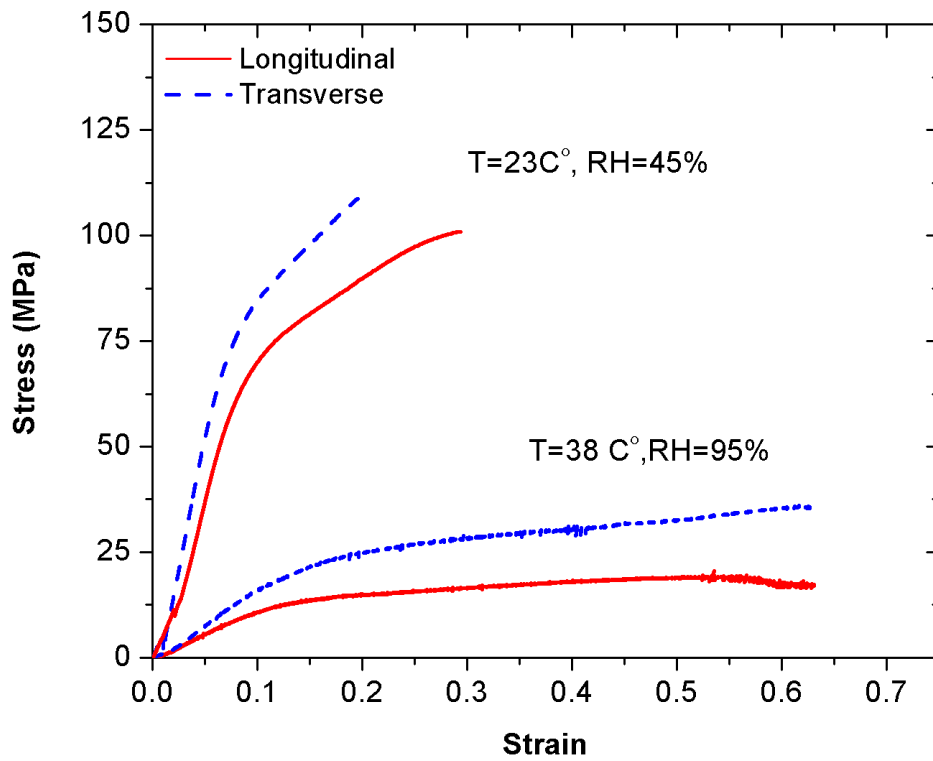
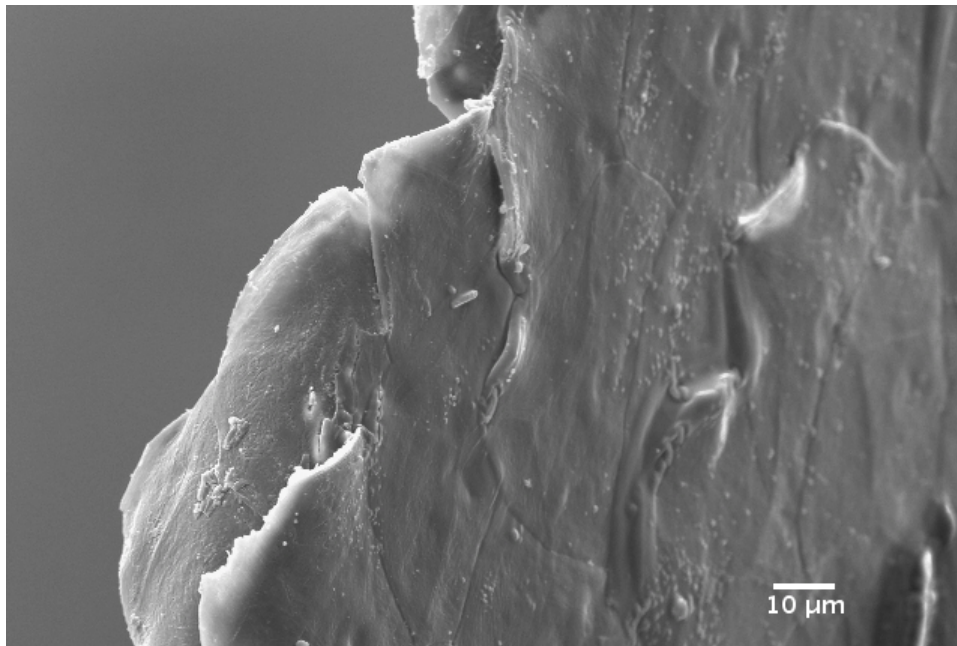
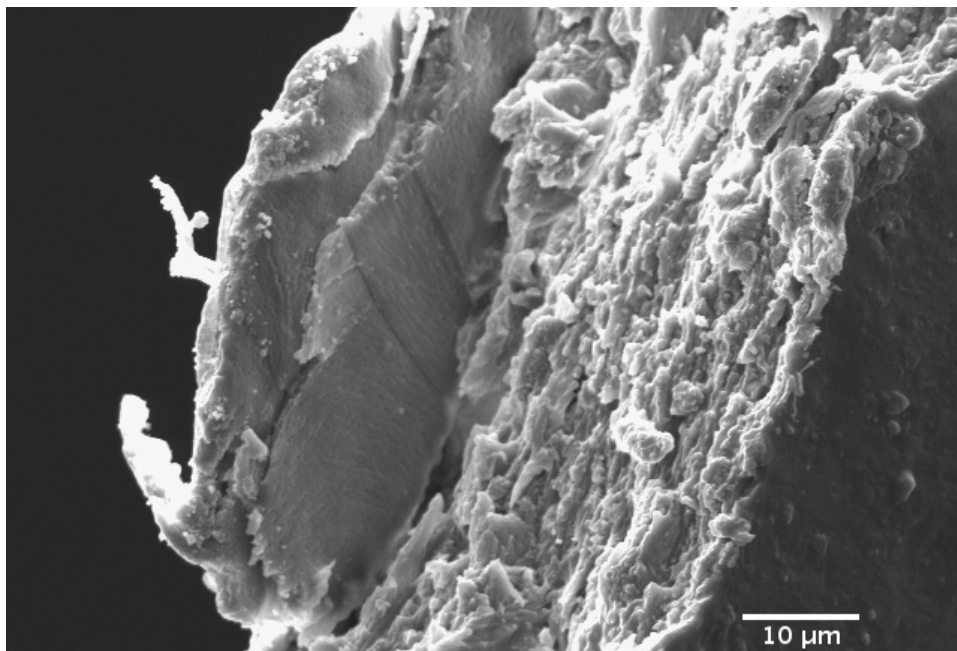


Figure 4.29: Stress-strain curves of keratins at RH 45% and 95%.



(a)

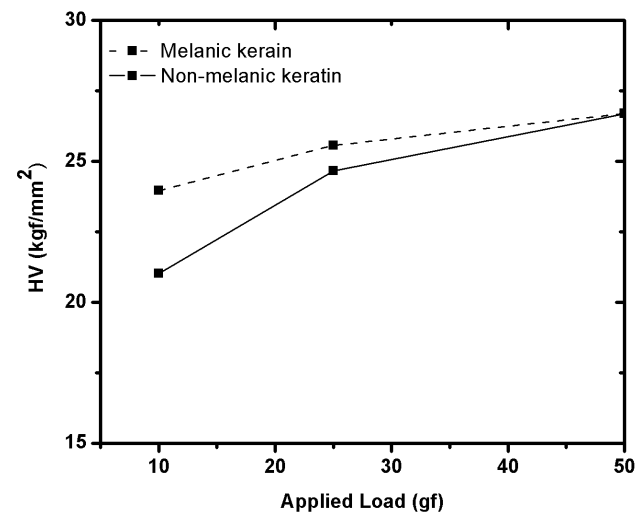


(b)

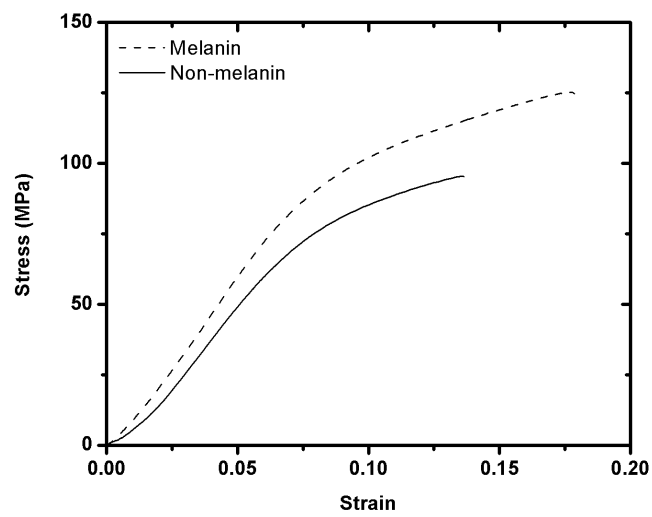
Figure 4.30: Scanning electron micrographs of fractured toucan ramphotheca;(a) the fractured keratin surface ;(b) cross section of torn keratin.

4.3.4 Mechanical Role of Melanized Keratin

The color in feathers and beaks is thought to play a role in mechanical properties. Especially, the mechanical role of melanin of bird beaks and feathers for abrasion resistance is discussed in literature [52, 150, 195, 196]. Bonser and Witter first discussed the mechanical role of melanin by microhardness measurement of European Starling beak [52]. The hardness of melanic keratin exhibits 67 % high hardness compared to unmelanized keratin [52]. We have also confirmed that the melanized beak keratin shows high hardness at a load up to 50 gf, shown in 4.31(a). As the applied load increases, the hardness of melanized and unmelanized beak keratins becomes comparable. The mechanical properties of transversely sectioned melanized and unmelanized toucan beak keratins are also compared in tension. The Young's modulus of unmelanized keratin is 1.12 ± 0.13 GPa and that of melanized keratin is 1.35 ± 0.31 GPa. The Young's modulus of melanized beak keratin is 21 % higher than that of unmelanized keratin. The tensile strength of unmelanized keratin is 112.3 ± 19.9 MPa and that of melanized keratin is 105.7 ± 38.2 MPa. The strength of unmelanized keratin is higher than melanized keratin; however, we need to consider the high standard deviation of melanized keratin. A high strength of melanized avian keratin from Osprey feather barb is reported by Bulter and Jonson [150]. The mechanical role of melanin might be associated with an increase of the stiffness and hardness.



(a)



(b)

Figure 4.31: Comparison of melanized and unmelanized keratins;(a) HV vs applied loads; (b) Stress-strain curves of melanized and unmelanized keratins.

4.3.5 Beak Rhamphotheca

It is interesting to compare with mechanical properties of beak keratins and other bird keratins from literatures. The microhardness of toucan and hornbill keratins is similar to European Starling bill [52]. The beak might be mechanically conservative in different species in microscale. Young's modulus of the toucan and hornbill beak keratins from tensile test are similar to the avian claws, however, not as stiff as feather [48]. Mechanical behavior of the beak also appeared to be identical to the avian claw keratin. Structural pattern of the beak keratins is also quite similar to the avian claws distinct from feathers [36, 37]. The toucan and hornbill beak keratins show a some degree of anisotropy of Young's modulus and tensile strength in longitudinal and transverse directions. Bonser has reported the Young's modulus of the ostrich claw has 30 % differences in along and perpendicular to the claw directions [197]. The tensile behaviors of toucan and hornbill keratins in longitudinal and transverse directions are opposite. This would be associated with the arrangement of keratin scales and adhesive property of the glue.

Young's modulus and hardness from nanoindentation tend to be higher than other mechanical tests at micro and macro scale. For example, Young's modulus of the toucan beak keratin from nanoindentation is three times higher than Young's modulus in tension. The difference is more distinct for hornbill and the Young's modulus is nine folds higher. The nanohardness is also higher than microhardness. These differences have been observed nanoindentation measurement of bone [94]. Nanoindentation avoids the influences of inhomogeneities and innate defect of the biological materials and can be influenced by the mineral interaction. Nanoindentation techniques offer intrinsic mechanical properties of the material and provide useful information of the biological materials.

We observed deformation pattern changes with increasing strain rate, distinctive in viscoelastic materials. This deformation mode change has been observed in hoof wall [44]. As strain rate increases, keratins becomes stiffer. Although we our results

could not provide enough data to prove the deformation change of beak keratins, we have observed the hardening behavior of keratins protecting animals from natural environment.

4.4 Mechanical Properties of Beak Foam

4.4.1 Micro- and Nanoindentation

The comparison of micro- and nanoindentation hardness for the trabeculae is illustrated in Figure 4.32. Nanoindentation hardness values are almost twice as high as microhardness.

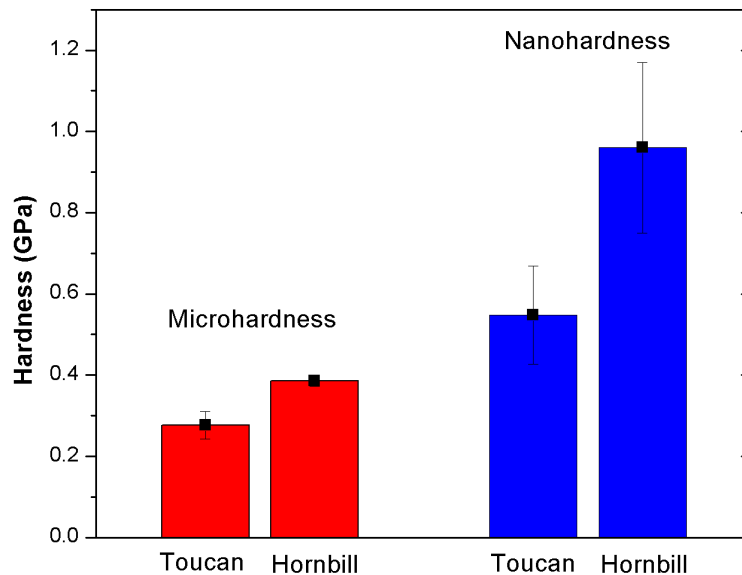


Figure 4.32: Comparison of micro and nano hardness of toucan and hornbill trabeculae.

In the case of bone, higher nanoindentation values, as discussed by Rho et al. [86, 94]. are caused by a scale dependence of the mineral and collagen interaction. The difference in hardness between toucan and hornbill rhamphotheca is also significant at the nano scale. The hardness of hornbill trabeculae is 44 % higher in macroindentation and 34 % higher in nanoindentation than that of toucan. The microhardness of hornbill beak trabecula is comparable to avian humeral trabecular bone (~ 0.40 GPa) [53]. The summary of hardness and reduced Young's modulus of beak trabeculae is listed in Table 4.2.

Table 4.2: Mean elastic modulus and hardness of trabeculae

	Mean hardness Microindenta- tion	hard- (GPa)	Mean hardness nanoindenta- tion	hard- (GPa)	Reduced Young's mod- ulus (GPa)
Toucan trabecula	0.27 ± 0.03		0.55 ± 0.12		12.7 ± 1.50
Hornbill trabecula	0.39 ± 0.01		0.96 ± 0.21		21.4 ± 5.25

We compared with bone and antler, being other mineralized and collagenized biological materials. The microhardness of trabecular bone is reported to be ~ 0.3 GPa [198] and 0.34 GPa [199] in dry condition. The nanoindentation results from Rho et al. [94] show the hardness of trabecular bone in transverse direction is 0.56 GPa and Young's modulus is 16.6 GP. The microhardnesses are 0.21 GPa and 0.16 GPa for 3-year old and 5-year old antler, respectively [200]. The microhardness of bone is close to hornbill trabeculae while nanoindentation results for bone fall in range of those values measured for toucan and hornbill. The microhardness of antler is less than beak trabeculae, which might be associated with the mineral density. The higher hardness of bone and rhamphotheca keratin is due to its mineralization, from which we suggest that mineralization of hornbill beak trabeculae is higher than in the toucan beak trabeculae.

Figure 4.33 shows force-depth displacement curve of toucan trabeculae. We have observed the creep effect on toucan trabeculae and hornbill trabeculae as we have seen in beak keratin, evidenced by an increase of displacement of 44 nm.

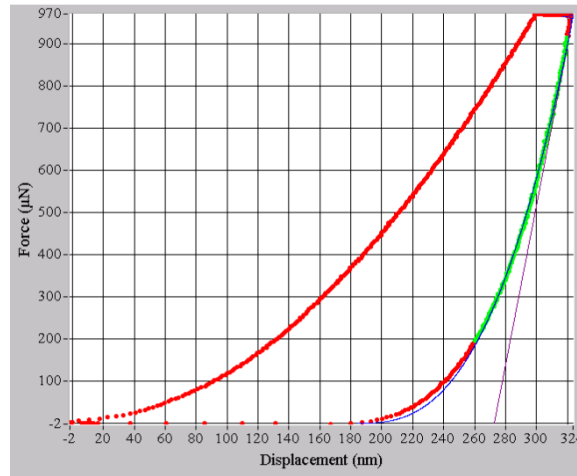


Figure 4.33: Force-displacement curve. Nanoindentation load were applied $1000\mu\text{N}$ on toucan trabecula.

4.4.2 Mechanical Behavior of Foam

The compressive behavior of toucan and hornbill foams is characterized by brittle crushing behavior, from linear elasticity to fracture. The large fluctuation of the stress was exhibited in stress-strain curves after linear elastic regime, shown in Figure 4.34. The spikes at the plateau correspond to individual cell collapse. The large fluctuation of the stress of toucan foam corresponds to the number of lobes from the local buckling of toucan foam, shown in Figure 4.34 (a). In the case for hornbill, the fluctuation of stress is associated with the shell collapse and the complete fracture of trabeculae.

The Young's modulus of toucan foam ranges from 0.5 to 13 MPa. The crushing stress vary from 0.07 to 0.3 MPa. The initial Young's modulus and crushing strength

of hornbill foam is 28 MPa and 2 MPa, respectively. The toucan foam shows low Young's modulus and strength compared to the hornbill foam. There is at least an order of magnitude difference between toucan and hornbill foam in strength and a 2 to 5 times difference in Young's modulus. The crushing strength and initial Young's modulus of hornbill foam is approximately 4 folds higher than that of toucan foam. This is due to the difference in the apparent density of foam and mineralization of the beak trabecular bone. The difference in apparent density between hornbill and toucan foam is ~ 4 folds.

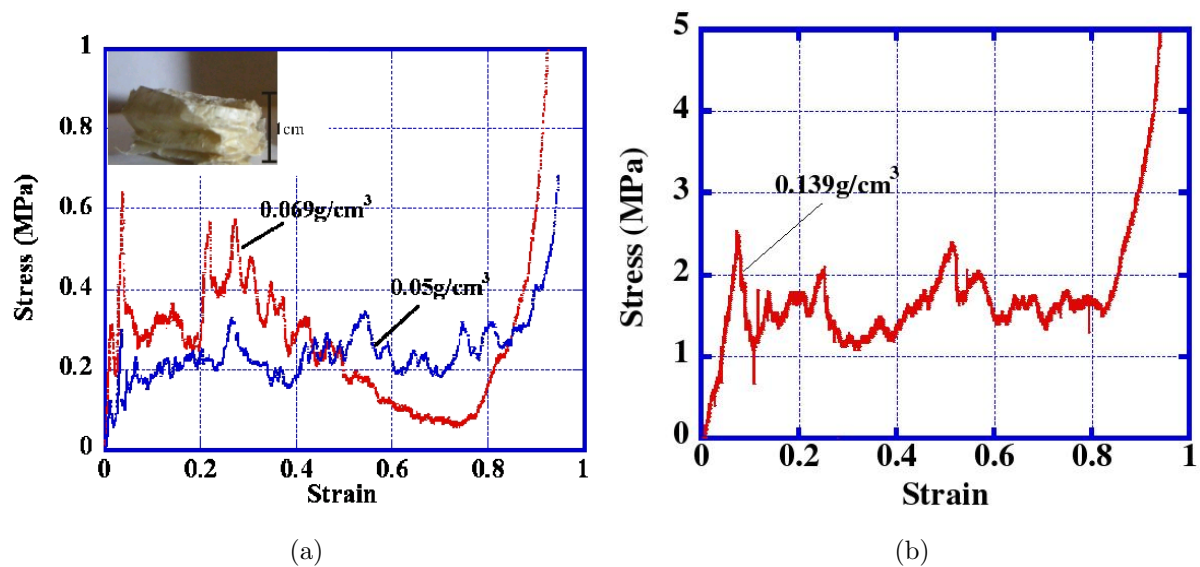


Figure 4.34: Typical compressive stress-strain curves for beak foam; (a) toucan; (b) hornbill.

4.4.3 Fracture Analysis

Figures 4.35 and 4.36 show the fracture pattern in foams. It is composed of a mixture of plastic deformation, partial, and total fracture of the trabeculae. The trabeculae have a fibrous structure similar to wood and can fracture partially when

they are subjected to bending (Figure 4.35 (b)). In other locations, the trabeculae undergo total fracture. It is visible in Figures 4.35 (c) and 4.36. The "green twig" appearance of the trabeculae is evident in Figure 4.35 (b). Hence, the cellular material does not crumble when compressed to its maximum strain. Rather, the toucan trabeculae collapse in a semi-plastic manner.

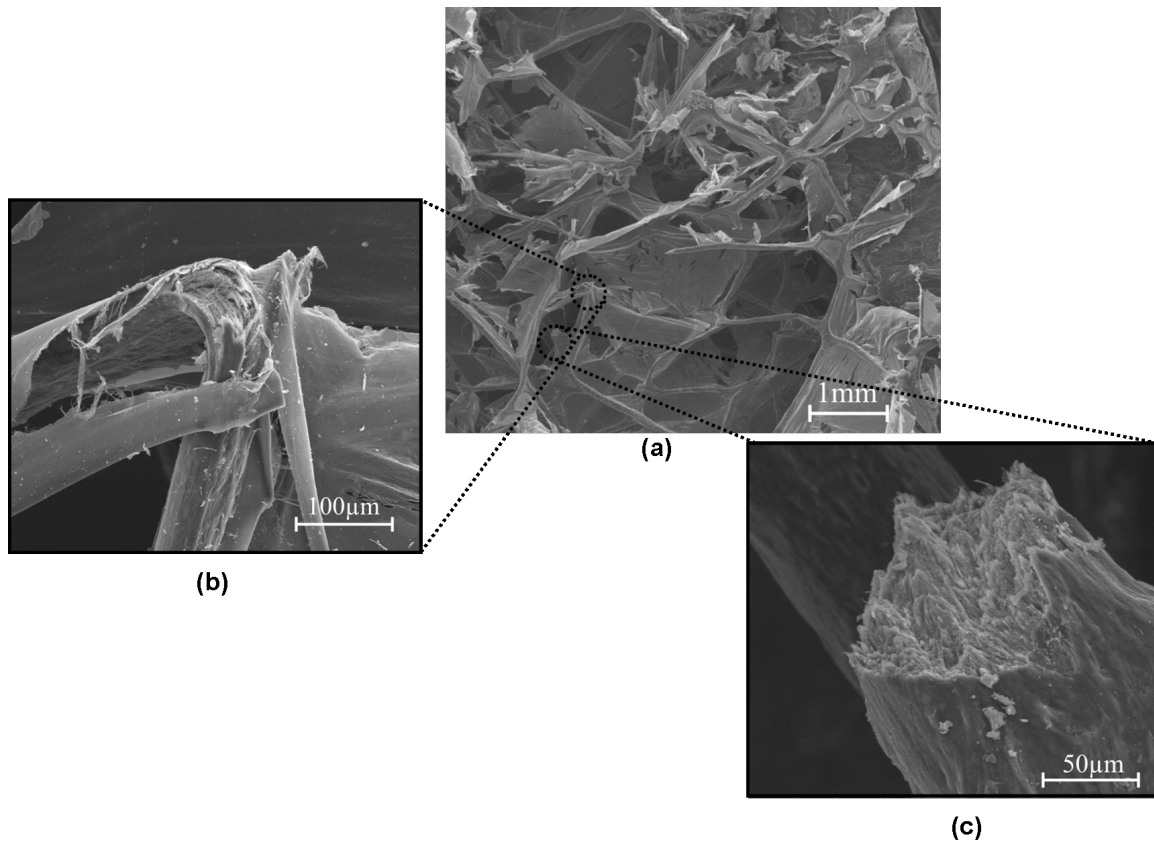


Figure 4.35: Fracture morphology of toucan closed-cell foam showing profuse trabecula bending ; (a) overall view ; (b) "green twig" fracture; (c) total fracture of trabecula.

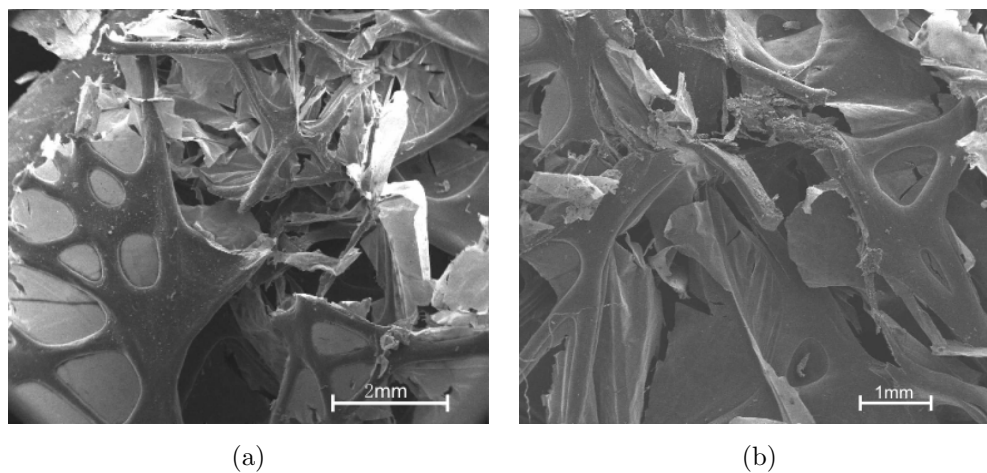
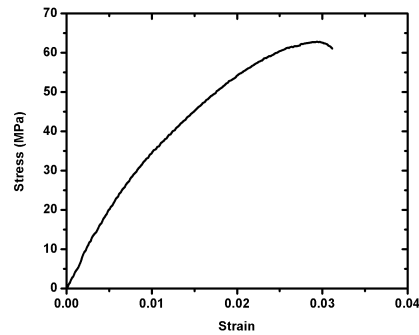


Figure 4.36: Fracture of morphology of hornbill hornbill closed-cell foam; (a) magnification $\times 32$; (b) magnification $\times 38$.

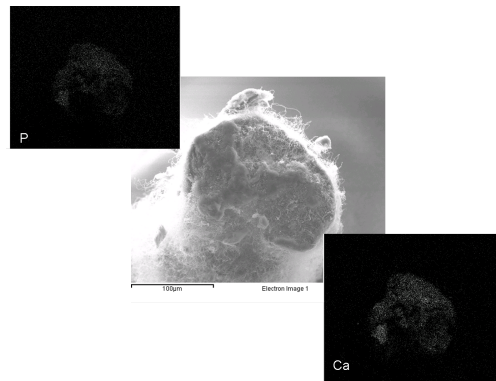
4.4.4 Mechanical Properties of Foam Materials

Figure 4.37 (a) shows a typical stress-strain curve of single trabecula from toucan beak skull. The average Young's modulus is 3.0 ± 1.87 GPa based on twenty-seven measurements. The high standard deviation is associated with the irregularity of sample dimension and degree of mineralization. In fact, We evaluated the mineralization of the tested specimens by EDX. Figure 4.37 (b) shows the fracture surface of a trabecula specimen with compositional analysis by EDX. Calcium and phosphorus is evenly distributed in trabeculae. We investigated the relationship between calcification and stiffness of trabeculae. Fig.4.37 (c) shows Young's modulus is plotted as a function of the content of calcium salt. The calcification of the trabeculae is analyzed by energy dispersive X-ray. The Young's modulus of the trabeculae increases with an increase of calcification. The amount of calcium ranges from 10 to 30 wt%. The Young' modulus of trabeculae fluctuates between 1 GPa and 7 GPa. The effect of adhesive also must be considered for the variations and might increase the stiffness.

The wide variation in elastic modulus of trabeculae has been reported in a number of literatures. The Young's modulus of single trabeculae varied from 1 GPa to 19 GPa in tension [162–164,201]. Lucchinetti et al. [162] discussed the limitations and error sources associated with micro-mechanical testing. For comparison, the Young's modulus of toucan trabeculae is 12 GPa by nanoindentation technique [202]. The high Young's modulus attributes by the size effect and mineral interactions.

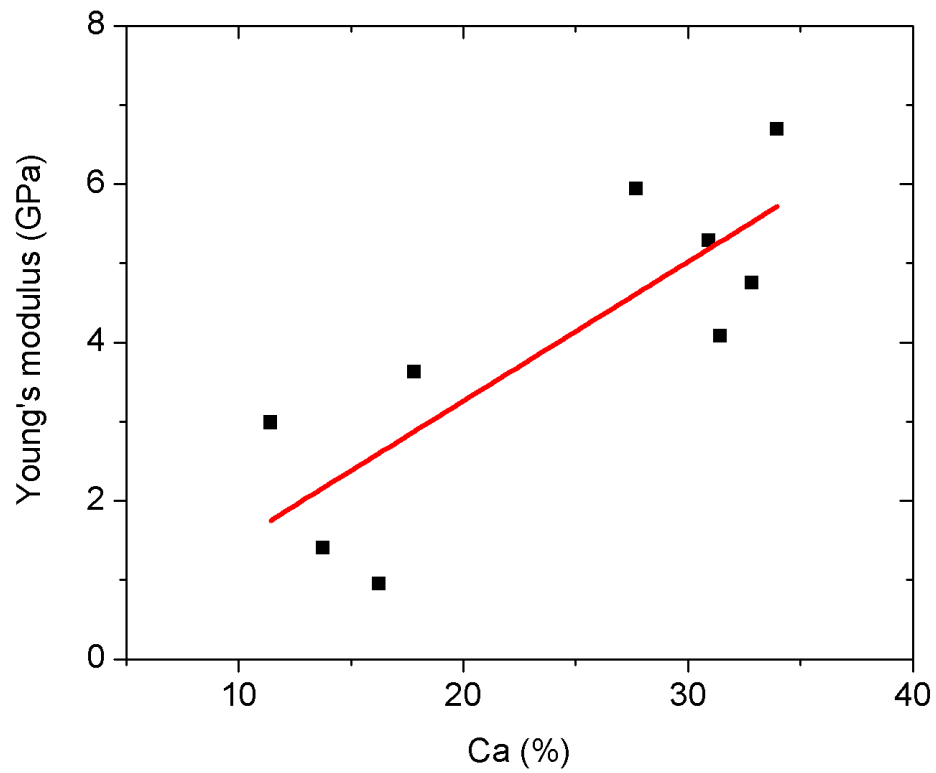


(a)



(b)

Figure 4.37: (a) Typical stress-strain curve of toucan trabecula;(b) Scanning electron micrographs of fractured trabecula with EDX dot mapping ;(c)Young's modulus vs calcium.



(c)

Figure 4.37: (a) Typical stress-strain curve of toucan trabecula; (b) Scanning electron micrographs of fractured trabecula with EDX dot mapping ; (c) Young's modulus vs calcium.

The strength of the trabeculae is statically plotted with Weibull distribution in 4.38. The probability of failure for brittle materials, $F(V)$ is described by

$$F(V) = 1 - \exp\left(-\left(\frac{\sigma}{\sigma_0}\right)^m\right) \quad (4.3)$$

where σ is applied stress, σ_0 is characteristic strength, m is Weibull modulus. The characteristic strength is 107 MPa at the failure probability of 63 % ($F(V) = 0.63$) and Weibull modulus is 1.5 for toucan beak trabeculae, which is typical for brittle materials ($m < 3$). From the microhardness measurement of toucan beak trabeculae, we could predict a yield stress $\sigma_y = 91$ MPa from Vickers hardness HV by using $\sigma_y = HV/3$. The difference is 15 % between microhardness and micro-tensile testing results.

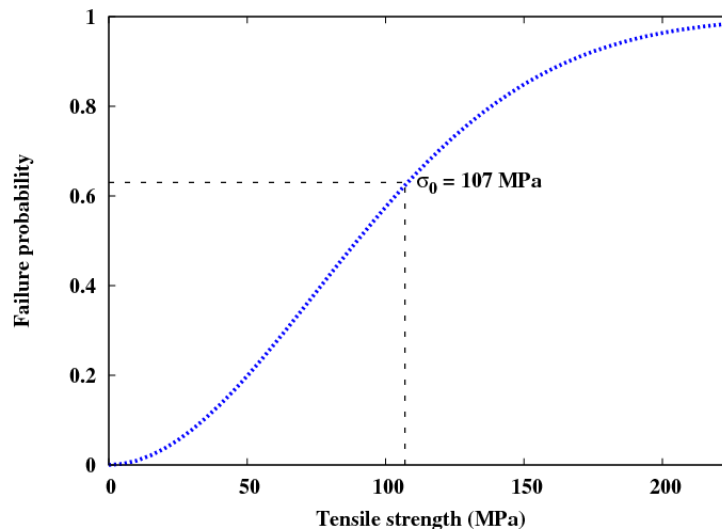


Figure 4.38: Weibull distribution (strength vs probability).

Although the tensile properties of trabeculae are of great importance when they fail by tension, in the most of cases, the trabecular bone fails by the buckling and

bending of struts. We evaluated the buckling of single trabeculae from berak foam in compression.

Elastic buckling load of beam is :

$$P = \frac{n^2\pi^2 EI}{L^2} (n = 1, 2, 3..) \quad (4.4)$$

where E is the Young's modulus, I is the moment of inertia, L is the length of beam. Since we fixed both ends, the critical load P_{cr} is given by:

$$P_{cr} = \frac{4\pi^2 EI}{L^2} \quad (4.5)$$

The corresponding critical stress σ_{cr} is:

$$\sigma_{cr} = \frac{P_{cr}}{A} = \frac{4\pi^2 EI}{AL^2} = \frac{4\pi^2 E}{(L/r)^2} \quad (4.6)$$

where A is the cross section area, $r = \sqrt{I/A}$ is the radius of gyration. The equation for critical loads is valid for ideal column and relatively long column. In this study, the column is less than slenderness ratio of 100, which leads to inelastic buckling. Figure 3d shows that the Euler curve predicted from results in tension and results from the compression testing. The compressive response of trabeculae shows lower buckling stress than the Euler curve (Fig.4.39). We found the Young's modulus of trabeculae is 1.0 GPa in compression (Fig.4.39) and the modulus is lower than the material modulus determined by our tensile testing. While the error is associated in micro-scale when we determine the mechanical properties of trabeculae, the Young's modulus is within the same order of magnitude. The predicted modulus of human

trabeculae by the Euler equation is 1.4 GPa and 1.1 GPa for dry and wet condition, respectively [203]. Our results suggest that the stiffness of bird beak trabeculae is close to the human trabeculae.

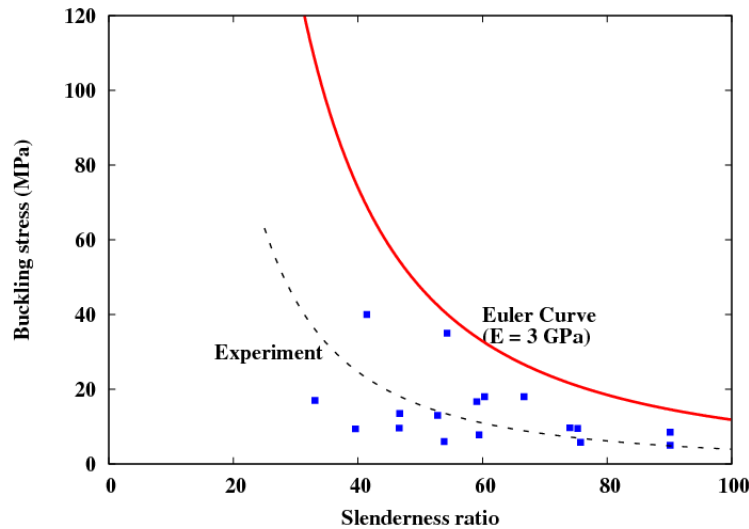


Figure 4.39: Euler curve of trabeculae.

The cortical shell of beak skull was tested in tension in 3 directions; longitudinal, transverse, 45 degree. The Youngs modulus of bony exterior ranges from 0.20 ~ 0.65 GPa and the tensile strength is 5 ~ 21 MPa in three directions. The stiffness and strength of cortical bone is substantially lower than the trabecular bone. In the case of human trabecular and cortical bone, the results are contrary to the results of toucan beak trabecular bone. The Youngs modulus of trabecular bone is significantly lower than the cortical bone [164,204]. In bird bone study, the Youngs modulus of cortical bone of Emu is about 25% lower than human bone [205]. The obtained material parameters of trabeculae and cortical shell will be used for FEM calculation.

4.4.5 Gibson-Ashby Constitutive Models

Relative density of the toucan foam was described by geometrical configuration. The thickness and length of the foam was measured from scanning electron micrographs. The weight of the thin outer shell of foam is measured by digital mass measurement allowed to measure until 10^{-4} g. The relative density of the toucan foam is described by following equation.

$$\frac{\rho^*}{\rho_s} = 1.1 \left(\frac{t}{l} \right) \quad (4.7)$$

From this equation, the density of the trabecula can be predicted. The density of the toucan trabecula was approximately 0.5 g/cm^3 . This result also matched with measured density of the trabeculae.

Plastic collapse strength and plastic indentation of foam data [167, 171–174] with toucan data were plotted in Figure 4.40(a). Table 4.3 shows parameters we obtained from toucan foam in compression. The ratio of the volume is $\phi \approx 1$ in toucan foam. Parameter p_0 and p_{at} are also identical in this case. Consequently, equation 2.8 became following equation.

$$\frac{\sigma_{pl}^*}{\sigma_{ys}} = 0.3 \left(\frac{\rho^*}{\rho_s} \right)^{3/2} \quad (4.8)$$

This equation is identical to equation for open cell. The relative density of the toucan foam and hornbill foam is approximately 0.09 and 0.1, respectively, from experimental data. The yield stress $\sigma_{ys} = 91 \text{ MPa}$ is estimated from microindentation ($H \approx 3\sigma_y$). Likewise, the yield stress of hornbill foam is estimated to be $\sigma_{ys} = 128 \text{ MPa}$. The relative yield strength of toucan foam ranges from 7×10^{-4} to 3×10^{-3} . When plastic collapse occurs, the stress of membranes can be ignored. The closed cells behave like open cells in toucan foam. In fact, from nanoindentation data, a hardness and

reduced Young's modulus of the membranes is lower than the trabeculae (not mentioned in this paper).

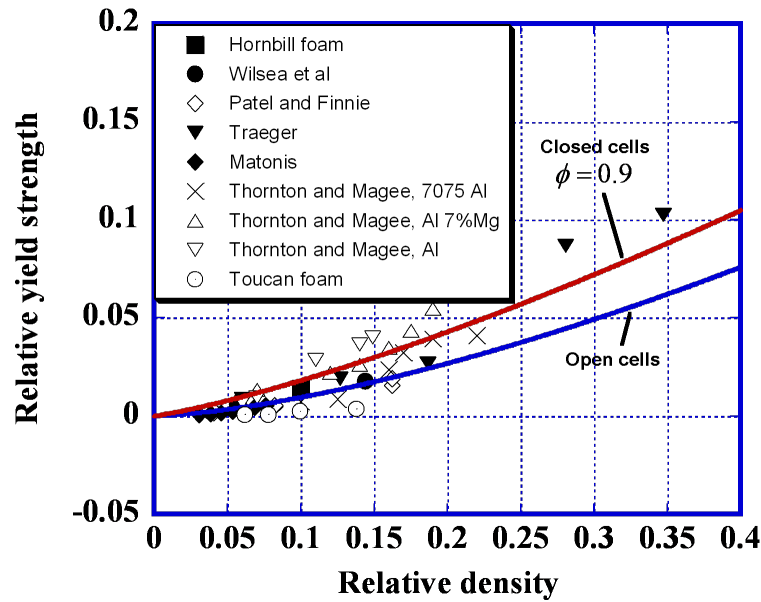
Table 4.3: Model parameters of toucan foam

Toucan foam	Density (g/cm³)	Yield strength (MPa)	Relative density	Relative strength
1	0.031	0.065	0.0618	0.00071
2	0.039	0.080	0.078	0.00087
3	0.050	0.230	0.01	0.0025
4	0.070	0.330	0.14	0.0036

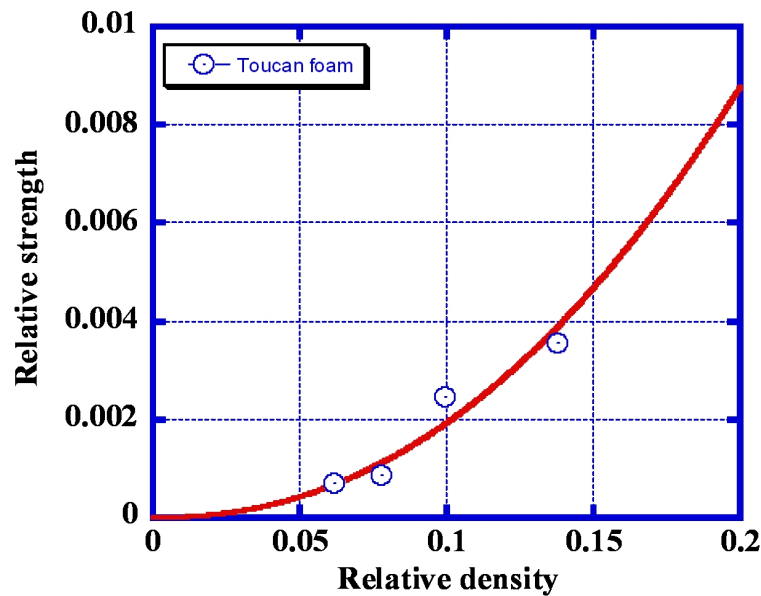
While the relative strength of toucan foam is relatively lower than other ceramics and polymeric materials, it has good agreement with the open cell model. Figure 4.40(b) shows that normalized strength and the relative density of the toucan foam are plotted. The relationship was established by following power-law equation.

$$\frac{\sigma_{pl}^*}{\sigma_{ys}} = 0.29 \left(\frac{\rho^*}{\rho_s} \right)^{2.2} \quad (4.9)$$

Although this curve does not have enough data for the toucan foam, this curve best describes crushing behavior of the toucan foam for now. The relative strength of the foam clearly increased with density of the foam.



(a)



(b)

Figure 4.40: (a) Comparison data normalized relative strength $\sigma_{pl}^*/\sigma_{ys}$ plotted relative density. Lines represent open cell and closed cell foams;(b) Relative strength vs Relative density for toucan foam.

4.4.6 Beak Foam

The mechanical performance of foams depends on its density. The mechanical behaviors of hornbill and toucan foams have similarities; viscoelastic collapse preceded the viscoplastic collapse. We could not confirm the mechanical role of the membranes as a closed-cell system. The toucan foam seems to behave like open cell even though its appearance is closed cell, and there is no contribution of internal gas in this study. The influence of the membranes might be very small, however, we have little data to judge this influence. If animals are alive, the contribution would be significant with hydrated trabeculae. The compressive behavior of toucan and hornbill foams should be similar to cancellous bone. There are similarities in structure and compositions and it should reflect on the mechanical performance. However, the beak foams failed in more brittle manner compared to cancellous bone [166]. This would be related to the dessicated trabeculae and bigger cell size of beak foam. The effect of dessication has been discussed by Gibson [18].

While crushing strength of the toucan foam is relatively small compared to that of the shell, compression test demonstrates that the foam contributes to increase the level of crushing strength. We employed the model introduced by Hanssen et al. [56]. There are differences between the model and experimental results due to geometrical differences and innate defects of the beaks. By this model, we first modeled the synergistic effect of the shell and foam of toucan beak. The model seems valid for the toucan beak. We still need to do more experiments to confirm the validity.

The wide variation in elastic modulus of trabeculae has been reported in a number of literatures, varying from 1 GPa to 19 GPa in tension [162–165, 201]. Lucchinetti et al. have discussed the limitations and error sources associated with mechanical testing in microscale [162]. Seki et al. [202, 206] found that the reduced Young's modulus of toucan trabeculae from nanoindentation is 12.7 GPa. The high Young's modulus attributes by the size effect and mineral interactions.

4.5 Mechanical Functions of Bird Beaks

4.5.1 Synergism of Bird Beak

Figure 4.41 shows compressive stress-strain curves of shell+foam, foam-filled shell of toucan beak. After reaching a maximum, the stress level of shell and foam filled shell drops significantly because of global buckling. The foam core increases the stress level of foam filled shell and prevents local buckling. As a result, the stress level of foam-filled shell is higher than superposition of stress of shell and foam. This effect is referred to be "synergism" between foam and shell. Because of the synergism, energy absorption capacity of the beak significantly increases.

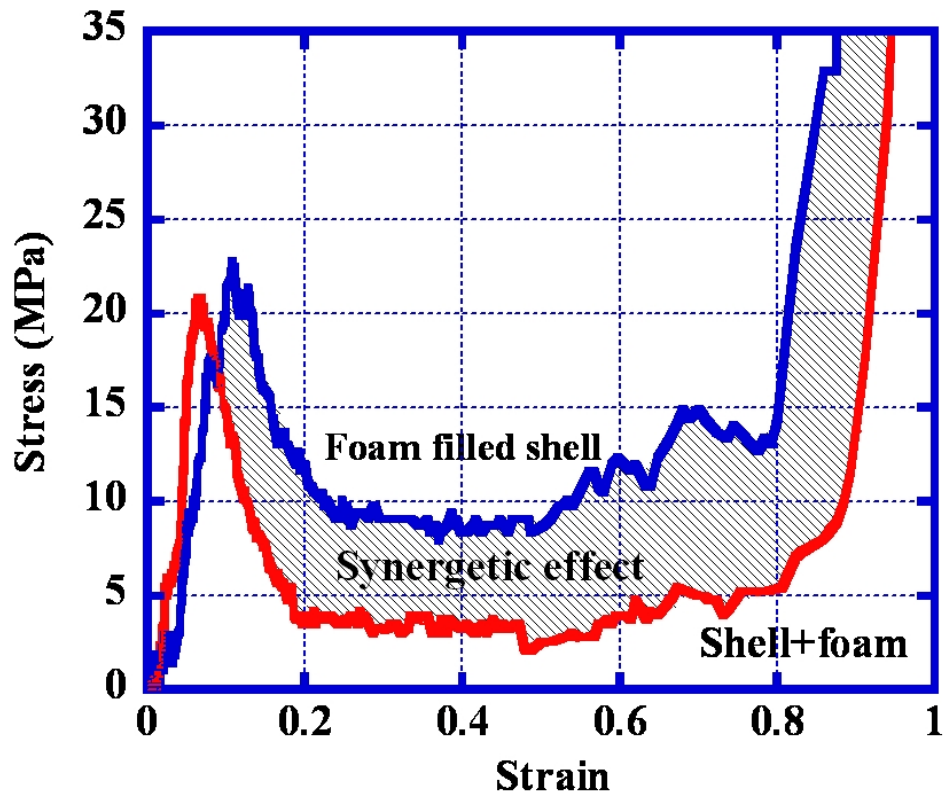
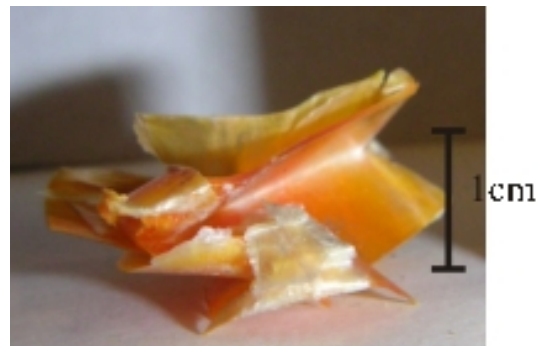
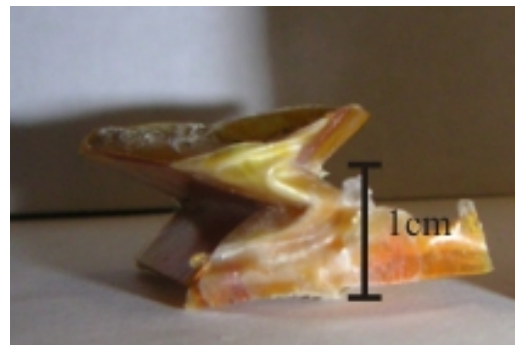


Figure 4.41: Stress-strain curves, shell+foam and foam-filled shell (toucan).

Figure 4.42 shows the picture of the crushed shell without foam and with foam. The shell deforms into an irregular shape and fractures at different point of shell when shell is not supported by foam. The deformation pattern of shell with foam was relatively symmetric. The foam stabilizes the deformation pattern of the shell and prevents the irregular buckling. The densification strain of non-foam filled shell was 0.88, while that for foam filled shell was 0.8. This demonstrates that there is a decrease of densification strain for the foam filled shell.



(a)



(b)

Figure 4.42: Pictures of compressed specimens;(a) toucan beak shell;(b) toucan foam filled shell.

We used the model developed by Hanssen et al. to estimate the average force

and densification strain of the toucan beak [56,57]. The model parameters of toucan beak is calculated from experimental data, shown in Table 4.4. The parameters are used for equations 2.9 and 2.11. Figure 4.43 shows a comparison of the prediction and experimental data. The average model force is higher than the experimental average force and there is 17 % difference in densification strain. The difference is due to the geometry and imperfection of the beak sample.

Table 4.4: Model parameters of toucan beak

Model parameters	
σ_0	40MPa
$\sigma_{0.2}$	30MPa
σ_u	50MPa
σ_f	0.2MPa
b	23mm
h	0.48mm
b_m	22.5mm
b_i	20.0mm
C_{avg}	5
F_{avg}^{mo}	684N
F_{avg}^{ex}	574N
D_S^{mo}	0.67
D_S^{ex}	0.88

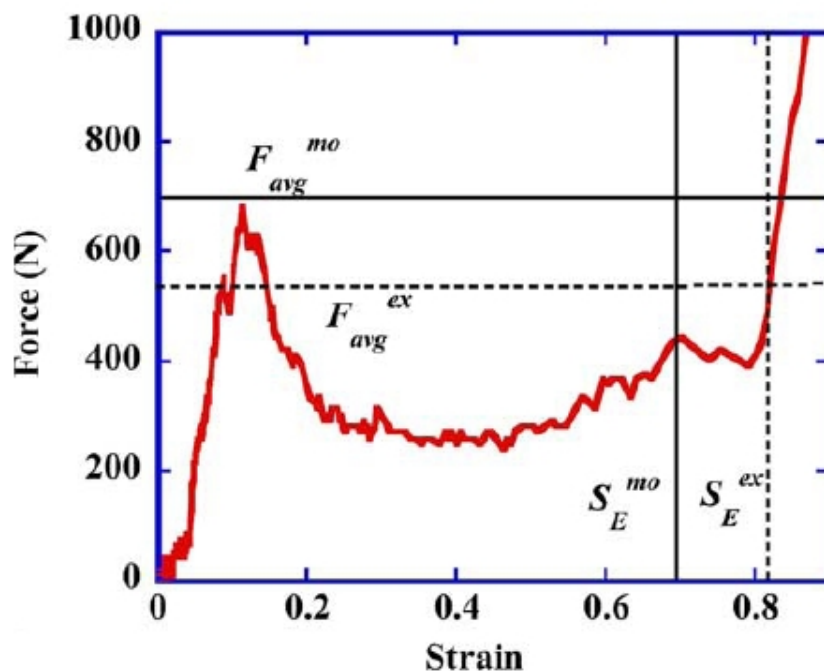


Figure 4.43: Comparison of compressive response of foam-filled shell between experiment and model. The model is indicated by black lines (F_{avg}^{mo} and S_E^{mo}) and experimental results are indicated by black dotted lines (F_{avg}^{ex} and S_E^{ex}).

4.5.2 Stability Analysis

Gibson and Karam categorized the design of sandwich structure by radius to thickness ratio [58]. Figure 4.44 shows radius to thickness ratio of biological and engineering cylindrical sandwich structures. The ratio of typical biological and civil structures range from 10 to 100 while other engineering cylindrical structures group is within the range of 100 to 10000. The sandwich design of biological structure is limited to low radius to thickness ratio due to its functionality.

Karam and Gibson [58, 207] and Gibson et al. [16] analyzed the elastic stability of the porcupine quill, a cylindrical shell with a foam core. The foam core acts as

elastic foundation, resisting the bending of the shell. The core increases the local buckling resistance of the thin shell.

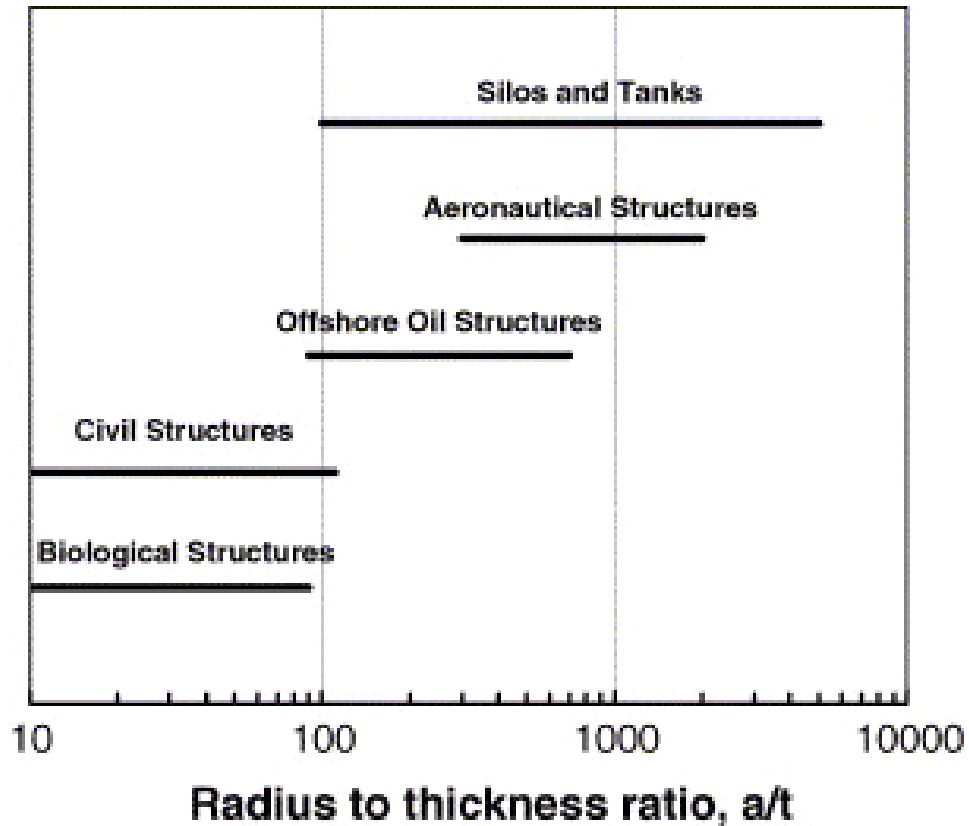


Figure 4.44: Radius to thickness ratio a/t for typical engineering cylindrical structures (from Karam and Gibson [58]).

4.5.2.1 Closed-Cell Foam

Karam-Gibson model can be applied to the present case. It is interesting to note that Karam and Gibson [58] eliminated the central part of the cellular core, since they reasoned that it does not contribute significantly to the enhancement of the stability. This is exactly the configuration inside the toucan beak, as sketched in

Figure 4.45. The core is indeed hollow. The Karam-Gibson analysis is based on a cylindrical beam. Figure 4.45 shows the cross section of the beak, with characteristic dimensions. We make a conversion into a cylindrical beam, shown in Figure 4.45, with dimensions shown: diameter, $2a = 35$ mm and thickness, $\delta = 0.5$ mm, yielding $a/\delta = 35$. This ratio is in the range given by Gibson et al. [16] for biological materials. Karam and Gibson [58] analyzed two loading configurations, shown in Figure 4.45 (c) and (d): compressive loading and bending.

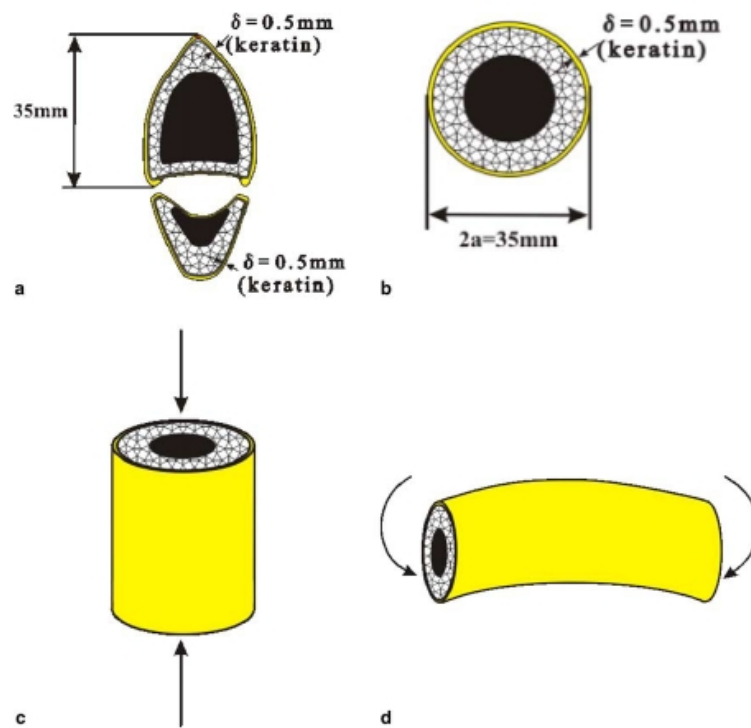


Figure 4.45: (a) Cross section of top and bottom portion of beak;(b) equivalent circular section for stability analysis;(c) equivalent beam subjected to compression and (d) equivalent beam subjected to bending.

In order to apply the Karam-Gibson equations, it is necessary to estimate the

relative Young's modulus of the foam. This is accomplished through the following Gibson Ashby [55] equations:

$$\frac{E^*}{E_s} = C_1 \left(\frac{\rho^*}{\rho_s} \right)^2 \quad (4.10)$$

Eq. 4.10 applies for open cells. The value of C_1 is approximately 1. For closed cell foams,

$$\frac{E^*}{E_s} = \phi^2 \left(\frac{\rho^*}{\rho_s} \right)^2 + (1 - \phi) \frac{\rho^*}{\rho_s} + \frac{P_0(1 - 2\nu^*)}{E_s(1 - \rho/\rho^*)} \quad (4.11)$$

where ϕ is the fraction of foam consisting of the membranes, ν^* is the Poisson ratio for the foam, and P_0 is the atmospheric pressure ($= 10^{-4}$ GPa), E^* is Young's modulus of foam, E_s is Young's modulus of solid.

Karam and Gibson [58] expressed the maximum (buckling) load (in compression) and moment (in bending) in terms of the maximum values. They assumed that both foam and solid had the same Poisson ratio: 0.3. They compared equivalent beams having the same weight and outer diameter: (a) entirely concentrated in the external shell and (b) distributed between the external shell and cellular core. Hence, their calculations indicate the relative increase in load and moment bearing ability, at the same weight. For axial loading,

$$\frac{Pr_{cr}}{(P_0)_{eq}} = \frac{\left[1 + 5 \frac{\lambda_{cr}}{\delta} \frac{E^*}{E_s} \frac{\rho^*}{\rho_s} \left(1 - 2.5 \frac{\lambda_{cr}/\delta}{a/\delta} \right) \right] f}{0.605 \left[1 + 5 \frac{\lambda_{cr}}{\delta} \frac{\rho^*}{\rho_s} \left(1 - 2.5 \frac{\lambda_{cr}/\delta}{a/\delta} \right) \right]^2} \quad (4.12)$$

For bending, two values are determined by Karam and Gibson [58]: the Brazier moment, which is the maximum value of the bending moment, and the buckling moment, corresponding the actual folding of the structure. They are given, respectively, by the following equations:

$$\frac{M_{Br}}{(M_{Br})_{eq}} = \frac{\left[1 + 1.747 \left(\frac{a}{\delta}\right)^3 \frac{E^*}{E_s} \frac{5\lambda_{cr}/\delta}{a/\delta} \left(2 - \frac{5\lambda_{cr}/\delta}{a/\delta}\right)\right]^{1/2}}{\left[1 + 5 \frac{\lambda_{cr}}{\delta} \frac{\rho^*}{\rho_s} \left(1 - 5 \frac{\lambda_{cr}/\delta}{2a/\delta}\right)\right]^2} \times \frac{\left\{1 + \frac{5}{4} \frac{\lambda_{cr}}{\delta} \frac{E^*}{E_s} + 0.0095 \frac{a}{\delta} \frac{E^*}{E_s} \left[1 - \left(1 - \frac{5\lambda_{cr}/\delta}{a/\delta}\right)^4\right]\right\}}{1 + \frac{5}{4} \frac{E^*}{E_s} \frac{\lambda_{cr}}{\delta}} \quad (4.13)$$

The buckling moment, M_{1b} , is given by (Eq. (35) from Karam and Gibson [58])

$$\frac{M_{1b}}{(M_{1b})_{eq}} = \frac{\left(1 + 1.25 \frac{E^*}{E_s} \frac{\lambda_{cr}}{\delta}\right) \left(1 + \frac{0.12 \frac{E^*}{E_s} \frac{\lambda_{cr}}{\delta}}{1 + 1.25 \frac{E^*}{E_s} \frac{\lambda_{cr}}{\delta}} - \frac{3}{2} \zeta\right) f}{0.312 \left[1 + 5 \frac{\lambda_{cr}}{\delta} \frac{\rho^*}{\rho_s} \left(1 - 2.5 \frac{\lambda_{cr}/\delta}{a/\delta}\right)\right]^2 (1 - \zeta)} \quad (4.14)$$

The parameter λ_{cr} represents a critical instability wavelength, which is equal to Eq. 4.15 from Karam and Gibson [58]),

$$\lambda_{cr} = \frac{\delta}{[12(1 - \nu^2)]^{1/4}} \left(\frac{a}{\delta}\right)^{1/2} \quad (4.15)$$

The parameter f is equal to Eq.4.16 from Karam and Gibson [58]

$$f = \frac{1}{12(1 - \nu^2)} \frac{a/\delta}{(\lambda_{cr}/\delta)^2} + \frac{(\lambda_{cr}/\delta)^2}{a/\delta} + \frac{2E^*/E_s}{(3 - \nu^*)(1 + \nu^*)} \frac{\lambda_{cr}}{\delta} \frac{a}{\delta} \quad (4.16)$$

The parameter ζ represents a correction for the decrease in the moment of inertia produced by the ovalization of the circular section. It is extracted from a nomograph plot (Fig. 6 from [58]).

The dimensional parameters for toucan beak can be estimated from the measurements and mechanical tests. From Figure 4.45(b), we measure from actual measurements on the cross section of the upper beak: $a/\delta = 35$. The foam-free cylindrical

shell has $a/\delta = 22$. We assume, to a first approximation, that $\nu_s = \nu^* = 0.3$. Inserting these values into Eq.4.15, we obtain,

$$\lambda_{cr} = 1.63 \quad (4.17)$$

The ratio between the Young moduli of cellular and solid material is obtained for the closed-cell geometry (Eq. 4.11). The fraction of the foam consisting of membranes is approximately equal to 0.1. This yields,

$$\frac{E^*}{E_{SF}} = 0.018 \quad (4.18)$$

However, the foam ligaments have a much higher mineralization level than the keratin shell. This is expressed in their higher Young's modulus ($E_{SF} = 12.7$ GPa, Table 4.1). In order to establish the ratio of the foam Young's modulus to that of the keratin shell, a correction needs to be introduced

$$\frac{E^*}{E_S} = \frac{E^*}{E_{SF}} \frac{E^{SF}}{E_S} = 0.018 \frac{12.7}{6.7} = 0.034 \quad (4.19)$$

This is almost twice the ratio for open cells. The parameter ζ is equal to approximately 0.005 for the toucan. Thus, this correction in Eq. 4.14 is negligible.

The same treatments can be applied to the stability analysis of hornbill beak. The dimensional parameters of hornbill beak are following; $2a = 40$ mm and thickness $\delta = 1$ mm, yielding $a/\delta = 20$. The relative density of hornbill foam is 0.1. The ratio of the foam Young's modulus to that of the keratin shell is obtained from equations 4.11 and 4.19;

$$\frac{E^*}{E_S} = \frac{E^*}{E_{SF}} \frac{E^{SF}}{E_S} = 0.01 \frac{21.1}{9.3} = 0.023 \quad (4.20)$$

Figure 4.46 and 4.47 present the Karam-Gibson predictions of the loads and moments as a function of a/δ . The range considered, from 10^0 to 10^2 , represents the actual range of ratios for biological materials [159]. The range of ratio for hornbill is from 15 to 30 and that of toucan is from 30 to 50, estimated from obtained beak samples. The results are indeed revealing. For the ratio of $a/\delta = 40$ for toucan, a mean value of the ratio measured for the toucan beak, the buckling load in compression does not significantly increase. Indeed, $P_0/(P_0)_{eq}$ for $E^*/E_S = 0.034$ is close to 1. However, the Brazier and buckling moments are significantly increased. The Brazier moment ratio is 8 to 10 and the buckling moment ratio is 2 to 3 for $a/\delta = 35$ and $E^*/E_S = 0.034$.

Similarly, the ratio of $a/\delta = 20$ for hornbill, a mean value of the ratio measured for the hornbill beak, there is a less improvement in the uniaxial buckling loading in compression than that for toucan. $P_0/(P_0)_{eq}$ for $E^*/E_S = 0.023$ is less than 1. The Brazier and buckling moments shows improvement. The Brazier moment ratio is 5 to 8 and the buckling moment ratio is $1\sim 2$ for $a/\delta = 20$ and $E^*/E_S = 0.023$.

Thus, the presence of a closed-cell foam increases the ability of the beak to resist bending moments significantly. This is the type of loading that the beak is subjected to most commonly. It is interesting to observe that the closed cell foam presents a considerable advantage over the open-cell foam. The presence of a closed-cell foam in the beak proves that the system is indeed designed for the loads encountered by beaks.

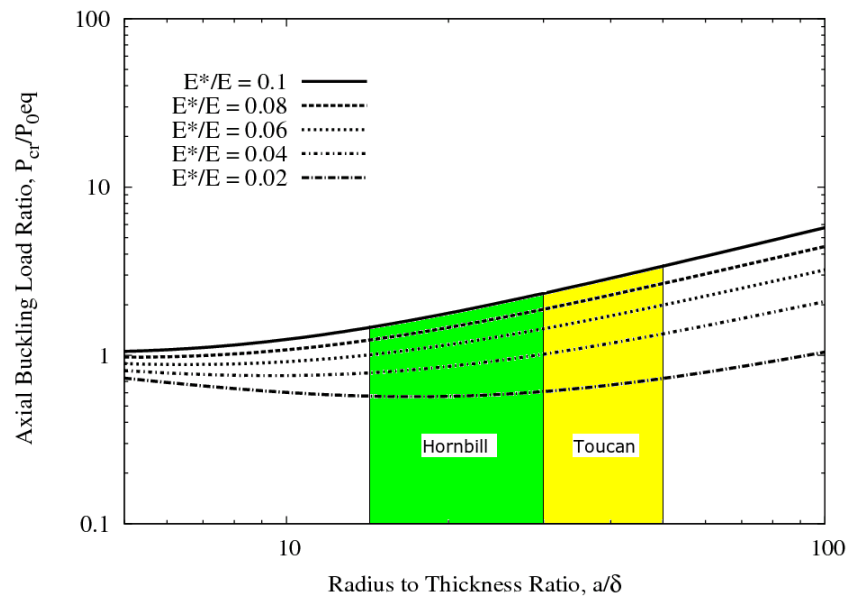


Figure 4.46: Ratio of buckling load in uniaxial compression between hollow circular shell with and without cellular core, at the same weight ($\rho^*/\rho_s = 0.1$).

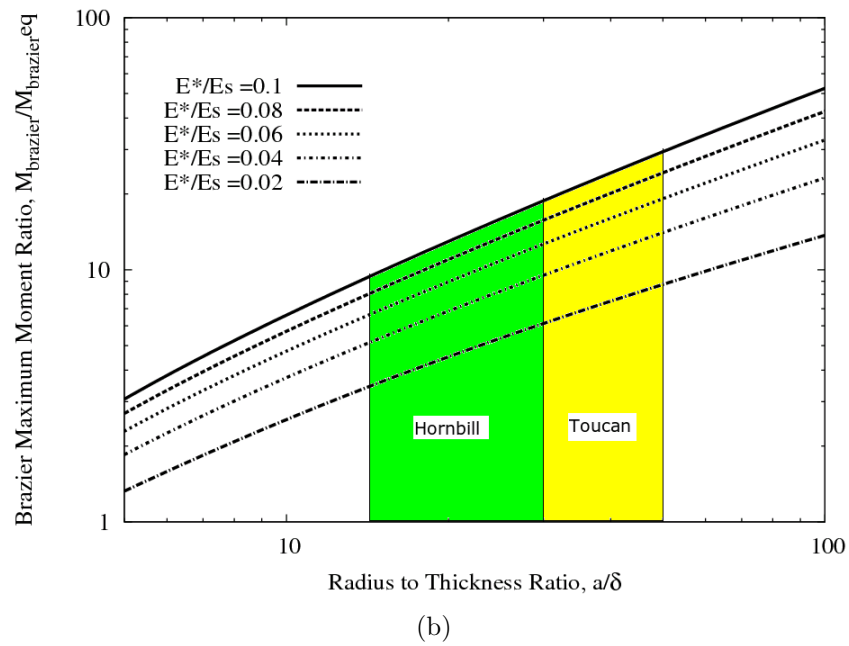
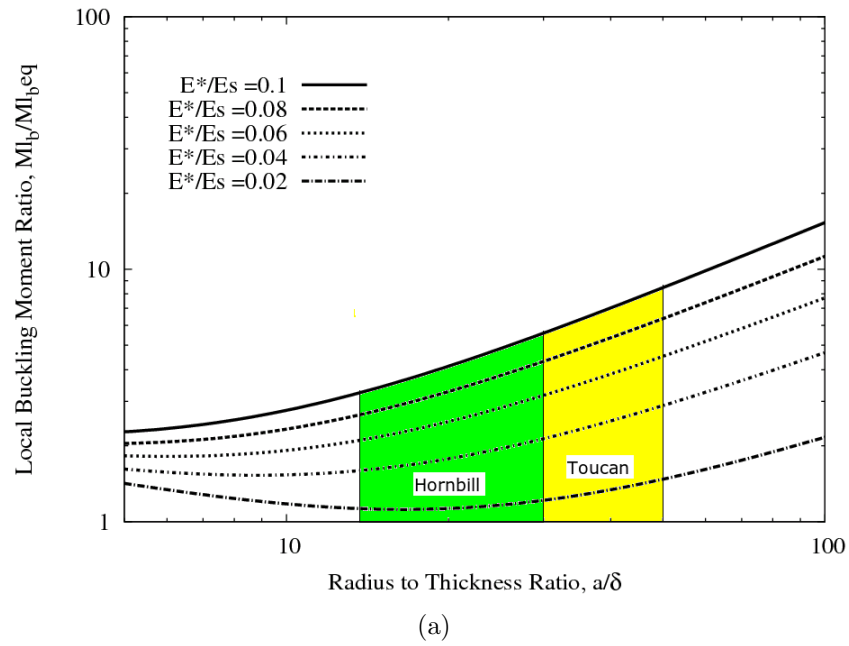


Figure 4.47: Ratio of:(a) maximum (Brazier) and (b) buckling moments between hollow cylinder shell with and without cellular core, at the same weight ($\rho^*/\rho_s = 0.1$).

4.5.2.2 Open Cell Foam

While the beak foam is structurally closed-cell configuration, the mechanical response of beak foam behaves as an open cell in dry condition, likely because many of the membranes sealing the cells are desicated and ruptured by the time of testing. Figure 4.48 presents the Karam-Gibson predictions of the loads and moments as a function of a/δ . The range considered, from 10 to 100, represents the actual range of ratios for biological materials. Ratios ranging from 15 to 30 for hornbill and from 30 to 50 for toucan were measured from obtained beak samples. The results are indeed revealing. For the ratio of $a/\delta=30\sim 50$ for toucan, the buckling load in compression actually decreases. Indeed, $P_0/(P_0)_{eq}$ for $E^*/E_S = 0.01\sim 0.02$ is close to 0.5 to 0.6. However, the Brazier moment is significantly increased. The Brazier moment ratio is 3 to 5 and while the buckling moment ratio is 0.9 to 1.5 for $a/\delta = 30\sim 50$ and $E^*/E_S = 0.015$.

Similarly, the ratio of $a/\delta = 15\sim 30$ for hornbill, $P_0/(P_0)_{eq}$ for $E^*/E_S = 0.02\sim 0.03$ is 0.7 to 0.8. The Brazier moment ratio is 3 to 6 and the buckling moment ratio is $1.5\sim 1.7$ for $a/\delta = 15\sim 30$ and $E^*/E_S = 0.02\sim 0.03$. In the open cell configuration, the beak exhibits an improvement in Brazier moment. This indicates that the cellular sandwich structure increases the maximum flexural load of the beam in dramatic manner. The improvement was not as significant as in the closed-cell configuration used in the previous analysis [202]. The Brazier moment is the most important structural parameter, because the beaks cannot be loaded beyond this point without incurring permanent damage.

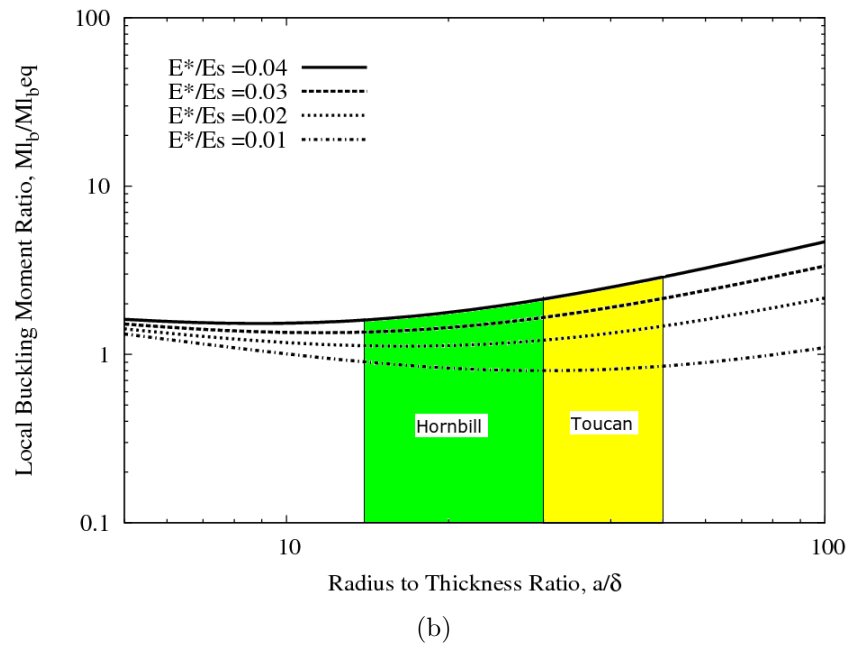
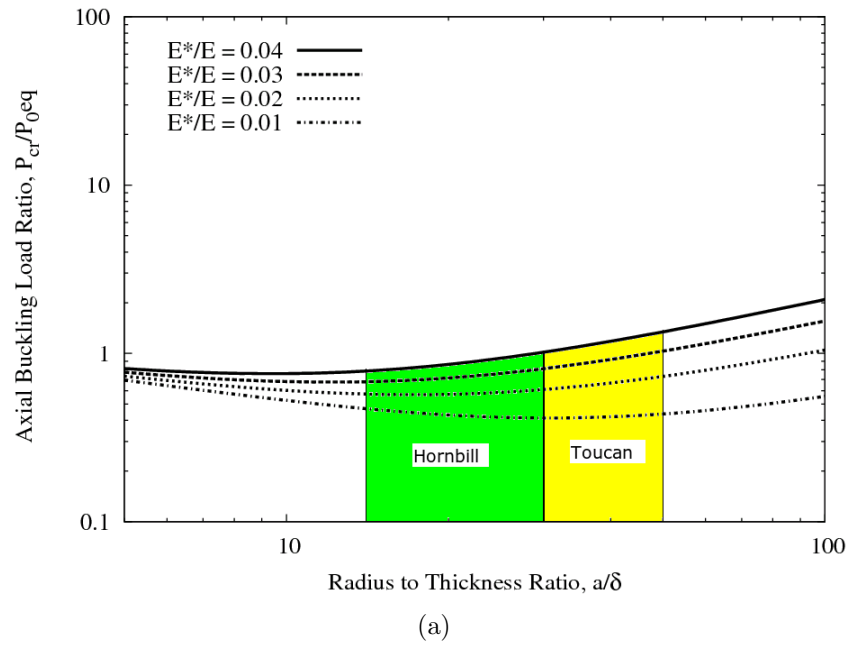


Figure 4.48: Ratio of (a) buckling load in uniaxial compression and (b) buckling moment and (c) maximum (Brazier) between hollow circular shell with and without cellular core, at the same weight ($\rho^*/\rho_s = 0.1$).

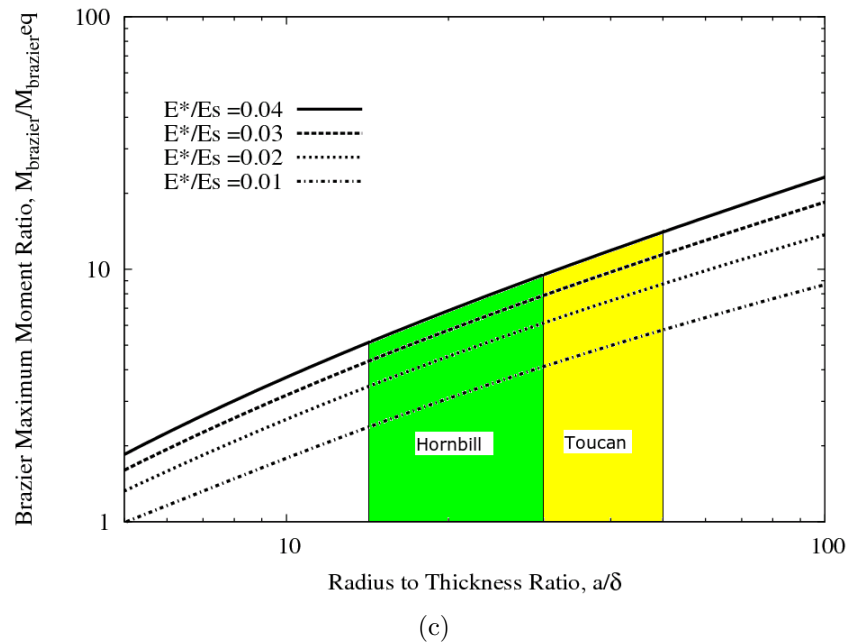


Figure 4.48: Ratio of (a) buckling load in uniaxial compression and (b) buckling moment and (c) maximum (Brazier) between hollow circular shell with and without cellular core, at the same weight ($\rho^*/\rho_s = 0.1$).

4.5.3 Optimization Analysis

In addition to the stability analysis in the previous section, Dawson-Gibson model [59, 208] was applied to evaluate toucan and hornbill beaks in uniaxial compressive loading and flexure. Dawson and Gibson [59, 208] incorporated plasticity theory into Karam and Gibson model and introduced two modes of failures; buckling failure and material failure. Because the shape of the beak is homeomorphic with a hollow cylindrical beam, we modeled the beak as such in our evaluation of toucan and hornbill optimization. We made conversion of hornbill and toucan beaks to circular beam for analysis. The stability is described by the compressive loading and bending moment ratio of cylindrical shell to cylindrical shell with hollow foam core. The shell and shell with foam core have the same weight. The transition from buckling failure to material failure in uniaxial compression is given by:

$$\left(\frac{E^*}{E_s}\right)_{P\text{-transition}} = \frac{2}{3}(1 - v_c)(3 - v_c)(\sqrt{1 - v^2}) \left(\frac{\sigma_f}{E_s}\right)^{2/3} \quad (4.21)$$

where E^* is core modulus, E_s is shell modulus, v and v_c are Poission's ratio of shell and core respectively, σ_f is failure stress of shell.

The buckling failure in uniaxial loading is described by:

$$\left(\frac{P_C}{P_H}\right)_{transition} = \frac{\sigma_f a t \sqrt{3(1 - v^2)}}{E_{SF} t_{eq}^2} \quad (4.22)$$

$$for \left(\frac{E^*}{E_s}\right)_{P\text{-transition}} > \frac{2}{3}(1 - v_c)(3 - v_c)(\sqrt{1 - v^2}) \left(\frac{\sigma_f}{E}\right)^{2/3} \quad (4.23)$$

where the equivalent thickness of the hollow cylinder t_{eq} and the thickness of the compliant cellular core t_c are:

$$t_{eq} = t \left(1 + \frac{t_c \rho^*}{2t \rho_s} \left[2 - \frac{t_c}{a} \right] \right) \quad (4.24)$$

$$t_c = 5 \left[\frac{(3 - v_c)(1 + v_c)}{12(1 - v^2)} \right]^{\frac{1}{3}} \left[\frac{E_{SF}}{E^*} \right]^{\frac{1}{3}} \quad (4.25)$$

where $v_s=v^*=0.3$. The material failure in uniaxial loading is:

$$\left(\frac{P_C}{P_H} \right)_{transition} = \frac{2.27at\sqrt{(1 - v^2)}^{(1/6)}}{\left[(3 - v_c)(1 + v_c) \frac{E_{SF}}{E^*} \right]^{2/3} t_{eq}^2} \quad (4.26)$$

$$for \left(\frac{E^*}{E_s} \right)_{P-transition} < \frac{2}{3}(1 - v_c)(3 - v_c)(\sqrt{1 - v^2}) \left(\frac{\sigma_f}{E} \right)^{2/3} \quad (4.27)$$

The transition in bending configuration is described by following equation.

$$\left(\frac{E_c}{E} \right)_{M-transition} = \frac{2}{3}(1 - v_c)(3 - v_c)(\sqrt{1 - v^2}) \left(\frac{\sigma_f}{(1 - \frac{3}{2}\zeta)E_s} \right)^{2/3} \quad (4.28)$$

where ζ is ovalization of beam at local buckling. The experimentally determined failure stress and Young's moduli of keratin and foam cores used in our calculation are listed in Table 4.5. The degree of ovalization ζ is 0.01 for toucan and hornbill beaks. The ratio of diameter of cylinder a to shell thickness t is ranging from 15 to 50 for toucan and hornbill beaks. Table 4.6 shows modulus ratio in experiments according to experimental results and predicted by the model.

Table 4.5: Material parameters of hornbill and toucan beaks

	Shell modulus (E_s GPa)	Core modulus (E^* GPa)	Failure stress (σ_f MPa)
Toucan beak	1.0	0.013	90
Hornbill beak	1.2	0.035	120

Table 4.6: Experimental and optimum modulus ratio

	Experimental results (E^*/E_s)	Compressive loading configuration (E^*/E_s)	Bending configuration (E^*/E_s)
Toucan beak	0.013	0.06	0.054
Hornbill beak	0.029	0.07	0.11

There are differences in model and experimental results. The lower modulus ratios in experimental results compared to analytical results might be associated with the sampling method for beak foam. The foam samples are fragile, and defects can be introduced from cutting and handling. Figure 4.49 illustrates a transition between buckling failure and material failure in axial loading and bending. The transitional point, from buckling failure to material failure, corresponds to the maximum optimal design of cylindrical shell with hollow foam. After the transition point, the compressive load and moment of shell over that of shell with hollow core decreases as E^*/E_s ratio increases. The modulus ratios of toucan and hornbill are considerably the higher than other synthetic sandwich composites, in Fig.4.50. It should be noted that we considered $a/t=100$ for this analysis and assumed that foam and shell are made from the same material, which we know not to be the case, however the mechanical properties of keratin shell and foam materials are within the same order. The ratio a/t of 100 is not typical for toucan and hornbill beaks; however, the proximal termini of both do achieve that ratio. This analysis shows that the toucan

and hornbill beaks achieve higher resistance to uniaxial loading compared to other synthetic materials.

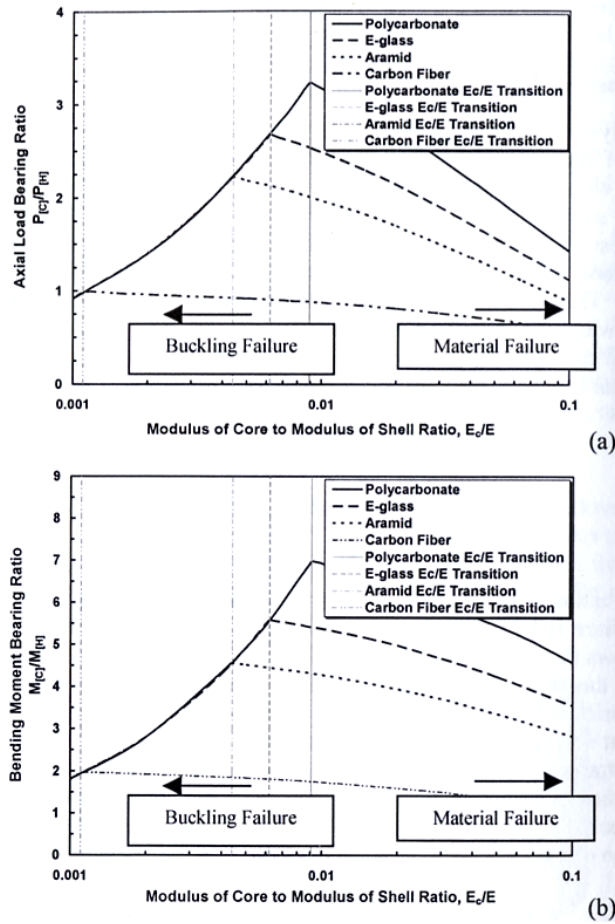


Figure 4.49: Load ratio vs modulus ratio for a range of materials ;(a)uniaxial compression; (b) pure bending (From Dawson and Gibson [59])

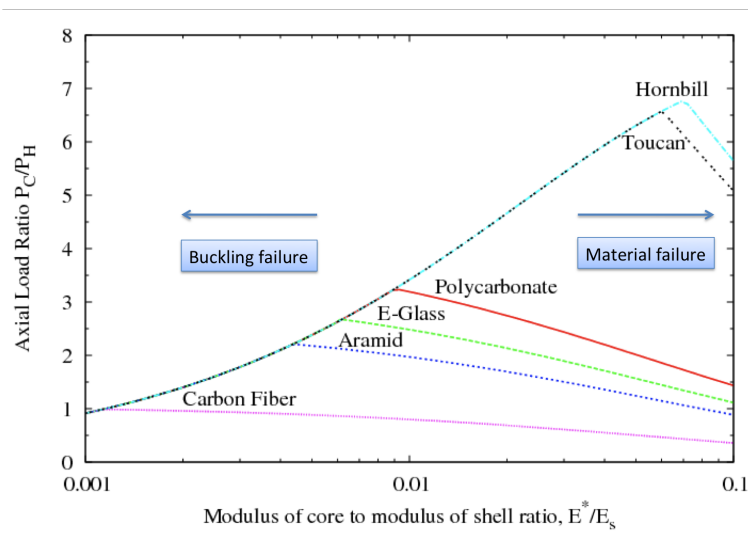


Figure 4.50: Axial load ratio vs. modulus ratio, $a/t=100$ (adapted from Dawson and Gibson [59]), transition from buckling to material failure occurs at much higher normalized axial load for toucan and hornbill beaks than for synthetic sandwich structures.

4.5.4 Bird Beak

Stability analysis of the hornbill and toucan beaks by utilizing Karam and Gibson model [58] illustrates that foam core increases the local buckling and Brazier buckling load. Axial buckling load did not show an increase of buckling resistance. This suggests that toucan beak is subjected to the local and Brazier buckling rather than axial buckling load. It is reasonable to assume that toucan and hornbill beaks have the high resistance to bending moment because the breakage of huge beak is mainly caused by the bending. The beak hollow foam core might be the most efficient core because sandwich structure with a hollow core save the weight and moreover has more energy absorption capacity than the completely filled core [209]. The beak is allowed to be hollow at proximal where the maximum bending occurs when it is

subjected to the bending.

4.5.5 Sandwich Construction of Bird Beak

We have evaluated the separate mechanical response and structure of rhamphotheca and internal foam cores. Figure 4.51 shows a variation in Young's modulus of keratinous materials plotted as Young's modulus vs density.

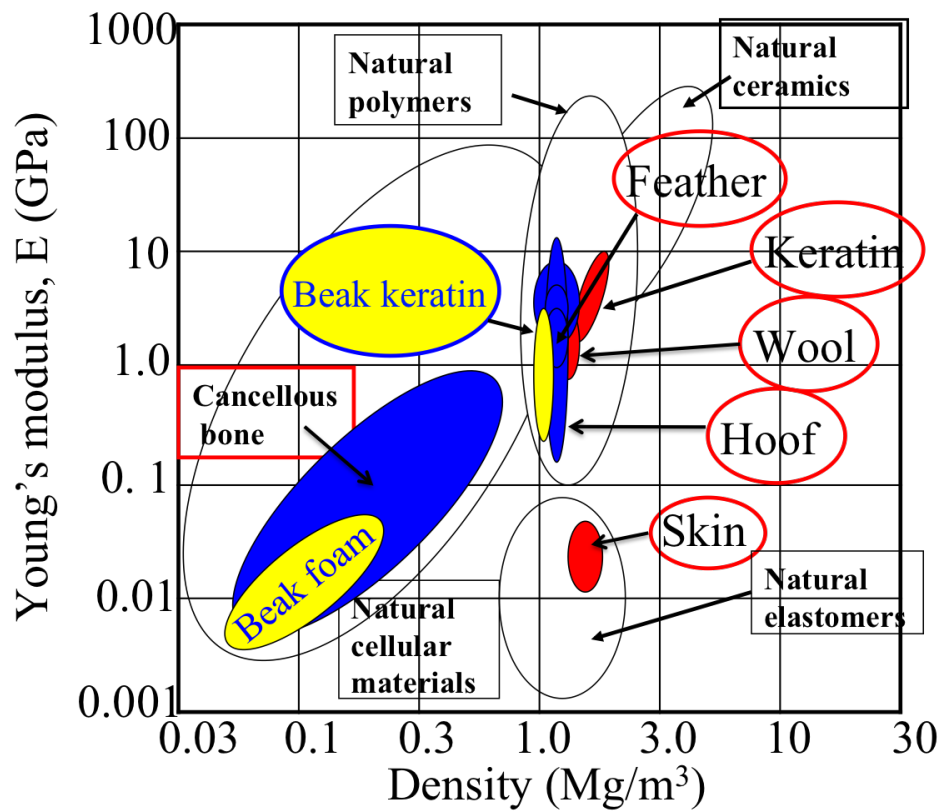


Figure 4.51: Wegst-Ashby plot showing Young's modulus as a function of density. This is simplified diagram of Fig 2.11

The density of beak keratin is ~ 1 and the Young's modulus ranges from 0.2 to 2 GPa at macroscale, including dry and wet conditions. Figures 4.52 and 4.53 shows

the sandwich structure of toucan and hornbill beaks. The beaks are covered by a biological composite of layered structure of keratin scales and supported by bony closed-cell foam. The mechanical properties of the outer shell and foam core differ in the use of properties.

Table 4.7 shows a summary of Young's modulus of the beak keratins and trabeculae. The reduced Young's modulus of beak keratins from nanoindentation is always higher than that from tensile testing due to the size effect [202, 206]. The moduli of trabeculae are almost two folds higher than that of exterior beak keratins in nanoindentation, shown in Figure 4.54. The hardness of toucan trabeculae is low in comparison to that of hornbill trabeculae; however, the hardness of hornbill trabeculae is comparable to that of avian bone [53]. The sandwich structure of bird beak is unlike the case for industrial sandwich panels that typically combine a high modulus of face skins and low modulus of foam cores for load bearing. The sandwich construction of beak is made from the low modulus of rhamphotheca and high modulus of bony foam, connected by the dermis as a glue between two entities, described by Fig. 4.54. The sandwich construction of toucan beak exhibits a synergism between the bony foam and keratin skin and increases the energy absorption [209]. The optimization of beaks is achieved by having a hollow foam. The similar sandwich construction can be observed in feather rachis. The hollow foam is inserted at the root and the tip is completely filled with foam. The tubular sandwich construction has been evaluated with a foam core and a hollow foam core in bending configuration [202]. The sandwich composite with a hollow deforms easily under low load in bending. On the other hand, the complete filled foam increases the flexural strength; however, it fails earlier at smaller deformation [209]. The advantage of a hollow foam is to increase the energy absorption capacity. Furthermore, the stability of the beak is improved in comparison with the beak shell having the same weight by having a hollow core, discussed in the previous Sections.

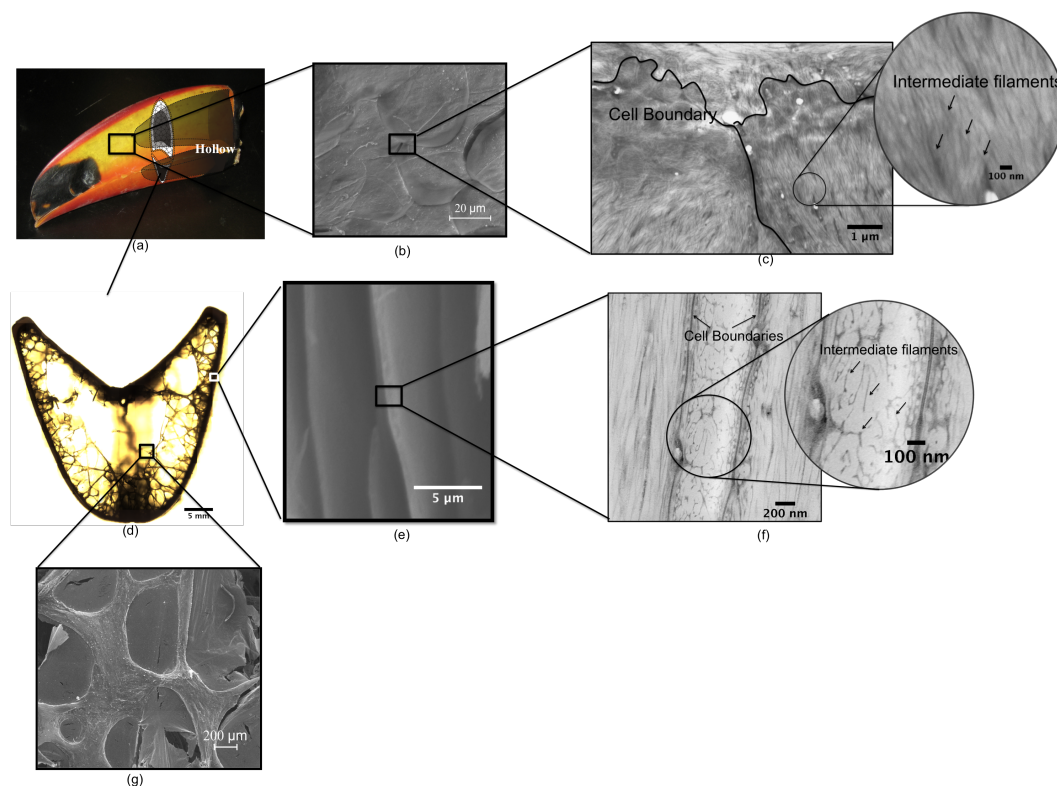


Figure 4.52: Hierarchical structure of toucan beak; (a) picture of toucan beak, hollow parts are indicated by schematics; (b) surface morphology of beak keratin by SEM; (c) keratin scale structure by TEM, intermediate filaments are indicated by arrows; (d) cross sectional mosaic of lower beak by confocal microscopy; (e) cross section of keratin exterior by SEM ; (f) TEM of cross section of beak keratin, arrows indicate intermediate filaments; (g) scanning electron micrograph of foam structure, the cells are sealed by membranes.

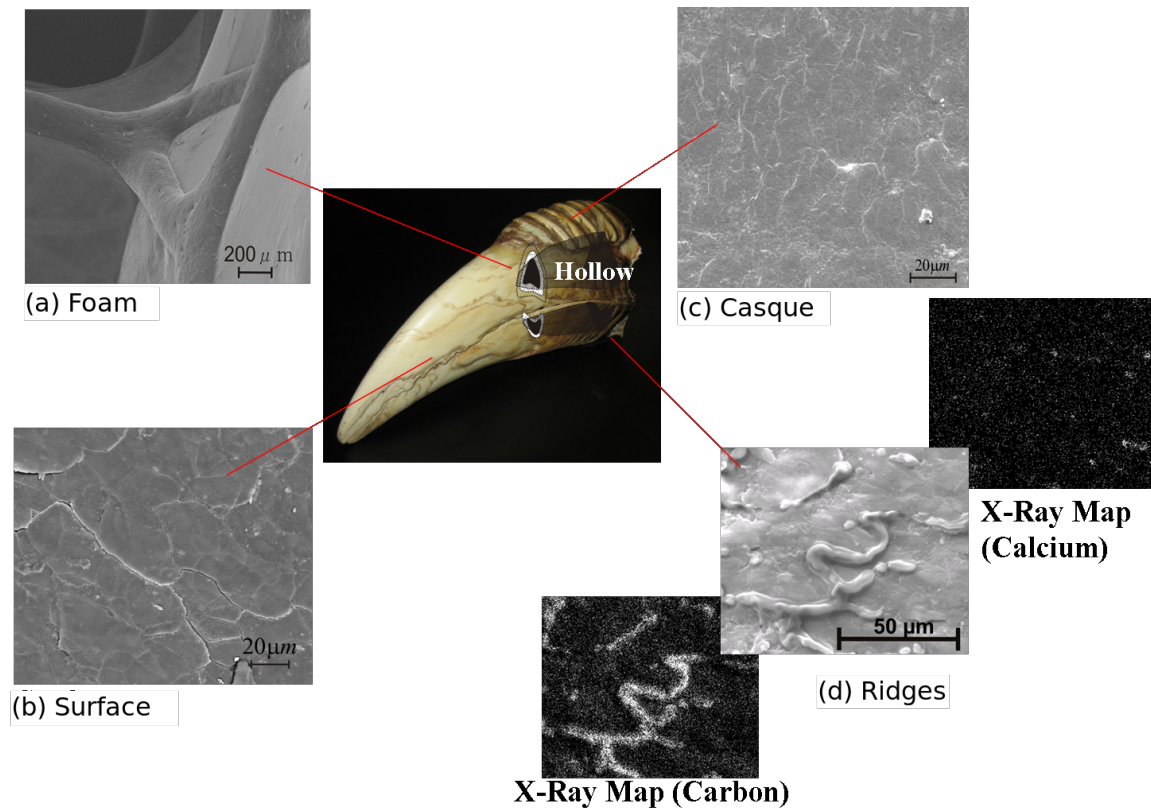


Figure 4.53: Structure of hornbill beak with scanning electron micrographs and X-ray dot map; (a) interior foam structure ;(b) structure of keratin scales;(c) structure of casque; (d) structure of ridges with X-Ray dot mappings

Table 4.7: Summary of Young's modulus of trabeculae and beak keratins

	Young's modulus (GPa)
Toucan keratin longitudinal (Tension)	1.04 ± 0.06
Toucan keratin transverse (Tension)	1.12 ± 0.13
Toucan keratin (Nanoindentation)	6.5 ± 0.78
Toucan trabecula (Tension)	3.0 ± 1.87
Toucan trabecula (Compression)	1.0
Toucan trabecula (Nanoindentation)	12.7 ± 1.5
Hornbill keratin longitudinal (Tension)	1.22 ± 0.34
Hornbill keratin transverse (Tension)	0.813 ± 0.06
Hornbill keratin (Nanoindentation)	9.3 ± 1.8
Hornbill trabecula (Nanoindentation)	21.4 ± 5.3

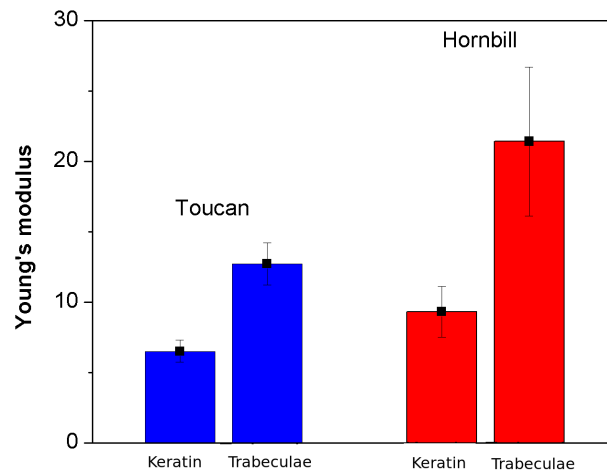


Figure 4.54: Comparison of Young's modulus between keratin and trabeculae;(a) toucan; (b) hornbill.

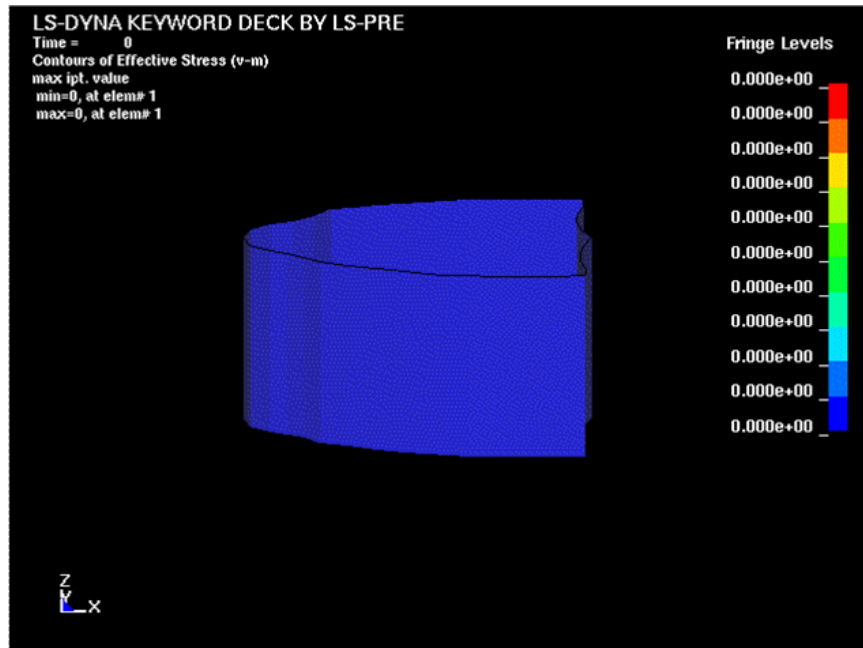
4.6 Computational Modeling

4.6.1 Finite Element Analysis

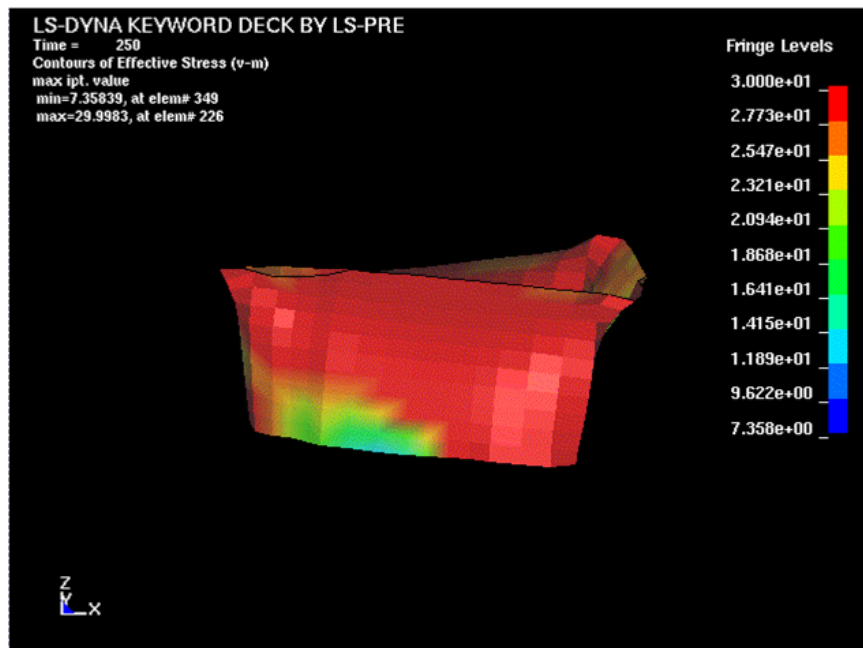
Finite element analysis of the toucan beak using LS-DYNA [210] was performed to characterize the deformation pattern. Approximately 14,000 shell elements were used, and the stress strain response was modeled with isotropic plasticity with linear hardening,

$$\sqrt{\frac{3}{2}\sigma' : \sigma'} = \sigma_y + h\epsilon^p \quad (4.29)$$

where σ_y is the initial yield stress, h is the hardening exponent, and ϵ^p is the equivalent plastic strain. For the calculation shown here, E is 1.4 GPa, σ_y is 30 MPa, and h is 1 MPa. This corresponds to a good match with the experimental results. The collapse of the shell, loaded in compression, is shown in Figure 4.56. The shell (Figure 4.56(a)) starts to deform and the applied stress folds it to the Figure 4.56(b) condition. The shell is fully buckled in Figure 4.56(c) and is completely crushed in Figure 4.56(d). The mechanical response will be discussed later.

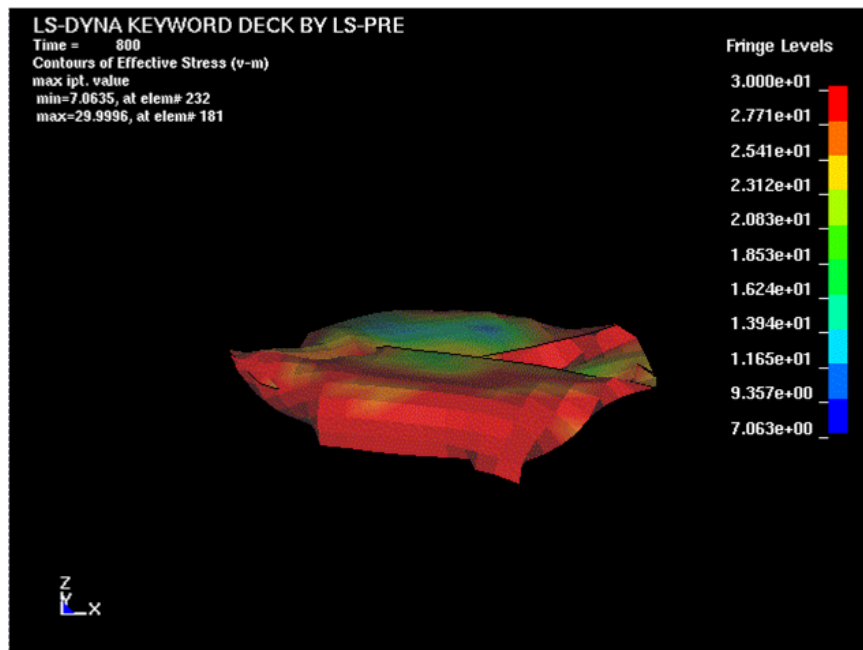


(a)

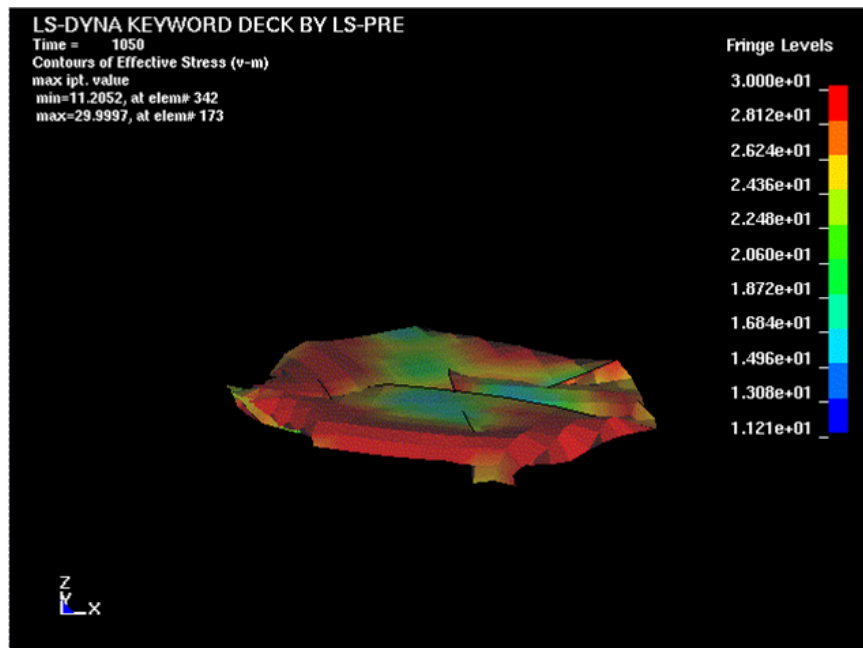


(b)

Figure 4.56: FEM simulation of the beak shell under compression testing;(a) FEM model of shell; (b) onset of folding;(c) buckled shell;(d) completely collapsed shell.



(c)



(d)

Figure 4.56: FEM simulation of the beak shell under compression testing;(a) FEM model of shell; (b) onset of folding;(c) buckled shell;(d) completely collapsed shell.

The foam was modeled with 8000 solid elements using a crushable foam model, material model 63 in LS-DYNA [210]. Figure 4.57(a) shows initial condition of the foam having a hollow region in the center. This shape reproduces the cross section of the beak. The deformed foam expands in the lateral direction, which produces shrinkage of hollow center, shown in Figure 4.57(b). The crushable foam model used tabulated data from the actual compression tests to specify the nominal flow stress as a function of the volumetric strain in compression. The tabular data are also used in tension until the material reaches a tension cut-off, after which it is elastic-perfectly-plastic. Initially the stress is updated elastically each time step,

$$\sigma_{ij}^{Tr} = \sigma_{ij}^n + E\epsilon_{ij}\Delta t \quad (4.30)$$

The three principal stresses, $\hat{\sigma}_{ij}^{Tr}$ are obtained by an eigenvalue analysis, indicates a principal value. If a principal value exceeds the yield stress, it is scaled back appropriately,

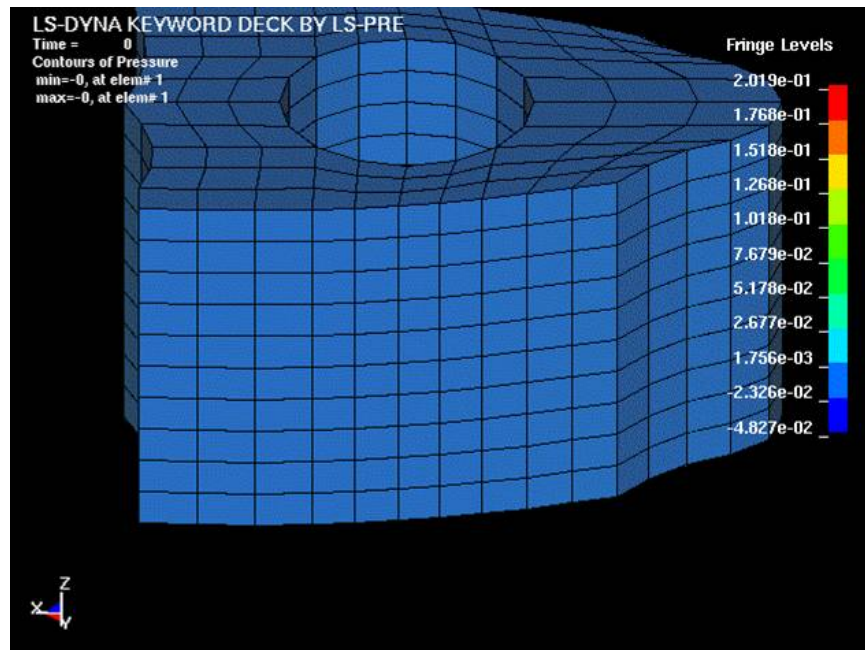
$$\text{If } \sigma_y < |\sigma_{ij}^{Tr}| \text{ then } \hat{\sigma}_i^{n+1} = \sigma_y \frac{\hat{\sigma}_i^{n+1}}{|\hat{\sigma}_i^{n+1}|}, \text{ otherwise, } \sigma_{ij}^{n+1} = \sigma_{ij}^{Tr} \quad (4.31)$$

If plastic flow has occurred, the final stress tensor is

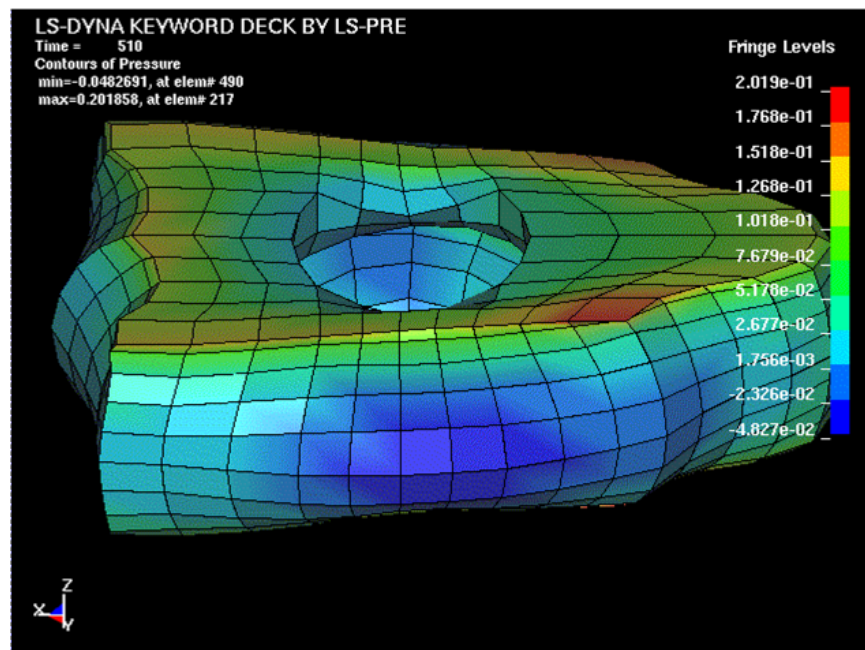
$$\sigma_{ij}^{n+1} = \sum_{i=1,3} \hat{\sigma}_i^{n+1} \Lambda_i \otimes \Lambda_i \quad (4.32)$$

where Λ_i is the i -th eigenvector, otherwise the final stress is the stress updated elastically. For the current study, Young's modulus is 5.6×10^{-3} GPa, and the flow stress is 0.1 MPa.

Figure 4.59(a) shows force-displacement curves of shells subjected to uniaxial compression testing. They were calculated by LS-DYNA; an experimental curve for a thickness of 0.6 mm is given for comparison. The compressive collapse of the shell was calculated for three thicknesses: 0.5, 1, and 2 mm. This is shown in Figure 4.59(a) where the FEM and experimental results are compared. The maximum load



(a)

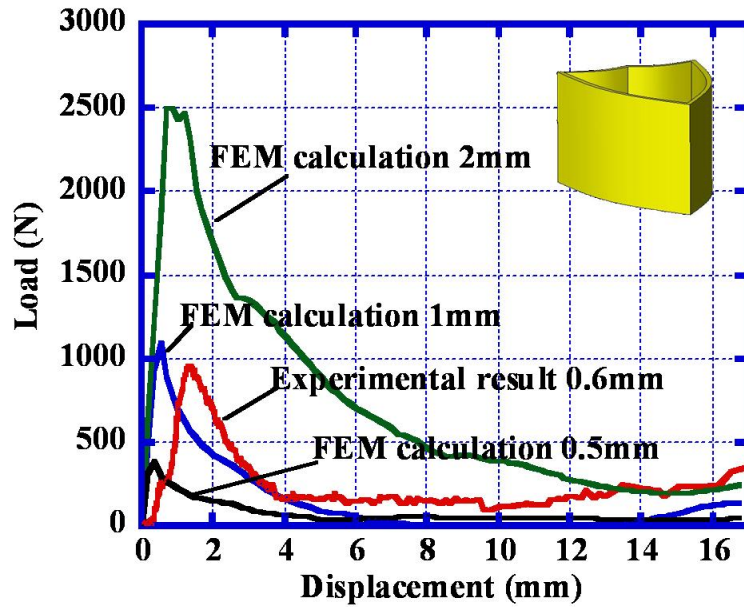


(b)

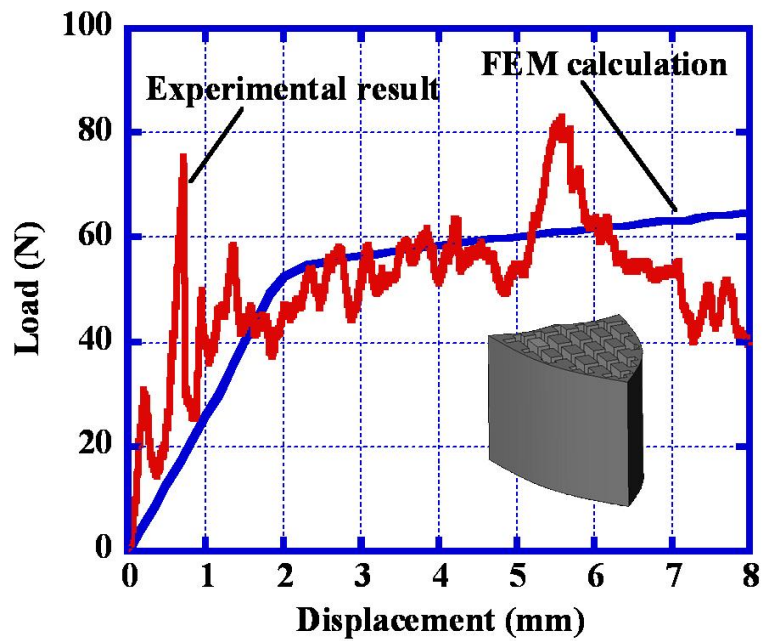
Figure 4.57: FEM simulation of the beak foam under compression testing;(a) undeformed foam;(b) deformed foam.

is followed by a rapid decrease due to buckling. This computed response is analogous to the experimental result (shell thickness of 0.6 mm). The FEM response shows a higher stiffness due to the lack of the imperfections and curvature. The experimentally determined and calculated responses of foam are shown in Figure 4.59(b). The experimental results contain a larger number of spikes due to the individual fiber fracture events, while the FEM computation is smooth. The calculated and experimental results show a good match.

Figure 4.59(c) shows the combined shell + foam response. The shell thickness is 0.4 mm for both, a value slightly lower than the one in Figure 4.59(a). The simulation shows that the presence of the foam prevents local buckling and therefore the load drops after the maximum is reduced. Thus, the stability of the structure is enhanced. This is a unique advantage of the sandwich structure. The foam corresponds to approximately 21% of the total weight. The calculations and experiments demonstrate that the deformation performance of the shell can be improved by using a foam core.

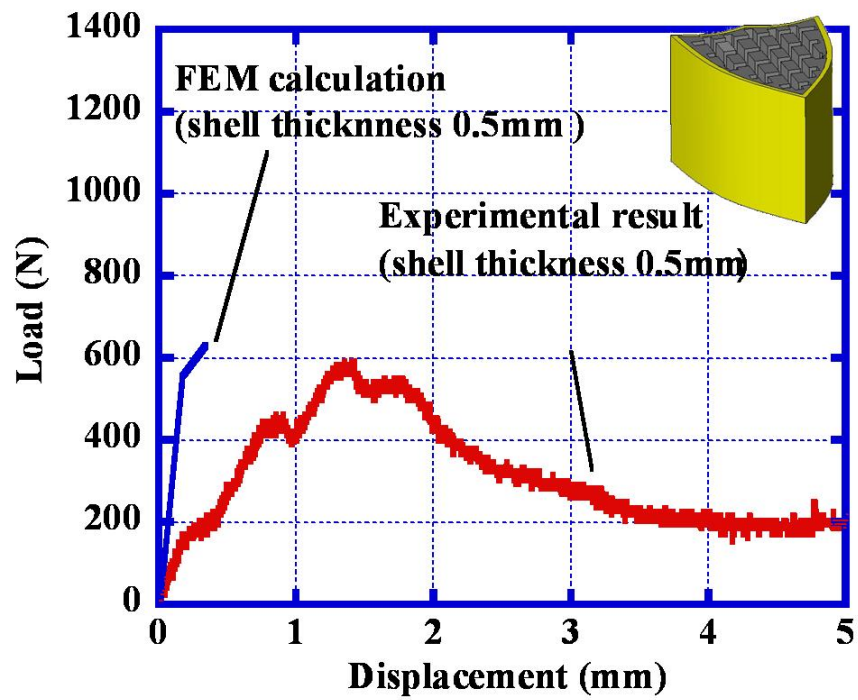


(a)



(b)

Figure 4.59: Comparison between load vs. displacement curves from FEM calculation and experimental test results for thickness of 0.6 mm; (a) shell compression; (b) foam compression; (c) shell + foam compression (shell thickness: 0.4 mm).



(c)

Figure 4.59: Comparison between load vs. displacement curves from FEM calculation and experimental test results for thickness of 0.6 mm; (a) shell compression; (b) foam compression; (c) shell + foam compression (shell thickness: 0.4 mm).

4.6.2 Computed Tomography

Computed Tomography is widely used as medical imaging techniques. We can extract 3D volumetric data of human body. Especially, the studies of cancellous or trabecular bone such as evaluation of bone mineral density, structure, and mechanical properties, by computed tomography abound [211–215]. In present study, we used micro-CT for evaluating the structure of beak skull, extracting 3 dimensional volumetric configuration, and further establishing the relationship between the mechanical properties and structure of bird beaks.

Figure 4.60 shows bird beaks scanned by micro-CT with three planes; frontal, sigittal, and transverse planes. We processed 435 images data set of toucan and hornbill beak skull with a free software, MicroView (GE). The xyz planes show scanned toucan beak skull and hornbill beak skull with keratin exterior, shown in Fig.4.60 (a) and (b). We will describe the methods that extract 3 dimensional volumetric data of bird skulls in next sections.

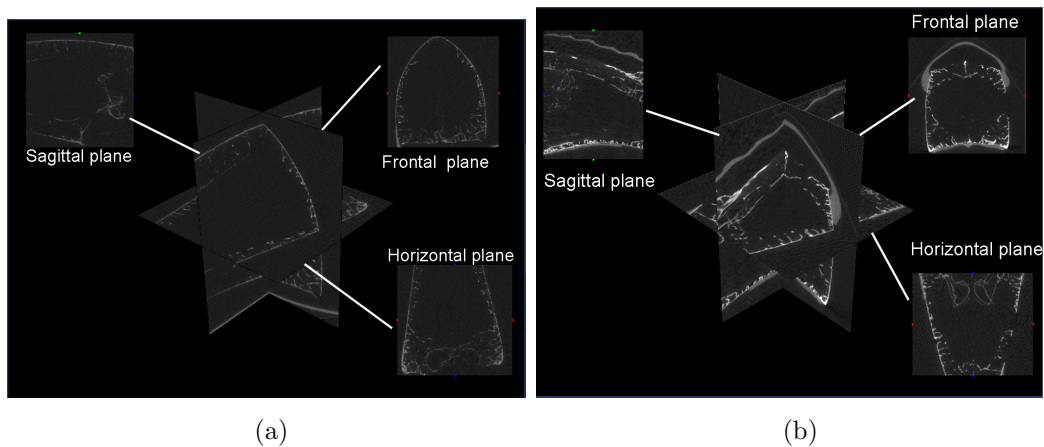


Figure 4.60: Computed tomography;(a) toucan foam;(b) hornbill foam.

4.6.2.1 Marching Cubes

Marching squares in 2D and marching cubes in 3D is commonly used as surface rendering methods. This is accomplished by contouring or color mapping that we can construct the boundaries according to the color or intensity of the image. The boundaries are contour lines (2D) or surfaces (3D) of constant scalar value [180]. The algorithms of marching cubes are the following.

1. Select a cell.
2. Calculates the inside or outside of each vertex of the cell.
3. Creates index by storing the binary state of each vertex in separate bit.
4. Use index to look up the topological state of the cells in a case table.
5. Calculate the contour location for each edge in case table.

While there is an ambiguity when we connect the isovalues as the number of isovalue increases in the cell, we can use the case table to avoid the ambiguity. The marching squares in 2D have sixteen cases with 2 ambiguity, shown in Fig4.61. There are possible 256 marching cube cases for 3 dimensional isosurface generation; however, the cases will be reduced to be 15 cases due to symmetry, shown in Fig. A simple case is described in Figure 4.62 (a), showing the process of marching cube. We select a cell having a certain scalar vale at the node. We take a isovalue of 4 in this case and connect isovalue. As a result, we can define isosurface.

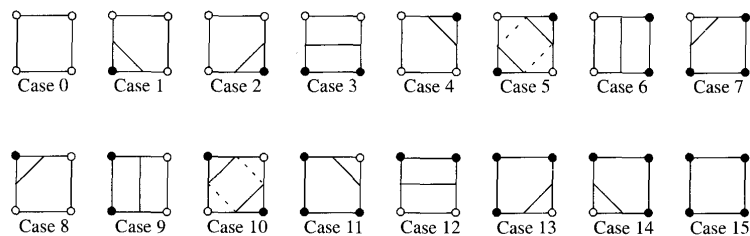


Figure 4.61: 16 cases for marching squares (from [180])

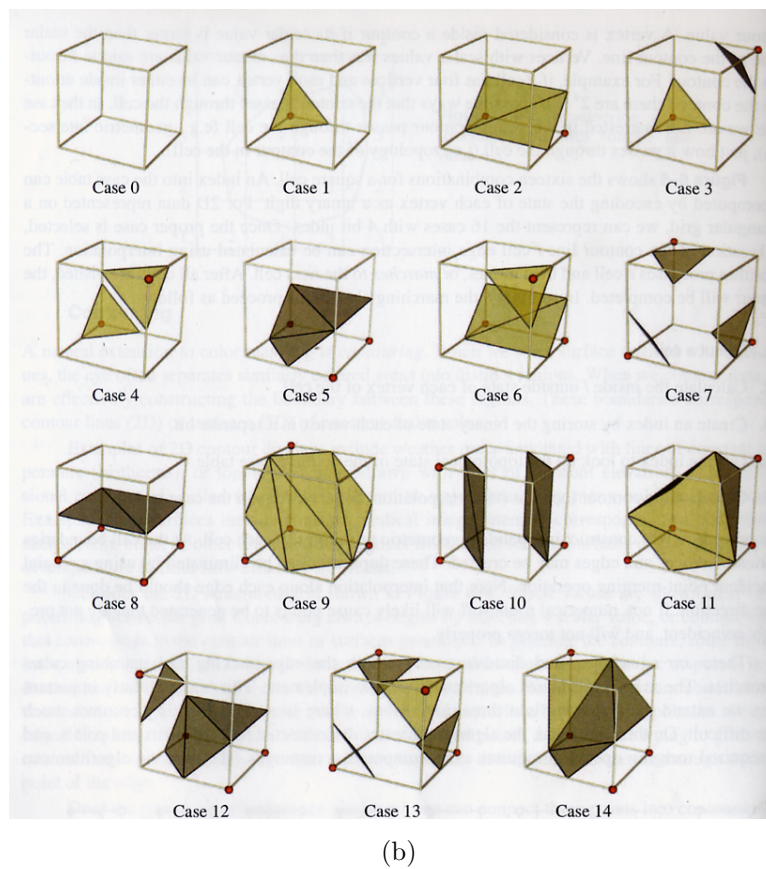
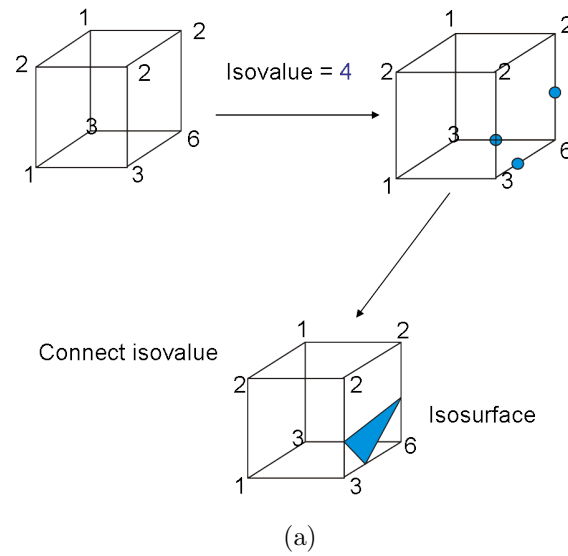


Figure 4.62: (a) Process of marching cube; (b) 15 cases for marching cube (from [180]).

The complex foam interior structure was reconstructed by a 3D visualization technique. We have used 200 image slices from microcomputed tomography with a resolution of $93 \mu\text{m}$. DDV (Digital Data Viewer) and VTK (Visualization Toolkit) were used to generate isosurface mesh by using marching cube algorithm [216] developed by Lorensen and Cline. ImageJ converts the DICOM format of images to tiff format to read the input by DDV. We took half the size of original image dataset (hornbill; 505×555 , and toucan; 450×505) and doubled the size in visualization process. After isosurfaces was generated by DDV (Digital Data Viewer), we have treated the model by VTK. Figure 4.63 shows the algorithm for marching cube generation. The stl format of model was read by `vtkSTLReader`. The ploydata set was shrunk by `vtkShrinkPolyData`. In order to smooth the surface of the model, `vtkWindowedSincPolyDataFilter` was applied. The surface normal was defined by `vtkPolyDataNormals`. Triangle polygons were generated by `vtkStripper`. The model was mapped by `vtkPolyDataMapper`.

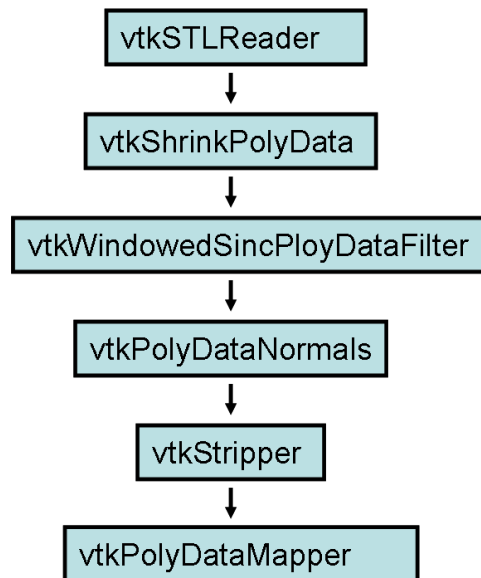


Figure 4.63: Algorithm of marching cube method in VTK

We applied marching squares to a slice of CT image to reconstruct the image in 2D, shown in Figure 4.64. The image is filled with white colored isosurface and is identical to the original image.

Fig. 4.65 shows the 3 dimensional structure of (a) toucan and (b) hornbill foams. 1,373,000 (toucan) and 1,800,000 (hornbill) mesh elements were used to create the contour surface. The exterior of toucan is eliminated and only bony foam is reconstructed. The hornbill foam includes exterior keratin and a secondary hole is observed between bony foam and casque, shown in Fig. 4.65(b). The models clearly show the hollow structure of foam cores. The beak foams consist of thin walled structure with an interconnected network of the rods. The membranes disappeared from the models due to the low intensity of the membranes in CT images.

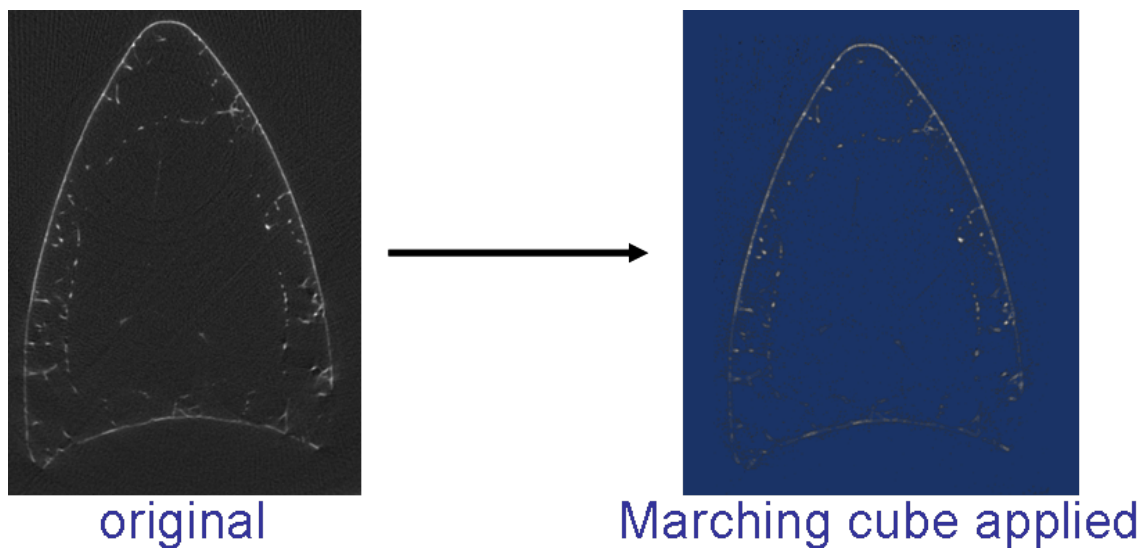
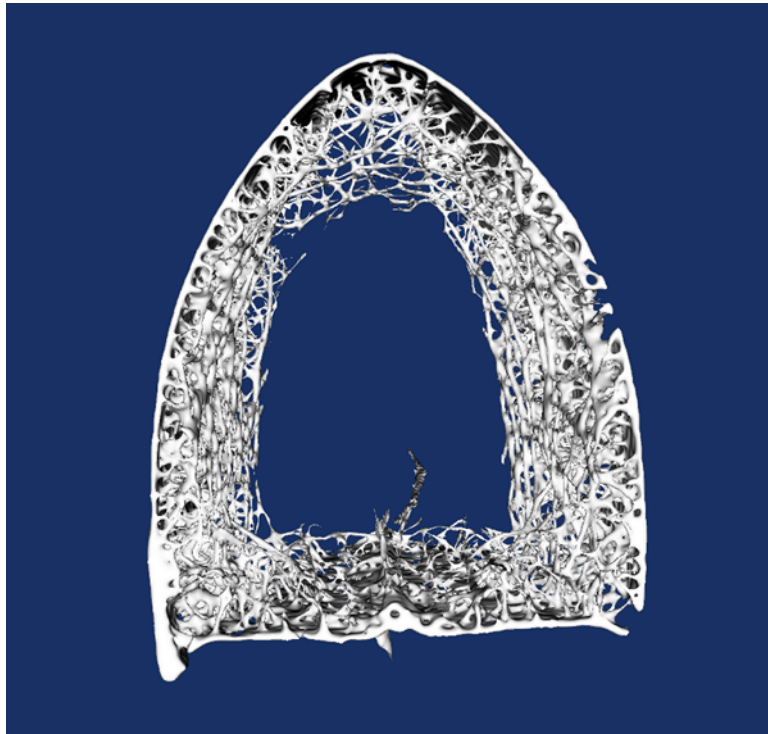
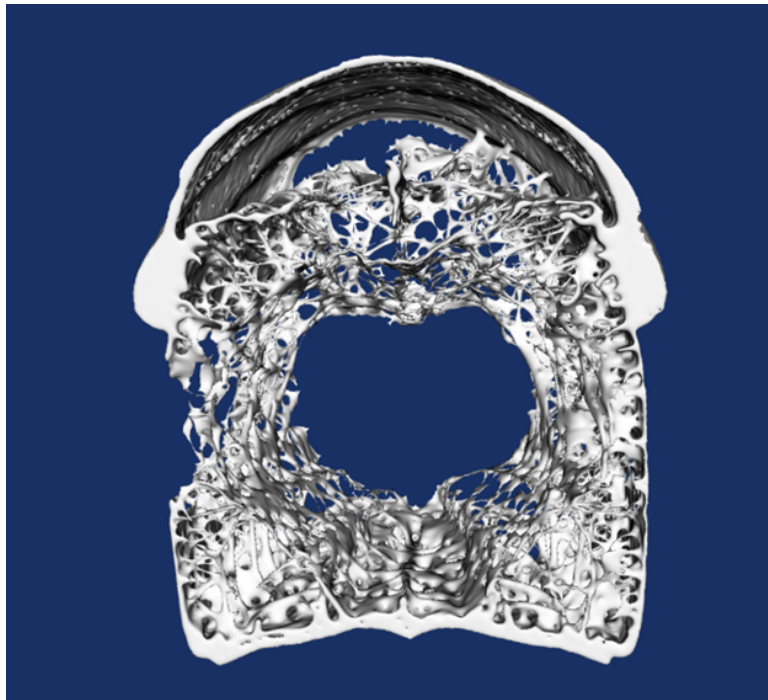


Figure 4.64: The original image is convert to image that marching squares are applied.



(a)



(b)

Figure 4.65: 3D models generated by marching cube;(a) toucan foam;(b) hornbill foam.

4.6.2.2 Ray Casting Method

Ray casting method is widely used method for volumetric rendering. Most of the medical images inherently contain volumetric data. Ray casting method allows effectively conveying volumetric data information from large quantities of data. The basic idea of ray casting is that we send the ray with determine the pixel value in the image through the pixels. The ray projects on to the scene according to the current camera parameter [180]. Figure 4.66 shows the process of ray casting. All rays are parallel to each other and perpendicular to view plane. The data values along the each ray are processed with ray function that contains opacity and color information.

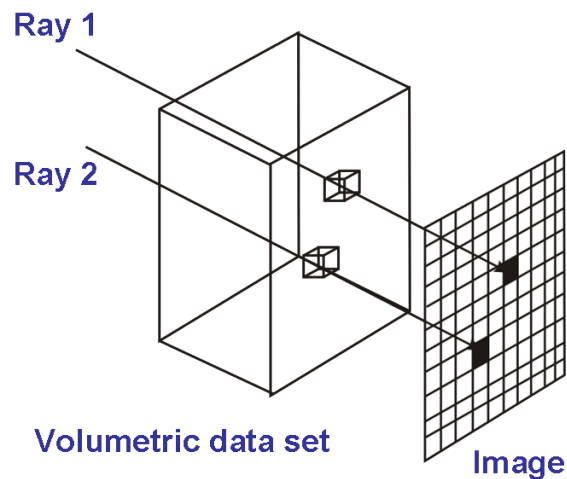


Figure 4.66: The ray casting method

The volumetric rendering by ray casting for hornbill beak is shown in Fig.4.67. In this case, the ray function contains the maximum scalar value along the ray and converts into a gray pixel value, where the minimum pixel value provide black color and the maximum scalar value provide white color, shown in Fig.4.67 produced by MicroView. The maximum intensity projection or MIP produces fairly reasonable image when we process noisy data. MIP technique provides an intuitive understand-

ing of data [180]. By MIP, foam and keratin of honbill beak are distinguished by the maximum intensity.

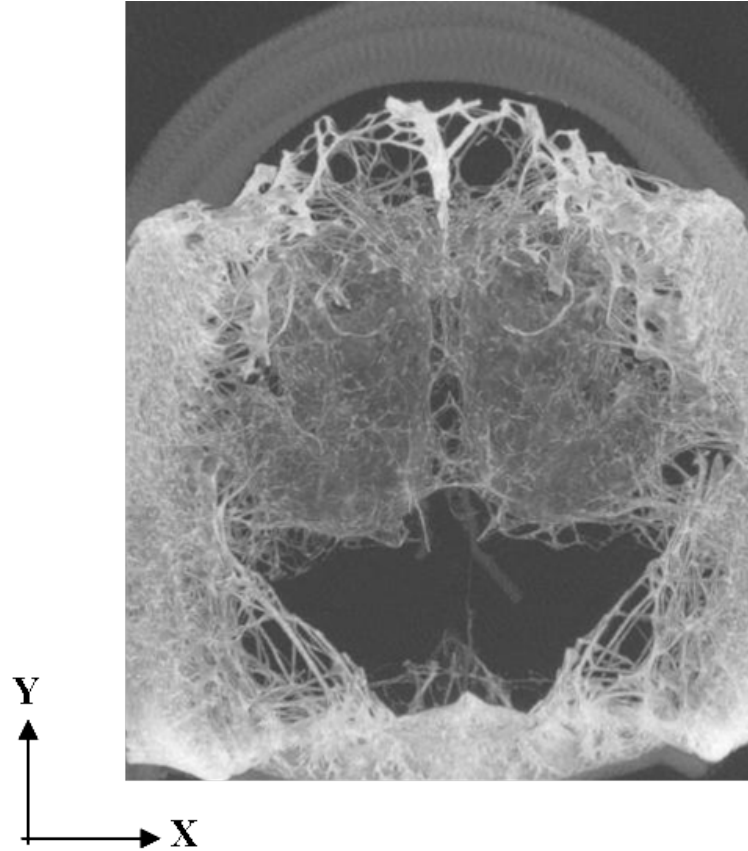


Figure 4.67: Hornbill beak visualized with maximum intensity value.

The 3D interior foam structure is visualized by VTK (Visualization Toolkit), and we have implemented a volumetric ray casting algorithm, shown in Fig 4.68. The image dataset was read by `vtkTIFFReader` and misclassified voxels were treated with `vtkImageIslandRemoval2D` to remove isolated pixels. The images were shrunk by `vtkImageShrink3D`. The transparency and color were defined by `vtkPiecewiseFunction` and `vtkColorTransferFunction`. The property of volume rendering is associated

with `vtkVolumeProperty`. `vtkFiniteDifferenceGradientEstimator` calculates the surface normal of the model. We have selected `vtkVolumeRayCastCompositeFunction` for volume rendering. `vtkVolumeRayCastMapper` performs ray casting operation and `vtkLODProp3D` improves the performance of rendering. We implemented all ray casting volumetric renderings by this algorithms

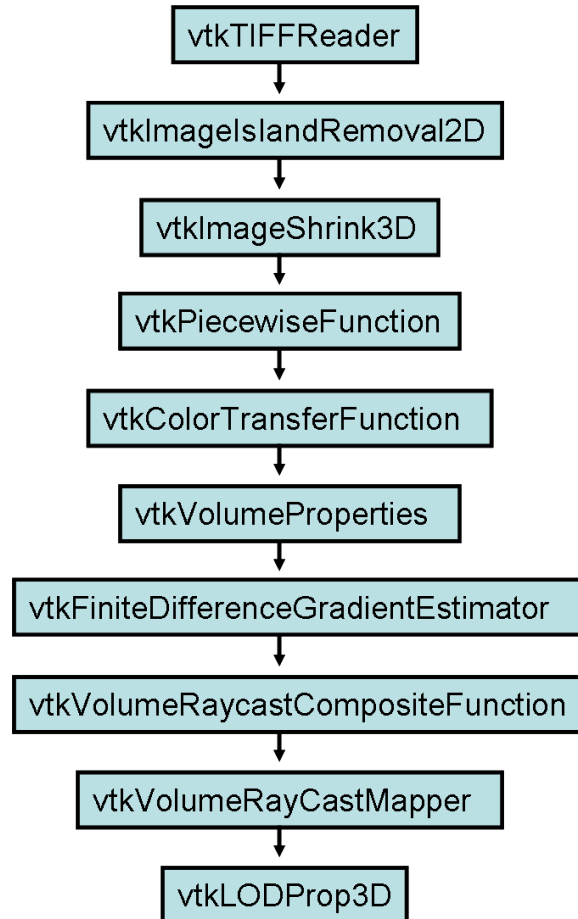
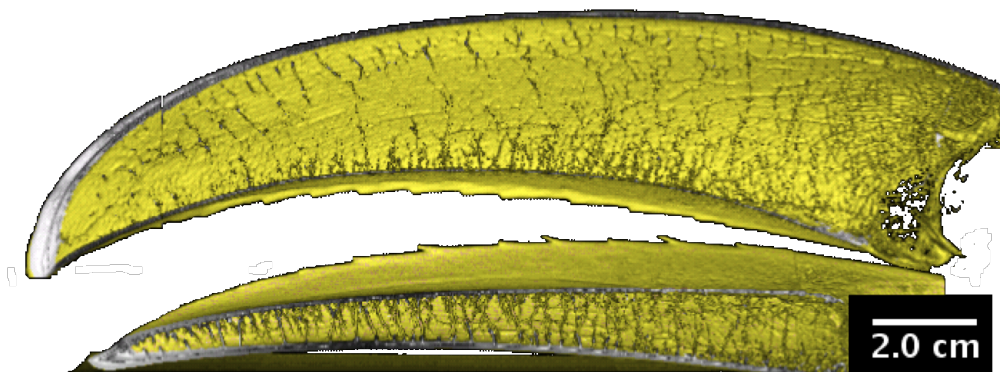


Figure 4.68: Algorithm of ray casting method in VTK

The toucan maxillary and mandibular beaks are reconstructed by ray casting method in Figure 4.69. The beak is colored with yellow by `vtkColorTransferFunction`. The length of maxillary beak is 18.5 cm and mandible be is 17cm. The beak is longitudinally sectioned and the interior bone structure of visible in Figure 4.69 (b). For segmentation rendering of beak foams in Fig.4.70, we used brown and white color for the distinction between bone and soft tissue, respectively. The foams are bisected at the center with proximal and distal views, which reveals a network of osteal rods comprising the foam interior. The toucan exterior is completely stripped and only the internal foam structure is reconstructed in Fig.4.70 (a).The volumetric rendering of hornbill rostrum depicts both keratinous rhamphotheca and foam interior. There is a secondary hollow region observed between casque and bony foam shown in Fig. 4.70(b). This secondary hollow region closes at the end of casque from proximal end. Because the lipid membranes were not detected by the X-ray computed tomography technique, it is possible that the casque may contain continuous membranes. However, considering that the casque of the hornbill has been associated with acoustic function or syrinx signal amplification, we do not expect this to be the case. The parts of foam were rendered at higher resolution of μ -CT. An edge of toucan foam and casque of hornbill are shown in Figure 4.71 . The trabecular rods are connected to bony shell which has a thickness of $\sim 150 \mu\text{m}$ in Fig.4.71(a). The cell membranes are located at concaved trabecular rods, indicated by arrows, while membranes are not visible. The presence of membranes in toucan foam is difficult to detect even at $27 \mu\text{m}$ resolution. The casque region is rendered at resolution of $93 \mu\text{m}$ in Fig.4.71(b). The bony exterior of hornbill has the thickness of $\sim 300\mu\text{m}$. The thickness of casques is $\sim 4 \text{ mm}$ and thickened keratin is connected to bony exterior. The structure of hornbill trabeculae includes rod and plate-like structure.

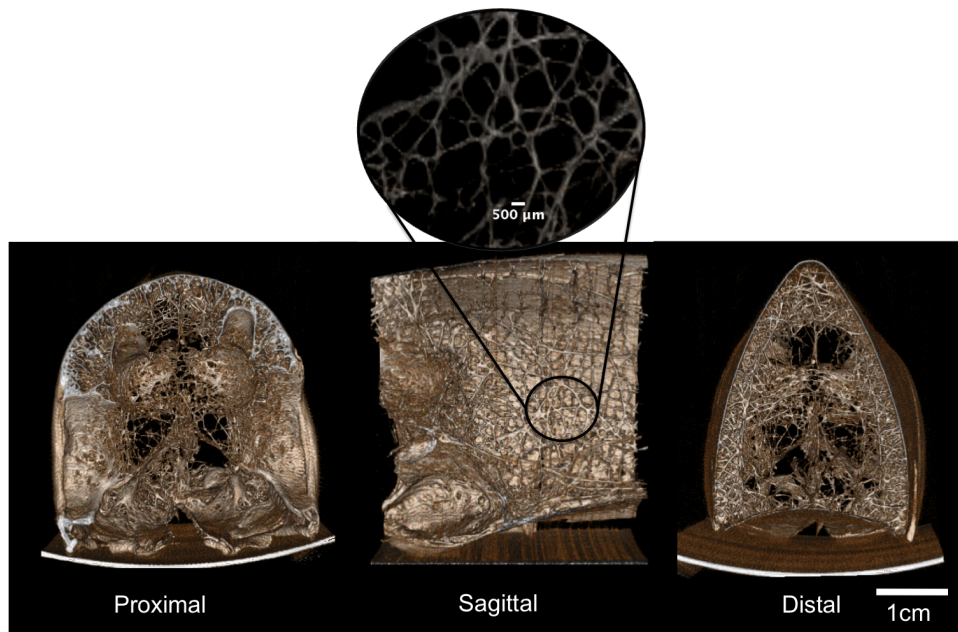


(a)

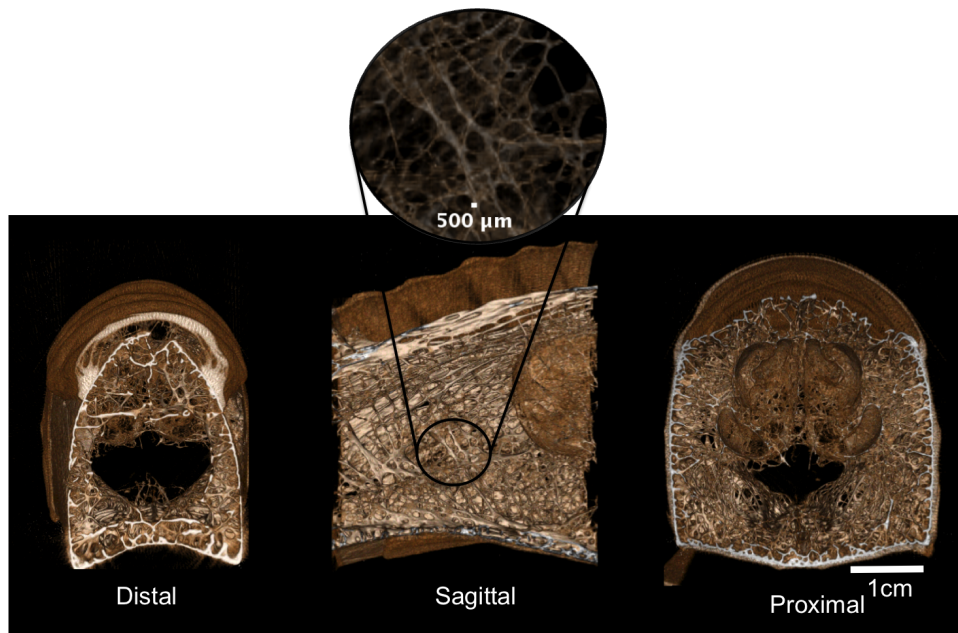


(b)

Figure 4.69: 3 dimensional rendering of maxillary and mandibular beaks of toucan generated by ray casting ;(a) entire beak; (b) longitudinal sectioned entire beak.

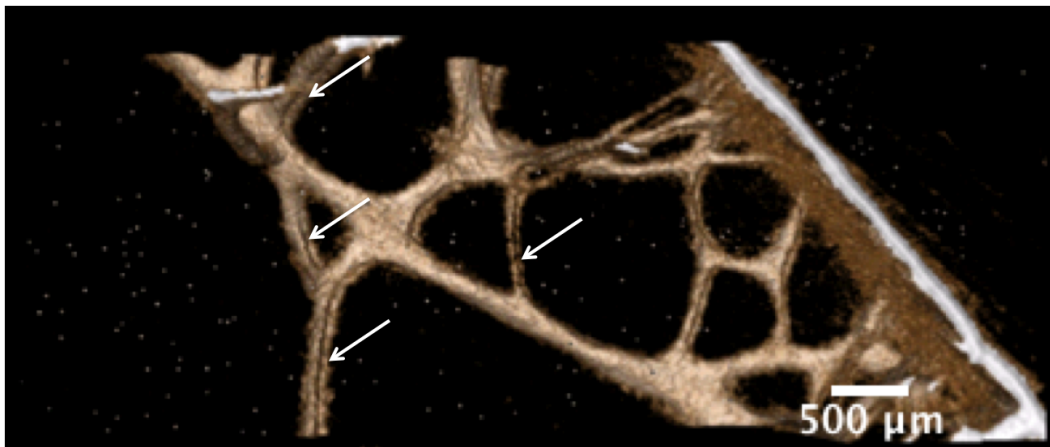


(a)

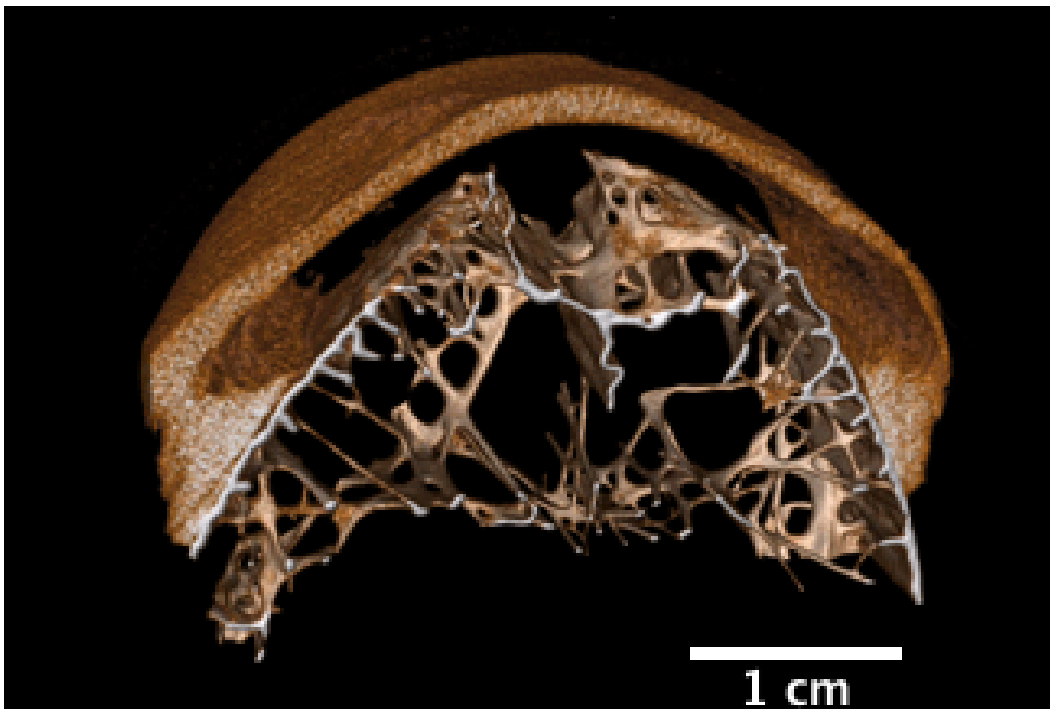


(b)

Figure 4.70: 3 dimensional rendering generated by ray casting;(a) toucan foam with two cross sections (front and back side) ;(b) hornbill foam with two cross sections (front and back side).



(a)



(b)

Figure 4.71: 3 dimensional rendering generated by ray casting;(a) an edge of toucan foam captured by $27\ \mu\text{m}$ resolution of $\mu\text{-CT}$. (arrows indicate concave) ;(b) casque region of hornbill captured by $45\ \mu\text{m}$ of $\mu\text{-CT}$.

4.6.3 Finite Element Analysis with Computed Tomography

The number of studies utilize computed tomography for finite element analysis on trabecular bone [217–221]. The conversion of CT image to FE model is shown in Fig.4.72. The CT images are scanned at a resolution of 97 μm and 150 images are used for this model. The CT images are converted to 3 dimensional structure of trabeculae and cortical shell by marching cube algorithm (Fig.4.72b). We re-meshed the 3 dimensional models and finally assembled shell and foam for finite element analysis (Fig.4.72c). The cortical shell and trabeculae consist of $\sim 36,500$ triangular and $\sim 672,400$ tetrahedron elements, respectively. The details of the conversion are explained in Chapter 3.

After creating the model, we used LS-DYNA [210] for calculations and elastic-plastic model (material type 24) for both trabeculae and cortical bone. The deviatoric strain is defined by

$$\phi = \frac{1}{2}s_{ij}s_{ij} - \frac{\sigma_y^2}{3} \leq 0 \quad (4.33)$$

where s_{ij} is deviatoric stress, $\sigma_y = \beta[\sigma_0 + f_n(\varepsilon_{eff}^p)]$ where the hardening function $f_n(\varepsilon_{eff}^p)$ can be specified in tubular form as an option.

Otherwise

$$f_n(\varepsilon_{eff}^p) = E_p(\varepsilon_{eff}^p) \quad (4.34)$$

where effective plastic strain ε_{eff}^p and plastic hardening modulus E_p is

$$\varepsilon_{eff}^p = \int_0^t \left(\frac{2}{3} \dot{\varepsilon}_{eff}^p \dot{\varepsilon}_{eff}^p \right)^{1/2} dt \quad (4.35)$$

$$E_p = \frac{\beta}{\varepsilon_{eff}^p} \left(\left[1 + \left(\frac{\dot{\varepsilon}}{C} \right) \right]^{-1} \sigma_y - \sigma_0 \right) \quad (4.36)$$

where σ_0 is initial yield stress, C and p are user defined input constant, β is parameter

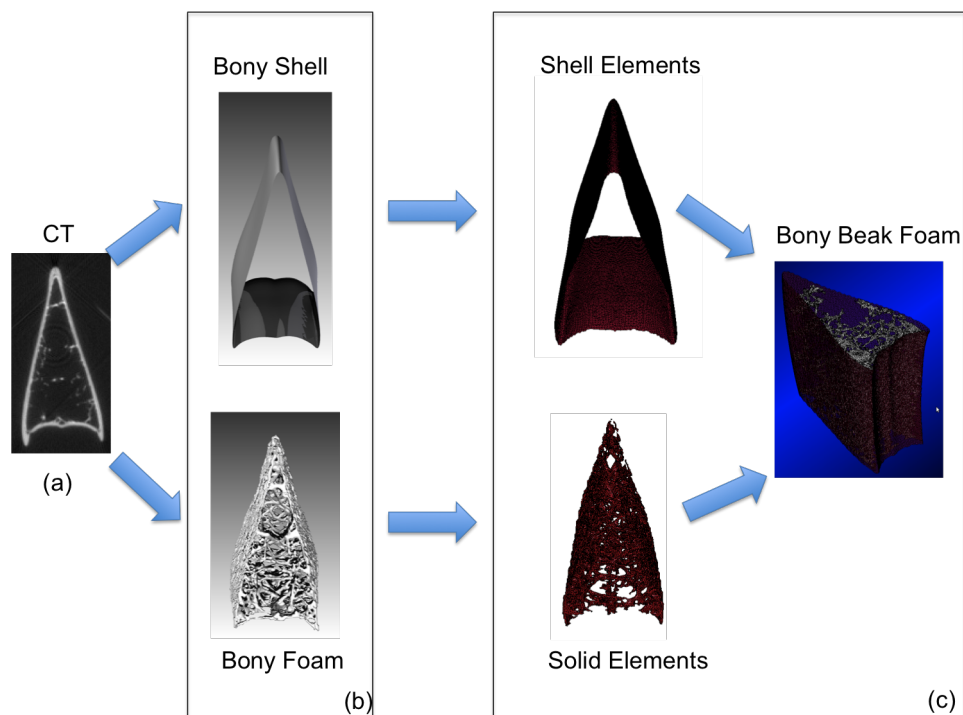


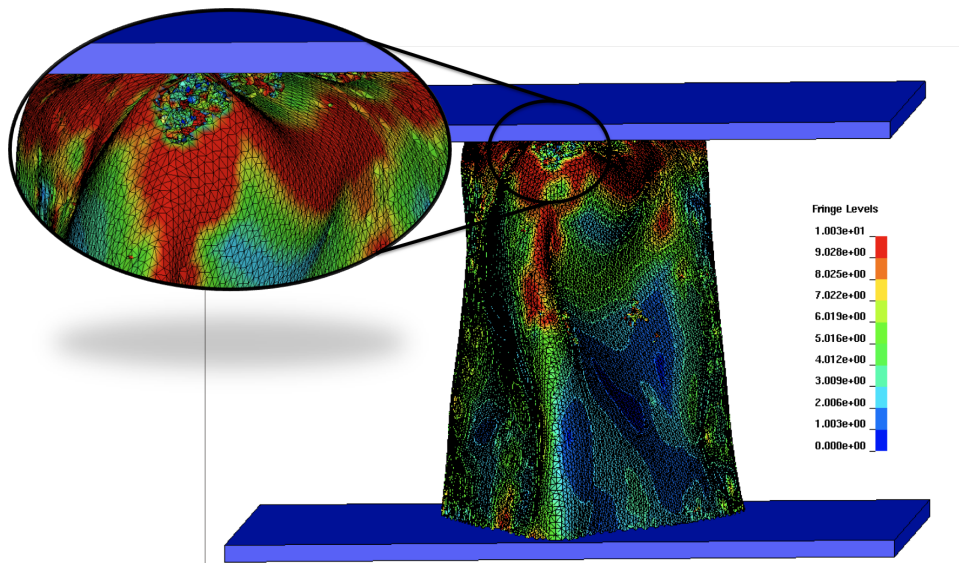
Figure 4.72: Comparison of image to the model for finite element analysis;(a) CT image; (b) tri-dimensional models of cortical shell and trabeculae; (c) FE models of cortical shell and trabeculae, finally assembled.

that accounts for strain rate effect.

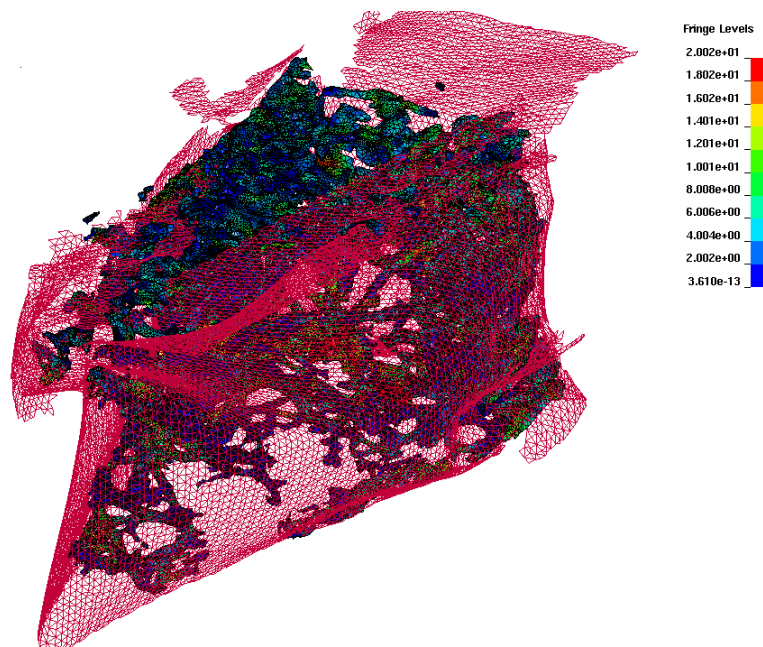
We used a yield stress $\sigma_y = 10$ MPa for cortical shell and $\sigma_y = 20$ MPa for trabeculae. The Young's modulus of trabeculae is taken as 1 GPa for trabeculae and 0.3 GPa for cortical shell. The trabecular and cortical bone are allowed to be failed at strain of 0.03 and 0.1, respectively. The failure strain of cortical bone is larger due to the ductile dermis, which encloses cortical bone.

Figures 4.73 (a) and (b) exhibit the deformation pattern of foam under compression at three strain conditions (0, 0.25, 0.5) in experiment and calculation. The simulation is represented in Von Mises criterion. We used the section of foam that completely filled with trabeculae. The height of foam specimen is ~ 13 mm. The

thickness of cortical shell is taken to be 0.15 mm for FEM calculation. The shell splitting is visible at the culmen ridge of beak foam at a strain of 0.1 in simulation, shown in Fig 4.74 (a). At the strain of 0.25, the shell splitting is observed in experiment. After the shell splitting, the foam is failed by the buckling, which can be observed at a strain of 0.5 (Figs.4.73(a) and (b)). Since there was a crack at the bottom of the sample at the beginning, the crack passes through the entire sample in the experiment. The foam specimen in experiment slide on the bottom plate due to little friction between the specimen and plate. From the top part of the foam, cortical shell is buckled and completely tore at the culmen edge and tomia edge (Fig.4.74(b)). The trabeculae are either fractured or buckled at this strain. In the case of hollow foam under compression, the foam fails by the shell splitting from the culmen edge, shown in Figure4.73 (c). The compressive stress-strain curves of beak foam in experiment shows spikes after linear elastic region, the foam deformed by semi-plastic manner (Fig.4.75). The two stress-strain curves of foam represent the different relative density (0.06 with lower modulus and 0.07 with higher modulus). The calculation shows the average stress at plateau after the linear elastic region, which has a good agreement with experiment.



(a)



(b)

Figure 4.74: (a) Splitting of cortical shell at 0.1 strain;(c) Complete Buckled foam at 0.5 strain.

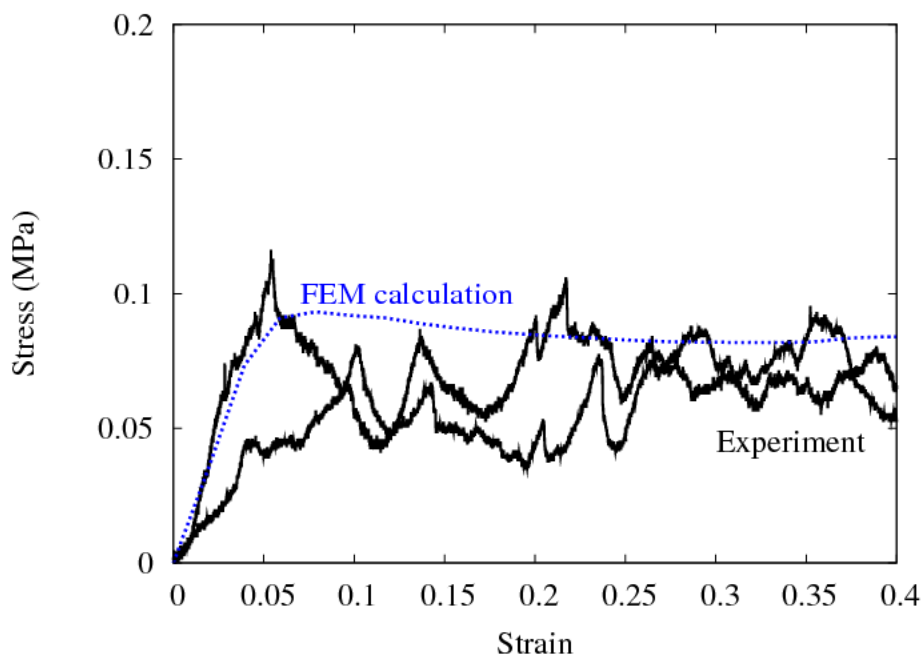
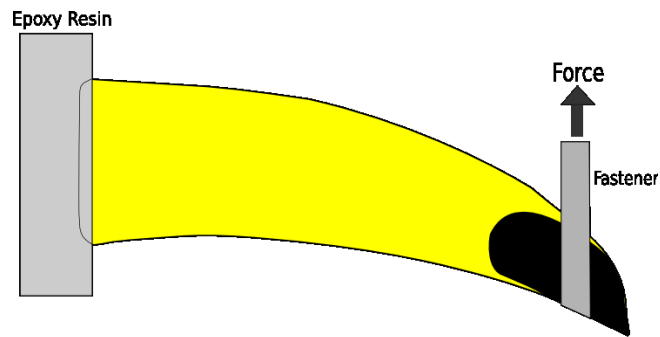


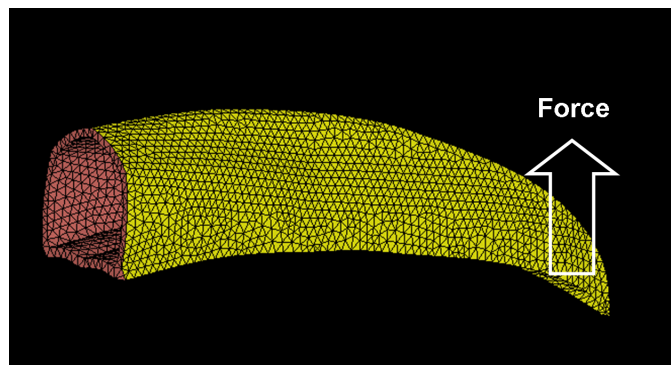
Figure 4.75: Comparison of experiment and finite element analysis in compression.

4.6.4 Bending Behavior of Beak

The bending response of toucan upper beak is evaluated by experiment and finite element calculation. In experiment, the proximal extremity of the beaks was immobilized epoxy resin while the distal extremity was fixed with a nylon fastener, shown in Fig 4.76(a). This nylon fastener was connected to the movable headstock of a dynamometer through a brace of steel. Finite element calculations were performed using LS-DYNA for modeling the bending behavior of unfractured, intact maxilla. The model consists of 5,471 shell elements (rhamphotheca) and 37,076 solid elements (foam), shown in Fig 4.76(b). The foam was allowed to be hollow from proximal to mid-section. The force-displacement response was modeled using an elastic plastic kinematic hardening (material model 3) and the crushable foam model (material



(a)



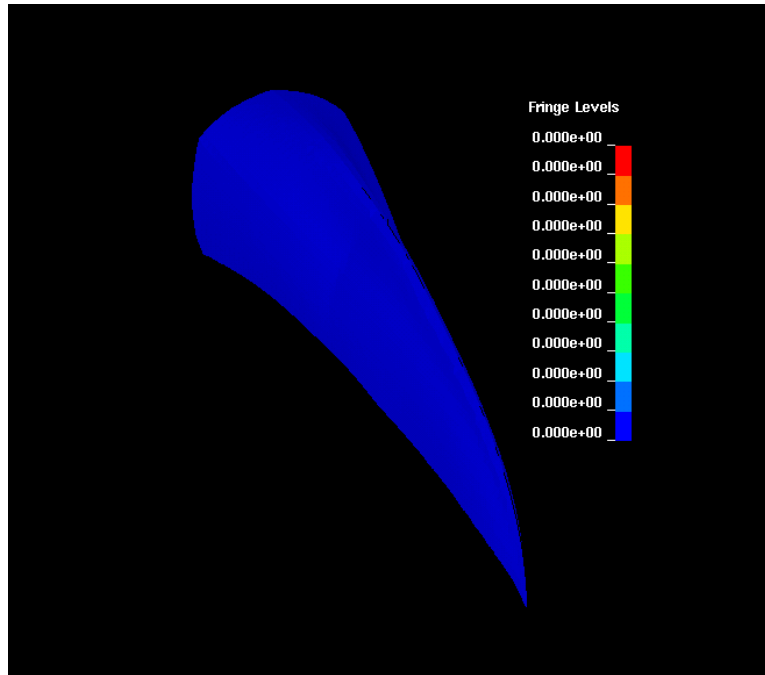
(b)

Figure 4.76: Experimental setup;(a) Bending configuration in experiment; (b) bending configuration in finite element model.

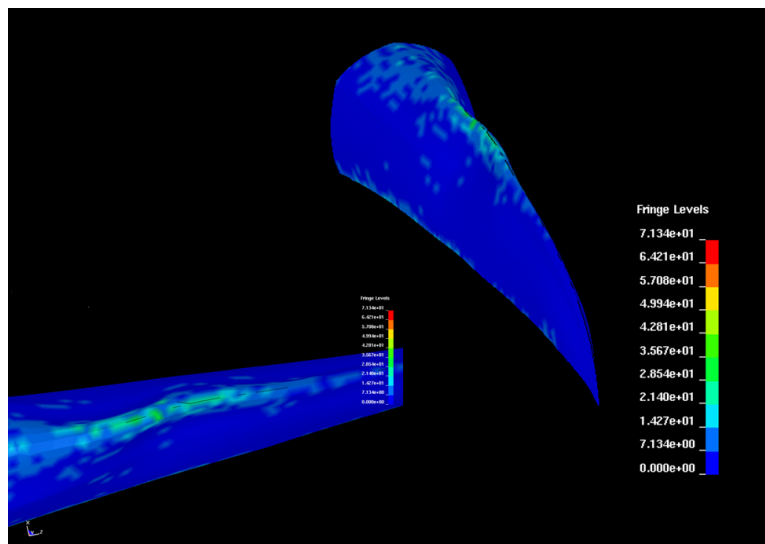
model 63) for interior foam. We used a Young's modulus of 1.5 GPa and yield stress of 120 MPa for shell. The Young's modulus for foam was taken as 5 MPa and flow stress $h = 0.2$ MPa.

Figure 4.77 shows the deformation pattern of beak in bending configuration. Fig.4.77(a) shows initial condition of beak and Fig4.77(b) shows onset of buckling of beak. The buckling starts at the middle of beak at the displacement of 15 mm.

Fig. 4.78 shows a comparison between experiment and calculation by LS-DYNA.



(a)



(b)

Figure 4.77: (a)Initial condition;(b)buckling

We calculated for the shell thicknesses of 0.5 mm, 1 mm, and 1.2 mm in bending. The calculation of the thickness of 0.5 mm shows the lowest buckling load of 52 N. The maximum buckling load of 303 N is achieved by the shell thickness of 1.2 mm. The experimental results show the maximum buckling displacement in Fig 4.78. The slope of force-displacement curve in experiment is close to that with the shell thickness of 0.5 mm, whereas the maximum buckling load in experiment is close to that with the shell thickness of 1.2 mm. The differences between calculation and experiment are due to geometrical difference of beak and the assumption of uniformity of shell thickness. The thickness of 1.2 mm is close to the experimental results. The bending behavior of beak is mainly dominated by the shell, in this case rhamphotheca, whereas foam stabilizes the deformation and resists the buckling of beak caused by bending.

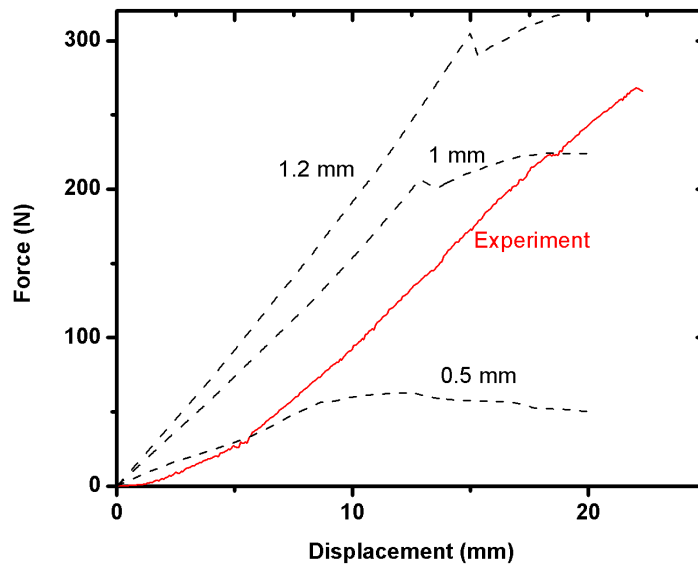


Figure 4.78: Comparison of experimental results and computational results with three different thickness of shell.

The work in this chapter is quoted from the materials published in the following journals.

Yasuaki Seki, Matthew S. Schneider, Marc A. Meyers, "Structure and mechanical behavior of a Toco toucan beak ", *Acta Materiala*, 53, 5281-5296,2005.

Yasuaki Seki, Bimal Kad, David J Benson, Marc A. Meyers, "The toucan beak: Structure and mechanical response", *Materials Science and Engineering C* , 26, 1412-1420,2006.

Y.Seki, Sara G. Bodde, Marc A. Meyers, "Toucan and Hornbill Beaks:Comparative Study", *Acta Biomaterialia* submitted 2009.

Chapter 5

Conclusions

This study revealed the mechanical properties and structure of the Toucan and wrenhorned hornbill beaks. The sandwich structured bird beaks demonstrated an ingenious solution of the design and the advantages over separate mechanical response of face skin and cellular core. The following are the principal conclusions.

5.1 Structure

(I) The beak keratins are composed of polygonal keratin scales with a diameter of $\sim 50 \mu\text{m}$ and thickness of $1 \mu\text{m}$. These keratins are glued together with staggered patterns, leading to total thickness of 0.5 mm and 1.5 mm for toucan and hornbill, respectively. The morphology of hornbill casque and ridges differs from that of toucan. The keratin tile consists of the matrix and homogeneously distributed branched filaments.

(II) The beak skull is closed-cell foam that comprise of rod like structured trabeculae and thin membranes. The closed-cell foam of toucan has a density of 0.05 g/cm^3 and that of hornbill has a density of 0.14 g/cm^3 . Thus, the relative density

of toucan foam is 0.1 and that of hornbill is 0.17.

(III) The beak keratin is mostly composed of protein and contains 3~4wt% of sulfur. The content of calcium salts is less than 2 wt% in the beak keratin. In contrast, beak trabeculae contained 50 wt% of minerals. The dominant minerals of calcium occupy approximately 20 to 30 wt% of minerals in beak trabeculae.

(IV) Confocal microscope provide a more detailed feature of foams over scanning electron microscope, especially the resolution at depth. Mosaic of cross section of toucan mandible was reconstructed and foam structure with a depth from 0 to 500 μm were evaluated. By acquiring data set through the depth, three dimensional structure of trabecular bone can be reconstructed with visualization techniques.

(V) Computed tomography was used for 3 dimensional rendering for beak foam. The volumetric reconstruction of toucan and hornbill beaks, using marching cube and ray casting algorithms, was successfully achieved by Visualization ToolKit.

5.2 Mechanical Properties

(I) Tensile properties of toucan beak keratins showed isotropic while hornbill is anisotropic in longitudinal and transverse directions. The toucan beak keratin showed high strength in transverse direction; conversely, the hornbill keratin showed high strength in longitudinal direction. This may associate with the geometry and orientation of scales.

(II) We evaluated the moisture sensitive of beak keratin. The stiffness of beak keratin dropped by an order of magnitude with a 10 % increase of moisture.

The ductility increases by two holds, compared in ambient condition.

(III) The mechanical role of melanized beak keratin is evaluated. The high stiffness and hardness of melanized keratin, compared to unmelanized beak keratin, are confirmed by tensile testing and hardness measurement.

(IV) The keratin shell exhibited a failure mode that was strain-rate dependent. In toucan's case, the failure occurred by pull-out of the scales at 5×10^{-5} /s. The failure occurred by the scale fracture at 1.5×10^{-3} /s. In hornbill's case, the severe fracture took place at 5×10^{-2} /s. The smooth fracture occurred at 3×10^{-4} /s. It is proposed that the viscoplastic response of the glue is responsible for the change in failure mode.

(V) The deformation behavior of the toucan and hornbill foams in compression occurs by a mixture of brittle crushing and ductile bending ligaments with viscoplastic response of membranes. The toucan and hornbill foams start the densification at the same strain due to similar relative density. It was successfully modeled by Gibson-Ashby constitutive equations for closed- and open-cell configurations.

(VI) The mechanical properties of individual trabeculae from toucan beak were investigated. The stiffness and strength of trabeculae exceed that of foam in compression due to scaling effect and imperfection of foam. The strength obtained from Weibull distribution is agreeable to the strength estimated from the hardness measurement.

5.3 Sandwich Design

(I) The combined response of the toucan shell and foam core was compared with the model by Hanssen et al. [56]. The model reveals that there is a synergism between the shell and the foam, i.e., the energy absorbed by the shell + foam assembly is higher than the sum of the separate energy absorption of shell and foam.

(II) The stability analysis using Karam and Gibson models [58] demonstrates the significant improvement of sandwich structured bird beaks in local and Brazier buckling moment, compared to a structure of the same weight having no foam, a correspondingly higher shell thickness.

(III) The optimization analysis using Dawson and Gibson models [59] predicted the transition between buckling failure and material failure of bird beaks. The model predicted higher material failure than experiment due to the variation in experimental results.

5.4 Modeling

(I) The finite element method demonstrates that the compressive buckling loads for the sandwich structure of the beak is higher than shell alone. This is due to the stabilizing effect exerted by the foam on the thin shell, retarding its collapse.

(II) The bending behavior of toucan beak in experiments was compared with finite element calculation. The calculation demonstrated that agreeable bending behavior to experimental results with thickness of 1.2 mm. The results suggested that the mechanical response of beak in bending is prevailed by the shell.

(III) The image data set, acquired from μ -CT, was successfully converted to the model for finite element calculation with an aid of visualization techniques. The model demonstrated good match with experimental results.

Chapter 6

Future Work

(I) The mechanical properties of melanized keratin showed an increase of stiffness. This result associates with melanin. We should conduct TEM analysis on melanized keratin to establish the relation between mechanical properties and role of melanin.

(II) We confirmed that beak foam is closed foam consisting of trabeculae and thin membranes. The role and composition of membranes are still unknown. The further investigation needs to be conducted for the membranes.

(III) The mechanical behavior of beak foam was investigated and typified by brittle crushing in dry condition. However, if the bird is alive, the mechanical behavior of the foam would behave differently because the foam is exposed to wet condition. The mechanical behavior of the foam in wet condition should be investigated and the mechanical role of membranes also needs to be studied when the membranes are not desiccated.

References

- [1] M. Sarikaya. An introduction to biomimetics: A structural viewpoint. *Microsc Res Tech*, 27(360), 1994.
- [2] A.V. Srinivasan, G.K. Haritos, and F.L. Hedberg. Biomimetics: advancing man-made materials through guidance from nature. *Appl. Mech. Rev*, 44:463, 1991.
- [3] J.F.V. Vincent. *Structural Biomaterials*. Princeton University Press, 1990.
- [4] E. Baer, A. Hiltner, and R.J. Morgan. Biological and synthetic hierarchical composites. *Phys. Today*, 45:60, 1992.
- [5] S. Mann. *Biomineralization*. Oxford University Press, 2002.
- [6] J.V. Laraia and A.H. Heuer. Novel composite microstructure and. mechanical behavior of mollusk shell. *J Am Ceram Soc*, 72:2177, 1989.
- [7] R. Menig, M.H. Meyers, M.A. Meyers, and K.S. Vecchio. Quasi-static and dynamic mechanical response of *Haliotis rufescens* (abalone) shells. *Acta.Mat*, 48:2383, 2000.
- [8] R. Menig, M.H. Meyers, M.A. Meyers, and K.S. Vecchio. Quasi-static and dynamic mechanical response of *Strombus gigas* (conch) shells. *Mat.Sci.Eng.A*, 297:203, 2001.
- [9] A. Lin and M.A. Meyers. Growth and structure in abalone shell. *Mater Sci and Eng*, 90:27, 2005.
- [10] M.Hidaka and K. Takahashi. Fine structure and mechanical properties of the catch apparatus of the sea-urchin spine, a collagenous connective tissue with muscle-like holding capacity. *J.Exp.Bio.*, 103:1, 1983.

- [11] K.S. Vecchio, X. Zhang, J.B. Massie, M. Wang, , and C.W. Kim. Conversion of sea urchin spines to mg-substituted tricalcium phosphate for bone implants. *Acta Biomater.*, 3:785, 2007.
- [12] G. Mayer and M. Sarikaya. Rigid biological composite materials: Structural examples for biomimetic design. *Exp Mech*, 4:395, 2002.
- [13] J.M. Gosline, M.E. DeMont, and M.W. Denny. The structure and properties of spider silk. *Endeavour*, 10:37, 1986.
- [14] F. Vollrath. Strength and structure of spiders' silks. *Rev Mol Biotechnol*, 74:67, 2000.
- [15] L.J. Gibson. Biomechanics of cellular solids. *J.Biomech.*, 38:377, 2005.
- [16] G.N. Karam and L.J. Gibson. Biomimicking of animal quill and plant stems:Natural cylindrical shells with foam core. *Mat.Sci.Eng.*, C2:113, 1994.
- [17] L.J. Gibson, K.E. Easterling, and M.F. Ashby. The structure and mechanics of cork. *Proc.Roy.Soc.*, A377:99, 1981.
- [18] L.J. Gibson. The mechanical behaviour of cancellous bone. *J.Biomech.*, 18:317, 1985.
- [19] L.L. Short and J.F.M. Horne. *Toucans, Barbets and Honeyguides*. Oxford University Press, 2001.
- [20] A. Kemp and M. Woodcock. *The Hornbills: Bucerotiformes*. Oxford University Press, 1995.
- [21] R.D.B. Fraser, T.P. Macrae, and G.E. Rogers. *Keratin Their Composition, Structure, and Biosynthesis*. Thomas, 1972.
- [22] K.M. Rudall. X-ray studies of the distribution of protein chain types in the vertebrate epidermis. *Biochimica et Biophysica Acta*, 1:549, 1947.
- [23] R.D.B. Fraser, T.P. Macrae, D.A.D. Parry, and E. Suzuki. The structure of β -keratin. *Polymer*, 12:810, 1971.
- [24] R.D.B Fraser, T.P. Macrae, D.A.D. Parry, and E. Suzuki. The structure of feather keratin. *Polymer*, 12:35, 1971.

- [25] R.D.B. Fraser and D.A.D. Parry. The molecular structure of reptilian keratin. *Int.J.Bio.Mocro*, 19:207, 1996.
- [26] R.D.B. Fraser and T.P. Macrae. The structure of α -keratin. *Polymer*, 14:61, 1973.
- [27] R.C. Marshall, D.F. Orwin, and J.M. Gillespie. Structure and biochemistry of mammalian hard keratin. *Electron Microsc. Rev.*, 4:47, 1991.
- [28] W.T. Astbury and A. Street. X-ray studies of the structure of hair, wool, and related fibres. I. general. *Phil. Trans. Roy. Soc. London*, 230(75), 1932.
- [29] K.E. Wilk, V.J. James, and Y. Amemiya. The intermediate filament structure of human hair. *Biochimica et Biophysica Acta*, 1245:392, 1995.
- [30] P. Mason. Density and structure of alpha-keratin. *Nature*, 197:179, 1963.
- [31] P.J. Harget and S. Krimm. Macromolecular structure and organization of alpha keratin. *Biopolymers*, 13:157, 2004.
- [32] W. Montagna and P.F. Parakkal. *The structure and function of skin (3rd ed.)*. Academic press, 1974.
- [33] R.D.B. Fraser and D.A.D. Parry. Molecular packing in the feather keratin filament. *J. Stru. Biol.*, 162:1, 2008.
- [34] M. Stewart. The structure of chicken scale keratin. *J.Ultra. Res.*, 60:27, 1977.
- [35] M.J. Frenkel and J.M. Gillespie. The protein of the keratin component of the bird's beak. *Aust.J.Bio.Sci*, 29:467, 1976.
- [36] A.H. Brush and J.A. Wyld. Molecular organization of avian epidermal structures. *Com.Biochem.Physiol*, 73B:313, 1982.
- [37] A.H. Brush. Tissue specific protein heterogeneity in keratin structures. *Biochem.Sys.Ecolo*, 14:547, 1986.
- [38] Y. Yuan and R. Verma. Measuring microelastic properties of stratum corneum. *Colloids and Surfaces B: Biointerfaces*, 48:6, 2006.
- [39] Y.S. Papir, K.H. Hsu, and R.H. Wildnauer. The mechanical properties of stratum corneum: I. The effect of water and ambient temperature on the tensile properties of newborn rat stratum corneum. *Biochemi. et Biophy Acta*, 399:170, 1975.

- [40] B. Bhushan. Nanoscale characterization of human hair and hair conditioners. *Prog.Mat.Sci.*, 53:585, 2008.
- [41] B. Bhushan and N. Chen. Afm studies of environmental effects on nanomechanical properties and cellular structure of human hair. *Ultramicroscopy*, 106:755, 2006.
- [42] A.K. Kitchener and J.F.V. Vincent. Composite theory and effect of water on the stiffness of horn keratin. *J.Mat.Sci.*, 20:1385, 1987.
- [43] M.A. Kaspi and J.M. Gosline. Micromechanics of the equine hoof wall;Optimizing crack control and material stiffness through modulation of the properties. *J.Exp.Bio.*, 202:377, 1999.
- [44] M.A. Kaspi and J.M. Gosline. Strain-rate dependant mechanical properties of equine hoof wall. *J.Exp.Bio.*, 199:1133, 1996.
- [45] M.A. Kaspi and J.M. Gosline. Design complexity and fracture control in the equine hoof wall. *J.Exp.Bio.*, 200:1639, 1997.
- [46] J.E.A. Bertram and J.M. Gosline. Functional design of horse keratin:The modulation of mechanical properties through hydration. *J.Exp.Bio.*, 130(121), 1987.
- [47] J.E. Douglas, T.L. Biddick, J.J. Thomason, and J.C. Jofriet. Stress/strain behavior of the equine laminar junction. *J.Exp.Bio.*, 201:2287, 1998.
- [48] R.H.C. Bonser and P.P. Purslow. The Young's modulus of the feather keratin. *J.Exp.Bio.*, 198:1029, 1995.
- [49] C.J. Cameron, T.J. Wess, and R.H.C. Bonser. Young's modulus varied with differential orientation of keratin in feathers. *J.Stru.Bio.*, 143:118, 2003.
- [50] R.H.C. Bonser. Hydrogen sensitivity of ostrich claw keratin. *J.Mat.Sci.let.*, 21:1563, 2002.
- [51] R.H.C. Bonser, L. Saker, and G. Jeronimidis. Toughness anisotropy in feather keratin. *J.Mat.Sci.*, 39:2895, 2004.
- [52] R.H.C. Bonser and M.S. Witter. Indentation hardness of the bill keratin of European starling. *Condor*, 95:736, 1993.

- [53] H.C. Bonser R. Longitudinal variation in mechanical competence of bone along the avian humerus. *J.Exp.Bio.*, 198:209, 1995.
- [54] L.J. Gibson. Woodpecker pecking: how woodpeckers avoid brain injury. *J.Zoolo.*, 270:462, 2006.
- [55] L.J. Gibson and M.F. Ashby. *Cellular Solids:Structure and Properties 2nd*. Cambridge University Press, 1997.
- [56] A.G. Hanssen, M. Langseth, and O.S. Hopperstad. Static crushing of square aluminium extrusion with aluminium foam filter. *Int.J.Mech.Sc.*, 41:967, 1999.
- [57] A.G. Hanssen, M. Langseth, and O.S. Hopperstad. Static and dynamic crushing of aluminium extrusions with aluminium foam filter. *Int.J.Imp.Eng.*, 24:347, 2000.
- [58] G.N. Karam and L.J. Gibson. Elastic buckling of cylindrical shells with elastic cores-I. Analysis. *Int.J.Solids.Stru.*, 32:1259, 1995.
- [59] M. A. Dawson and L. J. Gibson. Biomimetics: extending nature's design of thin-wall shells with cellular cores. In C.A. Brebbia, editor, *Design and Nature III: Comparing Design in Nature with Science and Engineering*, chapter 3, pages 145–155. WIT Press, 2006.
- [60] H. Gao, B. Ji, M.J. Buehler, and H. Yao. Flaw tolerant bulk and surface nanostructures of biological systems. *MCB*, 1:37, 2004.
- [61] B. Ji and H. Gao. Mechanical properties of nanostructure of biological materials. *J.Mech.Phys.Sol.*, 52:1963, 2004.
- [62] H. Gao, X. Wang, H. Yao, S. Gorb, and E. Arzt. Mechanics of hierarchical adhesion structures of geckos. *Mech.Mat.*, 37:275, 2005.
- [63] H. Warshawsky. Organization of crystals in enamel. *Anat.Rec.*, 224:242, 1989.
- [64] W. Tesch, N. Eidelman, P. Roschger, F. Goldenberg, K. Klaushofer, and P. Fratzl. Graded microstructure and mechanical properties of human crown dentin. *Calcif.Tissue.Int.*, 69:147, 2001.
- [65] D.W. Thompson. *On growth and form*. Cambridge University Press, 1966.
- [66] Y.C. Fung. *Biomechanics:Mechanical Properties of Living Tissues 2ed*. Springer, 1993.

- [67] J.D. Currey. *The mechanical adaptations of bones*. Princeton press, 1984.
- [68] J.D. Currey. *Bones: structure and mechanics*. Princeton University Press, 2002.
- [69] M.A. Meyers, A.Y.M. Lin, P.Y. Chen, and Y. Seki. Biological materials:structure and mechanical properties. *Prog. Mat. Sci.*, 53:1, 2008.
- [70] P. Fratzl and R. Weinkamera. Nature's hierarchical materials. *Prog.Mat.Sci.*, 52(1263), 2007.
- [71] P.Y. Chen, A.Y.M. Lin, Y.S. Lin, Y. Seki, A.G. Stokes, M.A. Meyers, and J. McKittrick. Structure, function and mechanical properties of selected biological materials. *Mech. Behav. Biomed. Mat*, 1:208, 2008.
- [72] P.Y. Chen, A.Y.M. Lin, A.G. Strokes, Y. Seki, S.G.Bodde, J. McKittrick, and M.A. Meyers. Structural biological materials:overview of current research. *JOM*, June 2008.
- [73] M.A. Meyers, A.Y.M. Lin, Y.S. Lin, E.A. Olevsky, and S. Georgalis. The cutting edge: Sharp biological materials. *JOM*, 60:19, 2008.
- [74] B. Alberts, A. Johnson, J. Lewis, M. Raff, K. Roberts, and P. Walter. *The molecular biology of the cell 4th edition*. Garland Science, 2001.
- [75] K. Simkiss and K.M. Wilbur. *Biom mineralization cell biology and mineral deposition*. Academic Press, 1989.
- [76] F.G.E. Pautard. Mineralization of keratin and its comparison with the enamel matrix. *Nature*, 199:531, 1963.
- [77] B. Huo, Q.S. Zheng, Q. Zhang, and J.D. Wang. Effect of dentin tubules to the mechanical properties of dentin. Part II: Experimental study. *Acta. Mechan. Sinica.*, 16:75, 2000.
- [78] J.H. Kinney, J. Oliveira, D.L. Haupt, G.W. Marshall, and S.J. Marshall. The spatial arrangement of tubules in human dentin. *J.Mat.Sci.Mat.Med.*, 12:743, 2001.
- [79] A. Kishen, U. Ramamurty, and A. Asundi. Experimental studies on the nature of property gradients in the human dentine. *J. Biomed. Mater. Res.*, 51:650, 2000.

- [80] J.E. Palamara, P.R. Wilson, and C.D. Thomas H.H. Messer. A new imaging technique for measuring the surface strains applied to dentine. *J Dentist*, 28:141, 2000.
- [81] H. Follet, G. Boivin, C. Rumelhart, and P. J. Meunier. The degree of mineralization is a determinant of bonenext term strength: a study on previous termhumannext term calcanei. *Bone*, 34:783, 2004.
- [82] R. B. Ashman, G. Rosinia, S. C. Cowin, M. G. Fontenot, and J. C. Rice. The bonenext term tissue of the canine mandible is elastically isotropic. *J.Biomech.*, 18:717, 1985.
- [83] X. Neil Dong and X. Edward Guo. The dependence of transversely isotropic elasticity of human femoral cortical bone on porosity. *J. Biomech.*, 37:1281, 2004.
- [84] A.P. Jackson and J.F.V. Vincent. The mechanical design of nacre. *Proc.Roy.Soc.Lon.*, 234(415), 1988.
- [85] A.Y.M Lin, M.A. Meyers, and K.S. Vecchio. Mechanical properties and structure of *Strombus gigas*, *Tridacna gigas*, and *Haliotis rufescens* sea shells:A comparative study. *Mat.Sci.Eng.C*, 26:1380, 2006.
- [86] J.Y. Rho, L.K. Spearing, and P. Zioupos. Mechanical properties and hierarchical structure of bone. *Med.Eng.Phy*, 20:92, 1998.
- [87] H. Yamada. *Strength of biological materials*. The William and Wilkins Company, 1970.
- [88] A. Asenzi and E. Bonucci. The tensile properties of single osteons. *Anat.Res*, 158:375, 1967.
- [89] A. Asenzi and E. Bonucci. The compressive properties of single osteons. *Anat.Res*, 161:377, 1968.
- [90] A. Asenzi and E. Bonucci. The shearing properties of single osteons. *Anat.Res*, 172:499, 1972.
- [91] A. Asenzi, P. Baschieri, and A. Benvenuti. The bending properties of single osteons. *J.Biomech.*, 23:763, 1990.
- [92] A. Asenzi, P. Baschieri, and A. Benvenuti. The torsional properties of single osteons. *J.Biomech.*, 27:875, 1994.

- [93] R. Lakes. On the torsional properties of osteons [letter]. *J.Biomech.*, 28:1409, 1995.
- [94] J.Y. Rho, M.E. Roy II, T.Y. Tsui, and G.M. Pharr. Elastic properties of microstructural components of human bone tissue as measured by nanoindentation. *J.Biomed.Mat.Res*, 45:48, 1999.
- [95] H. Shin, S. Jo, and A.G. Mikos. Biomimetic materials for tissue engineering. *Biomaterials*, 24:4353, 2003.
- [96] S.Mann. Molecular tectonics in biomineralization and biomimetic materials chemistry. *Nature*, 365:499, 1993.
- [97] T. Graham and M. Sarikaya. Growth dynamics of red abalone shell: a biomimetic model. *Mat.Sci.Eng.C*, 11:145, 2000.
- [98] P. Fratzl. Biomimetic materials research: what can we really learn from nature's structural materials? *J. R. Soc. Interface*, 4:637, 2007.
- [99] D.A. LaVan and J.N.Cha. Approaches for biological and biomimetic energy conversion. *PNAS*, 103:5251, 2003.
- [100] S. Deville, E. Saiz, R.K. Nalla, and A.P. Tomsia. Freezing as a path to build complex composites. *Science*, 311:515, 2006.
- [101] Z. Tang, N.A. Kotov, S. Magonov, and B. Ozturk. Nanostructured artificial nacre. *Nature materials*, 2:413, 2003.
- [102] A.K. Geim, S.V. Dubonos, I.V. Grigorieva, K.S. Novoselov, A.A. Zhukov, and S.Y. Shapoval. Microfabricated adhesive mimicking gecko foot-hair. *Nature materials*, 2:461, 2003.
- [103] J. Lee, C. Majidi, B. Schubert, and R. S. Fearing. Sliding-induced adhesion of stiff polymer microfibre arrays. I. Macroscale behaviour. *J.Roy.Soc.Int.*, 5:835, 2008.
- [104] B. Schubert, J. Lee, C. Majidi, and R. S. Fearing. Sliding-induced adhesion of stiff polymer microfibre arrays. II. Macroscale behaviour. *J.Roy.Soc.Int.*, 5:845, 2008.
- [105] R.D.B. Fraser and T.P. Macrae. Molecular structure and mechanical properties of keratins. *Symposia of the Society for Experimental Biology*, 34:211, 1980.

- [106] D.J. Tomlinson, C.H. Mulling, and T.M. Fakler. Invited review: Formation of keratin in the bovine claw: Roles of hormones, minerals, and vitamins in functional claw integrity. *J.Dairy.Sci*, 87:797, 2004.
- [107] J.M. Gillespie and M.J. Frenkel. The diversity of keratin. *Comp.Biochem.Physiol*, 47B:339, 1974.
- [108] U.G.K. Wegst and M.F. Ashby. The mechanical efficiency of natural materials. *Philo.Mag*, page 2167, 2004.
- [109] M.F. Ashby, L.J. Gibson, U. Wegst, and R. Olive. The mechanical properties of natural materials I: Material property charts. *Proc.Roy.Soc*, A450:123, 1995.
- [110] G. Wei, B. Bhushan, and P.M. Torgerson. Nanomechanical characterization of human hair using nanoindentation and sem. *Ultramicroscopy*, 105:742, 2005.
- [111] J.M. Maxwell and M.G. Huson. Scanning probe microscopy examination of the surface properties of keratin fibres. *Micron*, 36:127, 2005.
- [112] J.W.S. Hearle. A critical review of the structural mechanism of wool and hair fibers. *Int.J.Bio.Macro*, 27:123, 2000.
- [113] M. Feughelman. Creep of wool fibers in water. *J.Textile Int*, 45:T634, 1954.
- [114] M. Feughelman. *Mechanical properties and structure of alpha-keratin fibers*. UNSW press, 1997.
- [115] F.J. Wortmann and H. Zahn. The stress/strain curve of alpha-keratin fibers and the structure of the intermediate filament. *Text. Res. J.*, 64:737, 1994.
- [116] J. Cao. Is the α - β transition of keratin a transition of α -helices to β -pleated sheets? Part I. In situ XRD studies. *J.Mole.Stru*, 553:101, 2000.
- [117] J. Cao. Is the α - β transition of keratin a transition of alpha-helices to beta-pleated sheets II. Synchrotron investigation for stretched single specimens. *J.Mole.Stru*, 607:69, 2002.
- [118] M. Feughelman. Natural protein fibers. *J. Appl. Polym. Sci.* 83: 489 507, 2002, 83:489, 2002.
- [119] R. Marks and G. Plewig. *Stratum corneum*. Springer-Verlag, 1983.

- [120] H. Oxlund, J. Manschot, and A. Viidik. The role of elastin in the mechanical properties of skin. *J.Biomech.*, 3:213, 1988.
- [121] R.H. Wildnauer, J.W. Bothwell, and A.B. Douglass. Stratum corneum biochemical properties I. Influence of relative humidity on normal and extracted human stratum corneum. *J. Inves. Dermatology*, 56:72, 1971.
- [122] K. S. Koutroupi and J. C. Barbenel. Mechanical and failure behaviour of the stratum corneum. *J. Biomech*, 23:281, 1990.
- [123] Y.S. Papir, K.H. Hsu, and R.H. Wildnauer. The mechanical properties of stratum corneum I. The effect of water and ambient temperature on the tensile properties of newborn rat stratum corneum. *Biochem.Biophy.Acta*, 399:170, 1975.
- [124] K.S. Wu, W.W. van Osdolb, and R.H. Dauskardt. Mechanical properties of human stratum corneum: Effects of temperature, hydration, and chemical treatment. *Biomaterials*, 27:785, 2006.
- [125] K.S. Wu, M.M. Stefik, K.P. Ananthapadmanabhan, and R.H. Dauskardt. Graded delamination behavior of human stratum corneum. *Biomaterials*, 27:5861, 2006.
- [126] D.H. Leach. *The structure and function of equine hoof wall*. PhD thesis, University of Saskatchewan, 1980.
- [127] M.L. Ryder. Structure of rhinoceros horn. *Nature*, 193:1199, 1962.
- [128] T.L. Hieronymus, L.M. Witmer, and R.C. Ridgely. Structure of white rhinoceros (*ceratotherium simum*) horn investigated by x-ray computed tomography and histology with implications for growth and external form. *J.Morphology*, 267:1172, 2006.
- [129] J.L. Rachlow and J. Berger. Conservation implications of patterns of horn regeneration in dehorned white rhinos. *Convervation Biology*, 11:84, 1997.
- [130] A. Kitchener. Effect of water on linear viscoelasticity of horn sheath keratin. *J.Mat.Sci.let.*, 6:321, 1987.
- [131] M. Druhala and M. Feughelman. Dynamic mechanical loss in keratin at low temperatures. *Collid.Poly.Sci*, 252:381, 1974.

- [132] Z. Alexander and E. Joyce. Studies in reptilian colour response. I. The bio-nomics and physiologu of the pigmentary activity of the chameleom. *Phil. Tran. Roy. Soc. Lon. B*, 223:27, 1934.
- [133] N.J. Alexander and P.F. Parakkal. Formation of α and β -type keratin in lizard epidermis during the molting cycle. *Z Zellforsch*, 101:72, 1969.
- [134] Alexander NJ. Comparison of α -and β keratin in raptiles. *Z Zellforsch*, 110:153, 1970.
- [135] C.F. Carlton. The color changes in the skin of the called Florida chameleon, *Anolis Carolinensis* cuv. *Proc. Amer. Acad. Arts. Sci.*, 39:259, 1903.
- [136] N.J. Alexander and W.F. Fahrenbach. The dermal chromatophores of *Anolis carolinensis* (Reptilia, Iguanidae). *AM. J. Anat.*, 126:41, 1969.
- [137] S.T. Rohrlich and R.W. Rubin. Biochemical chracterization of crystals from the dermal iridophores of a chamelron *anolis carolinensis*. *The J Cell Bio*, 66:635, 1975.
- [138] R.H.C. Bonser. Melanin and the abrasion resistance of feathers. *The Condor*, 95:590, 1995.
- [139] R.H.C. Bonser and J.W. Farrent. Influence of hydration on the mechanical performance of duck down feathers. *Bri.Poul.Sci.*, 42:271, 2001.
- [140] R.C.H. Bonser and C. Dawson. The structural mechanical properties of down feathers and biomimicking natural insulation materials. *J.Mat.Sci.let.*, 18:1769, 1999.
- [141] R.C.H. Bonser and C. Dawson. The mechanical properties of down feathers from gentoo penguins (*pygoscelis papua*). *J.Zool*, 251:535, 2000.
- [142] J. Zi, X.Yu, Y. Li, X. Hu, C. Xu, X. Wang, X. Liu, and R. Fu. Coloration strategies in peacock feathers. *PNAS*, 100:12576, 2003.
- [143] K. Nassau. *The physics and chemistry of color 2nd ed.* Wiley, New York, 2001.
- [144] J. Bereiter-Hahn, A.G.P. Matolts, and K.S. Richards. *Biology of the integument:Vertebrate*, volume 2. Springer, 1986.
- [145] D.J. Brink and N.G. van der Berg. Structural colours from the feathers of the bird *Bostrychia hagedash*. *J Phys D: Appl Phys*, 37:813, 2004.

- [146] P.P. Purslow and J.F. V. Vincent. Mechanical properties of primary feathers from the pigeon. *J.Exp.Bio.*, 72:251, 1978.
- [147] W.R. Corning and A.A. Biewener. In vivo strains in pigeon flight feather shafts: Implications for structural design. *J.Exp.Bio.*, 201:3057, 1998.
- [148] A.M. Taylar, R.H.C. Bonser, and J.W. Farrent. The influence of hydration on the tensile and compressive properties of avian keratinous tissues. *J.Mat.Sci.*, 39:939, 2004.
- [149] R.H.C. Bonser. The mechanical performance of medullary foam from feather. *J.Mat.Sci.let.*, 20:941, 2001.
- [150] M. Butler and A.S. Johnson. Are melanized feather barbs stronger? *J.Exp.Bio.*, 207:285, 2003.
- [151] P.R. Stettenheim. The integumentary morphology of modern birds-an overview. *Amer.Zoo*, 40:461, 2001.
- [152] A.U. Luescher. *Manual of Pirrot Behavior*. Number 252. Blackwell Publishing, 2006.
- [153] P. Bhler. The visual peculiarities of the toucans bill and their principal biological role (Ramphastidae), aves. In H. Ulrich, editor, *Tropical Biodiversity and Systematics*. Zoologisches Forschungsinstitut und Museum Alexander Koenig, 1997.
- [154] D.H. Clayton and P. Cotgreave. Relationship of bill to grooming behavior in birds. *Anim. Behav*, 47:195, 1994.
- [155] R.S. Lakes. Foam structures with a negative poisson's ratio. *Science*, 235:1038, 1987.
- [156] Y. Seki, S.G Boddess, and M.A. Meyers. unpublished results. 2009.
- [157] S. Jain, R. Kumar, and U.C. Jindal. Mechanical behaviour of bamboo and bamboo composite. *J.Mat.Sci.*, 27:4598, 1992.
- [158] S. Amada and R.S. Lakes. Viscoelastic properties of bamboo. *J.Mat.Sci.*, 32:2693, 1997.

- [159] L.J. Gibson, M.F. Ashby, G.N. Karam, U.G.K. Wegst, and H.R. Shercliff. The mechanical properties of natural materials II: Microstructures for mechanical efficiency. *Proc.Roy.Soc*, A450:141, 1995.
- [160] S.P. Silva, M.A. Sabino, E.M. Fernandes, V.M. Correlo, L.F. Boesel, and R.L. Reis. Cork: properties, capabilities and applications. *Int.Mat.Rev*, 50:345, 2005.
- [161] R. Huiskes, R. Ruimerman, G.H. van Lenthe, and J.D. Janssen. Effects of mechanical forces on maintenance and adaptation of form in trabecular bone. *Nature*, 405:704, 2000.
- [162] Lucchinetti E, Thomann D, and Danuser G. Review: Micromechanical testing of bone trabeculae-potentials and limitations. *J.Mat.Sci.*, 35(6057), 2000.
- [163] S.D Ryan and J.L. Williams. Tensile testing of rodlike trabeculae excised from bovine femoral bone. *J.Biomech.*, 22:351, 1989.
- [164] J.Y. Rho and C.H. Turner R.B. Ashman. Young's modulus of trabecular and cortical bone material: ultrasonic and microtensile measurements. *J.Biomech.*, 26:111, 1993.
- [165] K.L. Reed and T.D. Brown. Elastic modulus and strength of emu cortical bone. *Iowa. Orthop. J.*, 21:53, 2001.
- [166] W.C. Hayes and D.R. Carter. Postyield behavior of subchondral trabecular bone. *J.Biom.Mat.Res*, 7:537, 1976.
- [167] P.H. Thornton and C.L. Magee. The deformation of aluminium foams. *Met. Tran.*, 6A:1253, 1975a.
- [168] E.Andrews, W. Sanders, and L.J.Gibson. Compressive and tensile behavior of aluminum foam. *Mat.Sci.Eng.*, A270:113, 1999.
- [169] A.G.Evans, J.W. Hutchinson, and M.F.Ashby. Multifunctionality of cellular metal systems. *Prog.Mat.Sci*, 43:171, 1999.
- [170] A.G.Evans, J.W. Hutchinson, N.A. Fleck, M.F.Ashby, and H.N.G Wadley. The topological design of multifunctional cellular metal. *Prog.Mat.Sci*, 46:309, 2001.
- [171] R.K. Traeger. Physical properties of rigid polyurethane foams. *J.Cell.Plast*, 3:405, 1967.

- [172] V.A. Matonis. Elastic behavior of low density rigid foams in structural applications. *Soc.Plast.Eng.J*, page 1024, Sep 1964.
- [173] M. Wilsea, K.L. Johon, and M.F. Ashby. Indentation of foamed plastics. *Int.J.Mech.Sci*, 17:457, 1975.
- [174] M.R. Patel and I. Finnie. Structural features and mechanical properties of rigid cellular plastics. *J.Mater*, 5:457, 1970.
- [175] J.R. Vinson. *The Behavior of Sandwich Structures of Isotropic and Composite Materials*. CRC, 1999.
- [176] A. Vautrin. *Mechanics of Sandwich Structures*. Springer, 1998.
- [177] H.G. Allen. *Analysis and design of structural sandwich panels*. Pergamon press, 1969.
- [178] A.G. Hanssen, M. Langseth, and O.S. Hopperstad. Static and dynamic crushing of circular aluminium extrusions with aluminium foam filter. *Int.J.Imp.Eng.*, 24:475, 2000.
- [179] A.G. Hanssen, M. Langseth, and H. Ilstad. Validation of constitutive models applicable to aluminium foam. 44:359, 2002.
- [180] W. Schroeder, K. Martin, and B. Lorensen. *The Visualization Toolkit, An Object-Oriented Approach To 3D Graphics, 4th edition*. Kitware, Inc., 2006.
- [181] *The Visualization Toolkit User's Guide*, kitware, inc. 5th edition edition, 2006.
- [182] B. Dresp, P. Jouventin, and K. Langley. Ultraviolet reflecting photonic microstructures in the king penguin beak. *The Anatomical record part A*, 22:310, 2005.
- [183] B. Dresp and K.Langley. Fine structural dependence of ultraviolet reflections in the king penguin beak horn. *The Anatomical record part A*, 288A:213, 2006.
- [184] T. C. Lee, S. Mohsin, D. Taylor, R. Parkesh, T. Gunnlaugsson, F. J. OBrien, M. Giehl, and W. Gowin. Detecting microdamage in bone. *J.Anat.*, 203:161, 2003.
- [185] T.L.A. Moore and L.J Gibson. Microcrack accumulation in bovine trabecular bone in uniaxial compression. *J.Biomech.Eng.*, 124:63, 2002.

- [186] T. Clive Lee, F.J. OBrien, and D. Taylor. The nature of fatigue damage in bone. *Int.J.Fatigue.*, 22:847, 2000.
- [187] T. C. Lee, F.J. OBrien, and D. Taylor. The effect of bone microstructure on the initiation and growth of microcracks. *J.Orth.Res.*, 23(475), 2005.
- [188] N. L. Fazzalari, M. R. Forwood, B.A. Manthey, K. Smith, and P. Kolesik. Three-dimensional confocal images of microdamage in cancellous bone. *Bone*, 23:373, 1998.
- [189] F.J. O brien, D. Taylor, G.R. Dickson, and T.C. Lee. Visualisation of three-dimensional microcracks in compact bone. *J.Anat.*, 197:413, 2000.
- [190] I.O. Smith, F. Ren, M.J. Baumann, and E.D. Case. Confocal laser scanning microscopy as a tool for imaging cancellous bone. *J.Biomed. Mat. Res. B.*, 79B:185, 2005.
- [191] R.L. Riggs, W. Wahner, W.L. Dunn, B. Mazess, K.P. Offord, and L.J. Melton III. Differential changes in bone mineral density of appendicular and axial skeleton with aging. *J.Clin.Invest*, 67:328, 1981.
- [192] L.B. Freund. unpublished results. 2009.
- [193] E. Evans and K. Ritchie. Strength of weak bond connecting flexible polymer chains. *Biophy. J.*, 76:2439, 1999.
- [194] E. Evans and K. Ritchie. Dynamic strenght of molecular adhesion bonds. *Biophy. J.*, 72:1541, 1997.
- [195] E.H.Jr. Burt. Tips on wings and other thing. In E.H.Jr. Burt, editor, *The Behavioral Significance of Colour*, page 75. STPM press, New York: Garlan, 1979.
- [196] E.H.Jr. Burt. An analysis of physical, physiological and optical aspects of avian colouration with emphasis on wood-warblers. *Ornithol.Monogr*, 38(1), 1986.
- [197] R.H.C. Bonser. The Young's modulus of the ostrich claw keratin. *J.Mat.Sci.let.*, 19:1039, 2000.
- [198] M. Todoh, M. Ihara, T. Matsumoto, and M. Tanaka. Relationship between mechanical property of cancellous bone and hardness of trabeculae. *JSEM Int. J. C.*, 40:1075, 2004.

- [199] E. Dall'Ara, C. Ohman, M. Baleani, and M. Viceconti. The effect tissue component and applied load on vickers hardness of human trabecular bone. *J.Biomech*, 40:3267, 2007.
- [200] G.P. Evans, J.C. Behiri, J.D. Curry, and W. Bonfield. Microhardness and young's modulus in cortical bone exhibiting a wide range of mineral volume fractions, and in a bone analogue. *J.Mat.Sci.*, 1:38, 1990.
- [201] C. Hernandez, S. Tang, B. Baumbach and P. Hwu, A. Sakkee, A. van der Ham, J. DeGroot, R. Bank, and T. Keaveny. Trabecular microfracture and the influence of pyridinium and non-enzymatic glycation-mediated collagen cross-links. *Bone*, 37:832, 2005.
- [202] Y. Seki, M.S. Schneider, and M.A. Meyers. Structure and mechanical behavior of a toucan beak. *Acta.Mat.*, 53:5281, 2005.
- [203] P.R. Townsend, R.M.Rose, and E.L Radin. Buckling studies of single human trabeculae. *J. Biomech.*, 8:199, 1975.
- [204] C.H.Turner, J. Rho, Y. Takano, and T.Y. Tusi. The elastic properties of trabecular and cortical bone tissues are similar:results from two microscopic measurement technique. *J.Biomech*, 32:437, 1999.
- [205] K.L Reed and T.D Brown. Elastic modulus and strength of emu cortical bone. *Iowa Orthop, J*, 21:53, 2001.
- [206] Y. Seki, B. Kad, D. Benson, and M.A. Meyers. The toucan beak: Structure and mechanical response. *Mat.Sci.Eng.*, 26:1412, 2006.
- [207] G.N. Karam and L.J. Gibson. Elastic buckling of cylindrical shells with elastic cores-II.Experiments. *Int.J.Solids.Stru*, 32:1285, 1995.
- [208] M. A. Dawson and L. J. Gibso. Optimization of cylindrical shells with compliant cores. *Int. J. Solids. Stru.*, 44:1145, 2007.
- [209] C. Habering. The range of applications of structural foams based on cellular metals and alternative polymer solutions. In H.P. Degischer and B. Kriszt, editors, *Handbook of Cellular Metals*, chapter 7, pages 299–312. Wiley-Vch, 2002.
- [210] Livermore Software Technology Corporation. *LS-DYNA Keyword User's Manual*, 2003.

- [211] D. Dempster, R. Mller, H. Zhou, T. Kohler, E. Shane, M. Parisien, S. Silverberg, and J. Bilezikian. Preserved three-dimensional cancellous bone structure in mild primary hyperparathyroidism. *Bone*, 41:19, 2007.
- [212] T. Hildebrand, A. Laib, R. Mller, J. Dequeker, and P. Regsegger. Direct three-dimensional morphometric analysis of human cancellous bone: Microstructural data from spine, femur, iliac crest, and calcaneus. *JBMR*, 14:1167, 1999.
- [213] A. Nazarian, B.D. Snyder, D. Zurakowski, and R. Mller. Quantitative micro-computed tomography: A non-invasive method to assess equivalent bone mineral density. *Bone*, page 302, 2008.
- [214] J.C.M. Teo, K.M. Si-Hoe, J.E.L. Keh, and S.H. Teoh. Correlation of cancellous bone microarchitectural parameters from microct to ct number and bone mechanical properties. *Mat.Sci.Eng.C.*, page 333, 2007.
- [215] L.J. van Ruijven, E.B.W. Giesen, L. Mulder, M. Farella, and T.M.G.J. van Eijden. The effect of bone loss on rod-like and plate-like trabeculae in the cancellous bone of the mandibular condyle. *Bone*, page 1078, 2005.
- [216] W.E. Lorensen and H.E. Cline. Marching cubes: A high resolution 3d surface construction algorithm. *ACM Computer Graphics*, 21:163, 1987.
- [217] M.H. Luxner, A.Woesz, J. Stampfl, P. Fratzl, and H.E. Pettermann. A finite element study on the effects of disorder in cellular structures. *Acta Biomat.*, 2008 in Press.
- [218] H.H. Bayraktar and T.M. Keaveny. Mechanisms of uniformity of yield strains for trabecular bone. *J.Biomech.*, 37:1671, 204.
- [219] D. Ulricha, B. van Rietbergena, H. Weinansb, and P. Regsegger. Finite element analysis of trabecular bone structure: a comparison of image-based meshing techniques. *J.Biomech.*, 12:1187, 1998.
- [220] B. van Rietbergen, H. Weinans, R. Huiskes, and A. Odgaardt. A new method to determine trabecular bone elastic properties and loading using micromechanical finite-element models. *J.Biomech.*, 28:69, 1995.
- [221] N.M. Harrison, P.F. McDonnell, D.C. OMahoney, O.D. Kennedy, F.J. OBrien, and P.E. McHugh. Heterogeneous linear elastic trabecular bone modelling using micro-ct attenuation data and experimentally measured heterogeneous tissue properties. page 2589, 2008.